université
PARIS-SACLAY

TELECOM
ParisTech

Photon-pair generation in hollow-core photonic-crystal fiber

Thèse de doctorat de l'Université Paris-Saclay
préparée à Télécom ParisTech

École doctorale n°572 Ondes et Matière (EDOM)
Spécialité de doctorat: Physique

Thèse présentée et soutenue à Paris, le 17 mai 2019, par

Martin CORDIER

Composition du Jury :

Mme. Virginia D'AURIA
Maître de conférences, Université Nice Sophia Antipolis   Rapporteur
M. Nicolas TREPS
Professeur, Laboratoire Kastler Brossel   Rapporteur
Mme. Catherine LEPERS
Professeur, Télécom SudParis   Président du Jury
M. Michael RAYMER
Professeur, University of Oregon   Examinateur
Mme. Eleni DIAMANTI
Chargée de Recherche, LIP6   Invitée
M. Fetah BENABID
Directeur de recherche, XLIM   Invité
Mme. Isabelle ZAQUINE
Professeur, LTCI, Télécom ParisTech   Directeur de thèse
M. Philippe DELAYE
Directeur de recherche, Laboratoire Charles Fabry   Co-directeur de thèse

Contents

Acknowledgements

Comme chacun le sait, la recherche est un travail au long cours avec des issues souvent incertaines. C'est ce qui la rend à la fois très difficile et incroyablement satisfaisante. J'ai passé de nombreuses heures dans l'obscurité la plus totale, fixant un écran d'ordinateur rougi pour les verres colorés des lunettes de protections laser, à « chercher des paires de photons ». Et pourtant, derrière cette scène un peu absurde du quotidien d'un physicien expérimentaliste, il y avait là, l'aboutissement de ma thèse. En effet, un nouveau record été battu sous mes yeux, preuve ultime de la démonstration d'une idée que nous avions eu deux ans auparavant. En prenant du recul sur ces trois ans et demi de thèse, ce qui me marque le plus, c'est la confiance sans faille qui m'a été accordée. Dans ces quelques lignes, je voudrais remercier toutes les personnes qui l'ont exprimée.

En premier lieu, je voudrais remercier Isabelle Zaquine pour son encadrement de tous les instants lors de cette thèse et du stage qui a précédé. C'est grâce à son dévouement et sa combativité que j'ai pu obtenir une bourse de thèse. Tout en m'offrant une grande liberté d'action sur l'orientation que je voulais donner à ces recherches, sa présence au quotidien a donné un cadre idéal à ce travail de thèse. Sa grande écoute et ses conseils avisés m'ont permis de prendre du recul et ont été une grande source d'encouragement.

Je souhaiterais également remercier Philippe Delaye qui a co-encadré cette thèse. Je ne pourrais compter le nombre de fois où sa fine connaissance d'optique non linéaire est venue éclairer mes interrogations. Tant j'ai pu y apprendre, ces longues discussions ont été l'un des pivots de ma thèse et une grande source d'enrichissement personnel. J'ai eu également la grande chance de passer du temps dans son équipe à l'Institut d'Optique et de travailler avec mon ami Thibault Harlé qui effectuait une thèse en parallèle de la mienne.

Un grand merci également à Fetah Benabid qui m'a accueilli dans son équipe à Limoges pendant plus d'un an et qui a tout mis en œuvre pour que cette collaboration soit fructueuse. L'enthousiasme et la passion qu'il avait pour mon travail m'ont grandement inspiré et encouragé. Cette collaboration a aussi été rendue possible grâce à Frédéric Gérome et Benoit Debord qui m'ont régulièrement prodigué de précieux conseils sur les fibres. Bien sûr ces journées à Limoges n'auraient pas été les mêmes sans la Dream Team du GPPMM: Foued, Matthieu,

1

Martin, David, P'tit Fred, Aymeric, Jonas, Mustafa, Thomas, Maxime, Ali ainsi que celle de GLO : Alex, Ando, Grand Ben'. C'était un plaisir quotidien de travailler avec vous tous!
Merci à tous mes collègues de Télécom, Eleni Diamanti pour ses précieux conseils, sa bonne humeur et son humour ! Je remercie Adeline Orieux à qui ce travail doit beaucoup tant elle m'a aidé. Merci à Julien et Mathieu pour la bonne ambiance au labo et d'avoir partagé leur passion pour la musique et à Eliseu pour toutes les passionnantes discussions philosophiques que nous avons eues. Merci aux permanents du groupe Romain Alléaume, Filippo Miatto et à Renaud Gabet pour avoir pris le temps de m'introduire à l'OLCI. Merci aussi à Ravi pour ses nombreux conseils !

Mes remerciements vont également à mes deux rapporteurs, Virginia D'Auria et Nicolas Treps et aux examinateurs Catherine Lepers et Michael Raymer d'avoir porté intérêt et considérations à mes travaux. Merci à l'ensemble du jury pour leurs remarques, questions et échanges lors de la soutenance.

Je souhaiterais aussi adresser mes remerciements aux professeurs qui ont éveillé en moi une passion pour la physique. En particulier, Arnaud Devos, dont les cours de physique quantique ont été une vraie claque et dont le stage que j'ai effectué avec lui a été une expérience passionnante, fondatrice de mon parcours de recherche. Un grand merci également à Bruno Grandidier, Christophe Delerue et Agnès Maitre qui m'ont permis de faire un master de physique fondamentale en parallèle de mes études d'ingénieur.

Merci à mes parents et à mes deux sœurs qui m'ont toujours soutenu et encouragé à suivre ma propre voie. Enfin, un immense merci, Daga, pour le bonheur et l'amour que tu apportes à ma vie.

Abstract [En]

The thesis reports on the design of photon-pair sources based on fluid-filled hollow-core photonic crystal fiber (FF-HCPCF). It combines two important properties: (1) Raman-free generation thanks to the use of a fluid and to a minute overlap with silica within the hollow-core ; (2) a high versatility in the phase-matching conditions thanks to the fiber microstructuration and choice of fluid.

In order to design a versatile Raman-free photon-pair source, we explored two approaches that entails different waveguiding designs and fluid-filling processes.

On the one hand, we investigate the use of a liquid-filled photonic bandgap HCPCF. We demonstrate that there exists Raman-free spectral range at telecom wavelength compatible with photon-pair generation. On the other hand, we develop, to our knowledge, the first photon-pair source in a gas-filled inhibited-coupling HCPCF which goes along with the first demonstation of Raman-free photon-pair generation in a fiber medium. The source was designed to operate at convenient wavelengths for heralded single photon source; the idler wavelength lies in the telecom wavelength range, while the signal wavelength is in the range of atomic transitions and Silicon single photon detectors. Moreover, we demonstrate experimentally a passive and active control over the generated photon spectral properties. In particular, spectral correlations can be tailored, allowing spectrally entangled and factorable states to be obtained within the same device. More specifically, a gallery of different joint spectral intensity, including exotic shape, is measured by tuning various parameters: gas pressure, pump spectral width, spectral chirp and pump spectral envelope. Furthermore, this photon-pair state is generated over a tunable frequency-range that spans well over tens of THz.

Thus, the present thesis presents both theoretical and experimental results demonstrating the capability of hollow-core photonic crystal fibers to generate Raman-free photon-pair with controllable spectral properties.

Abstract [Fr]

Cette thèse porte sur la conception de fibres à cristaux photoniques à coeur creux remplies de fluide (FF-HCPCF) pour la génération de paires de photons. Ces sources combinent deux propriétés importantes: (1) l'absence de bruit Raman grâce à l'utilisation de fluides et d'un recouvrement optique très limité avec la silice au sein de la fibre; (2) une grande polyvalence dans les conditions d'accord de phase grâce à la microstructuration de la fibre et au choix du fluide.

Dans l'objectif de concevoir une source de paires de photons sans bruit Raman, nous avons exploré deux approches impliquant à la fois des mécanismes de guidages et des types de fluides de remplissages différents.

D'une part, nous avons étudié l'utilisation de fibres à coeur creux à bande interdite photonique, remplies de liquide. Nous démontrons qu'il existe une gamme spectrale aux longueurs d'ondes télécom sans bruit Raman compatible avec la génération de paires de photons. D'autre part, nous avons également développé la première source de photons dans une fibre HCPCF à couplage inhibé remplie de gaz qui a permis la première démonstration de génération de paires de photon sans Raman dans un milieu fibré. La conception de la fibre a été choisie pour fonctionner à des longueurs d'ondes utiles aux sources de photons annoncées ; la longueur d'onde idler se situe dans le domaine télécom, tandis que la longueur d'onde signal est dans la gamme visible des détecteurs de photon unique silicium. De plus, nous démontrons expérimentalement un contrôle actif et passif des propriétés spectrales des photons générés. En particulier, les corrélations spectrales peuvent être modifiées afin d'obtenir un état spectrallement factorisable ou corrélé au sein du même dispositif. Plus précisément, une variété d'intensités spectrales jointes (JSI) de formes différentes, dont certaines exotiques, ont été mesurées en faisant varier différents paramètres : la pression du gaz, la largeur spectrale de la pompe, le chirp ainsi que l'enveloppe spectrale de la pompe. Enfin, la paire de photons est générée sur une plage de fréquence accordable qui s'étend sur des dizaines de THz.

Ainsi, la présente thèse expose des résultats théoriques et expérimentaux démontrant la génération de paires de photons sans diffusion Raman et avec des propriétés spectrales contrôlables.

List of Acronyms

AOPDF: acousto-optic programmable dispersive filter

Ar: argon

BS: beam splitter

BSMF: birefringent single mode fiber

CAR: coincidences to accidental ratio

CW: continuous wave

DC: dark count

DM: dichroic mirror

DSF: dispersion shifted fiber

DUT: device under test

FDFD: finite difference frequency domain

FT: Fourier transformation

FWHM: full width at half maximum

FWM: four-wave mixing

GF: gas-filled

GVD: group-velocity dispersion

GVM: group-velocity matching

HCPCF: hollow-core photonic crystal fiber

HWP: half-wave plate

IC: inhibited-coupling

JSA/JSI: joint spectral amplitude/intensity

JTA/JTI: joint temporal amplitude/intensity

LF: liquid-filled

OLCI: optical low coherence interferometry

OSA: optical spectrum analyser

PBG: photonic bandgap

PBS: polarising beam splitter

PCF: photonic-crystal fiber

RS: Raman-scattering

SDM: spectral density map

SEM:scanning electron microscope

SET: stimulated emission tomography

Si: silica

SLM: spatial light modulator

SM: surface mode

SMF: single mode fiber

SNR: signal to noise ratio

SPD: single photon detector

S-SPD: superconducting single photon detector

SPDC: spontaneous parametric down conversion

TIR: total internal reflection

TM: temporal mode

WDM/CWDM/DWDM: wavelength division multiplexer / coarse WDM / dense WDM

Xe: xenon

ZDW: zero dispersion wavelength

INTRODUCTION

Based on the laws of quantum mechanics, quantum information science has the potential for significantly improving our modern technologies. More specifically, it paves the way to an improvement in terms of computational power (quantum computing) and communication security (quantum communication). The conjoint ability to encode, manipulate and communicate quantum mechanical objects are the sine qua non condition on the roadmap toward the development of quantum technologies. In this fast-growing field, the capability to distribute quantum bits (qubits) to remote locations is highly desirable and photons provide the ideal *flying qubits* - the quantum information carrier for large distance communication [1].

In this context, non-classical states of light, encompassing single photons, entangled photon-pair states and squeezed states are one of the central element of quantum information. The development of non-classical light source at telecom wavelength is the focus of this work.

Photon pair sources

One of the most widespread sources of non-classical states of light are photon-pair sources, also called heralded single photon sources. The photon generation process is based on nonlinear effects allowing to probabilistically annihilate photons from an intense pump and simultaneously generate two photons at different frequencies (called signal and idler). In general, these effects are either spontaneous parametric down conversion (SPDC) or four-wave mixing (FWM) depending on whether the medium has a $\chi^{(2)}$ or $\chi^{(3)}$ nonlinearity.

Fig. 1: *Schematic describing a photon-pair source. The filled dots corresponds to photons whereas the empty dots corresponds to a non-generation (probabilistic process).*

Among the numerous platforms, $\chi^{(2)}$ nonlinear media and, in particular, bulk crystals have

been historically the workhorse for photon pair generation due to the relative ease in terms of experimental setup, their cost and their availability. Today, KDP (potassium dideuterium phosphate), BBO (beta barium borate), LiNbO3 (lithium niobate) and LiIO3 (lithium iodate) are typically chosen for the strength of their $\chi^{(2)}$ nonlinearity, which is directly linked to the photon pair generation efficiency. As far as the use of cristals is concerned, the pioneering work of Kwiat *et al.* [2] should be mentioned.

Although generally less nonlinear, $\chi^{(3)}$ media, and in particular waveguides and optical fibers have gained much attention in the recent years, offering new prospects in terms of scalability and integrability. For instance, more than 550 photonic components have been recently integrated on a single silicon chip, including 16 identical four-wave mixing photon-pair sources [3]. Alternatively, fiber-based photon-pair sources have many advantages; they are easily manufacturable, cost effective, robust, alignment-free and compatible with fiber optical network since the photon pairs are directly emitted in the fundamental transverse mode of a fiber.

Fiber architectures

As far as fibers are concerned, photon-pairs have been produced in many different architectures encompassing single-mode fiber (SMF) [4, 5], dispersion-shifted fiber (DSF) [6, 7, 8, 9], birefringent single-mode fiber (BSMF) [10, 11] and photonic crystal fiber (PCF) [12, 13, 14, 15, 16, 17, 18]. However, the performances of these photon-pair sources are most often plagued by a concomitant nonlinear effect, Raman-scattering (RS). Indeed, in addition to the four-wave mixing which leads to photon-pair generation, an interaction between the pump and phonons in the medium results in the generation of scattered photons. Due to the amorphous nature of silica (i.e. the fiber core material), the Raman gain is broadband [19], thus generating a large amount of scattered photons around the pump frequency. In fact, whatever the photon-pair frequencies, some Raman-scattered photons will also be generated at the same frequencies, that cannot be filtered. For this reason, Raman-scattering degrades the achievable signal to noise ratio. Raman-scattering can be reduced by cooling down the fiber to cryogenic temperature with nitrogen (T = 77 K) [4, 8, 9] or even helium (T = 4 K) [7], however it cannot be completely suppressed and it adds a layer of experimental difficulty making it much less practical for applications and limited in terms of integration.

An ideal solution consists in changing the propagation medium (silica) to one without a broadband Raman gain. Unfortunately, any other glass (chalcogenide, tellurite, fluoride, etc.) does not solve this issue since all amorphous materials exhibit broad Raman gain spectra [20, 21]. In contrast, there is a particular kind of fiber which allows to guide light with a negligible overlap with the glass: *hollow-core photonic crystal fiber* (HCPCF).

INTRODUCTION

Hollow-core photonic crystal fiber

Since their first developments 20 years ago, hollow-core photonic crystal fibers (also called hollow-core fiber) have attracted huge interest by virtue of their optical properties that are non-existent in conventional fibers. The empty core can be filled (with a gas, liquid, cold atoms, biological compunds, etc.) allowing to microconfine light and matter over lengths up to kilometers. For these reason, HCPCF have become a remarkably useful tool in many fields such as: atom optics, nonlinear optics, metrology as well as high optical field physics and plasma (see [22, 23] for reviews). More specifically, HCPCF can be subdivided into two families denominated by their guidance mechanisms, namely, *photonic bandgap* (PBG) and *inhibited coupling* (IC) HCPCF. As we will detail later on, they exhibit very different optical properties (e.g. transmission bandwidth, loss, dispersion, etc) and geometrical designs (see Fig. 3).

Our strategy is to fill HCPCFs with a fluid with either discrete Raman lines (liquid) or non-existent (noble gas) in order to avoid the overlap between Raman-scattered photons and photon-pairs. By eliminating the Raman-scattering issue, the principal motivation behind this work is to design photon pair sources with a high signal to noise ratio while keeping a fiber based architecture and its advantages (room temperature, alignment-free, robustness, etc.). In the past, HCPCFs have already demonstrated the ability to explore Raman-free nonlinear optics [24] but only few works have investigated quantum information applications. Barbier *et al.* [25] use a Liquid-filled PBG-HCPCF to obtain what is to our knowledge the first and, apart from the work presented in this manuscript, only demonstration of photon pairs in such media. In [25], the authors have shown that Raman-scattering is reduced by three orders of magnitude compared to a silica-core fiber. In another regime, Finger *et al.* [26, 27] report a Raman-free squeezed-vacuum bright twin-beam source based on IC-HCPCF filled with a noble gas (argon).
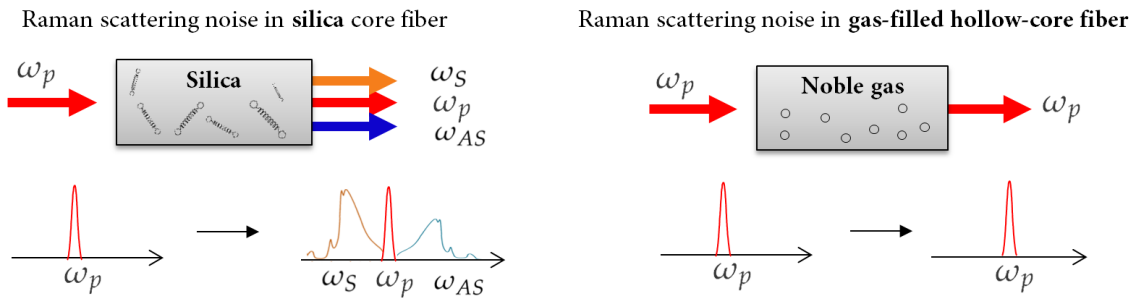

Raman scattering noise in **silica** core fiber — Raman scattering noise in **gas-filled hollow-core fiber**

Fig. 2: *Comparison between Raman scattering in silica core fibers (SMF, DSF, BSMF, PCF) and in a hollow-core fiber (HCPCF) filled with a noble gas. In silica, the Raman process generates noise at lower (Stokes) and higher (Anti-Stokes) frequencies than the pump whereas in a monoatomic noble gas, no Raman-scattering occur because of the absence of molecules. Relative intensities are arbitrary.*

Objectives of the thesis

The main objective of the thesis was to design photon-pair sources based on hollow-core fibers.

Initially, I have undertaken to extend the work of Barbier et al. in order to have a hollow-core photon-pair source at telecom wavelengths (rather than in the near infrared). Starting from scratch, at the beginning of the thesis the first step has been to find a good architecture of fiber and liquid. In this regard, I have developed simulation tools to infer the optical properties of these fibers depending on their geometrical design and of the filling medium and I have performed experimental linear and nonlinear characterizations. Once the fiber architecture was found, I built an experimental setup to characterize its performance in the photon-pair regime.

In parallel to this work, I have also investigated how to adapt hollow-core fiber designs in order to explore spectral correlation engineering. A control of the photon-pairs spectral properties is of utmost importance in most quantum information applications. I showed that it can be realized by tailoring the dispersion properties of the fiber using a control of the fiber micostructure. As a result from this study, I discovered how a specific type of hollow-core fiber (the inhibited-coupling fiber) exhibits all the requirements in that regard. More specifically, I have identified that the multiband dispersion profile of such fibers can be used to tailor the phase-matching conditions and to control the degree of time-frequency entanglement. I took the opportunity of an on-going collaboration with the GPPM group of XLIM, which detains state of the art hollow-core fabrication facility, to test this hypothesis experimentally. I identified a new fiber design, here based on a gas-filling (xenon) and demonstrate the first photon-pair generation in such a medium. Emphasis was placed onto designing the photon-pair source for heralded-single photon source. Signal and idler are created at benchmark wavelengths (telecom and visible range) and the photon-pair spectral properties are tailored (into factorable state). Moreover, as I will detail, the gas-filling allows reaching unprecedented signal to noise ratio compared to other fiber architectures.
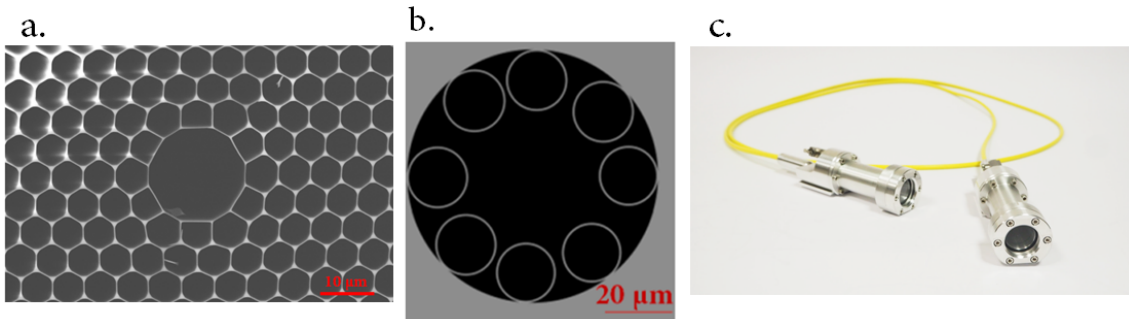

Fig. 3: *Cross section of **a.** the liquid-filled photonic bandgap HCPCF used in Part B **b.** the gas-filled inhibited coupling HCPCF used in Part C. The white areas correspond to silica and the black areas are filled with either the liquid or gas. **c.** Photo showing the sealed gas cells and fiber from Part C.*

Outline of the thesis

The manuscript is composed of three parts.

- *Part A* provides the theoretical framework. The first chapter A1 describes FWM photon-pair generation in an optical fiber. The second chapter A2 introduces useful tools to describe the spectral properties of the photon-pair: the Joint Spectral Amplitude (JSA) and the Schmidt decomposition. In particular, the notion of spectral correlation/spectral entanglement and its consequences are discussed. Finally, the Raman scattering process and its characteristics depending of the medium (diatomic, silica, liquid, gas, etc.) are described in chapter A3.

- *Part B* presents a Liquid-filled PBG-HCPCF based on a commercial HCPCF. While the first demonstration of photon-pair in this medium was in the infrared wavelength range [25], herein we design a source toward the generation of photon-pairs at telecom wavelength. In the first chapter, several combinations of liquids and fibers are investigated through experimental characterizations and simulations. The second chapter describes how the Raman-scattering noise can be avoided in such liquid-filled fibers and our experimental setup.

- *Part C* describes the Gas-filled IC-HCPCF. We demonstrate for the first time to our knowledge a photon-pair source in such media and its Raman-free property. The first chapter introduces the concept of spectral correlations manipulation and why it is important in view of quantum information applications. Moreover, after describing the inhibited coupling guidance mechanism, we show theoretically how the IC fibers design offer a huge versatility in tailoring the photon-pair spectral properties (including spectral correlations). We demonstrate experimentally this versatility in the second chapter by performing a spectral tomography of the generated biphoton state. Finally, the third chapter presents the characterisation of the source in the photon-pair regime.

Part A

Spontaneous four-wave mixing for photon-pair generation

Part A of the manuscript introduces the different theoretical concepts that will be useful in the following of the manuscript. In the first chapter, a model is given to describe spontaneous four-wave mixing nonlinear process and to derive the photon-pair state as a function of both medium and pump parameters. The second chapter introduces key-concepts: (i) the joint-spectral amplitude function and (ii) the spectral density map which describe the photon-pair time-frequency properties. The last chapter describes another nonlinear effect of importance in this manuscript, Raman-Scattering, and why it is generally detrimental for photon-pair generation.

Chapter A1: Spontaneous Four-Wave Mixing in Optical Fiber

Chapter A2: Joint Spectral/Temporal Amplitude

Chapter A3: Avoiding Raman scattering

Chapter A1

Spontaneous Four-Wave Mixing in Optical Fiber

In this chapter, we derive a semi-quantum description to detail the spontaneous four-wave mixing nonlinear effect. In this approach, the electromagnetic fields describing individual photons are quantized whereas the pump and the medium are considered classical. Starting from the Schrödinger equation, the nonlinear Hamiltonian and the photon pair wavefunction are derived.

The development is inspired by the thesis manuscripts of Warren Paul Grice [28] and Margaux Barbier [29] who both derived a semi-classical and a quantum model for describing the generation of photon pair through four-wave mixing.

1.1 Dielectric Polarization

a) Linear regime

In the linear regime, the propagation of an electromagnetic wave in matter is influenced by the dielectric polarization induced by the electric field of the wave. The dielectric susceptibility $\chi^{(1)}$ relates the dielectric polarization to the electric field [30]:

$$\hat{P}_i(\mathbf{r}, t) = \epsilon_0 \sum_j \chi_{ij}^{(1)}(\omega) \hat{E}_j(\mathbf{r}, t) \tag{A1.1}$$

where ϵ_0 is the vacuum permittivity, $\chi^{(1)}$ is a rank 2 tensor, expressed in the form of a 3x3 matrix, and the indices i and j take the values of the Cartesian coordinates (x,y,z).

b) Nonlinear regime

In a regime of strong electromagnetic field, the dielectric response to the electromagnetic field is no longer linear and Eq. (A1.1) is no longer valid. Then, the polarization of a transparent media is given by [30]:

$$\hat{P}_i = \epsilon_0 \underbrace{\sum_j \chi_{ij}^{(1)} \hat{E}_j}_{\text{linear}} + \epsilon_0 \underbrace{\sum_j \sum_k \chi_{ijk}^{(2)} \hat{E}_j \hat{E}_k + \epsilon_0 \sum_j \sum_k \sum_l \chi_{ijkl}^{(3)} \hat{E}_j \hat{E}_k \hat{E}_l}_{\text{non linear}} + ... \tag{A1.2}$$

where each $[\chi^{(k)}]$ is a real k+1 rank tensor composed of $(k+1)^{k+1}$ components such that $\chi_{ij}^{(1)} = \mathbf{e}_i.[\chi^{(1)}]\mathbf{e}_j$, $\chi_{ijk}^{(2)} = \mathbf{e}_i.[\chi^{(2)}]\mathbf{e}_j\mathbf{e}_k$ and $\chi_{ijkl}^{(3)} = \mathbf{e}_i.[\chi^{(3)}]\mathbf{e}_j\mathbf{e}_k\mathbf{e}_l$, with $\mathbf{e}_i$ is the unit vector of axis i.

In the following, we will consider only isotropic media (invariance along three spatial directions). In that case the dielectric polarization and the electric field are parallel, such that the equation simplifies to:

$$\hat{\mathbf{P}}(\mathbf{r}, t) = \epsilon_0 \chi^{(1)}\hat{\mathbf{E}}(\mathbf{r}, t) + \epsilon_0 \chi^{(2)}\hat{\mathbf{E}}(\mathbf{r}, t)\hat{\mathbf{E}}(\mathbf{r}, t) + \epsilon_0 \chi^{(3)}\hat{\mathbf{E}}(\mathbf{r}, t)\hat{\mathbf{E}}(\mathbf{r}, t)\hat{\mathbf{E}}(\mathbf{r}, t) + ... \tag{A1.3}$$

We define:

$$\hat{\mathbf{P}}_{\text{L}} = \epsilon_0 \chi^{(1)}\hat{\mathbf{E}}(\mathbf{r}, t) \tag{A1.4}$$

$$\hat{\mathbf{P}}_{\text{NL}} = \epsilon_0 \chi^{(2)}\hat{\mathbf{E}}(\mathbf{r}, t)\hat{\mathbf{E}}(\mathbf{r}, t) + \epsilon_0 \chi^{(3)}\hat{\mathbf{E}}(\mathbf{r}, t)\hat{\mathbf{E}}(\mathbf{r}, t)\hat{\mathbf{E}}(\mathbf{r}, t) + ... \tag{A1.5}$$

The dielectric polarization is an electronic response from the medium. Hence it is expected that the nonlinear terms become non-negligible when the amplitude of the applied field is of the order of the characteristic atomic electric field strength $E_{at} = e/a_0^2$, where e is the charge of the electron and $a_0 = \hbar^2/me^2$ the Bohr radius [30]. Since $\chi^{(1)}$ is of the order of unity, we can expect that $\chi^{(2)}$ is of the order of $1/E_{at}$ and thus $\chi^{(k)} \approx \chi^{(k-1)}/E_{at} = 1/E_{at}^{k-1}$. Since the susceptibilities quickly decrease for an increasing **k** order, only nonlinear effects of the second order $\chi^{(2)}$ and third order $\chi^{(3)}$ susceptibilities are generally accessible with a standard laser. Hence, the higher order terms are neglected.

Let us illustrate the role of the nonlinear dielectric polarization with examples. First, we consider the case where medium is pumped by an electromagnetic field consisting of a plane wave $E(t) = \epsilon_1 e^{-i\omega_1 t} + c.c..$ The term $\hat{\mathbf{P}}_{\text{L}}$ is the linear response of the medium. It consists of part of the electromagnetic field oscillating at the same frequency ω_1. The nonlinear term $\hat{\mathbf{P}}_{\text{NL}}$ contains components of the form E^2 and E^3 and therefore bears terms oscillating as twice the frequency (second harmonic) or three times the frequency and more. The situation becomes even

more diverse when considering an electromagnetic field in a superposition of fields with different central frequencies. Table A1.1 sums up all the possible different frequency components that can arise from a nonlinear interaction when considering a monochromatic field (first row) and a field which is a sum of two plane waves (second row). Note that the number of frequency components increases rapidly with the number of input wavelengths.

Tab. A1.1: Frequency components of the dielectric polarization induced by a plane wave. SHG: second harmonic generation, OR: optical rectification, SPM: self-phase modulation, THG: third harmonic generation, SFG: sum frequency generation, DFG: difference frequency generation

Input Field	$\chi^{(1)}$	$\chi^{(2)}$	$\chi^{(3)}$
$E(t) = \epsilon_1 e^{-i\omega_1 t}$ + c.c.	ω_1	$2\omega_1$ (SHG) 0 (OR)	$3\omega_1$ (THG) ω_1 (SPM)
$E(t) = \epsilon_1 e^{-i\omega_1 t}$ $+\epsilon_2 e^{-i\omega_2 t}$ + c.c.	ω_1 ω_2	$2\omega_1$ (SHG) $2\omega_2$ (SHG) $\omega_1 + \omega_2$ (SFG) $\omega_1 - \omega_2$ (DFG) 0 (OR)	$3\omega_1$ (THG) $3\omega_2$ (THG) $2\omega_1 + \omega_2$ $2\omega_1 - \omega_2$ $\omega_1 + 2\omega_2$ $\omega_1 - 2\omega_2$

c) Derivation

In practice, nonlinear media often exhibit symmetries such that many components of the nonlinear susceptibility tensor vanish. In the case of centrosymmetry (invariance under inversion through the origin) for instance, it can be easily shown [30] that all the even nonlinear susceptibilities vanish ($\chi^{(2)} = 0$, $\chi^{(4)} = 0$, etc.).

Optical fibers, whether composed of a silica core or of a hollow-core filled with a liquid or gas are centrosymmetric. Thus, the smallest nonlinear susceptibility order we consider is the third order. Discarding higher order odd terms, the dielectric polarization becomes:

$$\hat{\mathbf{P}}_{\mathrm{NL}}(\mathbf{r}, t) = \epsilon_0 \chi^{(3)} \hat{\mathbf{E}}(\mathbf{r}, t)\hat{\mathbf{E}}(\mathbf{r}, t)\hat{\mathbf{E}}(\mathbf{r}, t) \tag{A1.6}$$

Let us assume that the electromagnetic field **E** is composed of four distinctive fields designated as pump1, pump2, signal and idler oscillating at ω_{p1}, ω_{p2}, ω_s and ω_i. Since we are considering a fiber media, it is justified to restrict ourselves to electromagnetic fields propagating in the z direction, in the fundamental transverse mode of the fiber. We also consider that all four fields share the same linear polarization along **e** which greatly simplifies the notations.

$$\hat{E}(z, t) = \hat{E}_{p1}(z, t) + \hat{E}_{p2}(z, t) + \hat{E}_s(z, t) + \hat{E}_i(z, t) \tag{A1.7}$$

All the fields may be expressed in terms of their positive and negative frequency parts:

$$\hat{E}_k(z, t) = \hat{E}_k^{(+)}(z, t) + \hat{E}_k^{(-)}(z, t) \tag{A1.8}$$

Distributing the different terms of the product, the nonlinear dielectric polarization is composed of:

$$\begin{aligned}
\hat{P}_{NL}(z, t) = \epsilon_0 \chi^{(3)} \Big(&\hat{E}_{p1}(z, t)^3 + \hat{E}_{p2}(z, t)^3 + \hat{E}_s(z, t)^3 + \hat{E}_i(z, t)^3 \\
&+ 3\hat{E}_{p1}(z, t)^2 \hat{E}_{p2}(z, t) + 3\hat{E}_{p1}(z, t)^2 E_s(z, t) + 3\hat{E}_{p1}(z, t)^2 \hat{E}_i(z, t) \\
&+ 3\hat{E}_{p2}(z, t)^2 \hat{E}_{p1}(z, t) + 3\hat{E}_{p2}(z, t)^2 \hat{E}_s(z, t) + 3\hat{E}_{p2}(z, t)^2 \hat{E}_i(z, t) \\
&+ 3\hat{E}_s(z, t)^2 \hat{E}_{p1}(z, t) + 3\hat{E}_s(z, t)^2 \hat{E}_i(z, t) + 3\hat{E}_s(z, t)^2 \hat{E}_{p2}(z, t) \\
&+ 3\hat{E}_i(z, t)^2 \hat{E}_{p1}(z, t) + 3\hat{E}_i(z, t)^2 \hat{E}_s(z, t) + 3\hat{E}_i(z, t)^2 \hat{E}_{p2}(z, t) \\
&+ 6\hat{E}_{p1}(z, t)\hat{E}_s(z, t)\hat{E}_i(z, t) + 6\hat{E}_{p2}(z, t)\hat{E}_s(z, t)\hat{E}_i(z, t) \\
&+ 6\hat{E}_{p1}(z, t)\hat{E}_{p2}(z, t)\hat{E}_s(z, t) + 6\hat{E}_{p1}(z, t)\hat{E}_{p2}(z, t)\hat{E}_i(z, t) \Big)
\end{aligned} \tag{A1.9}$$

Such general expression describes the collection of all $\chi^{(3)}$ nonlinear effects which comprises the possible third harmonic generation, four-wave mixing, self phase modulation and cross phase modulation. In total, it contains 40 different frequency components around:

$$\begin{aligned}
\Big[&3\omega_{p1}, 3\omega_{p2}, 3\omega_s, 3\omega_i, \omega_p, \omega_s, \omega_i, 2\omega_{p1} \pm \omega_{p2}, 2\omega_{p1} \pm \omega_s, 2\omega_{p1} \pm \omega_i \\
&2\omega_{p2} \pm \omega_{p1}, 2\omega_{p2} \pm \omega_s, 2\omega_{p2} \pm \omega_i, 2\omega_s \pm \omega_{p1}, 2\omega_s \pm \omega_{p2}, 2\omega_s \pm \omega_i \\
&2\omega_i \pm \omega_{p1}, 2\omega_i \pm \omega_{p2}, 2\omega_i \pm \omega_s, \omega_{p1} \pm \omega_{p2} \pm \omega_s, \omega_{p1} \pm \omega_{p2} \pm \omega_i \\
&\omega_{p1} \pm \omega_s \pm \omega_i, \omega_{p2} \pm \omega_s \pm \omega_i \Big]
\end{aligned}$$

Typically, no more than one of these frequency components will be generated in the medium. In addition to energy conservation, the process must fulfil a certain phase-matching condition which ensures that the waves radiated by the nonlinear polarization in the whole crystal interferes constructively through the propagation. In the following, only the parametric four-wave mixing terms fulfilling $\omega_{p1} + \omega_{p2} - \omega_s - \omega_i = 0$ are kept. All other effects are considered not phase-matched and are therefore discarded. We are left with four terms:

$$\begin{aligned}
\hat{P}_{NL}(z, t) = \epsilon_0 \chi^{(3)} \Big(&6\hat{E}_{p1}^{(+)}(z, t)\hat{E}_s^{(-)}(z, t)\hat{E}_i^{(-)}(z, t) + 6\hat{E}_{p2}^{(+)}(z, t)\hat{E}_s^{(-)}(z, t)\hat{E}_i^{(-)}(z, t) \\
&+ 6\hat{E}_{p1}^{(+)}(z, t)\hat{E}_{p2}^{(+)}(z, t)\hat{E}_s^{(-)}(z, t) + 6\hat{E}_{p1}^{(+)}(z, t)\hat{E}_{p2}^{(+)}(z, t)\hat{E}_i^{(-)}(z, t) \Big) + h.c
\end{aligned} \tag{A1.10}$$

In fact, the different terms of Eq. (A1.10) lead to the same nonlinear effect of the form $\chi^{(3)}\hat{E}_{p1}^{(+)}\hat{E}_{p2}^{(+)}\hat{E}_s^{(-)}\hat{E}_i^{(-)}$ as we will see later when deriving the Hamiltonian (see section A.1.3). This degeneracy is known as the Kleinman's symmetry[1] which is valid whenever we consider frequencies far from resonances of the medium.
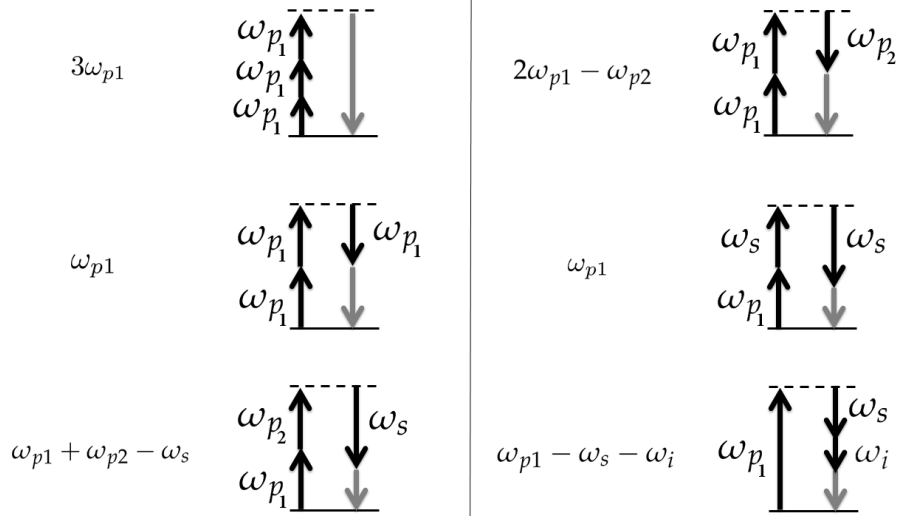
---

[1] for more details, see p.37 of [30]

Fig. A1.1: *Illustration of different possible $\chi^{(3)}$ nonlinear interactions leading to a dielectric polarization at some given new frequency. The black arrows are the interacting input fields and the nonlinear polarization frequency is represented by a gray arrow.*

1.2 Electromagnetic fields

a) Signal and idler fields

Assuming that the spectrum of each mode in the fiber is concentrated around a central frequency ω_j, the quantized electromagnetic field is given by [28]:

$$\hat{E}(z,t) = \sum_{k_j} i \sqrt{\frac{\hbar \omega_j}{2V_Q \epsilon_0 n^2(\omega_j)}} \, \hat{a}_{k_j} e^{i(\beta(\omega_j)z - \omega_j t)} + h.c \tag{A1.11}$$

where V_Q is the quantization volume, $n(\omega_j)$ is the frequency dependent index of refraction and $\hat{a}_{k_j}$ is the annihilation operator for the mode characterized by wave vector $\mathbf{k} = \beta(\omega_j)\mathbf{e}_z$. Note that, we use the notation convention of the fiber optic community where the z-component of the wavevector k_z is commonly denominated as β.

It is convenient to convert the finite summations into integrals [31, 29]:

$$\sum_{k_j} \rightarrow \int L_Q \frac{dk_j}{2\pi} \rightarrow \int L_Q \beta_1(\omega_j) \frac{d\omega_j}{2\pi} \tag{A1.12}$$

$$\hat{a}_{k_j} \quad \rightarrow \frac{\hat{a}(k_j)}{\sqrt{L_Q}} \quad \rightarrow \frac{\hat{a}(\omega_j)}{\sqrt{\beta_1(\omega_j)L_Q}} \tag{A1.13}$$

20

Such that:

$$\hat{E}(z,t) = A_j \int d\omega_j \, \hat{a}(\omega_j) e^{i(\beta(\omega_j)z - \omega_j t)} + h.c \tag{A1.14}$$

where $A_j = \frac{i}{2\pi} \sqrt{\frac{\hbar \omega_j \beta_1(\omega_j)}{2A_{\text{eff}} \epsilon_0 n^2(\omega_j)}}$, with $\beta_1 = \frac{dk}{d\omega}$ and $A_{\text{eff}} = \frac{V_Q}{L_Q}$ taken as the fiber transverse effective area with L_Q the quantization length.

We use the slowly varying envelope approximation, i.e. the bandwidth of the considered electric field is small compared to its central frequency. This allows us to extract the A_j from the integral. Such approximation is justified since we only consider narrow spectrum electric fields.

The creation and annihilation operators satisfy the usual commutation relations:

$$[\hat{a}(\omega), \hat{a}^\dagger(\omega')] = \delta(\omega - \omega') \tag{A1.15a}$$

$$[\hat{a}(\omega), \hat{a}(\omega')] = 0 \tag{A1.15b}$$

In the end, signal and idler field are described by:

$$\hat{E}_s(z,t) = A_s \int d\omega_s \, \hat{a}(\omega_s) e^{i[\beta(\omega_s)z - \omega_s t]} + h.c \tag{A1.16a}$$

$$\hat{E}_i(z,t) = A_i \int d\omega_i \, \hat{a}(\omega_i) e^{i[\beta(\omega_i)z - \omega_i t]} + h.c \tag{A1.16b}$$

b)   Pump fields

The pump fields are much stronger than the signal and idler fields and are assumed to be undepleted as they propagate through the fiber. Accordingly, the pump fields may be replaced by classical fields of the form:

$$\hat{E}_{p1}(z,t) \approx E_{p1}(z,t) = E_{p1}(t) e^{i\beta(\omega_{p1})z} + c.c \tag{A1.17a}$$

$$\hat{E}_{p2}(z,t) \approx E_{p2}(z,t) = E_{p2}(t) e^{i\beta(\omega_{p2})z} + c.c \tag{A1.17b}$$

And their Fourier decompositions are given by:

$$E_{p1}(z,t) = \int_{-\infty}^{+\infty} d\omega_{p1} \, \tilde{E}_{p1}(\omega_{p1}) e^{i(\beta(\omega_{p1})z - \omega_{p1} t)} \tag{A1.18a}$$

$$E_{p2}(z,t) = \int_{-\infty}^{+\infty} d\omega_{p2} \, \tilde{E}_{p2}(\omega_{p2}) e^{i(\beta(\omega_{p2})z - \omega_{p2} t)} \tag{A1.18b}$$

Where $\tilde{E}_p$ is the Fourier transform of the temporal envelope of the field. Note that, no assumption is made on the pump spectrum shape (Gaussian, non-Gaussian, etc).

Having defined the non-linear polarisation and the fields, we can derive the non-linear Hamiltonian to describe the four-wave mixing process.

1.3   Deriving the Hamiltonian

In quantum physics, there exist distinct representations among which the three most commonly used: (i) the Schrödinger, (ii) the Heisenberg and (iii) the Interaction pictures (the later being also called Dirac picture). While mathematically equivalent, they differ from each other in the role that the wavefunction and the operators bear. In the Schrödinger picture, the wavefunction is time-dependent as opposed to operators which remain fully time-independent. The Heisenberg picture it is the exact opposite. Finally, the Interaction picture lies halfway, with both the wavefunction and operators bearing a certain time-dependence. When an intense pulse of light propagates through the medium, the Hamiltonian describing the system can be decomposed into a linear part $\hat{H}_L$ and a non-linear part $\hat{H}_{NL}$, the latter being considered a perturbation ($\hat{H} = \hat{H}_L + \hat{H}_{NL}$).

Schrödinger	Heisenberg	Interaction
$i\hbar \dfrac{d}{dt} \left|\psi_S(t)\right\rangle = \hat{H} \left|\psi_S(t)\right\rangle$	$\dfrac{d}{dt} \left|\psi_H(t)\right\rangle = 0$	$i\hbar \dfrac{d}{dt} \left|\psi_I(t)\right\rangle = \hat{H}_{NL} \left|\psi_I(t)\right\rangle$
$\dfrac{d\hat{O}_S}{dt} = 0$	$i\hbar \dfrac{d\hat{O}_H}{dt} = \left[\hat{O}_H; \hat{H}\right]$	$\dfrac{d\hat{O}_I}{dt} = \left[\hat{O}_I; \hat{H}_L\right]$

In our case, we adopt the Interaction picture which has the advantage of allowing to focus on the nonlinear contribution only. Indeed, the state is determined by solving a Schrödinger equation of the form:

$$i\hbar \frac{d}{dt} \left|\psi(t)\right\rangle = \hat{H}_{NL}(t) \left|\psi(t)\right\rangle \tag{A1.19}$$

From which we deduce:

$$\left|\psi(t + dt)\right\rangle = e^{-\frac{i}{\hbar}\hat{H}_{NL}(t)\,dt} \left|\psi(t)\right\rangle \tag{A1.20}$$

Before the pump pulse interacts with the medium ($t < 0$), the signal and idler are void of any photon. The initial state at $t = t_0$ is then $|0_s, 0_i\rangle$ such that we can write:

$$\left|\psi(t')\right\rangle = e^{-\frac{i}{\hbar}\int_{t_0}^{t'}\hat{H}_{NL}(t)\,dt} |0_s, 0_i\rangle \tag{A1.21}$$

Since the nonlinear interaction has a low efficiency, we can then make a Taylor expansion of

the exponential [32]:

$$\left|\psi(t')\right\rangle \approx \left[\mathbb{1} + \frac{-i}{\hbar}\int_{t_0}^{t'} dt\, \hat{H}_{NL}(t)\right.$$
$$\left. + \frac{(-i)^2}{\hbar^2}\int_{t_0}^{t'} dt\int_{t_0}^{t''} dt''\hat{H}_{NL}(t)\,\hat{H}_{NL}(t'') + ...\right]\left|0_s, 0_i\right\rangle \tag{A1.22}$$

A derivation will show later that $\hat{H}_{NL}(t)$ contains the photon pair creation and annihilation operator $\hat{a}(\omega_s)/\hat{a}^\dagger(\omega_s)$ and $\hat{a}(\omega_i)/\hat{a}^\dagger(\omega_i)$. Thus, qualitatively, the kth order of the Taylor expansion, corresponds to the parametric generation of k-photons pair.

The term $(\iint \hat{H}_{NL}(t)\hat{H}_{NL}(t'')\,dt\,dt'')$ contains terms corresponding to double pair generation within the same interaction[2]. Experimentally, these terms correspond to processes that generally cannot be used as it is not possible to separate pairs deterministically. It is even detrimental as it decreases the signal to noise ratio [33]. In the following, we only consider a regime where the pump power is weak enough so that double-pair generation occurs with a negligible probability. With this assumption we can limit the mathematical treatment to the first order expansion:

$$\left|\psi(t')\right\rangle \approx \left(\mathbb{1} - \frac{i}{\hbar}\int_{t_0}^{t'}\hat{H}_{NL}(t)\,dt\right)\left|0_s, 0_i\right\rangle \tag{A1.23a}$$

$$= \left|0_s, 0_i\right\rangle - \frac{i}{\hbar}\int_{t_0}^{t'}\hat{H}_{NL}(t)\,dt\left|0_s, 0_i\right\rangle \tag{A1.23b}$$

Usually, in order to simplify the notation, the vacuum contribution is discarded so that we define the photon pair wavefunction (also called biphoton state) as:

$$\left|\psi_{pair}(t')\right\rangle = -\frac{i}{\hbar}\int_{t_0}^{t'}\hat{H}_{NL}(t)\,dt\left|0_s, 0_i\right\rangle \tag{A1.24a}$$

It is noteworthy that discarding the vacuum is only a notation simplification such that $\left|\psi_{pair}(t')\right\rangle$ is not normalised vector, it is $\left|\psi(t')\right\rangle$ which is normalised.

The interaction Hamiltonian is related to the nonlinear polarization according to [30]:

$$\hat{H}_{NL}(t) = \frac{1}{4}\int dV\,\hat{E}(\mathbf{r}, t)\hat{P}_{NL}(\mathbf{r}, t) \tag{A1.25}$$

$$= \frac{A}{4}\int dz\,\hat{E}(z, t)\hat{P}_{NL}(z, t) \tag{A1.26}$$

where A is the result of the spatial integrations of the fields along the transverse dimensions.

---

[2] more details in [32]

We recall that $\hat{E}(z,t) = E_{p1}(z,t) + E_{p2}(z,t) + \hat{E}_s(z,t) + \hat{E}_i(z,t)$. Injecting Eq. (A1.10), we obtain:

$$\hat{H}_{NL}(t) = 6\epsilon_0 \chi^{(3)} A \int dz E_{p1}^{(+)}(z,t) E_{p2}^{(+)}(z,t) \hat{E}_s^{(-)}(z,t) \hat{E}_i^{(-)}(z,t) + h.c. \qquad (A1.27)$$

First let us replace the signal $\hat{E}_s^{(-)}$ and idler $\hat{E}_i^{(-)}$ field by their respective expressions:

$$\hat{H}_{NL}(t) = \kappa \int dz \iint d\omega_s d\omega_i E_{p1}^{(+)}(z,t) E_{p2}^{(+)}(z,t) \qquad (A1.28)$$
$$\times \hat{a}^{\dagger}(\omega_s) e^{-i[\beta(\omega_s)z - \omega_s t]} \hat{a}^{\dagger}(\omega_i) e^{-i[\beta(\omega_i)z - \omega_i t]} + h.c.$$

where all constant factors are grouped together in the constant κ, along with the functions A_s and A_i.

Therefore, the biphoton state is given by:

$$\left|\psi_{pair}(t')\right\rangle = \kappa \int dt \int dz \iint d\omega_s d\omega_i E_{p1}^{(+)}(z,t) E_{p2}^{(+)}(z,t) \qquad (A1.29a)$$
$$\times \hat{a}^{\dagger}(\omega_s) e^{-i[\beta(\omega_s)z - \omega_s t]} \times \hat{a}^{\dagger}(\omega_i) e^{-i[\beta(\omega_i)z - \omega_i t]} \left|0_s, 0_i\right\rangle$$
$$= \kappa \int dt \int dz \iint d\omega_s d\omega_i E_{p1}^{(+)}(z,t) E_{p2}^{(+)}(z,t) \qquad (A1.29b)$$
$$\times e^{-i[\beta(\omega_s)z - \omega_s t]} \times e^{-i[\beta(\omega_i)z - \omega_i t]} \left|\omega_s, \omega_i\right\rangle$$

where $\left|\omega_j\right\rangle$ corresponds to a one photon Fock state at ω_j. Note that the hermitian conjugate has disappeared since $\hat{a}_{s,i}\left|0_{s,i}\right\rangle = 0$.

The term $|\omega_s, \omega_i\rangle$ describes a photon pair. The integral over time and space will impose constraints on the signal and idler frequencies that may or may not be generated.

The order of the time, space and frequency integrals can be modified in such a way that:

$$\left|\psi_{pair}(t')\right\rangle = \kappa \iint_0^{\infty} d\omega_s d\omega_i \int_0^L dz \left(\int_{t_0}^{t'} dt E_{p1}^{(+)}(z,t) E_{p2}^{(+)}(z,t) e^{-i(\omega_s + \omega_i)t} \right) \qquad (A1.30)$$
$$e^{-i(\beta(\omega_s) + \beta(\omega_i))z} \right) |\omega_s, \omega_i\rangle$$

The time dependent part $E_{p1}^{(+)}(z,t) E_{p2}^{(+)}(z,t) e^{-i(\omega_s + \omega_i)t}$ vanishes whenever one of the two fields reaches zero. Therefore, as we consider pulsed fields, this product is non-zero only for a short period of time when the two pump pulses are inside the medium. Obviously, the interaction cannot take place before they enter the medium or after they exit it. Thus, the time integration

can be extended to infinity, making the calculation easier to handle.

$$\left|\psi_{pair}(t')\right\rangle = \kappa \iint_0^\infty d\omega_s\, d\omega_i \int_0^L dz \left(\int_{-\infty}^\infty dt\, E_{p1}^{(+)}(z,t) E_{p2}^{(+)}(z,t) e^{-i(\omega_s+\omega_i)t} \right) \tag{A1.31}$$
$$\times\, e^{-i(\beta(\omega_s)+\beta(\omega_i))z} \left|\omega_s,\omega_i\right\rangle$$

Moreover, to perform the different integrations it is useful to replace the classical fields by their Fourier decompositions (Eq. A1.18b):

$$= \kappa \iiint\!\!\int_0^\infty d\omega_s\, d\omega_i\, d\omega_{p1}\, d\omega_{p2}\, \tilde{E}_{p1}^{(+)}(\omega_{p1}) \tilde{E}_{p2}^{(+)}(\omega_{p2}) \left(\int_{-\infty}^\infty dt\, e^{-i(\omega_{p1}+\omega_{p2}-\omega_s-\omega_i)t} \right) \tag{A1.32}$$
$$\times\left(\int_0^L dz\, e^{i(\beta(\omega_{p1})+\beta(\omega_{p2})-\beta(\omega_s)-\beta(\omega_i))z} \right) \left|\omega_s,\omega_i\right\rangle$$

a)   Time Integral

Let us first consider the term in parenthesis corresponding to time integration:

$$I_{time} = \int_{-\infty}^\infty dt\, e^{-i(\omega_{p1}+\omega_{p2}-\omega_s-\omega_i)t} \tag{A1.33a}$$
$$= 2\pi\, \delta(\omega_s + \omega_i - \omega_{p1} - \omega_{p2}) \tag{A1.33b}$$

One can already notice that the result of the time integral gives the energy conservation of the four-wave mixing process.

b)   Space Integral

This term is the integration over the fiber length in the propagation direction. The transverse integral is already included in κ. To simplify the notation we define:

$$\Delta\beta(\omega_{p1},\omega_{p2},\omega_s,\omega_i) = \beta(\omega_{p1}) + \beta(\omega_{p2}) - \beta(\omega_s) - \beta(\omega_i) \tag{A1.34}$$

$$I_{space} = \int_0^L dz\, e^{i\Delta\beta(\omega_{p1},\omega_{p2},\omega_s,\omega_i)z} \tag{A1.35}$$

This integral can be easily performed by noticing that A1.35 can be written as the spatial Fourier transform of a gate function which is a sinus cardinal function.

$$I_{space} = \int_{-\infty}^\infty dz\, \Pi(z) e^{i\Delta\beta(\omega_{p1},\omega_{p2},\omega_s,\omega_i)z} \tag{A1.36a}$$
$$= L\,\text{sinc}\left(\Delta\beta(\omega_{p1},\omega_{p2},\omega_s,\omega_i)\frac{L}{2} \right) e^{i\Delta\beta(\omega_{p1},\omega_{p2},\omega_s,\omega_i)\frac{L}{2}} \tag{A1.36b}$$

Where $\Pi(z)$ is a gate function corresponding to the fiber length:

$$\Pi(z) = \begin{cases} 1 & \text{if } 0 < z < L, \\ 0 & \text{otherwise} \end{cases}$$

Using the integral of the square function gives the intuitive interpretation that the sinc function comes from the finite boundaries of the fiber[3]. Such consideration will be important later while discussing the defects resulting from the rebounds of the sinc function.

c) Spectral integral over ω_{p2}

Injecting the result of the time and space integrals, we obtain:

$$\left|\psi_{pair}\right\rangle = \kappa \iiiint_0^\infty d\omega_s \, d\omega_i \, d\omega_{p1} \, d\omega_{p2} \, \tilde{E}_{p1}^{(+)}(\omega_{p1}) \tilde{E}_{p2}^{(+)}(\omega_{p2}) \delta(\omega_s + \omega_i - \omega_{p1} - \omega_{p2}) \quad \text{(A1.37)}$$
$$\times \text{sinc}\left(\Delta\beta(\omega_{p1}, \omega_{p2}, \omega_s, \omega_i) \frac{L}{2}\right) e^{i\Delta\beta(\omega_{p1}, \omega_{p2}, \omega_s, \omega_i)\frac{L}{2}} \left|\omega_s, \omega_i\right\rangle$$

Before developing the calculation further, one can already notice that Eq. (A1.37) bears two constraints on the signal and idler photons that can be generated. Firstly, $\tilde{E}_{p1}^{(+)}(\omega_{p1}) \tilde{E}_{p2}^{(+)}(\omega_{p2}) \delta(\omega_s + \omega_i - \omega_{p1} - \omega_{p2})$ relates the frequencies of the pumps signal and idler. Secondly, the *sinc* term which is maximum when $\beta(\omega_{p1}) + \beta(\omega_{p2}) - \beta(\omega_s) - \beta(\omega_i) = 0$ adds a constraint on the momentum of the signal and idler photons. These two relations will bear the energy and momentum conservation discussed in section A.2.1.

We can simplify the Eq. (A1.37) by recognizing a function of the type:

$$\int d\omega_{p2} X(\omega_{p2}) \delta(\omega_x - \omega_{p2}) = X(\omega_x) \quad \text{(A1.38)}$$

where $\omega_x = \omega_s + \omega_i - \omega_{p1}$, and $X(\omega_{p2}) = \tilde{E}_{p2}^{(+)}(\omega_{p2}) \text{sinc}\left(\Delta\beta(\omega_{p1}, \omega_{p2}, \omega_s, \omega_i) \frac{L}{2}\right) e^{i\Delta\beta(\omega_{p1}, \omega_{p2}, \omega_s, \omega_i)\frac{L}{2}}$.

Using the relation in Eq. (A1.38), the equation simplifies to:

$$\left|\psi_{pair}(t')\right\rangle = \kappa \iiint_0^\infty d\omega_s \, d\omega_i \, d\omega_{p1} \, \tilde{E}_{p1}^{(+)}(\omega_{p1}) \tilde{E}_{p2}^{(+)}(\omega_s + \omega_i - \omega_{p1}) \quad \text{(A1.39)}$$
$$\text{sinc}\left(\Delta\beta(\omega_{p1}, \omega_s, \omega_i) \frac{L}{2}\right) e^{i\Delta\beta(\omega_{p1}, \omega_s, \omega_i)\frac{L}{2}} \left|\omega_s, \omega_i\right\rangle$$

where $\Delta\beta(\omega_{p1}, \omega_s, \omega_i) = \beta(\omega_{p1}) + \beta(\omega_s + \omega_i - \omega_{p1}) - \beta(\omega_s) - \beta(\omega_i)$.

---

[3] a sinus cardinal is the Fourier transform of a gate function.

Finally we can rewrite the photon-pair state in the following way:

$$\left|\psi_{pair}(t')\right\rangle = \kappa \iint d\omega_s \, d\omega_i F(\omega_s, \omega_i) \left|\omega_s, \omega_i\right\rangle \tag{A1.40}$$

With:

$$F(\omega_s, \omega_i) = \int d\omega_{p1} \, \tilde{E}_{p1}^{(+)}(\omega_{p1}) \tilde{E}_{p2}^{(+)}(\omega_s + \omega_i - \omega_{p1})$$
$$\times \, \mathrm{sinc}(\Delta\beta(\omega_{p1}, \omega_s, \omega_i)\frac{L}{2}) e^{i\Delta\beta(\omega_{p1}, \omega_s, \omega_i)\frac{L}{2}} \tag{A1.41}$$

where we denominate F as the joint spectral amplitude function (JSA).

This JSA describes all the spectral properties of the generated photon pair [34, 35]. It is noteworthy that Eq. (A1.41) is completely general as no assumption on the pump field shape was made so far[4]. This is the equation used in the rest of the manuscript when studying the spectral properties of a given photon pair source.

Furthermore, in the case of degenerated pumps ($\tilde{E}_{p2}^{(+)} = \tilde{E}_{p1}^{(+)}$), it is common to introduce a simplified expression of the JSA in closed analytical form. By using a linear approximation for the phase mismatch $\Delta\beta$ over frequency, the remaining integral over ω_{p1} can be performed.

d) Linearised Joint Spectral Amplitude with degenerate pump

Restricting the computation to the case of degenerate pumps, which corresponds to our experimental scheme, we obtain $\omega_{p1} = \omega_{p2} = \omega_p$ and $\tilde{E}_{p1}^{(+)} = \tilde{E}_{p2}^{(+)} = \tilde{E}_p^{(+)}$. We recall that in the general case:

$$\Delta\beta(\omega_p, \omega_s, \omega_i) = \beta(\omega_p) + \beta(\omega_s + \omega_i - \omega_p) - \beta(\omega_s) - \beta(\omega_i) \tag{A1.42}$$

The linearization consists of using a first-order Taylor expansion series of each $\beta(\omega_k)$ around the frequencies ω_k^0 for which perfect phase-matching ($\Delta\beta^0 = \beta(\omega_p^0) + \beta(\omega_s^0 + \omega_i^0 - \omega_p^0) - \beta(\omega_s^0) - \beta(\omega_i^0) = 0$) is attained (where k = p, s, i):

$$\beta(\omega_k) \approx \beta(\omega_k^0) + (\omega_k - \omega_k^0)\frac{d\beta}{d\omega}\Big|_{\omega_k^0} \tag{A1.43}$$

This is equivalent to neglecting the group-velocity dispersion (second order term of the Taylor series) and higher order dispersion effects. Intuitively, this approximation allows to get rid of the terms which couple the propagation of the temporal pulses and the medium. For instance, if the medium exhibits a non negligible group-velocity dispersion, then the temporal shape of

---

[4] except the general slowly varying envelope approximation and the undepleted pump assumption

the pulses may broaden while propagating in the medium. Opposingly, if group-velocity dispersion is negligible, the temporal shape is unchanged through the propagation and is therefore decoupled from the medium.

Applying this first order expansion with respect to ω to the terms of $\Delta\beta$, we obtain linear phase mismatch $\Delta\beta_{\text{lin}}$:

$$\Delta\beta_{\text{lin}}(\omega_p, \omega_s, \omega_i) = \Delta\beta^0 + (\omega_p - \omega_p^0)\frac{d\beta}{d\omega}\Big|_{\omega_p^0} + (\omega_s + \omega_i - \omega_p - \omega_s^0 - \omega_i^0 + \omega_p^0)\frac{d\beta}{d\omega}\Big|_{\omega_p^0} \quad \text{(A1.44)}$$
$$- (\omega_s - \omega_s^0)\frac{d\beta}{d\omega}\Big|_{\omega_s^0} - (\omega_i - \omega_i^0)\frac{d\beta}{d\omega}\Big|_{\omega_i^0}$$

It can be noted that all the terms in ω_p vanish so that we are left with:

$$\Delta\beta_{\text{lin}}(\omega_s, \omega_i) = (\omega_s + \omega_i - \omega_s^0 - \omega_i^0)\beta_{1p} - (\omega_s - \omega_s^0)\beta_{1s} - (\omega_i - \omega_i^0)\beta_{1i} \quad \text{(A1.45)}$$

Where we used the notation $\beta_{1k} = \frac{d\beta}{d\omega}\Big|_{\omega_k^0}$

$$\boxed{\Delta\beta_{\text{lin}}(\omega_s, \omega_i) = (\omega_s - \omega_s^0)(\beta_{1p} - \beta_{1s}) + (\omega_i - \omega_i^0)(\beta_{1p} - \beta_{1i})} \quad \text{(A1.46)}$$

With the linearized $\Delta\beta(\omega_p, \omega_s, \omega_i) \rightarrow \Delta\beta_{lin}(\omega_s, \omega_i)$ the phase matching function can be extracted from the integral:

$$F_{\text{lin}}(\omega_s, \omega_i) = \int d\omega_p \, \tilde{E}_p^{(+)}(\omega_p)\tilde{E}_p^{(+)}(\omega_s + \omega_i - \omega_p)\text{sinc}(\Delta\beta_{\text{lin}}(\omega_s, \omega_i)\frac{L}{2})e^{i\Delta\beta_{\text{lin}}(\omega_s, \omega_i)\frac{L}{2}}$$
$$= \text{sinc}(\Delta\beta_{\text{lin}}(\omega_s, \omega_i)\frac{L}{2})e^{i\Delta\beta_{\text{lin}}(\omega_s, \omega_i)\frac{L}{2}} \int d\omega_p \, \tilde{E}_p^{(+)}(\omega_p)\tilde{E}_p^{(+)}(\omega_s + \omega_i - \omega_p)$$
$$= \underbrace{\text{sinc}(\Delta\beta_{\text{lin}}(\omega_s, \omega_i)\frac{L}{2})e^{i\Delta\beta_{\text{lin}}(\omega_s, \omega_i)\frac{L}{2}}}_{\phi(\omega_s, \omega_i)} \times \underbrace{\left[\tilde{E}_p^{(+)} * \tilde{E}_p^{(+)}\right](\omega_s + \omega_i)}_{\alpha(\omega_s, \omega_i)} \quad \text{(A1.47)}$$

where $\left[\tilde{E}_p^{(+)} * \tilde{E}_p^{(+)}\right](\omega_s + \omega_i)$ is the autocorrelation of the pump envelope amplitude.

Thus, thanks to the linearisation, we obtain a simplified analytical expression for the joint spectral amplitude:

$$\boxed{F_{\text{lin}}(\omega_s, \omega_i) = \alpha(\omega_s, \omega_i) \times \phi(\omega_s, \omega_i)} \quad \text{(A1.48)}$$

It is the product of two functions:
The energy conservation function $\alpha(\omega_s, \omega_i)$:

$$\boxed{\alpha(\omega_s, \omega_i) = \left[\tilde{E}_p^{(+)} * \tilde{E}_p^{(+)}\right](\omega_s + \omega_i)} \quad \text{(A1.49)}$$

The phase-matching function $\phi(\omega_s, \omega_i)$**:**

$$\phi(\omega_s, \omega_i) = \text{sinc}\left[\Delta\beta_{\text{lin}}(\omega_s, \omega_i)\frac{L}{2}\right] \times \exp\left[i\Delta\beta_{\text{lin}}(\omega_s, \omega_i)\frac{L}{2}\right] \qquad (A1.50)$$

The obtained linearised JSA expression has the advantage of being more intuitive as it decorrelates the pump contribution from the one of the medium.

e)   Note on the non-degenerate pump scenario

In the case of non-degenerate pumps, an analytical solution of the JSA can also be found with the additional assumption of considering $\tilde{E}_{p1}^{(+)}$ and $\tilde{E}_{p2}^{(+)}$ as gaussian pulses of width σ_1 and σ_2, respectively. In the degenerate pump scenario we did not use any assumptions on the pump spectral shape. As we will not use the non-degenerate regime in this work, we will not derive the calculation but only give the final expression [34].

$$\alpha(\omega_s, \omega_i) = e^{-\frac{(\omega_s - \omega_{s0} + \omega_i - \omega_{i0})^2}{\sigma_1^2 + \sigma_2^2}} \qquad (A1.51)$$

$$\phi(\omega_s, \omega_i) = MBe^{-B^2(\beta_{\text{lin}}L)^2}\left[\text{erf}(\frac{1}{2B} - iB\beta_{\text{lin}}L) + \text{erf}(iB\beta_{\text{lin}}L)\right] \qquad (A1.52)$$

where M is a normalization coefficient, erf is the error function and B is defined as $B = \frac{\sqrt{\sigma_1^2 + \sigma_2^2}}{\sigma_1 \sigma_2 L(\beta_{1p_1} - \beta_{1p_2})}$.

In such a configuration, one would have to consider the group velocity difference between the two pumps $(\beta_{1p_1} - \beta_{1p_2} \neq 0)$, which limits the interaction length to the effective distance where they overlap. This is the so-called group-velocity walk-off (contained in the term B).

Conclusion

In this chapter, the analytical expression of the photon pair wavefunction in the degenerated pump regime has been derived. We have shown that it can be written as a product of: (i) a phase matching function (in the form of a cardinal sine function) resulting from the spatial integration over the fiber length and (ii) an energy conservation function (in the form of an autocorrelation of the pump spectrum) resulting from the temporal integration over the total duration of interaction.

Using this result, the photon-pair frequencies and generation efficiency can be quantitatively

predicted from the knowledge of fiber parameters (length, dispersion, n_2) and the pump parameters (temporal/spectral shape).

We recall however that such derivation is valid only under the assumptions of a weak pump regime so that we can approximate the hamiltonian to its first order Taylor series and neglect the multipair contributions.

The next chapter is devoted to the study of the joint spectral amplitude function which describes the spectral correlations.

Chapter A2

Joint Spectral/Temporal Amplitude

This chapter describes the physical interpretation of the joint spectral amplitude function. It is a powerful tool to describe the joint effects of the pump and the medium. Moreover, a link between this function and the spectral properties of the photon-pairs is discussed. In particular, we will see how this function is related to the time-frequency correlations (= entanglement between the photons of the pairs) and the purity of individual signal and idler photons. In a second section, the Schmidt decomposition is introduced to give a quantitative characterization of the spectral entanglement and strategies to control the amount of spectral correlations are described in the third and fourth sections. The last section presents the spectral density map which is a useful tool to describe the phase-matching as a function of pump wavelength.

2.1 Joint Spectral Amplitude

As described in the last chapter, the state produced by spontaneous four-wave mixing in an optical fiber of length L is given by:

$$\left| \psi \right\rangle = \left| 0,0 \right\rangle + \kappa \iint \mathrm{d}\omega_s \, \mathrm{d}\omega_i F(\omega_s, \omega_i) \left| \omega_s, \omega_i \right\rangle \tag{A2.1}$$

Where we recall that the quantity κ is a constant corresponding to the generation efficiency, and $F(\omega_s, \omega_i)$ is the complex-valued joint spectral amplitude function (JSA), normalised to

31

$\iint d\omega_s\, d\omega_i |F(\omega_s, \omega_i)|^2 = 1$. Moreover, the JSA can be approximated as the product of the energy conservation function $\alpha(\omega_s, \omega_i)$ and the phase matching function $\phi(\omega_s, \omega_i)$:

$$F(\omega_s, \omega_i) \approx \alpha(\omega_s, \omega_i)\, \phi(\omega_s, \omega_i) \tag{A2.2}$$

Let us discuss in more details the physics contained in each terms of this approximated analytical expression[1] of the photon pair state:

a) The generation efficiency density κ

The efficiency of photon-pair generation is related to [29]:

$$|\kappa|^2 \approx \left(\frac{n_2\, \omega_p}{c\, A_{\text{eff}}} L P_p\, \tau_p \right)^2 \tag{A2.3}$$

with n_2 the medium non-linearity, A_{eff} the fiber transverse effective area, L the fiber length, P_p the peak power and τ_p the pulse duration of the pump.

The probability to generate a signal photon in the range $[\omega_{s0} - d\omega_s/2, \omega_{s0} + d\omega_s/2]$ and an idler photon in the range $[\omega_{i0} - d\omega_i/2, \omega_{i0} + d\omega_i/2]$ is given by:

$$\text{Proba}(\omega_s, \omega_i) = |\langle \omega_s, \omega_i | \psi_{\text{pair}} \rangle|^2\, d\omega_s\, d\omega_i \tag{A2.4a}$$

$$= |\kappa|^2 F(\omega_s, \omega_i)^2\, d\omega_s\, d\omega_i \tag{A2.4b}$$

F being a normalized function, it is $|\kappa|^2$ that bears the quantitative part of the generation efficiency. The quadratic dependence of the generation rate with respect to the pump intensity P_p favours the use of pump with high peak power[2].

In practice, fiber based photon pair sources usually exhibit efficiency in the order of 10^{-5} to 10^{-2} pairs/pulse for a length in the meter range and a few mW of average pump power with picosecond pulses.

b) Energy conservation function $\alpha(\omega_s, \omega_i)$

$$\alpha(\omega_s, \omega_i) = \left[\tilde{E}_{p1}^{(+)} * \tilde{E}_{p1}^{(+)} \right](\omega_s + \omega_i) \tag{A2.5}$$

This term bears the energy conservation condition, imposing that the energy of the created photons $\hbar\omega_s$ and $\hbar\omega_i$ corresponds to the energy of the two annihilated photons around $2\hbar\omega_{p0}$. Indeed, since $\tilde{E}_{p1}(\omega)$ is a function of $\omega - \omega_{p0}$, it follows that $\alpha(\omega_s, \omega_i)$ is centered around $\omega_s + $

---

[1]please refer to Eq. (A1.41) for the exact expression

[2]as opposed to SPDC where the brightness increases only linearly with pump power such that both continuous laser and pulse laser can be used.

$\omega_i - 2\omega_{p0}$. The fact that this function embodies the energy conservation function is an expected result since it is derived from the time integral of the interacting fields and it is well known that energy conservation is related to time invariance. The longer the pulse (= higher time invariance), the less the energy conservation is relaxed. In other words, since we consider a pulsed pump, $\tilde{E}_{p1}^{(+)}$ has a spectral width σ centered on ω_{p0}. The narrower σ, the stricter the energy conservation condition. In the limit of a monochromatic pump[3], it can be easily demonstrated that $\alpha(\omega_s, \omega_i)$ tends to $\delta(2\omega_{p0} - \omega_s - \omega_i)$.

<div align="center">Energy conservation</div>

<div align="center">Naive representation   More realistic representation</div>
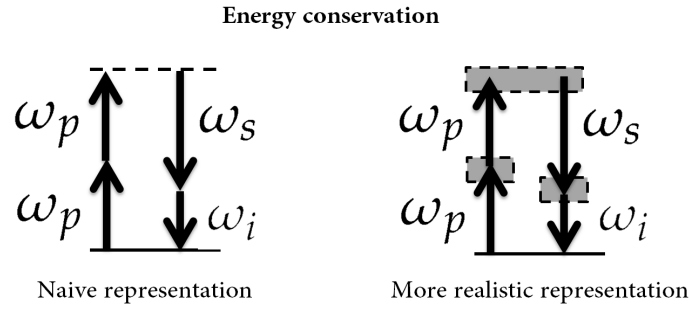
Fig. A2.1: *Schematics of the energy conservation. Representation on the right shows a more realistic scheme where, due to the spectral width of the pump, the energy conservation is slightly relaxed.*

Let us consider a Gaussian pump amplitude, $E(\omega_p) = E_0\, e^{-\frac{(\omega - \omega_{p0})^2}{2\sigma^2}}$. Such assumption legitimately describes the usual spectrum exhibited by a standard pulsed laser. The autocorrelation of the Gaussian spectrum also gives a Gaussian of the form:

$$\alpha(\omega_s, \omega_i) = E_0^2\, e^{-\frac{(\omega_s + \omega_i - 2\omega_{p0})^2}{4\sigma^2}} \tag{A2.6}$$

For a Gaussian spectrum the function α is fully described by two parameters:

- its width $\Delta\alpha$ related to the spectral width σ of the pump amplitude ($\Delta\alpha = \sqrt{2}\sigma$).

- its position in the 2D plane related to the central frequency ω_{p0} of the pump laser

This function can be displayed graphically in the 2D plane (ω_s, ω_i) to get a better insight of its physical meaning, as for instance in Fig. A2.2. It is noteworthy that α function always exhibits a slope of $-45°$, regardless of the shape of the pump spectrum (Gaussian or not). It comes from the equation: $2\omega_{p0} - \omega_s - \omega_i = 0$. **This slope is a signature of the anti-correlation between signal and idler frequencies, due to the energy conservation.**

Moreover, because the FWM comes from the interaction of two pump photons, the energy conservation function α is the autocorrelation of the pump spectrum. This is different from SPDC where, as only one pump photon is converted, α is directly proportional to the pump

---

[3]in that case there is a full time invariance causing the energy conservation to be strict

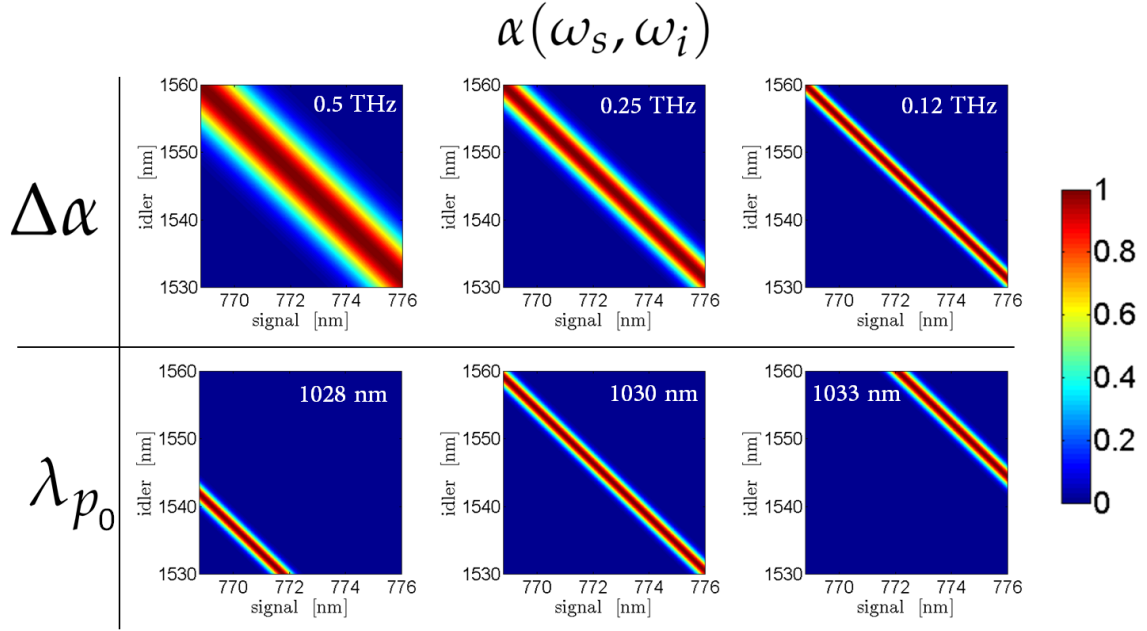$$\alpha\left(\omega_s,\omega_i\right)$$

Fig. A2.2: *Computed function $\alpha(\omega,\omega_i)$ when considering different parameters of the Gaussian pump amplitude. The first row shows different spectral widths $\Delta\omega$ for a fixed pump wavelength ($\lambda_p = 1030$ nm) whereas the second row different central wavelength $\lambda p0$ for a fixed spectral width ($\Delta\omega = 0.12$ THz).*

spectrum. When considering a standard gaussian pump spectrum, the difference between SPDC and FWM is not really remarkable as the autocorrelation of a gaussian is also a gaussian. However notable differences occur when considering non-gaussian pulses. Figure A2.3 shows such an example when considering a square pump spectrum.
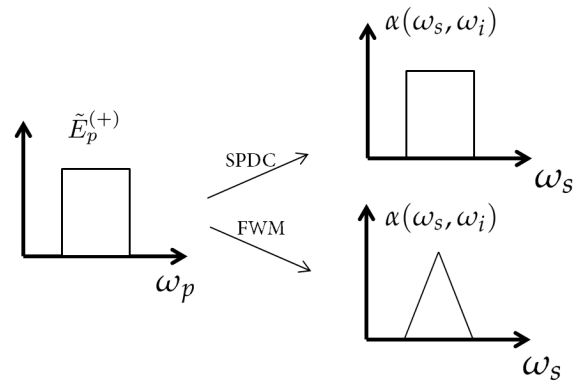
Fig. A2.3: *Example illustrating the difference between the energy conservation function for SPDC and for FWM when pumped with a square spectrum pump. The spectra in the right hand side correspond to a projection of $\alpha(\omega_s,\omega_i)$ along the signal axis.*

c) The phase matching function $\phi(\omega_s, \omega_i)$

$$\phi(\omega_s, \omega_i) = \mathrm{sinc}\left[\Delta\beta_{\mathrm{lin}}(\omega_s, \omega_i)\frac{L}{2}\right] \times \exp\left[i\Delta\beta_{\mathrm{lin}}(\omega_s, \omega_i)\frac{L}{2}\right] \tag{A2.7}$$

This third term is the phase matching function which expresses the momentum conservation. Indeed the term is maximal when the argument of the cardinal sine function cancels, which happens when $2\beta(\omega_p) = \beta(\omega_s) + \beta(\omega_i)$. As described, it derives from the spatial integral of the fields over the fiber length (Eq. A1.35). Once again, this is not surprising considering the well-known link between space invariance and momentum conservation[4]. Besides, due to the finite fiber length, the momentum conservation is relaxed. The longer the fiber, the sharper the momentum conservation and, in the limiting case where $L \to \infty$, the function would become a delta function $\frac{1}{L}\delta(2\beta(\omega_p) - \beta(\omega_s) - \beta(\omega_i))$.

Momentum Conservation
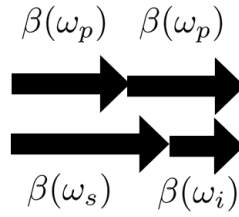
Fig. A2.4: *Illustration of the momentum conservation requirement. In the fiber, the different momentum vectors are parallel to the direction of propagation.*

For a given pump energy, an infinite number of frequency pair combination of (ω_s, ω_i) fulfil the energy conservation. The medium dispersion determines the likelihood of each of these possibilities through the phase matching condition. In others words, the pump brings the amount of energy available and the medium dictates how this energy is converted.

More quantitatively, if we zoom around a certain couple ω_s^0 and ω_i^0, the main lobe of the sinc can be approximated by a Gaussian of the form[5] [36]:

$$\left|\mathrm{sinc}\left[\Delta\beta_{\mathrm{lin}}(\omega_s, \omega_i)\frac{L}{2}\right]\right| \approx e^{-\gamma L^2\left(\Delta\beta_{\mathrm{lin}}(\omega_s, \omega_i)\right)^2} \tag{A2.8a}$$

$$= e^{-\gamma L^2\left((\omega_s - \omega_s^0).(\beta_{1p} - \beta_{1s}) + (\omega_i - \omega_i^0).(\beta_{1p} - \beta_{1i})\right)^2} \tag{A2.8b}$$

with $\gamma = 0.04822$.

---

[4] an another way to see this is to consider the gain-bandwidth trade-off. For a longer fiber, the gain increases but then, the bandwidth decreases.

[5] $\mathrm{sinc}(x/2)$ and $\exp(-\gamma x^2)$ have the same widths at half maximum.

Which corresponds to a Gaussian in the (ω_s, ω_i) plane of width $\Delta\phi$, making an angle θ relatively to the ω_s axis with:

$$\Delta\phi \approx \frac{1}{L\sqrt{2\gamma\left((\beta_{1p} - \beta_{1s})^2 + (\beta_{1p} - \beta_{1i})^2\right)}} \tag{A2.9a}$$

$$\theta = -\arctan\left(\frac{\beta_{1p} - \beta_{1s}}{\beta_{1p} - \beta_{1i}}\right) \tag{A2.9b}$$

Importantly, the width $\Delta\phi$ is inversely proportional to the length of the medium L whereas the angle θ is only related to the inverse group velocities $\beta_1(\omega) = \frac{1}{v_g(\omega)}$ in the medium. Figure A2.5 shows examples of different values of these two parameters.
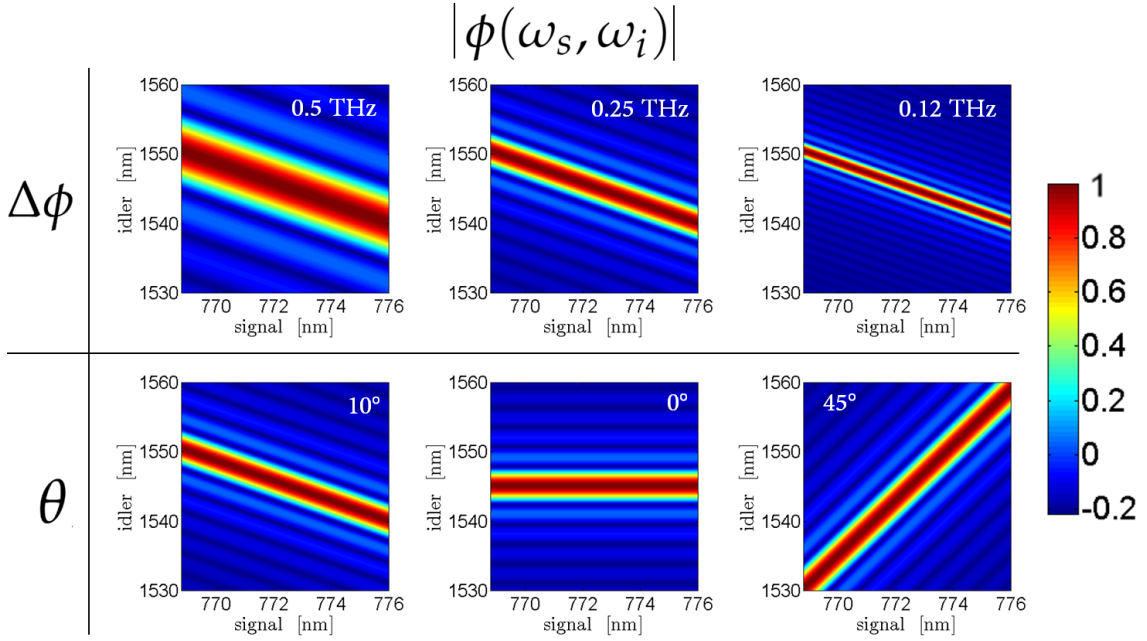
Fig. A2.5: *Computed $|\phi(\omega_s, \omega_i)|$ for different parameters. The first row represents modifications of the width (inversely proportional to the fiber length) for a fixed angle ($\theta = -10°$) and the second row modifications of the angle for a fixed length L. The rebounds are due to the sinc.*

One can already observe that the differences in β_1 between pump, signal, and idler are a decisive factor in determining the shape of the JSA as it governs the angle θ. Such angle will be crucial when considering the spectral correlations later on (section A2.3).

d) Joint Spectral Amplitude

Writing the JSA as the product of α and ϕ nicely separates the pump influence (represented by the energy conservation function) from the medium influence (represented by the phase matching function). Such a separation is useful as we will independently shape the medium

dispersion (through the control of the fiber dispersion, see chapter C2) and the pump amplitude (through pulse shaping). Figure A2.6 illustrates this by mapping α, φ and the resulting JSA.
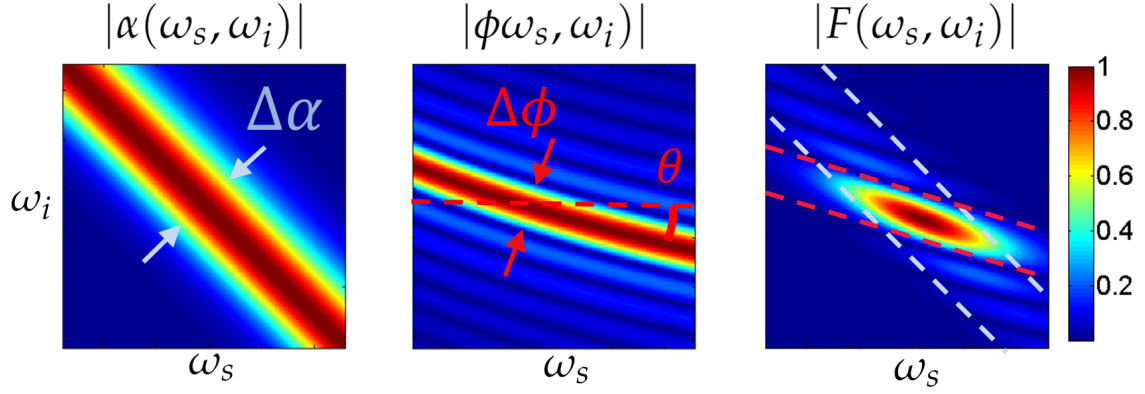

Fig. A2.6: *From left to right: energy conservation function* α*, phase matching function* φ *and corresponding joint spectral amplitude in the case of a Gaussian pump in an unengineered medium.*

Two informations can be extracted from the JSA function:

- **the position of the JSA in the 2D plane** gives the range of signal and idler wavelengths that will be generated in the FWM process for a given pump and medium. From an experimental point of view, this parameter is crucial if ones wants to aim at a specific wavelength such as an atomic transition or a telecom channel. Knowing the value of the two photon frequencies is also of utmost importance when considering the filtering. Indeed, in most experiments, the photon pairs are separated from the pump using gratings or dichroic mirrors.

- **the shape of the JSA** gives the spectral correlations between the signal and idler spectrum. The next section is devoted to the investigation of these correlations.

2.2 Schmidt decomposition

Formally, signal and idler photons are said to be spectrally correlated if their state cannot be factorized in a product state of functions depending only on signal and idler frequencies, respectively.

$$\boxed{\text{Spectrally entangled} \Longleftrightarrow F(\omega_s, \omega_i) \neq S(\omega_s) \times I(\omega_i)}$$ (A2.10)

$$\boxed{\text{Factorable} \Longleftrightarrow F(\omega_s, \omega_i) = S(\omega_s) \times I(\omega_i)}$$ (A2.11)

Such factorizability can be described in a quantitative way by performing the Schmidt decomposition.

a) Derivation

The Schmidt decomposition of the JSA rewrites the state in such a way that the signal and idler dependences are easily identifiable. It consists in finding the function sets S_n and I_n such that the state is a sum of product states [37]:

$$F(\omega_s, \omega_i) = \sum_{n=0}^{\infty} \sqrt{c_n}\, S_n(\omega_s)\, I_n(\omega_i) \tag{A2.12}$$

Where $S_n(\omega_s)$ and $I_n(\omega_i)$ define two sets of orthonormal functions depending only on the signal and idler frequencies, respectively. The weighting coefficients c_n satisfy the normalization condition:

$$\sum_{n=0}^{\infty} c_n = 1 \tag{A2.13}$$

S_n, I_n, and c_n are solutions of the integral eigenvalue equations [36]:

$$\int \mathrm{d}\omega'\, K_1(\omega, \omega') S_n(\omega') = c_n S_n(\omega) \tag{A2.14a}$$

$$\int \mathrm{d}\omega'\, K_2(\omega, \omega') I_n(\omega') = c_n I_n(\omega) \tag{A2.14b}$$

with $K_1(\omega, \omega') = \int \mathrm{d}\omega_2 F(\omega, \omega_2) F^*(\omega', \omega_2)$ and $K_2(\omega, \omega') = \int \mathrm{d}\omega_1 F(\omega_1, \omega) F^*(\omega_1, \omega')$.

More precisely, the Schmidt decomposition is a singular value decomposition [38, 39]. Note that the decomposition is generally unique (except in the cases with degenerate eigen values).

Substituting into the photon pair equation (Eq. (A2.1)), and renormalising[6], we obtain:

$$\left|\psi_{pair}\right\rangle = \iint \mathrm{d}\omega_s\, \mathrm{d}\omega_i \sum_{n=0}^{\infty} \sqrt{c_n} S_n(\omega_s) I_n(\omega_i)\, \hat{a}_s^{\dagger}(\omega_s)\, \hat{b}_i^{\dagger}(\omega_i)\, |0,0\rangle \tag{A2.15}$$

Which can be written as:

$$\boxed{\left|\psi_{pair}\right\rangle = \sum_{n=0}^{\infty} \sqrt{c_n}\, \hat{S}_n^{\dagger}\, \hat{I}_n^{\dagger}\, |0,0\rangle} \tag{A2.16}$$

where $\hat{S}_n^{\dagger} = \int \mathrm{d}\omega_s S_n(\omega_s) \hat{a}_s^{\dagger}(\omega_s)$ and $\hat{I}_n^{\dagger} = \int \mathrm{d}\omega_i I_n(\omega_s) \hat{b}_i^{\dagger}(\omega_i)$ define the time-frequency mode creation operators.

---

[6]this corresponds to a post-selection of the photon-pair state only whereas before the state was vaccuum + photon-pair state. In practice this means that κ is now removed

Thanks to this decomposition, it now becomes easily readable whether the photon-pair state is entangled. It is entangled if the number of nonzero eigenvalues is more than one. Conversely, the state is factorable if there is only one term in the right hand side of Eq. (A2.16). More quantitatively, **the mean number of mode K, also called Schmidt number, characterizes the amount of entanglement.**

$$K = \frac{1}{\sum_{n=0}^{\infty} c_n^2} \qquad (A2.17)$$

Thus, K = 1 for factorable state whereas K > 1 for entangled states.

Moreover, the decomposition also identifies the time-frequency modal contents of the photon pairs. If the signal photon is found in a S_k mode, then it is certain that the second photon is in the I_k mode. And the value of c_n determines the occupation probability of the corresponding pair of modes.

b)   The Temporal mode framework

The operators $\hat{S}_n^\dagger$ and $\hat{I}_n^\dagger$ create a photon exhibiting a spectral profile defined by S_n and I_n function, respectively. In the following, we will use the notation $\hat{S}_k^\dagger |0\rangle = |S_k\rangle$ and $\hat{I}_k^\dagger |0\rangle = |I_k\rangle$. The states $|S_k\rangle$ and $|I_k\rangle$ define two families of orthogonal modes such that:

$$\langle S_i | S_j \rangle = \delta_{ij} \qquad (A2.18a)$$

$$\langle I_i | I_j \rangle = \delta_{ij} \qquad (A2.18b)$$

These basis are commonly called *Temporal mode* (TM) basis (such framework is presented in [40]). Examples of such modes are given in Fig. A2.7. It is important to mention that the name "temporal mode" can be misleading since such modes correspond to wave-packets with a broadband temporal and frequency content. Interestingly, this basis can be exploited to encode quantum information, as in the case of polarization or orbital angular momentum. The main advantage is that, theoretically, TM modes basis span an infinite dimensional Hilbert space (as opposed to the 2 dimensional polarization basis). More realistically, a *Qudit* with dimension $d \gg 2$ can be generated. Encoding information in a high-dimensional basis results in better information capacity per photon as well as increased security in quantum communication protocols [41, 42]. And as opposed to orbital angular momentum, temporal mode have the further advantage of being compatible with existing single-mode fiber networks [40].

Parametric sources (FWM as well as SPDC) intrinsically generate quantum states as superposition of temporal modes pairs (one TM for the signal, and one for the idler) with weighting
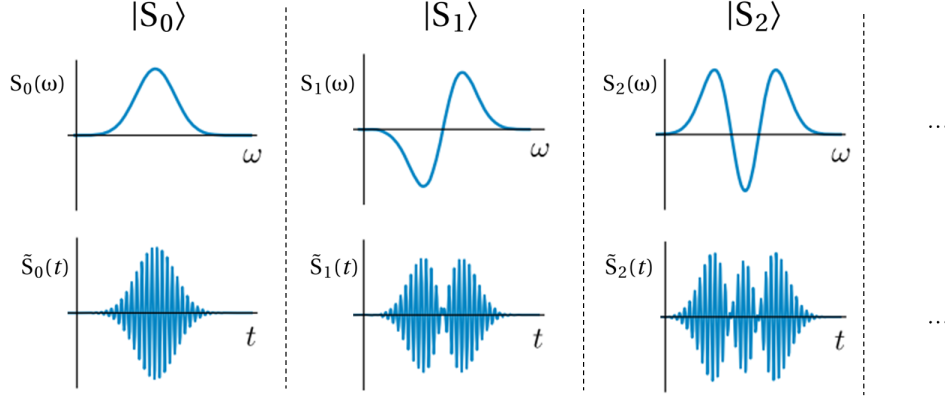
Fig. A2.7: *Examples of the first three eigenstates of a TM basis in the frequency domain (top) and time domain (bottom) for the signal. The idler photon is described by the same type of modes. Figure from [40]. Note that the signal and idler modes do not necessarily have the same spectral/temporal width.*

coefficients c_n:

$$\left|\psi_{pair}\right\rangle = \left(\sqrt{c_0}\,\hat{S}_0^\dagger\,\hat{I}_0^\dagger + \sqrt{c_1}\,\hat{S}_1^\dagger\,\hat{I}_1^\dagger + ... + \sqrt{c_n}\,\hat{S}_n^\dagger\,\hat{I}_n^\dagger + ...\right)|0,0\rangle \quad\text{(A2.19a)}$$

$$= \sqrt{c_0}\,|S_0,I_0\rangle + \sqrt{c_1}\,|S_1,I_1\rangle + ... + \sqrt{c_n}\,|S_n,I_n\rangle + ... \quad\text{(A2.19b)}$$

A typical example of TM decomposition obtained in a non-engineered medium is shown in Fig. A2.8 (note that the colormap is different due to the presence of negative values).
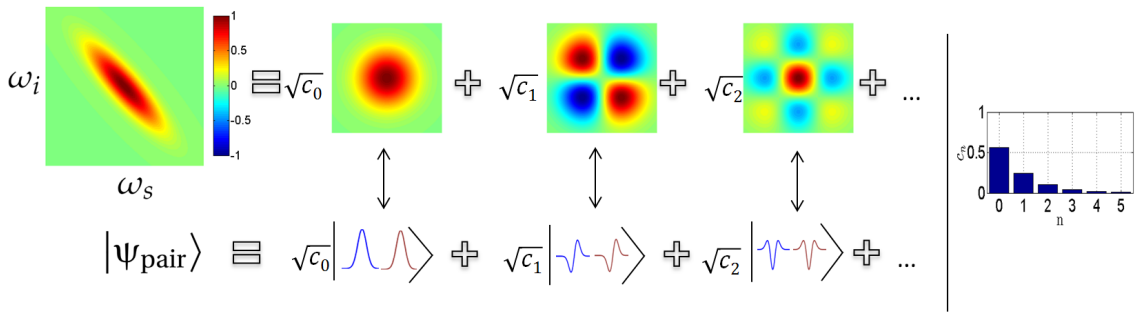
Fig. A2.8: *Left: JSA of a standard FWM source. It is decomposed into its different Schmidt components (with weighting coefficients c_n). Right: Corresponding Schmidt decomposition. Figure inspired by [40].*

In some specific cases, we will see that this decomposition can be limited so a single TM pair, as shown in Fig. A2.9.
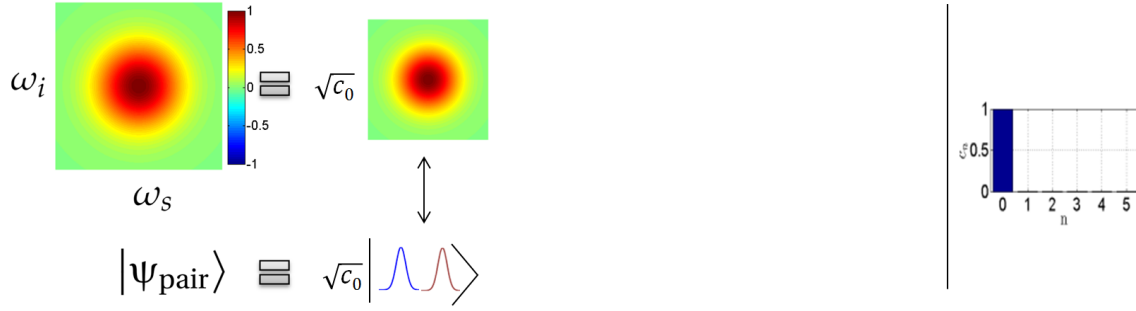
Fig. A2.9: *JSA of a spectrally engineered source leading to a unique TM pair (= factorable state).*

c) Purity of signal and idler photon

Such spectral entanglement between the signal and idler photon is essential when considering the purity of the individual photon [37]. In this section, we will use the density matrix representation instead of the wavefunction. For instance, if we consider a photon-pair state of the form: $\left|\psi_{pair}\right\rangle = |S_0\rangle\,|I_0\rangle$, the signal and idler subsystems are described by $|S_0\rangle$ and $|I_0\rangle$, respectively. However, if the photon-pair is in entangled superposition of the form $\left|\psi_{pair}\right\rangle = c_0\,|S_0\rangle\,|I_0\rangle + c_1\,|S_1\rangle\,|I_1\rangle$, the density matrix representation is required to infer the state of either one of the two subsystems.

Let us describe the photon-pair state by its density matrix:

$$\hat{\rho}_{pair} = \left|\psi_{pair}\right\rangle\left\langle\psi_{pair}\right| \tag{A2.20a}$$

$$= \sum_{n,n'} \sqrt{c_n c_{n'}^*}\,|S_n\rangle\,|I_n\rangle\,\langle S_{n'}|\,\langle I_{n'}| \tag{A2.20b}$$

Mathematically, a subsystem of a quantum state is described by tracing out the density matrix of the full state:

$$\hat{\rho}_{s/i} = \mathrm{Tr}_{i/s}(\hat{\rho}_{pair}) \tag{A2.21}$$

where $\hat{\rho}_x$ describes the subsystem x, Tr_x is the partial trace over the subsystem x, with x = s or i for signal and idler, respectively.

Another useful relation is that the purity of a given state described by a density matrix ρ is given by [43]:

$$P = \mathrm{Tr}(\rho^2) \tag{A2.22}$$

If P = 1, the state is pure, whereas if P < 1, the state is mixed.

Combining Eq. (A2.21) and Eq. (A2.22), the purity of the signal photon P_s and of the idler

photon P_i are given by:

$$P_{s/i} = \text{Tr}(\hat{\rho}_{s/i}^2) \tag{A2.23}$$

Since the photon pair is already written in terms of Schmidt decomposition, the signal and idler partial trace can be easily deduced:

$$\hat{\rho}_s = \sum_n c_n |S_n\rangle \langle S_n| \tag{A2.24a}$$

$$\hat{\rho}_i = \sum_n c_n |I_n\rangle \langle I_n| \tag{A2.24b}$$

Thus the purity gives:

$$P_s = P_i = \sum_n c_n^2 \tag{A2.25}$$

Such that:

$$\boxed{P_s = P_i = \frac{1}{K}} \tag{A2.26}$$

The spectral purity of the individual photons of the generated pairs is thus related to the Schmidt number. Looking at Eq (A2.26), one can see that the higher the mean number of TM modes, the lower the purity. In other words, if the pair is entangled which, as we have seen, means that $K > 1$, then, the single photon state is not pure ($P_s = P_i < 100\%$) i.e. the photon is in a mixed state.

Example: As an illustration, let us consider a Bell state of the form $|\psi\rangle = \frac{1}{\sqrt{2}}(|S_0, I_0\rangle - |S_1, I_1\rangle)$. As a matter of fact, it is already written as a Schmidt decomposition with $c_0 = \frac{1}{2}$ and $c_1 = -\frac{1}{2}$.

Accordingly, the Schmidt number is $K = \frac{1}{\sum_n c_n^2} = 2$ and the purity of each photons is $P = \frac{1}{K} = 50\%$.

Each of the photon taken individually is in a maximally mixed state (i.e $\hat{\rho}_s = \frac{1}{2}\left(|S_0\rangle \langle S_0| - |S_1\rangle \langle S_1|\right)$) with 50 % probability of being in the fundamental or the first excited mode.

Let us now illustrate these mathematical notions with the previous example of JSA shown in Fig. A2.8 and Fig. A2.9. First let us consider the non-engineered case (first row). Looking at the Schmidt coefficients c_n, it can be easily deduced that the state is entangled (the number of nonzero eigenvalues is more than one). In this example, the mean number is equal to K = 2.5 modes, meaning that the single-photon purity would be of P = 39 %.

Alternatively, in the engineered case, if the state is factorable with only one eigenvalue c_0 is

nonzero, then obviously, the mean number of modes is here K = 1 and thus each of the two photons is in a perfectly pure state P = 100%.
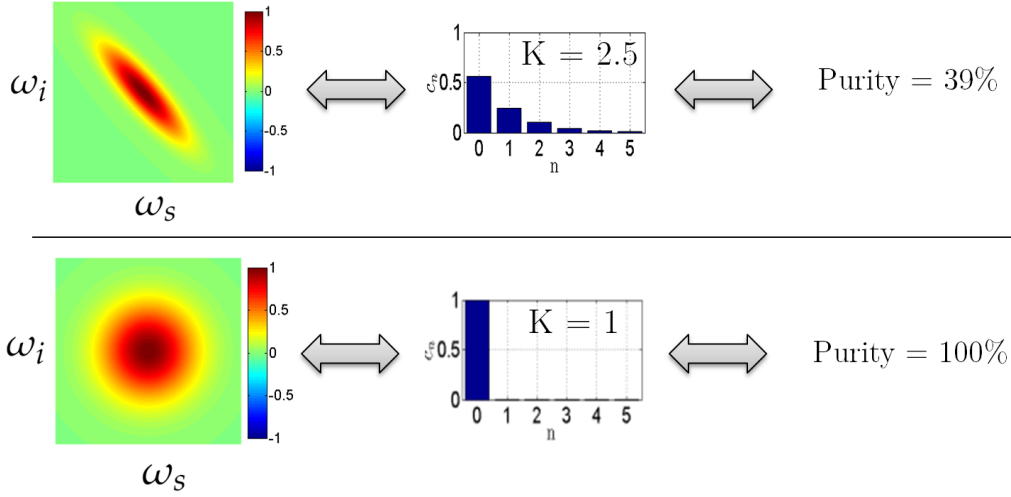

Fig. A2.10: *Two examples of JSA, their corresponding Schmidt decomposition and the associated purity.*

In the following, the conditions that are required to obtain a factorable state are described.

2.3 Group velocity matching

The parametric photons are generally spectrally correlated because the energy conservation constraint implies some anti-correlation between signal and idler frequencies. Two methods to obtain spectral factorability of a photon-pair state can be distinguished:

1. Canceling the anticorrelation of α with positive correlation of ϕ.

2. Asymptotically reducing the anticorrelation of α

Each of these two strategies adds constraints on the relations between the pump and the medium properties and more specifically on the group velocities relations between pump, signal and idler. These two strategies are commonly defined as symmetric and asymmetric group-velocity matchings (GVM) [34], that we detail in the following.

a) Symmetric group-velocity matching

Firstly, when the medium exhibits the group-velocity relation, $2\beta_{1p} = \beta_{1s} + \beta_{1i}$, the angle[7] of the phase matching function is then $\theta = 45°$. In addition, if the width $\Delta\phi = \Delta\alpha$, then the positive

---

[7] we recall that $\theta = -\arctan(\frac{\beta_{1p} - \beta_{1s}}{\beta_{1p} - \beta_{1i}})$ (Eq. A2.9b) with $\beta_{1,\mu} = \frac{d\beta}{d\omega}\big|_{\omega_\mu^0}$ being the inverse group-velocity.

correlations from ϕ perfectly cancel out anti-correlations from α. The resulting factorable JSA shapes as a circle (see Fig A2.11). The sidelobes beside the circle result from the rebounds of the cardinal sine function which tend to slightly decrease the factorability of the state.
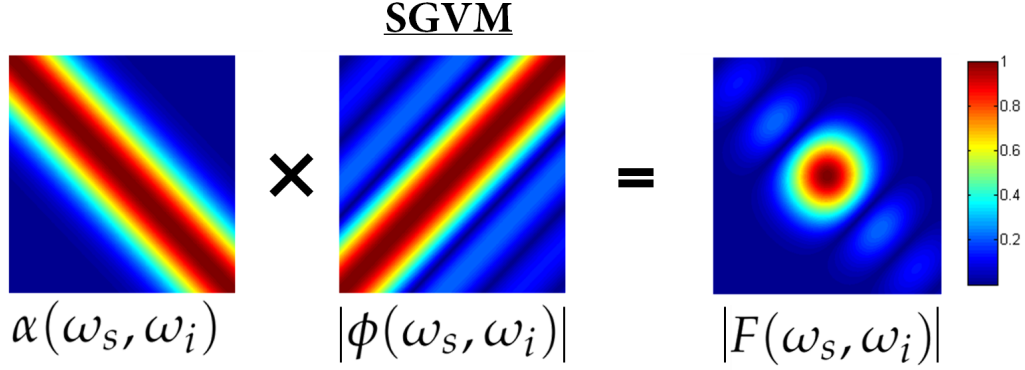
SGVM

Fig. A2.11: *From left to right: energy conservation function* α*, absolute value of the phase matching function* ϕ *and corresponding factorable joint spectral amplitude (absolute value) in the case of a symmetric group velocity matching.*

This condition is commonly referred as *symmetric group-velocity matching* as it leads to the generation of signal and idler photons with equal frequency bandwidths in contrast with the *asymmetric GVM* where signal and idler do not play symmetric roles any longer.

b)   Asymmetric group-velocity matching

Secondly, when the medium exhibits another particular group-velocity relation, $\beta_{1p} = \beta_{1s}$ or $\beta_{1p} = \beta_{1i}$, the angle of the phase matching function is equals to $\theta = 0°$ or 90°, respectively. This condition means that the pump has the exact same group velocity as one of the generated photon. However, such a condition between group velocities is once again insufficient to obtain a factorable state. In the asymmetric case, $\Delta\phi$ must be much thinner than $\Delta\alpha$ so that the JSA becomes an ellipse along either the horizontal or vertical axis (see Fig A2.12). Having $\Delta\phi << \Delta\alpha$, and $\theta = 0°$ or 90° ensures the asymptotical reduction of the correlation which results from the energy conservation. Note that in contrast with the symmetric case, the asymmetric GVM exhibits signal and idler photons with spectral widths being very distinct.

c)   Applications

In sum, two families are to be distinguished:

- The first one comprises factorable states where the signal and idler photons, being spectrally independent, are in a product state. When pumped by a Gaussian spectrum laser, this state can take the form of three distinct JSA geometry profiles forming a circle or an ellipse along either the horizontal or the vertical axis, each corresponding to a specific group-velocity relation between the photon pair and the pump.
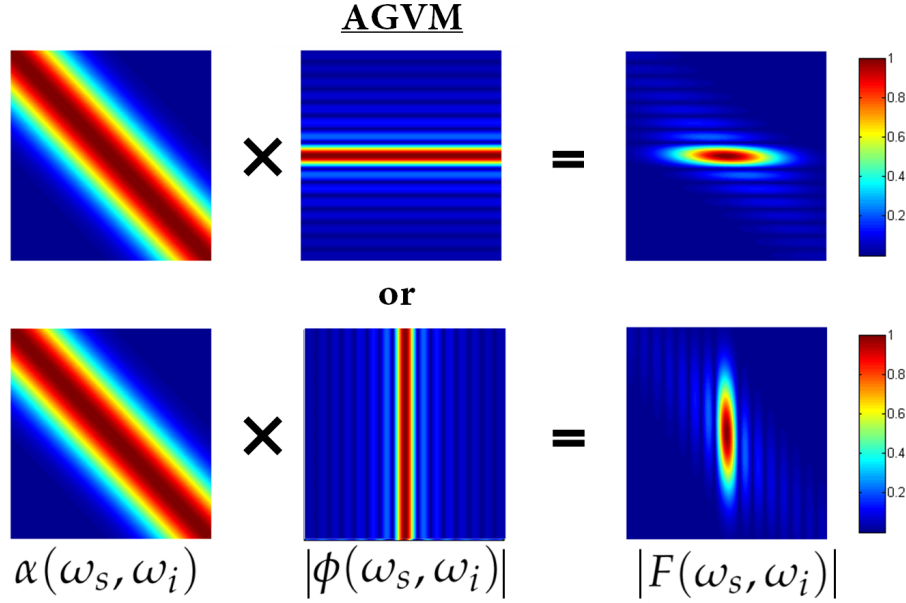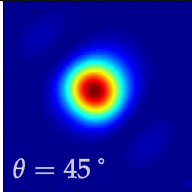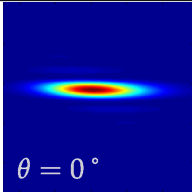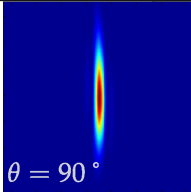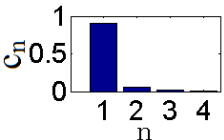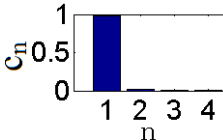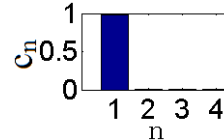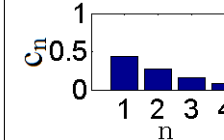
AGVM
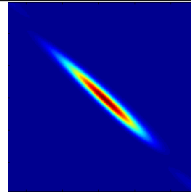
Fig. A2.12: *From left to right: energy conservation function α, phase matching function ϕ and corresponding factorable joint spectral amplitude in the case of the two asymmetric group velocity matching.*

- The second family of states that can be identified by JSA profiles relates to what is commonly referred to as correlated states. In such a scenario signal and idler photons are spectrally entangled. A representative JSA of such states is shown on the right hand side panel of Table A2.1. Here, the JSA typically shows a tilted ellipse profile.

Tab. A2.1: Sets of conditions required to obtain either factorable or correlated pair states. Each set defines i) a relation between medium length and pump bandwidth ii) a relation between the group-velocities of pump, signal and idler photons which in turn determines the angle θ.

FACTORABLE			CORRELATED
SGVM	AGVM		-
$\Delta\phi = \Delta\alpha$ $2\beta_{1p} = \beta_{1s} + \beta_{1i}$	$\Delta\phi << \Delta\alpha$ $\beta_{1p} = \beta_{1s}$	$\Delta\phi << \Delta\alpha$ $\beta_{1p} = \beta_{1i}$	- $\beta_{1p} < \beta_{1s,i}$
$\theta = 45°$	$\theta = 0°$	$\theta = 90°$	

These photon-pair states, being either spectrally factorable or entangled, are all useful in quantum technology applications.

As described previously, the less entangled the photon pair, the purer the two individual photons. For this reason, factorable states are the backbone for any applications requiring pure single photons as for instance, heralded single photon source [44, 45, 46], boson sampling [47] or temporal mode generation and manipulation [40, 48, 49].

Spectrally entangled states can be used for instance for improving the security of quantum key distribution [50] or for enlarging the information capacity of optical communication channel [40, 51].

2.4 Joint Temporal Amplitude and Phase Correlation

a) Joint Temporal Amplitude

Spectral and temporal properties are bound by Fourier relation. The joint temporal amplitude (JTA) is defined as the two-dimensional Fourier transform of the JSA:

$$\tilde{F}(t_s, t_i) = \mathbf{FT}\left[F(\omega_s, \omega_i)\right] \tag{A2.27a}$$

$$= \frac{1}{2\pi} \iint d\omega_s \omega_i F(\omega_s, \omega_i) e^{-i\omega_s t} e^{-i\omega_i t} \tag{A2.27b}$$

The JTA gives the joint probability of detecting a signal photon at time t_s and an idler photon at time t_i. As for the JSA, any entanglement between the two photons can be infered from the shape of the JTA.

In this manuscript we mainly focus on the spectral part (i.e. the JSA), because it is more closely related to what we measure experimentally. However, it is worth keeping in mind that spectral correlations are associated with their temporal counterparts. If the state is said to be correlated, signal and idler photon are spectrally **and** temporally correlated. Alternatively, if the frequencies of the signal and idler photons are uncorrelated, so are their emission times[8]. For concision, in this manuscript we only often refer to "spectral correlations" but obviously, it would be more suited to use the term "time-frequency correlation".

Figure A2.13 shows three examples of JTA together with their corresponding JSA assuming a Fourier transform limited pulse. One can see that photons which are anticorrelated in the spectral domain are positively correlated in the time domain. This means that they will tend to be detected with the same delay with respect to each other. Moreover, looking at the central figure

---

[8]that is not to say that the photons are emitted at random times. Each photon is emitted within a time interval whose duration is on the order of the pump-pulse duration. Beyond that constraint, however, the emission time of one photon is completely independent of the emission time of its conjugate.

of Fig.A2.13, when the frequency of a given photon (here the idler photon) is well-known, then, the uncertainty of its time of arrival is really large and vice versa as a direct consequence of the Fourier transform uncertainty relations.
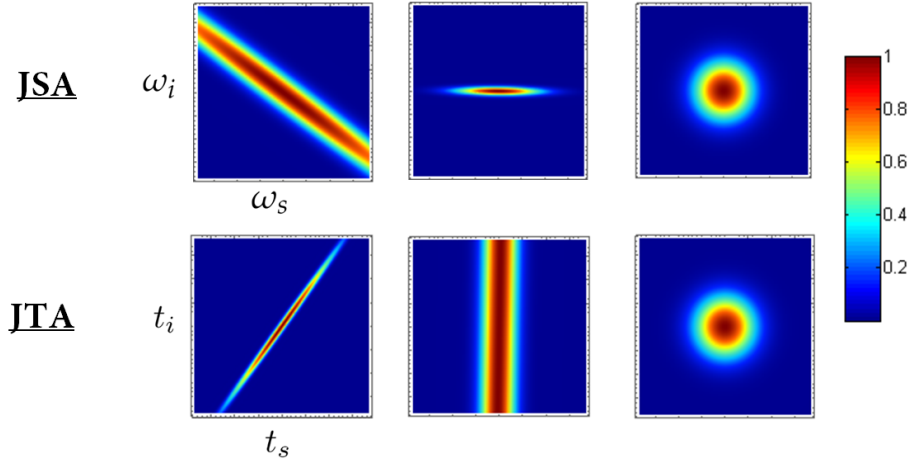

Fig. A2.13: *1st row: Three computed JSA corresponding to a correlated, the AGVM and the SGVM factorable JSA. 2nd row: associated JTA.*

b) Phase correlations

We have seen that the Schmidt decomposition of the JSA allows to infer the degree of spectral entanglement of the photon-pair. The JSA is a complex function with amplitude and phase. In general, if the pump is Fourier-transform limited, then the phase of the JSA does not induce any correlations[9]. Thus, until now, every time a JSA has been represented, only its absolute value was taken into consideration. Consequently, we have only discussed the consequences of spectral amplitude correlations. For instance, if the pulse contains a quadratic spectral phase (chirp), signal and idler spectra may exhibit strong phase-correlations. It is yet equally important to consider the phase-correlations which are also possible in some particular cases.

Let us define a pump with quadratic spectral phase by:

$$\tilde{\mathrm{E}}_{p,\mathrm{chirp}}(\omega) = \tilde{\mathrm{E}}_p(\omega) \underbrace{e^{+ia\omega^2}}_{\mathrm{chirp}} \tag{A2.28}$$

Where $\tilde{\mathrm{E}}_p(\omega)$ is a Fourier transfom limited pulse.

A chirped pulse has its different spectral components travelling at different velocities. In the temporal domain, this causes the temporal envelope to be broader than the usual Fourier limit.

---

[9]indeed the usual phase $e^{i\Delta\beta\frac{L}{2}}$ can be written as a product $e^{i(\beta(\omega_p)-\beta(\omega_s))\frac{L}{2}} \times e^{i(\beta(\omega_p)-\beta(\omega_i))\frac{L}{2}}$ where signal and idler are separated (= factorable)

The corresponding energy conservation function is:

$$\alpha(\omega_s, \omega_i) = \left[\tilde{E}^{(+)}_{p,\text{chirp}} * \tilde{E}^{(+)}_{p,\text{chirp}} \right](\omega_s + \omega_i) \tag{A2.29}$$

In the case of a gaussian pump we have:

$$E_p(\omega) = e^{-\frac{\omega^2}{2\sigma^2}} \Rightarrow \alpha(\omega) = \sqrt{\sigma} e^{-\frac{\omega^2}{4\sigma^2}} \tag{A2.30}$$

Then for a chirped pump, replacing $\sigma^2 \rightarrow \sigma^2 + \frac{2}{ia}$ we obtain:

$$E_p(\omega) = e^{-\frac{\omega^2}{2\sigma^2} + ia\omega^2} \Rightarrow \alpha(\omega) = \frac{1}{\sqrt{\frac{1}{\sigma^2} - 2ia}} e^{-\frac{\omega^2}{4\sigma^2} - \frac{ia\omega^2}{2}} \tag{A2.31}$$

In the case of a chirp, while the phase-matching function ϕ remains unchanged, the energy conservation function bears an imaginary part and an additional phase term ($e^{-\frac{ia\omega^2}{2}}$) which adds phase-correlations. Fig A2.14 depicts chirp-related JSA/JTA. As the chirp increases, the |JSA| remains the same whereas the JTA exhibits more and more entanglement.

To sum up, in the presence of non Fourier transform pulses, if one wants to infer the spectral correlations it is then required to look at both intensity and phase of the JSA or alternatively at the intensity of JSA and JTA.
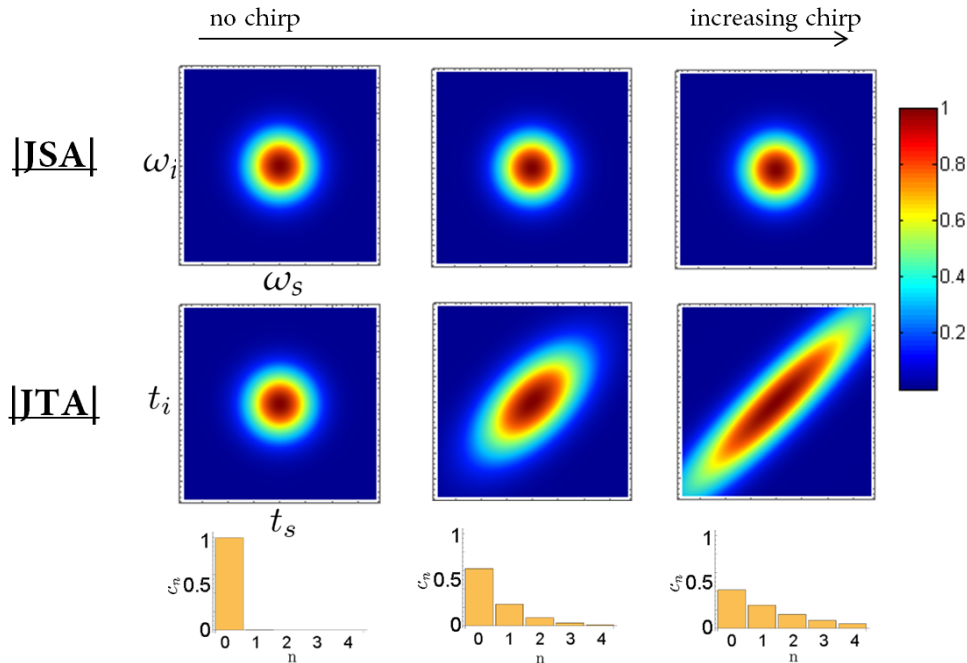

Fig. A2.14: *Absolute value of the JSA with its associated JTA and Schmidt decomposition. Going from left to right, the chirp increases. Starting from a factorable state with no chirp, increasing the amount of chirp results in a more and more entangled state.*

2.5 The spectral density map

It is also useful to introduce a handy tool called the spectral density map. Such a map is really useful, especially from an experimental point of view, as it predicts with accuracy the central position of the signal and idler wavelength that are going to be generated as a function of the pump wavelength.

In order to compute the wavelengths satisfying energy conservation and phase-matching as a function of pump wavelength, the general equation of the JSA (Eq. (A1.41)) has to be integrated:

$$|\psi_{\text{pair}}\rangle = \kappa \iiint_0^\infty d\omega_s \, d\omega_i \, d\omega_{p1} \, \tilde{E}_{p1}^{(+)}(\omega_{p1}) \tilde{E}_{p2}^{(+)}(\omega_s + \omega_i - \omega_{p1}) \tag{A2.32}$$
$$\text{sinc}\Big(\Delta\beta(\omega_{p1}, \omega_s, \omega_i)\frac{L}{2}\Big) e^{i\Delta\beta(\omega_{p1}, \omega_s, \omega_i)\frac{L}{2}} |\omega_s, \omega_i\rangle$$

However, in the general case such a map is 3 dimensional (depending on ω_p, ω_s and ω_i) and is therefore not straightforward to represent graphically.

The spectral density map (SDM) is a two dimensional approximated solution. It assumes a strict energy conservation $2\omega_{p0} - \omega_s - \omega_i = 0$ where ω_{p0} is the pump central frequency. Under such an approximation, a photon-pair state can be (see Annexe I) simplified to:

$$|\psi_{\text{pair}}\rangle \approx \kappa \iint d\omega_p \, d\omega_s \, \text{sinc}\Big((2\beta(\omega_p) - \beta(\omega_s) - \beta(2\omega_p - \omega_s))\frac{L}{2}\Big) |\omega_s, 2\omega_p - \omega_s\rangle \tag{A2.33}$$

which defines the spectral density map function:

$$\text{SDM}(\omega_p, \Delta\omega) = \text{sinc}\Big((2\beta(\omega_p) - \beta(\omega_p + \Delta\omega) - \beta(\omega_p - \Delta\omega))\frac{L}{2}\Big) \tag{A2.34}$$

where $\Delta\omega = \omega_p - \omega_s = \omega_i - \omega_p$.

Assuming $2\omega_{p0} - \omega_s - \omega_i = 0$ is a simplified way to incorporate the energy conservation condition, however, it does not take into account the shape and the width of the pump spectrum. In other words, it assimilates the pump spectrum to a Dirac function $\delta(\omega - \omega_{p0})$. Therefore, the SDM corresponds to the combination (ω_s, ω_i) that fulfils energy and momentum conservations **when considering a monochromatic pump at frequency ω_{p0}.**

The SDM usually exhibits two different behaviour depending on the relative signs and magnitude of the even derivative of $\beta(\omega)$ [19]. Indeed, a Taylor expansion of the phase-mismatch

around ω_p gives:

$$\Delta\beta(\omega_p, \Delta\omega) = 2\beta(\omega_p) - \beta(\omega_p - \Delta\omega) - \beta(\omega_p + \Delta\omega) \tag{A2.35a}$$

$$\approx -2 \sum_{m=1}^{+\infty} \frac{(\Delta\omega)^{2m}}{(2m)!} \beta_{2m}(\omega_p) \tag{A2.35b}$$

with $\beta_m = \frac{d^m\beta}{d\omega^m}$.

Which, in most fiber can often[10] be approximated by its first order:

$$\Delta\beta(\omega_p, \Delta\omega) \approx -(\Delta\omega)^2 \beta_2(\omega_p) \tag{A2.35c}$$

The sign of β_2, or more precisely the sign of $D(\lambda) = -\frac{2\pi c}{\lambda^2}\beta_2(\omega)$ commonly defines the normal ($D<0$) and anomalous ($D>0$) dispersion regime. Moreover, the zero-dispersion wavelength is by definition the wavelength for which $D(\lambda_{ZDW}) = 0$.

As illustrated in Figure A2.15 showing the $|SDM(\omega_p, \Delta\omega)|^2$ of the fiber presented in Part B, two different phase-matching are generally possible. On the one hand, there exist phase-matching solutions where the photon-pairs are generated around the pump wavelength in a broadband spectrum[11]. This defines the *modulational instability* regime (MI). On the other hand, photon-pairs well separated from the pump wavelength can also be generated. This defines *four-wave mixing*.

In this manuscript, we always work with four-wave mixing because the large wavelength separation between the signal/idler photon and the pump greatly facilitates their filtering from the pump. In the example of the fiber presented in Fig. A2.15, the FWM occurs in the anomalous regime.

---

[10]note that for the specific case of the fiber presented in Fig. A2.15, it is required to take into account a higher order $\Delta\beta(\omega_p, \Delta\omega) \approx -(\Delta\omega)^2\left(\beta_2(\omega_p) + \frac{(\Delta\omega)^2}{12}\beta_4(\omega_p)\right)$

[11]eventually, in the presence of strong self-phase modulation, it is possible to generate signal and idler whose frequencies are not overlapping with the pump spectrum [26]. However, such a high gain regime requirement is generally not compatible with photon pair generation.
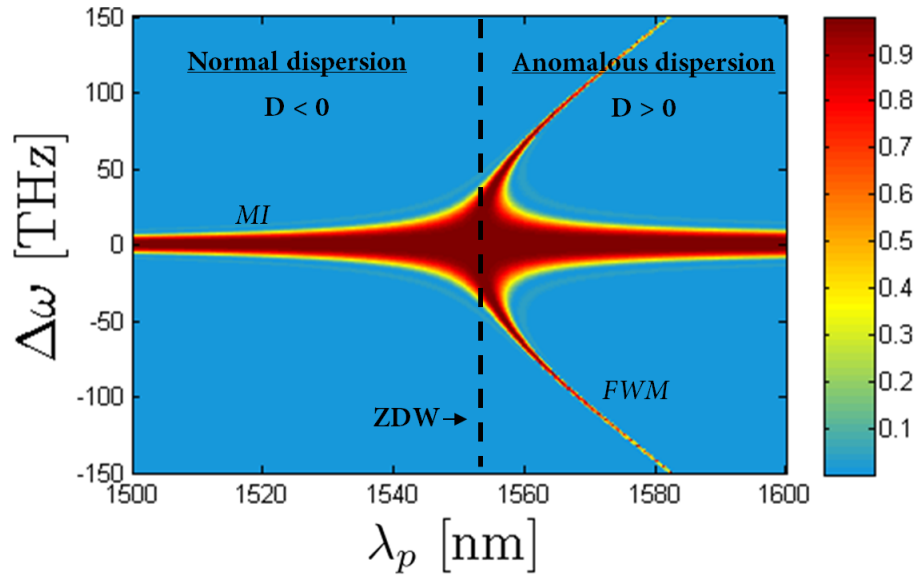
Fig. A2.15: *Computed squared modulus of the spectral density map of the PBG-HCPCF from part B. MI: modutional instability, FWM: four-wave mixing, ZDW: zero-dispersion wavelength.*

Chapter A3

Avoiding Raman scattering

Fiber-based sources are an attractive tool for photon pair generation. They can exhibit very low absorption ($\sim$ dB/km), strong confinement over long distance and high nonlinearities according to the chosen glass(n_2 from 10^{-20}m^2/W in silica to 10^{-17}m^2/W in chalcogenide). Moreover, they are easily manufacturable and integrable into optical networks.

However, the major intrinsic issue of standard fiber-based photon pair sources[1] is the Raman-scattering noise [10, 12, 13, 52] which can occur simultaneously with FWM, producing photons at signal and idler wavelengths and plaguing the quality of the fibered photon-pair source. This chapter describes the nonlinear process of Raman-scattering and it spectral properties depending on the medium (amorphous, crystal, liquid, gas). A state of the art of the solutions that have been investigated to address this issue is presented in the second section.

3.1   Description of Raman scattering

Third order nonlinear processes can be classified into two categories:

- **elastic processes** in which the optical state bears the same energy before and after the process. In other words, energy is conserved, there is no energy transfer between light and the nonlinear medium. These processes such as four-wave mixing or third harmonic generation are the ones we consider in our theoretical development in chapter A1 .

- **inelastic processes** where, conversely, energy exchange between the optical beam and the medium does take place. In optical fibers, it mainly includes Raman-scattering[2]

---

[1] fiber whose core is made of silica (i.e. conventional optical fiber and solid-core photonic crystal fiber)
[2] Brillouin scattering is another inelastic process that can occur in fiber however in the regime of femtosecond

a)   A molecular response

Fundamentally, Raman-scattering is a response from the molecules constituting the medium. In the presence of the optical field $E_p(t) = E_0 \cos(\omega_p t)$, each molecule becomes polarized and induces a dipole moment $p(t)$.

$$p(t) = \alpha(t)E_p(t) \tag{A3.1}$$

The medium polarization is approximately [30]:

$$P(t) = N\,p(t) \tag{A3.2}$$

with N being the volumetric molecules density.

Let us first consider the simple case of a material made up of diatomic molecules. It is assumed that the molecular polarizability depends on the internuclear distance $r(t)$, according to the equation[3]:

$$\alpha(t) = \alpha_0 + \frac{\partial\alpha}{\partial r}\Big|_{r_0}(r(t) - r_0) \tag{A3.3}$$

where α_0 and r_0 are the polarizability and the internuclear distance at equilibrium, respectively.

Each molecule can be described as a harmonic oscillator with a resonance frequency ω_v.

$$r(t) = r_0 + r_v\cos(\omega_v t) \tag{A3.4}$$

Injecting, Eq. (A3.3) into Eq. (A3.1) we obtain:

$$p(t) = \alpha_0 E_0 \cos(\omega_p t) + \frac{r_v E_0}{2}\big(\cos((\omega_p - \omega_v)t) + \cos((\omega_p + \omega_v)t)\big)\frac{\partial\alpha}{\partial r}\Big|_{r_0} \tag{A3.5}$$

This simplified calculation shows that, when subject to a field at ω_p, the molecular dipoles radiate two additional fields at $\omega_p - \omega_v$ and $\omega_p + \omega_v$. The created up- and down-converted fields are referred to as the anti-Stokes ($\omega_{AS} = \omega_p + \omega_v$) and Stokes ($\omega_S = \omega_p - \omega_v$), respectively. In terms of energy, the Stokes scattering can be described as the conversion of a pump photon with frequency ω_p, into a Stokes photon of lower frequency ω_S and a phonon of frequency ω_v. Similarly, the anti-Stokes Scattering can be viewed as the annihilation of a pump photon and a phonon, creating an anti-Stokes photon with higher frequency (see Fig. A3.1).

Once the Raman Stokes or Anti-Stokes photon is created, its presence can stimulate another

---

and picosecond pulses it has generally negligible consequences as opposed to Raman-scattering.
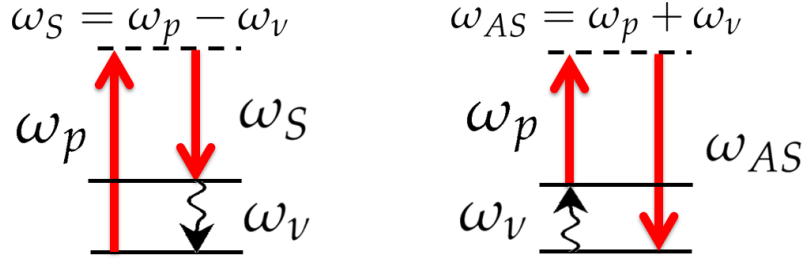
[3]see p. 458 from [30]

Fig. A3.1: *Energy level diagrams describing Raman Stokes (left) and anti-Stokes scattering (right). Straight and curved arrows correspond to photon and phonon frequencies, respectively.*

identical process. This self-stimulation Raman process can cascade resulting in the generation of large number of coherent identical Raman scattered photons [4].

Figure A3.2 depicts the Raman-scattering process. At equilibrium, Stokes scattering tends to be much stronger than anti-Stokes since the phonon population in the excited state is smaller (by an amount[5] $\propto e^{-\frac{\hbar\omega_v}{kT}}$).
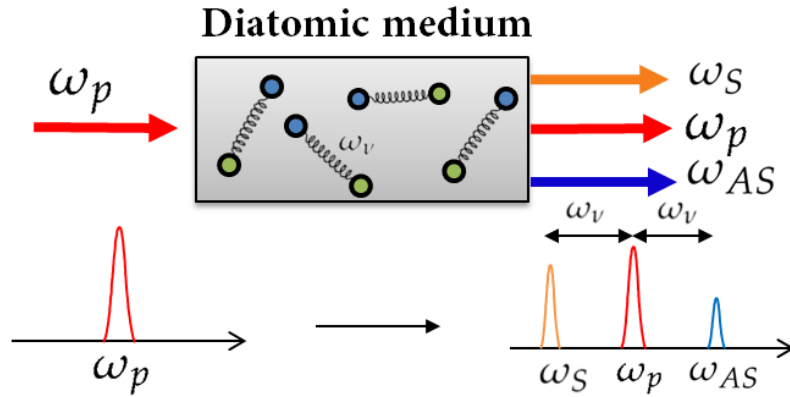

Fig. A3.2: *Illustration of the Raman-scattering process in a medium composed of identical diatomic molecules*

b) Raman scattering in different medium

Describing a medium as a combination of independent molecules is quite legitimate when considering dilute media. In gaseous and liquid media, the molecules move relatively freely and do not interact much with one another. As a consequence, the Raman spectra of liquids and gas consist of thin lines as a result of quantization of molecule vibrational states [54]. It is noteworthy that noble gases (neon, argon, xenon, etc.), as a result of the monoatomic form of

---

[4] reference [53] provides an insightful description of how spontaneous Raman-scattering, which is an intrinsically quantum mechanical process, results in a coherent beam of Raman-scattered photons.

[5] the phonon population at $E = \hbar\omega_v$ is given by the Bose Einstein statistic $n_{\text{phonons}}(T) = \frac{1}{e^{\frac{\hbar\omega_v}{kT}} - 1}$

their molecules, are completely devoid of Raman-scattering.

In a solid medium, the situation is somewhat different as atoms are at fixed positions and have strong interactions with their neighbors. The individual atoms, being linked to one another, are "frozen" at their positions which gives rise to lattice vibrations instead of individual molecule vibration. In contrast to a molecule, a lattice has an infinite number of vibrational degrees of freedom [54]. The allowed vibrational states solely depend on the symmetry of the lattice. In a crystal, due to its high symmetry, only a narrow range of lattice vibrational states is possible which results in thin lines Raman spectra. Inversely, the lack of symmetry in amorphous material allows a large range of lattice excitations, resulting in a broadband Raman spectrum.

Figure A3.4 shows the Raman-scattering spectrum in different medias as a function of the distance from the pump wavelength in cm^{-1}: $|\frac{1}{\lambda_p} - \frac{1}{\lambda}|$. It describes both Stokes and Anti-Stokes spectra which are identical (with difference in intensity though). For the Stokes, one simply considers $\lambda > \lambda_p$ whereas for the Anti-Stokes $\lambda < \lambda_p$.

Therefore, in standard fiber medium, due to the amorphous nature of silica, the Raman-scattering is broadband (see Fig. A3.3). This can be very useful for realizing broadband amplifiers [55], but quite deleterious for quantum optics applications such as photon pair generation. Indeed, the Raman spectrum covers all the frequencies around the pump and will overlap with signal and idler frequencies [56, 57], and therefore deteriorate the quality of the source. Using another glass (chalcogenide, tellurite, fluoride, etc.) does not solve the problem since all amorphous materials exhibit broad Raman spectra [20, 21].
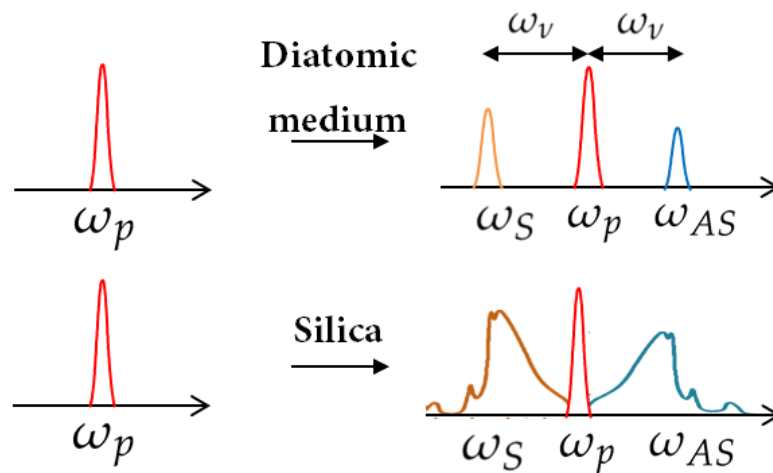

Fig. A3.3: *Comparison of Raman-scattering effects in a perfect diatomic medium and in silica. The intensities are arbitrary.*
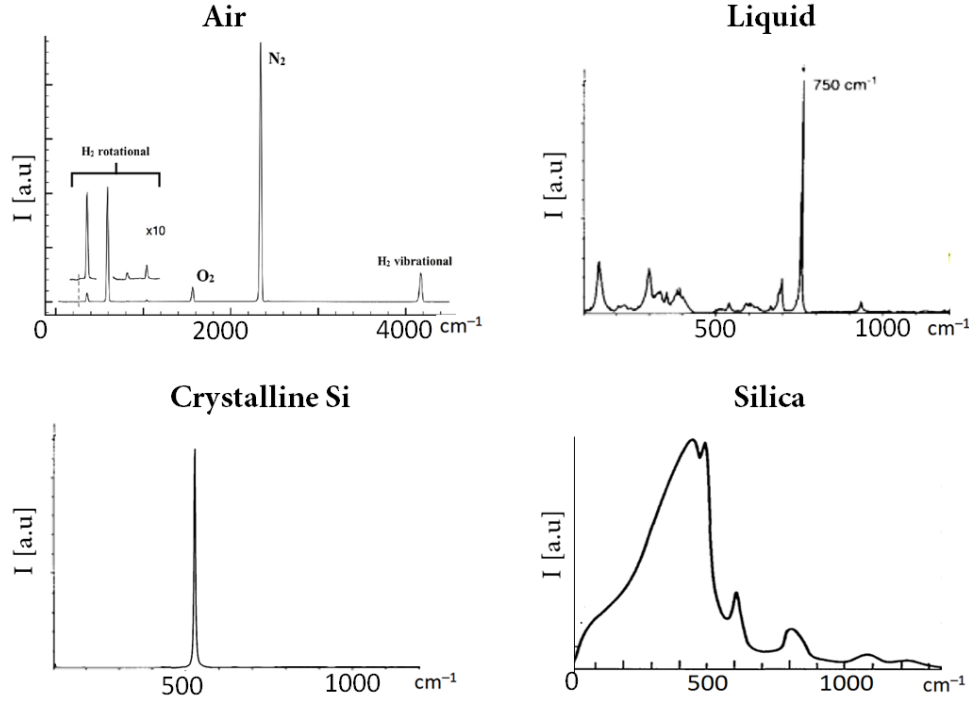
Fig. A3.4: *Raman-scattering spectrum of Air [58], of a given liquid (perfluorotripropylamine) [59], of silicon as well as in silica [60] showing very different behaviours. Note that the intensities are not normalized one to another.*

3.2 Possible Solutions

Several solutions exist to avoid or reduce Raman-scattering noise.

One solution is to generate the photon pair with a large spectral separation from the pump. Looking at the Raman spectra of silica (Fig. A3.4), one can observe that the noise is mostly concentrated in the 0 - 500 cm^{-1}, above this region, the Raman noise is less detrimental. This approach has been mostly investigated in PCF [61, 13, 14, 62] since the versatility of its design allows to favour the generation of photon-pairs with a large detuning from the pump wavelength. However, higher order Raman-scattering processes still corrupt the parametric process, as described in [13, 63, 64]. This results from a multiphonon interaction, in which the pump creates cascading Stokes and Anti-Stokes fields, spreading the Raman-scattering noise to an even larger separation from the pump.

Another investigated solution is to cool down the fiber to cryogenic temperature. At ∼ 77 K [65, 4, 66, 67, 68, 69], 4 K [7] or even 2 K [70], the efficiency of the spontaneous Raman-scattering is highly reduced. The main drawback of this approach is that it adds a layer of experimental difficulty, making it less practical for applications and limited in terms of integration.

Finally an ultimate solution to avoid the broadband Raman-scattering is to use a fiber whose core is not made of silica. **Our approach consists in using hollow-core photonic crystal fiber (HCPCF) which guide light through the medium filling its core, whatever it can be, either a liquid or a gas.** The discrete line Raman spectrum intrinsic to liquid or gas media are interesting to solve the issue of Raman contamination at signal and idler wavelength. Indeed, since the noise is concentrated in narrow lines or completely absent (noble gas), the spectral range of FWM parametric photons can be chosen to avoid the overlap with the Raman noise, in order to produce *Raman-free* photon pairs. This is what we demonstrate in chapter C3. Table **??** presents an overview of the reported hollow-core sources.

In the following, two hollow-core fiber sources are presented in the manuscript, based on two different guidance mechanisms and fillings:

1. a liquid filled hollow-core fiber source presented in *Part B*. The guidance mechanism of this fiber relies on photonic bandgap (PBG) presented in the next chapter.

2. a gas-filled hollow-core fiber source presented in *Part C*, relying on another guidance mechanism, namely, inhibited coupling (IC). The description of this guidance mechanism and of its distinctive features compared to PBG is performed in section C.1.2.

Tab. A3.1: Hollow-core sources

Guidance mechanism	Filling fluid	Non-linear process	$\lambda_s, \lambda_p, \lambda_i$ [nm]	Raman scattering	Correlation engineering	Regime	Refs
PBG	Liquid (Acetone-d6)	FWM	$\lambda_s = 857$ $\lambda_p = 885$ $\lambda_i = 916$	Limited	No	Photon-pair	[25]
PBG	Liquid (FC3283)	FWM	$\lambda_s = 1540$ $\lambda_p = 1550$ $\lambda_i = 1560$	Limited	No	Classical	**This Work** (*Part B*)
IC	Noble Gas (Argon)	MI	$\lambda_s = 697$ $\lambda_p = 800$ $\lambda_i = 937$	Absence	Yes	Squeezed vacuum	[26, 27]
IC	Noble Gas (Xenon)	FWM	$\lambda_s = 770$ $\lambda_p = 1030$ $\lambda_i = 1570$	Absence	Yes	Photon-pair	**This Work** (*Part C*)

Part B

Liquid-filled PBG Fiber: Toward Telecom Raman-free photon pair source

Part B of the manuscript is devoted to a study on the use of liquid-filled photonic bandgap HCPCF for Raman-free photon-pair generation at telecom wavelenght. Several combinations of liquids and fibers are investigated through experimental characterizations as well as simulations and the results are described in the first chapter. As a result of this investigation, a fiber/liquid combination compatible with the generation of photon-pairs in the C-band is identified. The second chapter describes how the Raman-scattering can be avoided in such a fiber and the experimental setup that has been built toward the detection of Raman-free photon-pairs.

This work is done in close colaboration with P. Delaye and his PhD student T. Harlé, whose team has demonstrated the first (and only to our knowledge) hollow-core photon pair source in the near-IR [25, 29].

Chapter B1: Design of the Liquid-filled PBG-HCPCF

Chapter B2: Toward Raman-free four-wave mixing

Chapter B1

Design of the Liquid-filled PBG-HCPCF

The first section of this chapter describes in details the guiding mechanisms of the fibers we use. Then, an investigation is performed to find a suitable combination of fiber design and choice of liquid compatible with a four-wave mixing at telecom wavelength. More specifically, a numerical study of the strong links between fiber and liquid parameters leads our study to three fiber/liquid combinations. Sections 3 and 4 are devoted to the experimental characterization of these combinations, where both dispersion and nonlinearity are measured. Finally the expected joint spectral amplitude of the source is discussed in the last section.

1.1   Guidance mechanism of Photonic Bandgap Fiber (PBG)

The standard total internal reflection (TIR) guidance mechanism is based on a refractive index mismatch between the core and the cladding, the former being higher than the latter. Therefore, TIR configuration is not compatible with a guidance within a hollow-core as it would require a refractive index for the cladding to be less than one which is generally not possible with natural material.

In the 1990's, P. Russell [71] proposed a novel idea which consists in trapping light in a defect of an elongated 2D photonic crystal (see Fig. B1.1). This defect forms the core of the fibre, while the lattice forms the cladding. This discovery quickly led to many new developments and fiber designs, such as the first kind of hollow-core fiber: **the hollow-core photonic bandgap fiber (PBG-HCPCF)**. The existence of the other type of hollow-core fiber, relying on inhibited

coupling, was later demonstrated by F. Benabid in 2002 [72, 73]. (Part C is devoted to our investigation of inhibited coupling hollow core fiber).
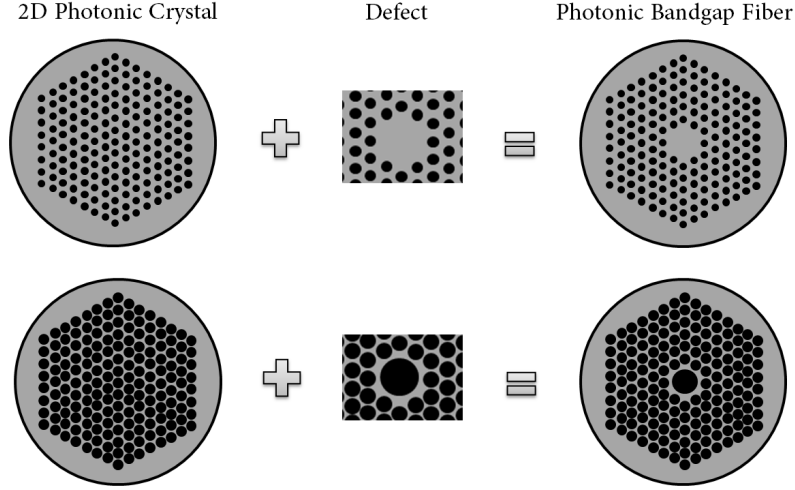

Fig. B1.1: *Basic principle of photonic bandgap fiber. Top Solid-core PBG. Bottom: Hollow-core PBG.*

a) The Bandgap

The light whose wavelength is of the same order of magnitude as the periodicity of a 2D photonic crystal cannot propagate in the lattice. Such forbidden wavelength range is commonly refered to as a bandgap in analogy with the density of electronic states of semi-conductors in condensed matter physics[1] [75]. Thus, the first characteristic of a PBG guidance is the existence of a spectral range void of cladding modes (i.e. modes localised in the photonic crystal). For the specific case of the hollow-core guidance mechanism where light is trapped in air/vacuum, it is further required that such bandgap lies below the light line of air [23, 75] defined by $n_{eff} = 1$ (with $n_{eff} = \frac{\beta(\omega)c}{\omega}$).

In Figure B1.2, a computed density of allowed photonic states of an infinite triangular lattice is shown as a function of effective index and normalized frequency kΛ. Here k is the wavenumber and Λ is the photonic structure pitch. The top left hand side inset shows the lattice pattern and defines the *apex* and the *strut*. The bandgap of the 2D crystal is the white area corresponding to a zero density of states. It is bound by three different types of cladding modes illustrated by the mode profiles (Fig. B1.2.b-d) [76]:

- left edge modes localised in the apexes of the 2D crystal

---

[1] the photonic tight-binding model [74] gives an intuitive relation between crystals in condensed matter physics and in photonics. Tranposing from condensed matter to photonics, the atoms are replaced by waveguide (one rod), the inter-atomic distance by the pitch Λ, and the energy levels by the propagation constant. Thus when the waveguides are close enough, the optical fields in the waveguide start overlaping, inducing bands of allowed states separated by bandgap.

- right edge modes localised in the struts

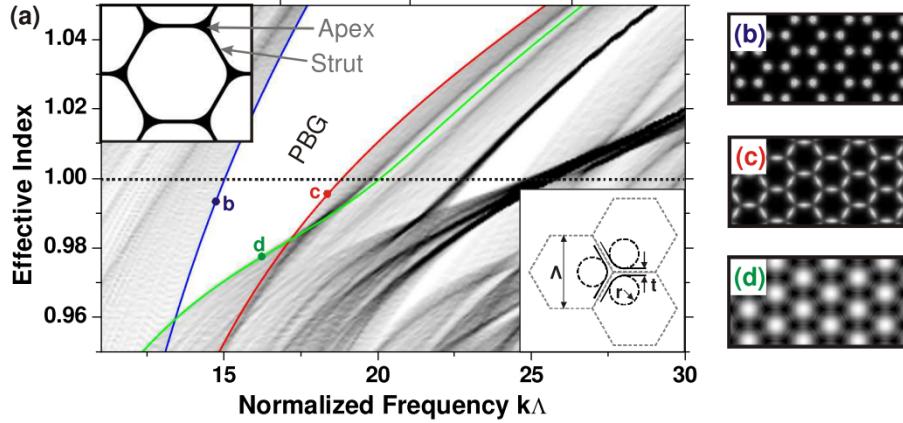- low edge modes formed by air localised modes

Fig. B1.2: *(a) Density of photonic states for an infinite cladding structure only (no core) whose lattice pattern is illustrated in the top-left inset. White represents zero density, and black maximum density. Hence, the photonic bandgap (PBG) is the region where light is forbidden in the cladding. Above and below the bandgap, light couples into the cladding. (b)-(d) Mode profiles calculated at the bandgap edge at the positions indicated in the left plot. Reproduced with permission from [77].*

b)   The Core/Defect

Then, if a suitable defect, able to support modes in this PBG region, is created in the cladding, light can be confined therein. For instance such defect can be obtained by omitting several unit cells of material from the cladding. An intuitive image is that the light, present in the core, is reflected whenever it encounters the 2D Bragg structure constituting the cladding.

Figure B1.3 shows a zoom of the density of states when adding a defect in the 2D photonic crystal, resulting in a core mode whithin the bandgap. Note that the modal content of "core modes" mainly depends on the size of the defect. The larger the core, the more multimode it becomes [23].

c)   A versatile platform for nonlinear optic

Interestingly, in such a waveguide, the optical properties depend on the core and cladding geometries (pitch of the lattice, symmetries, etc). For instance, since the pitch governs the wavelengths which are forbidden in the cladding, the position of the transmission band of the fiber can be tailored by controlling this geometrical parameter.
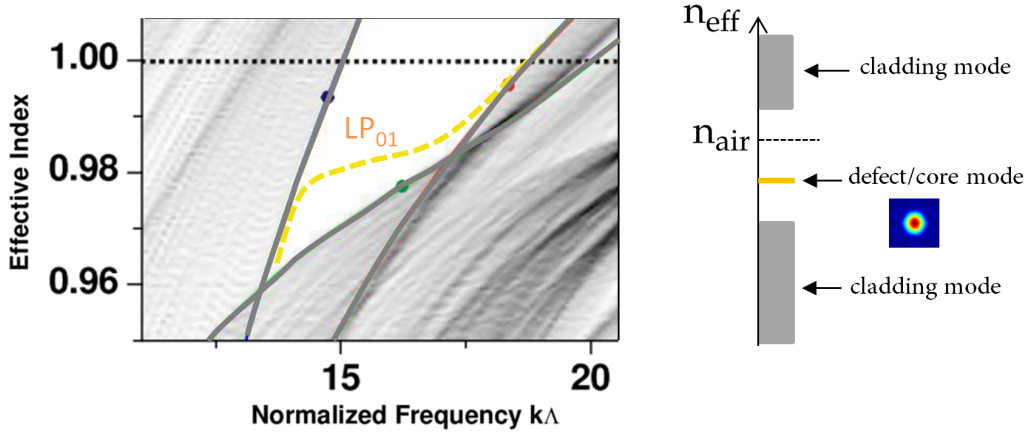
Fig. B1.3: *Left: Density of photonic states for the cladding structure (grey) and core (yellow). The core mode is an illustration and do not corresponds to actual computed data. Right: vertical slice at* $k\Lambda \sim 16$

Moreover, thanks to the PBG guiding mechanism, the core is not restricted anymore to have a higher index than the cladding. Consequently, PCF have allowed the emergence of hollow-core PCF, in which light is guided through air or vacuum. HCPCF can also be filled with a liquid or a gas in order to micro-confine together light and fluids within small modal areas and over interaction lengths that can reach up to kilometres with low optical losses ($\sim 10 - 300$ dB/km). Thanks to this ability HCPCFs are an exceptional tool for light and fluid-phase interactions.

In addition to the choice of HCPCF geometrical design, the choice of the fluid further increases the versatility with the possibilities of tailoring both optical nonlinearity and dispersion [75, 78].
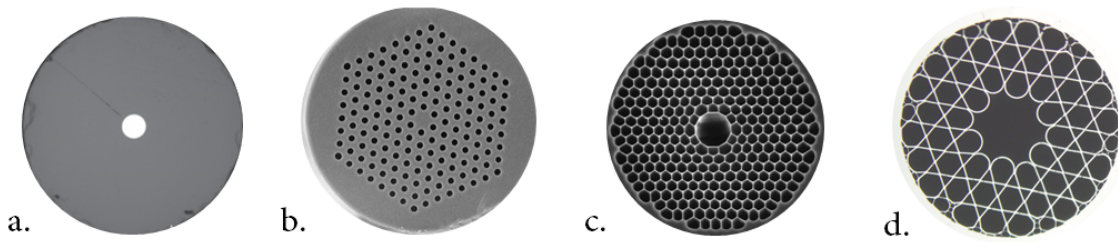

Fig. B1.4: *Cross section of **a.** SMF fiber (TIR) **b.** silica core photonic bandgap PCF **c.** hollow core photonic bandgap PCF **d.** hollow core inhibited coupling PCF (kagome fiber).*

1.2   Finding the right Fiber/Liquid combination

We want the photon pair source to operate around the telecom wavelength of 1.55 μm. To satisfy this requirement we have to select a combination of fiber geometry and liquid refractive index and dispersion. Moreover, the liquid is chosen such that it exhibits low absorption in

the IR, non toxicity and a relatively low viscosity (1 mPA.s) to minimize the fiber filling process duration.

a) A liquid-filled fiber

Prior to detailing the parameters of fiber and liquid, let us briefly describe what part of the fiber is filled and how. The fiber can be filled with the liquid either fully or selectively. A selective filling, with certain holes (either the core or holes in the cladding) being empty or filled with different liquids, is particularly useful for sensing applications [79, 80, 81].

In the context of this work we investigate fully filled fiber -whose core and cladding are both filled with the same liquid. Such a configuration has the advantage of being much easier to handle experimentally. In practice, the filling is achieved through capillarity by placing both ends of the fiber in liquid tanks. After typically less than one hour, a one meter long fiber is entirely filled. Obviously, the duration of the process depends on many parameters such as fiber length, fiber radius, applied pressure and the viscosity of the liquid. For the sake of this work, liquids with relatively low viscosity (1 mPa.s) are favoured in order to limit the fiber-filling process duration.
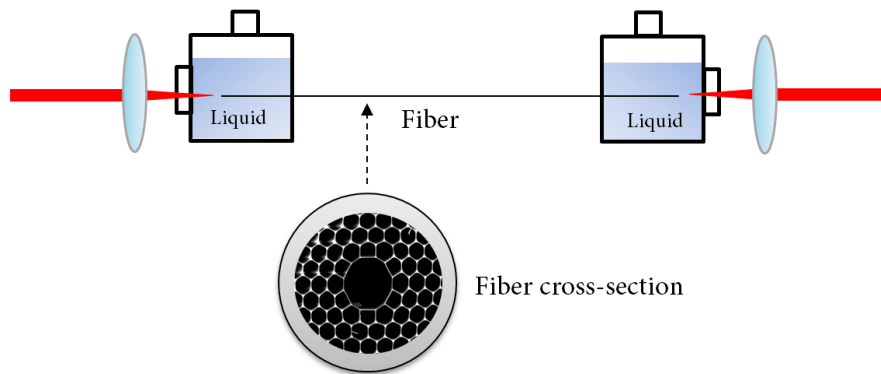

Fig. B1.5: *Schematic of the Liquid-filled photonic crystal fiber. The black area of the fiber cross-section is filled with liquid. The two sealed liquid tanks have windows for light injection and collection.*

b) Shift of the transmission

The first element to consider is the transmission window. In a fully filled fiber, the photonic band gap guiding property is conserved, but the transmission band is shifted toward lower wavelengths as a consequence of the reduced index contrast between the glass part and the filled holes. As a matter of fact, the transmission properties of PBG fibers are described by an

invariant quantity ν such that [82, 83]:

$$\nu^2 = \left(\frac{2\pi\Lambda}{\lambda_x}\right)^2 \left(n_{si}^2 - n_x^2\right) \tag{B1.1}$$

where Λ is the cladding pitch, n_{si} the index of the glass, n_x the index of the filling medium designated by x and λ_x is a characteristic wavelength of the filled fiber (band edge, zero dispersion wavelength, ...).

Therefore, considering a fiber with a given pitch Λ, we can deduce the relation describing the shift of the transmission towards lower wavelengths when the fiber is filled with a liquid of index n_{liquid}:

$$\lambda_{filled} = \lambda_{empty} \sqrt{\frac{n_{si}^2 - n_{liquid}^2}{n_{si}^2 - n_{air}^2}} \tag{B1.2}$$

Hence the empty PCF transmission range must be centered well beyond 1.55 μm, so that once filled, it is blue-shifted in the telecom range. Two commercial fibers (NKT Photonics) with transmission bands centered around 2.3 μm (Fiber A) and 2 μm (Fiber B) were therefore chosen.
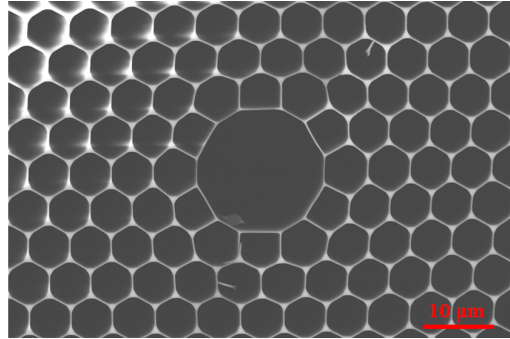

Fig. B1.6: *SEM image of the HC2300 fiber.*

Second, based on Eq. (B1.2), since we have $\lambda_{empty} = 2 - 2.3$ μm, the refractive index of the liquid should be set around ~ 1.2 to shift the transmission window to the telecom band (see Fig. B1.7). Fluorocarbon liquids can be used as they also satisfy the requirements of a low absorption[2] and non-toxicity. Three different liquids have then been selected (FC72, FC75 and FC3283) with refractive indices of 1.25, 1.27 and 1.28 respectively [85]. We use the 3M references FCxxx to designate the fluorocarbon liquids. The Raman-scattering spectra are given in Figure B1.8. Since they are related organic compounds, the three liquids exhibit similar Raman spectra with several discrete lines, the main one around 750 cm^{-1}.

---

[2]in particular, they do not have C-H bounds which exhibit vibrational absorption in the Near-IR [84]

$$CF_3 \!\!-\!\! (CF_2)_4 \!\!-\!\! CF_3$$

FC72

$n_{liquid} = 1.25 \;/\; C_6F_{14}$

FC75

$n_{liquid} = 1.271 \;/\; C_8F_{16}O$

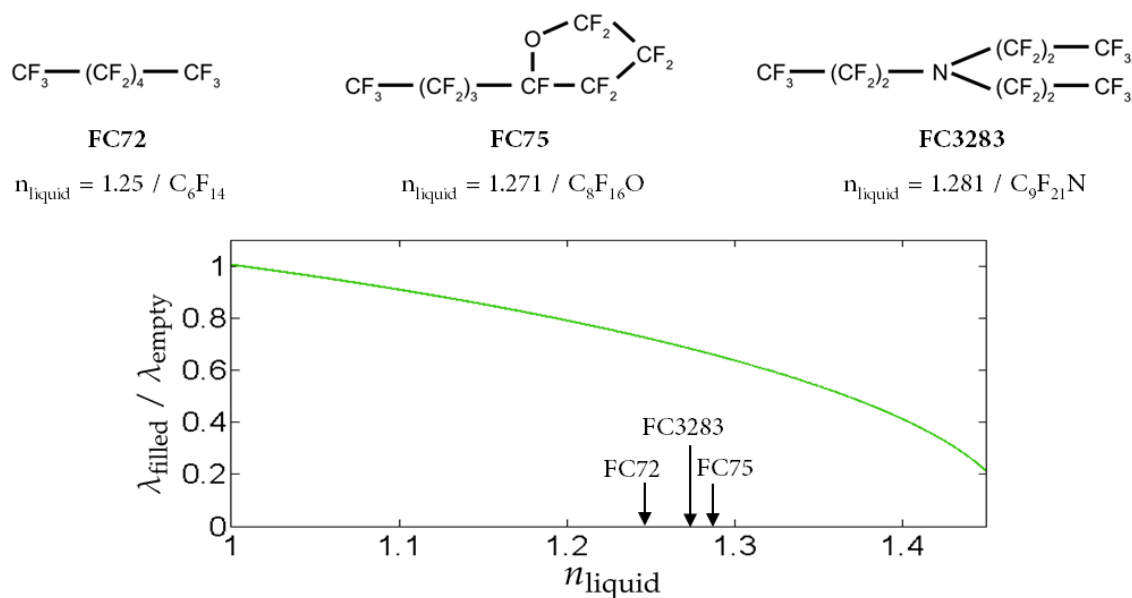**FC3283**

$n_{liquid} = 1.281 \;/\; C_9F_{21}N$

Fig. B1.7: *Top: Selected fluorocarbon liquids. Bottom: Ratio between a characteristic wavelength for a filled fiber and for an empty fiber as a function of the liquid index.*
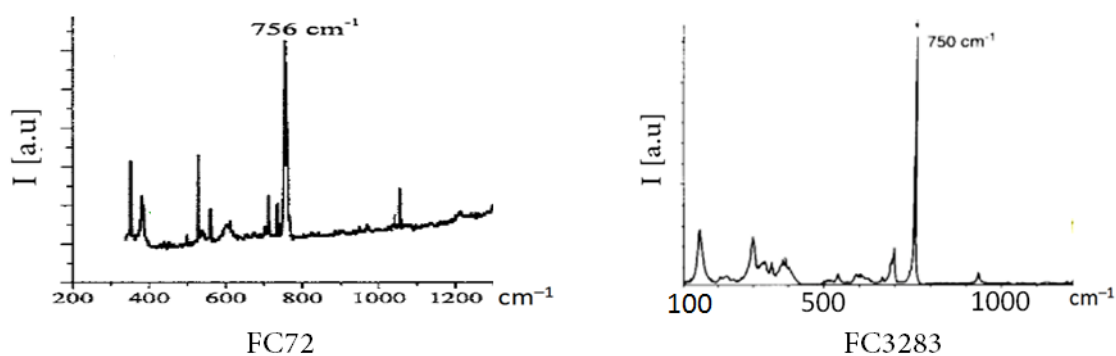

Fig. B1.8: *Raman-scattering spectra of FC72 and FC3283 [86].*

After identifying a liquid filled fiber with a transmission window in the telecom range, the next step is to check whether fiber dispersion is satisfying the required conditions to generate photon pairs when pumped with a telecom C-band pump laser. As described in section A.2.1, a photon pair (ω_s, ω_i) can be generated only if both $\omega_s + \omega_i = 2\omega_p$ and $\beta(\omega_s) + \beta(\omega_i) = 2\beta(\omega_p)$ are fulfilled. Therefore, if we want to check whether photon pairs can be generated with $\lambda_p \sim$ 1550 nm, we need to have access to the fiber dispersion $\beta(\omega)$. To do so, we investigate the dispersion of the aforementioned combinations of fibers and liquids, both numerically and experimentally.

c) Numerical simulation (FDFD)

We use finite difference frequency domain (FDFD) simulations [87] to compute the electromagnetic guided modes. Based on an image of the fiber geometry, FDFD simulation retrieves the dispersion of all the propagating modes. In our simulation, we feed the program with a generated reconstructed fiber geometry whose parameters are directly extracted from SEM images of the fiber cross section. Figure B1.9 shows an example of comparison between an SEM image and its numerical reconstruction obtained with our simulation. As shown in [88], it is important that the model takes into account the distortions around the core (parameter d_{ch}, d_{cp}, t_p, t_h) for accuracy reasons. Indeed, the pentagons and hexagons around the core are slightly different from the rest of the cladding. Note that an alternative would be to directly feed the FDFD simulation with binarized SEM image of fiber cross sections. While such a strategy has the advantage of easier implementation, it does not allow to tune the geometrical parameter individually.
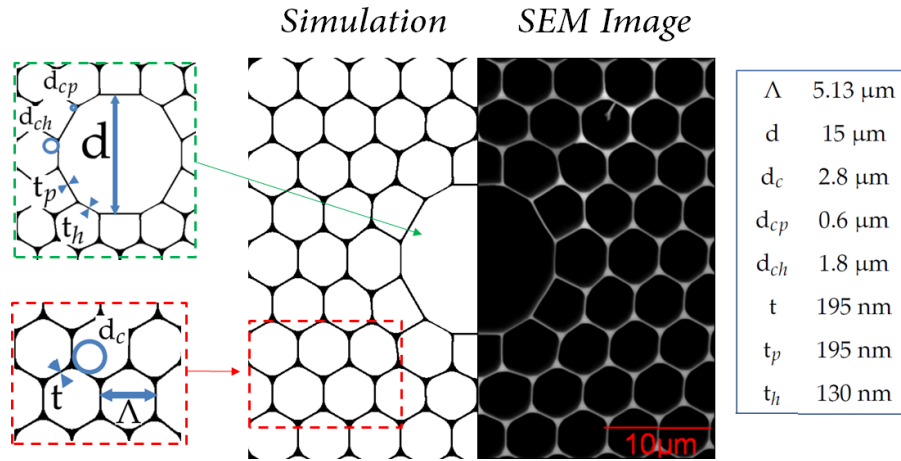

Fig. B1.9: *Scanning electron microscope image of the microstructured region of fiber A (right part of the image) and the reconstructed geometry used for the simulation (left part), with the reconstruction parameters in the table : pitch Λ , core diameter d, diameter of the round corners of the cladding hexagons d_c, diameters of the cladding pentagons d_{cp} and hexagons d_{ch} neighboring the fiber core, cladding thickness t and cladding thickness around the fiber core t_p and t_h.*

The results of simulations for three fibers and liquid combinations are shown in figure

B1.10. The simulation parameters are directly extracted from the SEM image. We plot a relative refractive index, subtracting n_{zdw} (index value at the zero-dispersion wavelength), to allow for an easier comparison. Compared to the equation giving the spectral shift caused by the filling (Eq. (B1.2)), the simulation gives a more precise and comprehensive description. In particular the position of the zero-dispersion wavelength can be inferred.
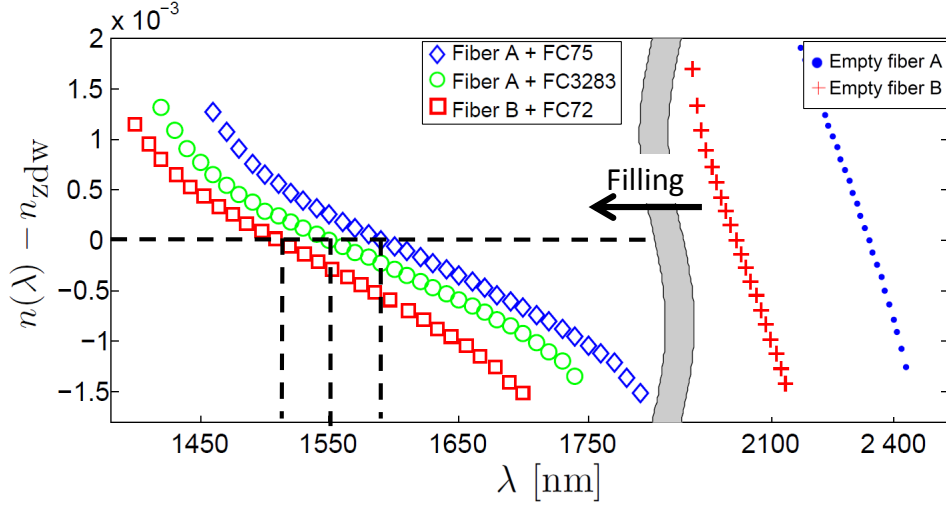

Fig. B1.10: *Computed effective index of the fundamental mode with FDFD simulation as a function of wavelength showing the dispersion of different liquid/fiber combinations. Note that the subtracted n_{zdw} has a different value for each curve.*

The dispersion curves for both empty and filled fibers exhibit a tilted "S shape" due to the photonic bandgap. In fact, as we have seen previously (see section B.1.1), in the bandgap region light is confined within the core such that the fundamental mode dispersion is evolving slowly whereas below and above this bandgap, the mode starts to leak in the cladding (either in apex or strut mode, see Fig. B1.2), which is a highly dispersive region. Thus, in overall, the fundamental mode exhibits a slow evolution wavelength range sandwiched between two ranges where it couples to dispersive cladding modes [77].

The ZDW is the reference wavelength around which the phase matching condition can be satisfied. **Therefore, with a ZDW close to 1.55 μm (Fig. B1.10), fiber A filled with FC3283 (perfluorotripropylamine, $C_9F_{21}N$) with a refractive index of 1.28 is the best candidate for photon pair generation in the C-band according to the FDFD simulations.**

To confirm these predictions, we experimentally characterize the LF-HCPCF dispersion using an "in house" Optical Low-Coherence Interferometry (OLCI) setup.

1.3 Experimental Linear Characterization

a) Optical Low-Coherence Interferometry

This technique allows measuring precisely the group velocity ($v_{g,k} = \frac{1}{\beta_{1,k}}$) of the different propagating modes indexed by the k subscript (transverse spatial modes, polarization modes, etc) [89]. Basically it is a Michelson interferometer illuminated by a broadband source where the device under test (i.e. the hollow-core fiber) is inserted in one of the two arms (the sample arm) with a translating mirror in the other one (the reference arm).

Starting from an initialized calibrated position where the interferometer paths are equal, we insert the fiber in the setup, hence, adding an optical path of $\Delta L_k = (1 - \frac{c}{v_{g,k}}) L_{\text{fiber}} = (1 - c\beta_{1,k}) L_{\text{fiber}}$ in the sample arm which unbalances the interferometer. The quantity $v_{g,k}$ can be deduced from the measurement ΔL_k by which the reference arm optical path must be changed in order to rebalance the interferometer.
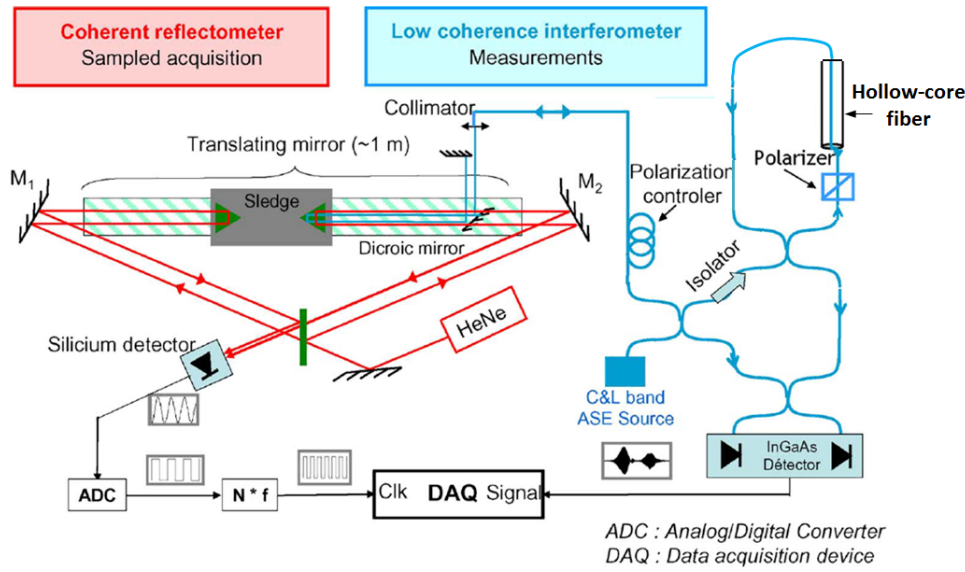

Fig. B1.11: *Optical low-coherence interferometry experimental setup [89]. The blue interferometer illuminated with the white source contains the hollow-core fiber. The red interferometer illuminated by a HeNe laser allows a precise measurement of the mirror displacement through interference fringes counting.*

By translating the mirror along its whole range, we acquire a global interferogram which gives the group velocities of the different modes. Figure B1.12.a shows an example of recorded interferogram for a one meter fiber as a function of the relative group delay **GD** $= \text{GD}_0 + L_{\text{fiber}}\beta_1$ where GD_0 is an unknown constant depending on the initial position of the stage. Although light is injected in the LP01 mode, we can see on the interferogram that we also detect the presence of several higher order modes which could be either LP$_{xy}$ modes or modes propagating in

the cladding. The fundamental mode is easily identifiable as it is the most intense and the one with the lowest group delay. The difference between the group delay of two given modes gives the relative group velocity difference[3].

More importantly, with such a setup we can infer the wavelength dependence of the inverse group-velocity $\beta_{1,k}(\lambda)$. One way would be to pump the interferometer with a tunable narrow spectrum laser and to record interferograms for each frequency. In our setup, we use an alternative solution which consists in recording only one interferogram pumped by a broadband source covering C+L band (1526 - 1605 nm) and performing a numerical Fourier analysis[4]. With this method, the $\beta_{1,k}(\lambda)$ of the different modes can be inferred individually as long as they do not overlap in the interferogram. Figure B1.12.b. shows the resulting 2D map after computing the Fourier analysis. The lowest red curve gives the dispersion of the fundamental mode. The other curves correspond to the dispersion of higher order modes which are often grouped in families. That is why there are several closely spaced red curves (a family of modes). For instance, the two LP_{11} modes with horizontal and vertical polarizations tend to have close dispersion whereas the LP_{20} has a very different dispersion. In our case we are only interested in the fundamental mode.
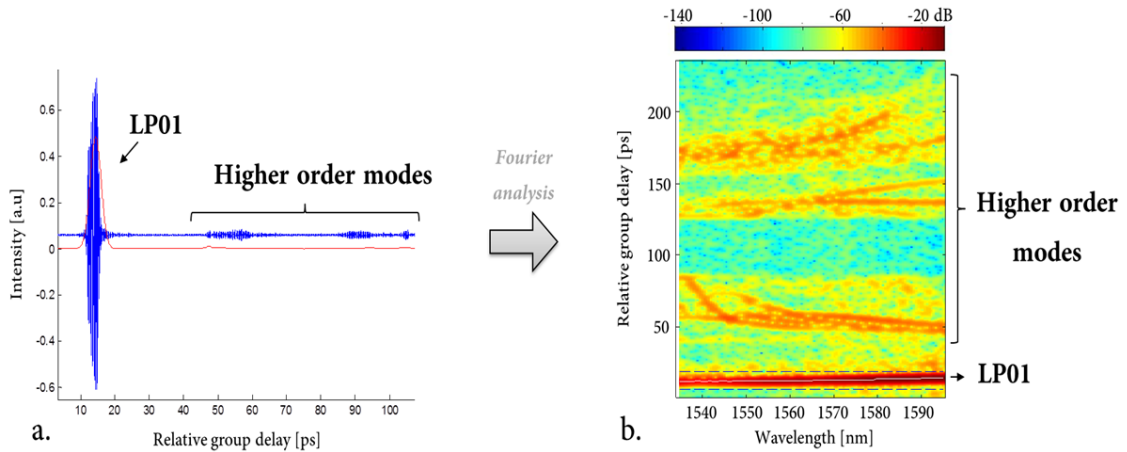

Fig. B1.12: *a. Experimental interferogram of Fiber A filled with FC3283. b. Corresponding mode mapping obtained by computing the Fourier analysis of the interferogram. Each column at λ_j, corresponds to an interferogram that would be obtained with a continuous laser center at such given frequency.*

---

[3] for instance we can see on the interferogram that **GD**$_{LP01}$ ~ 13 ps and **GD**$_{HOM}$ ~ 50 ps, therefore $\beta_{1,LP01} - \beta_{1,HOM} =$~ $\frac{37}{L} = 37$ ps/m

[4] the Fourier analysis consists of fourier transform and a sweeping numeric filter around a 2nm width window. More details in [89]

b) Dispersion of the fundamental mode

The dispersion of the fundamental mode (LP01) is extracted by fitting the lowest red curve in the mode mapping of Fig. B1.12.b.. The measured inverse group-velocity $\beta_{1,\text{LP01}}(\lambda) = \frac{\mathbf{GD}(\lambda)}{\mathbf{L}_{\text{fiber}}}$ is shown in Figure B1.13.a and compared with the result of the FDFD simulation. The simulated curve is in good agreement with the measured group velocity dispersion. The index of the liquid is the only parameter that has been slightly adjusted. Instead of 1.281 (measured in the visible range) [85], we use the value 1.283. This adjustment only shifts the simulation curve without affecting its shape. Moreover, from the knowledge of $\beta_{1,\text{LP01}}(\lambda)$, one can infer the group-velocity dispersion ($D_{\text{LP01}} = -\frac{2\pi c}{\lambda^2}\frac{d\beta_1}{d\omega}$) and thus the ZDW as shown in Figure B1.13.b.
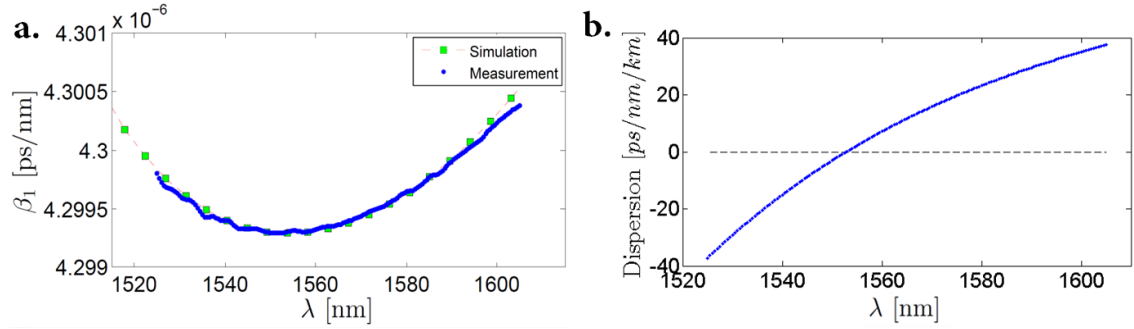

Fig. B1.13: *a. Inverse group velocity of the fundamental mode (i) measured with OLCI (Blue dots) (ii) calculated with the FDFD simulation (green squares). b. Chromatic dispersion of the fundamental mode inferred by fitting the measure β_1. The measured ZDW is $1552\,nm \pm 3nm$.*

The parameters of the polynomial fit of Fig.B1.13 are summarized at the end of the chapter, in Table B1.2.

The different fiber/liquid combinations have been characterized. The results are summarized in Table B1.1. The limited precision in fiber parameter extraction and the uncertainty on the exact refractive index value of the liquid at telecom wavelength contribute to an error on the absolute position of the ZDW. We can estimate an upper bound of ±30nm to this error that mostly corresponds to a global shift of the group velocity dispersion curve with no impact on the curvature.

With a ZDW at 1552 nm, the OLCI measurements confirm that the couple FiberA + FC3283 is the best-suited for photon pair generation with a pump in the C-band (1530-1565). The fiber A+FC72 (1460-1530) and fiber B+FC75 (1565-1625) would rather require a pump in the S- and L-band, respectively.

Tab. B1.1: OLCI results for the different fiber/liquid combinations. The 3M references FCxxx have been used for the fluorocarbon liquids. λ_{empty} is given in the specifications of the commercial fibers giving only an approximate idea of the position of the transmission band (cf NKT reference) whereas $\lambda_{\text{filled, ZDW}}$ has been measured. The configuration of Ref. [25] is also included for comparison.

Fiber	λ_{empty} [nm]	Liquid	n_{liquid}	$\lambda_{\text{filled, ZDW}}$ [nm]
A (HC2300)	2300	FC3283	1.28	**1552**
A (HC2300)	2300	FC75	1.27	**1592**
B (HC2000)	2000	FC72	1.25	**~ 1510**
[25] (HC1550PM)	1550	Acetone d6	1.36	**896**

c) Surface mode

As described, the mode mapping allows to unravel the dispersion of each mode individually. This technique can also be useful to highlight coupling between different guided modes. A common issue with hollow-core PBG fiber is the presence of surface modes (SM) [90]. SM are a second type of core mode which are confined within the silica struts region surrounding the core. Because they mostly lie in silica, their dispersion is much higher than the fundamental mode dispersion. Thus, if a surface mode exists within the bandgap, its high dispersion may cross the one of the fundamental mode which is rather flat as we have seen in Fig. B1.10. More specifically, the two modes anti-cross and couple to each other. The result is a hybrid mode which is combination of the fundamental mode and a surface mode (see Fig. B1.14). Such an hybrid mode has higher overlap with the silica structure than the fundamental mode, inducing higher loss, dispersion and Raman noise. We are therefore especially interested in trying to avoid surface mode coupling.

The left hand side of figure B1.14 shows the interferogram of the fiber/liquid combination (FiberA + FC75) that we have chosen to show a coupling between the fundamental mode and a higher dispersion mode which could be a surface mode. At the wavelength for which the two modes cross on the mode mapping (left hand side), we can see a dip in the dispersion of the fundamental mode (right hand side). This is a signature of a coupling with a higher order mode.

We have checked experimentally that the selected fiber-liquid combination (FiberA+FC3283) does not exhibit such an anti-crossing in a 100 nm wide window around the ZDW, where the photon pairs will be generated.
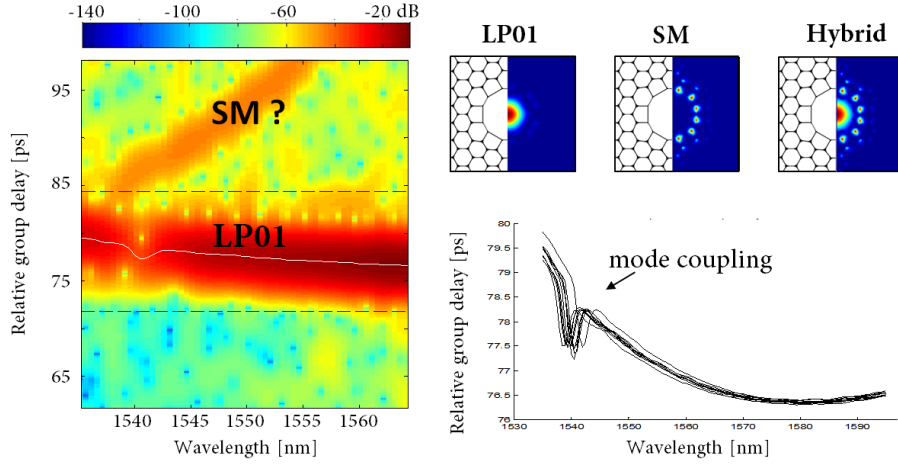
Fig. B1.14: *Left: Zoom on an interferogram exhibiting a coupling between, the fundamental mode and a higher order mode observed in the Fiber A + FC75 combination. Right: Computed transverse geometric profile of the fundamental mode and SM mode. Bottom: Recorded dispersion of the fundamental mode.*

1.4   Experimental Nonlinear Characterization

The nonlinearity of the liquid-filled HCPCF is also an important parameter as it is related to the brightness of the source (see section A.2.1). Since the fundamental propagation mode has a small overlap with the silica structure, it is determined solely by the nonlinear index of the liquid. Because our characterization method is based on self-phase modulation [91], let us start with a short introduction of this effect.

a)   Self-phase modulation

When travelling through a medium, an intense pulse induces a varying refractive index due to optical Kerr effect [30]:

$$n(t) = n_0 + n_2 \mathrm{I}(t) \tag{B1.3}$$

where $\mathrm{I}(t) = (n_0 c / 2\pi)|A(z,t)|^2$ is the optical pulse intensity and $n_2 = 3\chi^{(3)}/4 n_0^2 \epsilon_0 c$.

In the refractive index, the nonlinear term $n_2 \mathrm{I}(t)$ changes the phase accumulated by the transmitted pulse by an amount:

$$\Phi_{\mathrm{NL}}(t) = -n_2 \mathrm{I}(t) \frac{\omega_0 \mathrm{L}}{c} \tag{B1.4}$$

75

such that, at the fiber output, the field is given by:

$$E(L, t) = A(L, t)e^{i(-\beta(\omega_0)L + \omega_0 t + \Phi_{NL}(t))} \tag{B1.5}$$

This nonlinear phase induces modifications in the spectrum of the pulses and most often a broadening. Indeed, if we consider the instantaneous frequency $\Omega(t)$ of the pulse, it is described by:

$$\Omega(t) = \frac{d}{dt}\left(\omega_0 t + \Phi_{NL}(t)\right) \tag{B1.6a}$$

$$= \omega_0 + \frac{d\Phi_{NL}(t)}{dt} \tag{B1.6b}$$

$$= \omega_0 - n_2 \omega_0 \frac{L}{c} \frac{dI(t)}{dt} \tag{B1.6c}$$

This equation shows that the instantaneous frequency remains unchanged at the maximum (since $\frac{dI(t)}{dt} = 0$) and that frequencies are shifted whenever $\frac{dI(t)}{dt} \neq 0$.

Let us consider the case of Gaussian pulse travelling in a medium with $n_2 > 0$. While the central frequency stays identical, the leading edge of the pulse is shifted toward lower frequencies and the trailing edge toward higher frequencies, resulting in a general broadening around the central frequency (see B1.15).
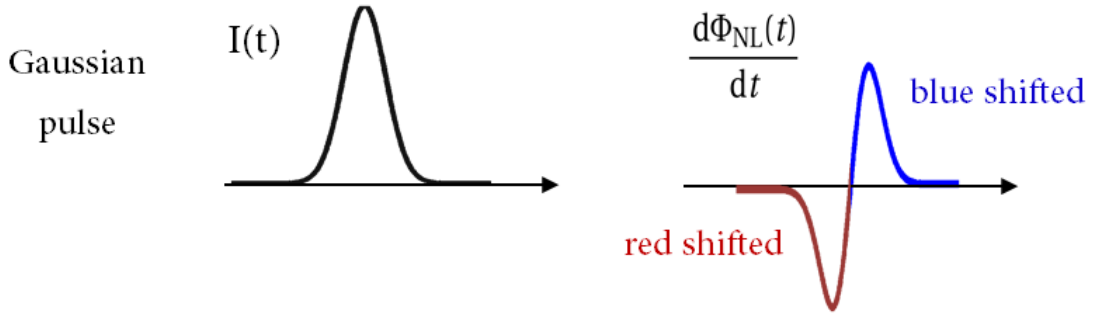

Fig. B1.15: *Intensity profiles and their corresponding instantaneous frequency modifications in the case of a gaussian pulse.*

Therefore, one can obtain the nonlinear index phase Φ_{NL} and consequently the nonlinear index n_2 of a medium by measuring the broadening of a known injected pulse.

Our experimental setup for measuring the SPM broadening uses an incident beam with a rectangular spectrum. The advantage of such shape is that the steepness of the flanks makes it easier to measure the broadening of the spectrum, forming symmetric pedestals on the flanks. The basic principle of the measurement is presented in B1.16.
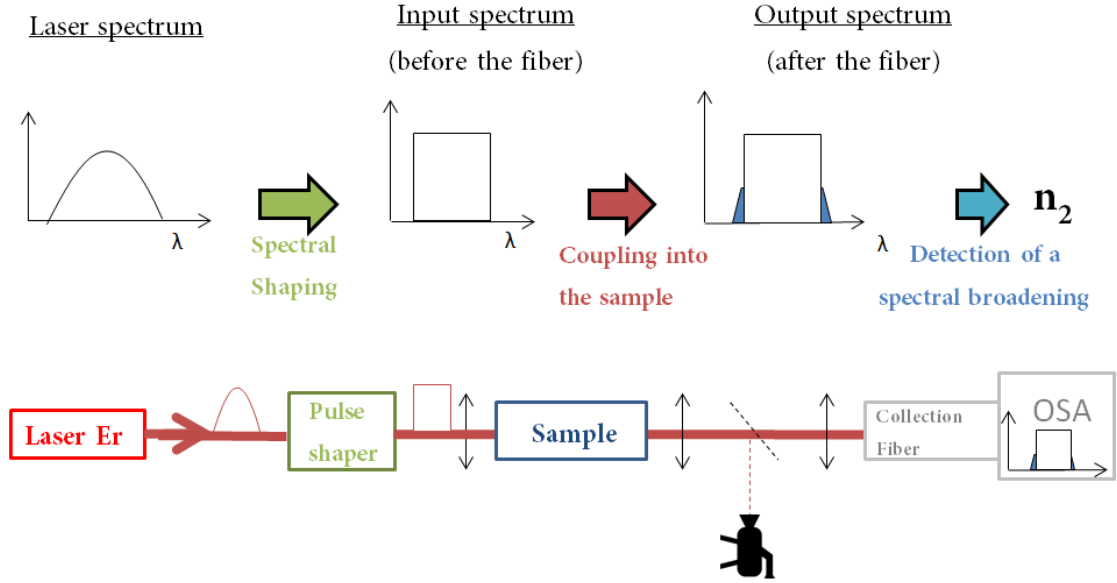
Fig. B1.16: *Top: Principle of the nonlinear characterization. Bottom: Experimental setup. The dashed lines correspond to an alternative path where the beam coming out of the sample is send to a camera in order to check the coupling of the fundamental mode of the fiber*

The experimental setup consists of a 1580 nm femtosecond amplified Erbium laser delivering 1.1 ps pulses at 50 MHz with a peak power of 18 W. The pulses are sent to a passive pulse shaper[5] to produce a rectangular spectrum, before being injected in the nonlinear sample to be tested (here HC2300 fiber filled with FC3283). The signal exiting the fiber is collected in a standard singlemode fiber and sent toward an Optical Spectrum Analyzer (OSA).

b) Results

When injecting 1 mW of pump average power into the fiber, one can observe a clear broadening of the spectrum. In comparison, a measure at low pump power (100 µW) where the effect of the SPM is negligible does not exhibit any broadening (see Fig. B1.17.a). Compared with simulated spectra (Fig. B1.17.b), the nonlinear phase shift Φ_{NL} can be derived from the measured spectral broadening. A nonlinear phase shift of Φ_{NL} = 10 mrad is obtained for an average power of 1 mW in the LF-HCPCF. This measured value is of the order of the one obtained with a polarization maintaining silica fiber of the same length (Fig. B1.19).

Taking into account the experimental parameters and the characteristics of the fiber (A_{eff} = 95 µm^2, L = 1 m), this leads to an estimated nonlinearity of the chosen liquid FC3283 n_2 = 1.1x10^{-20} m^2/W.

In practice, we record the transmission spectra for increasing incident power. As the power

---

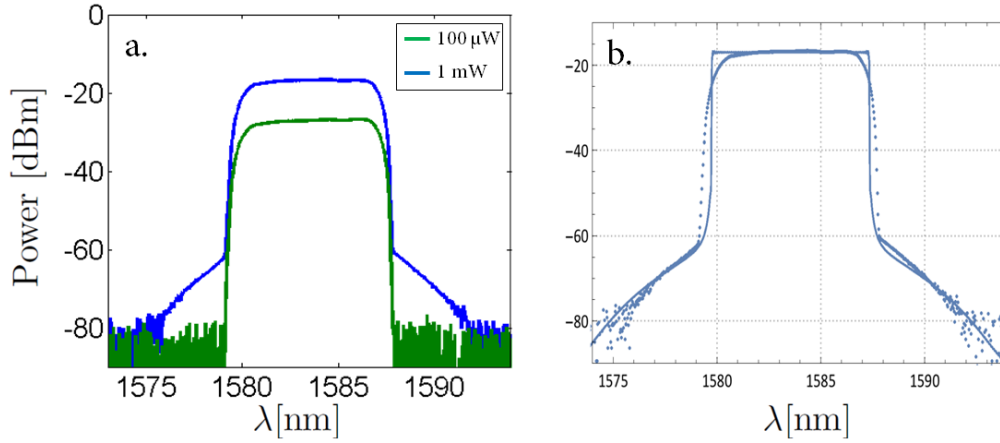[5] it consists of double grating, a translation and an adjustable slit (see [91])

Fig. B1.17: *a. Recorded spectra in the OSA for two different injected pump power. Starting from a situation where the SPM is negligible (green curve), increasing the pump power leads to a symmetric enlargement of the spectrum (blue curve). Note that the level of the two upper plateaux are not the same since the injected powers are not identical. b. Comparison between simulated (lines) and experimental (dots) spectra.*

increases, the pedestals intensity evolves quadratically with pump power, which is a signature of the SPM nonlinear effect (Fig. B1.18). The lowest nonlinear phase shift observed at 400 μW (see the pedestals on the spectra) is about 4 mrad.
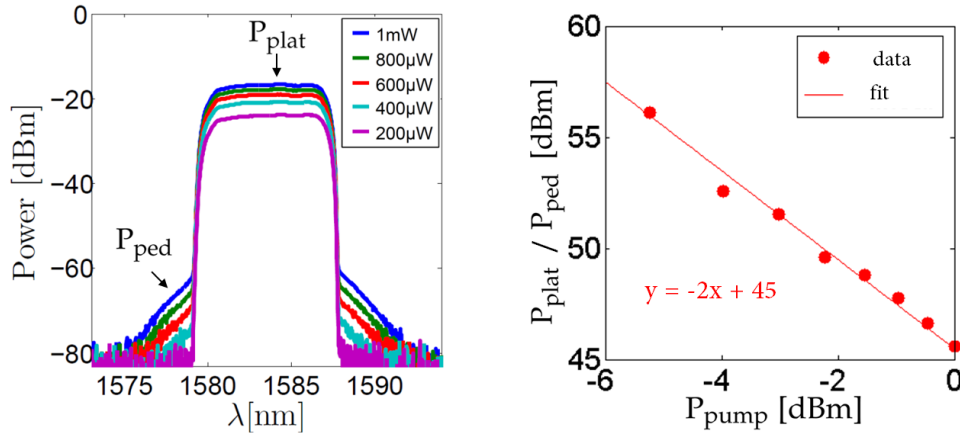

Fig. B1.18: *Left : Spectra of the square wave pulse generator transmitted by the fiber for different levels of injected power. Right : Power ratio between the power in the plateau and power in the pedestal. A linear fit curve gives a slope of 2, which indicates that the signal in the pedestal vary quadratically with the pump power*

Moreover, we also check whether this nonlinearity comes from the sample. As it can be seen from the experimental setup, the pulse actually crosses two fibers: the sample under test and the collection fiber to send the signal to the OSA. To make sure that the collection fiber

does not add any nonlinearity we check that, for the same amount of detected signal, decreasing the power before the collection fiber reduces the overall power linearly while keeping the pedestals, whereas if the power is decreased before the sample, the pedestals vanish.
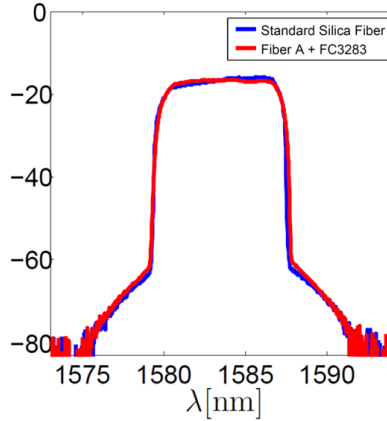

Fig. B1.19: *Comparison between the nonlinearity of a standard silica core SMF fiber (blue curve) and the LF-HCPCF (red curve) of the same length. The two fibers exhibit comparable nonlinearity.*

It is noteworthy that nonlinearities as large as two orders of magnitude higher than silica can be obtained with other liquids, such as carbon disulfide [92] (hence giving rise to a four orders of magnitude increase in the FWM efficiency). These high nonlinearities are often associated to a high refractive index, thus requiring the use of fibers with glass index higher than silica [93, 94]. Photonic bandgap hollow core fibers with similar structure as the one we are currently investigating have been reported [95], but they remain more difficult to obtain than silica PCF.

With the knowledge of our experimental parameters (dispersion and nonlinearity), we can now compute the expected JSA of the source.

1.5 Joint Spectral Amplitude

We recall that the JSA is a product of the energy conservation (α) and the phase matching (φ) functions. On the one hand the energy conservation function can be computed from the pump spectral properties (central wavelength and bandwidth). On the other hand the phase-matching can be computed thanks to the knowledge of the medium properties (dispersion, fiber length, nonlinearity). Figure B1.20 shows examples of such calculation: the α function considered a Gaussian centered at $\lambda_{p0} = 1555$ nm and of spectral width $\sigma = 1$ nm for the pump and the φ function is obtained with the measured LF-HCPCF parameters[6].

---

[6]based on a polynomial fit of the dispersion measured with OLCI setup and the nonlinear coefficient measured with the SPM broadening technique (see Tab. B1.1 for a summary of these parameters)

The angle of the phase matching is estimated to be $\theta \approx -51°$. Since, neither the symmetric ($\theta \approx 45°$) nor asymmetric ($\theta \approx 0°/90°$) group-velocity matching are fulfilled, consequently the signal and idler photons are expected to be spectrally correlated. The same holds true for any wavelength in the tunable range of our laser. In fact, as shown in Fig.B1.20, the different JSA that can be obtained always exhibit spectral correlations.

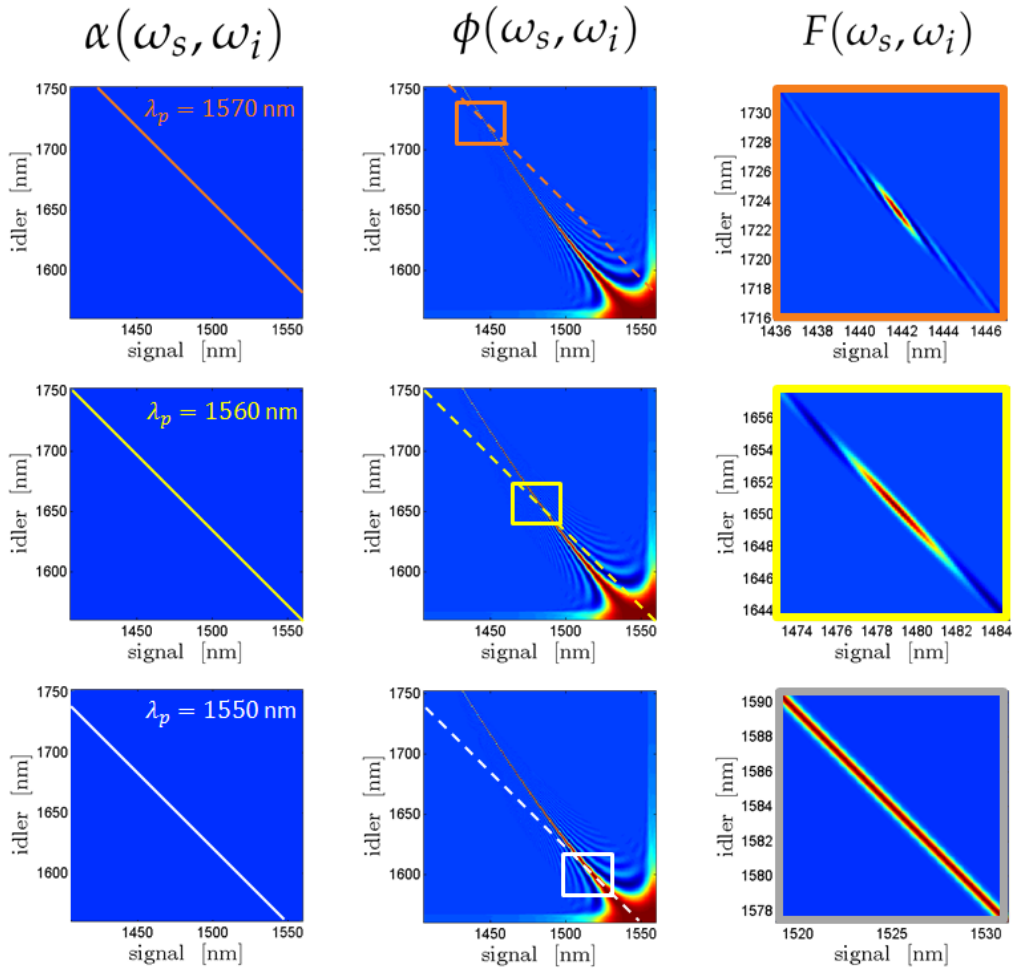**Fig. B1.20:** *From left to right, energy conservation, phase-matching and JSA functions for different configurations of pump wavelength (1570,1560,1550 nm). Changing the pump wavelength shifts the energy conservation function along the diagonal. It is noteworthy that α and φ are depicted with the same scale whereas the JSA is only represented in vicinity of the intersection between α and φ (coloured square area).*

Conclusion

In this chapter we have identified the combination of a commercial hollow-core (HC2300) and a fluorocarbon liquid (FC3283) to be a good candidate for the generation of photon pairs at a telecommunication wavelength through spontaneous four-wave mixing. We showed how the optimization procedure, in view of this application links the choice of the nonlinear liquid to the design parameters of the fiber.

The simulations performed to predict the transmission window and the dispersion of the fibers have been confirmed experimentally using the OLCI setup. Moreover, the nonlinearity has been measured using the self-phase modulation characterization of square pump spectrum.

Finally, based on simulation of the JSA, we have seen that the biphoton state would be spectrally correlated.

All the measured parameters of the source are summarized in Table B1.2.

Tab. B1.2: Summary of the parameters of the chosen LF-HCPCF

Fiber	HC2300 filled with FC3283 (perfluorotripropylamine, $C_9F_{21}N$)
Length	$L_{fiber} = 1$ m
Mean Field Diameter	MFD $\sim 11\mu$m
Liquid linear refractive index	$n_{liquid} = 1.281$
Zero Dispersion Wavelength	$\lambda_{ZDW} = 1552$ nm
Dispersion	$\beta_1(\omega) = C + \sum_{k=1}^{4} p_k \omega^k$ $C = 3.863742733424368 \times 10^{-8}$ s.m^{-1} $p_1 = -1.179674598548600 \times 10^{-22}$ s.m^{-1}.(rad.s^{-1})$^{-1}$ $p_2 = 1.525974816884953 \times 10^{-37}$ s.m^{-1}.(rad.s^{-1})$^{-2}$ $p_3 = -8.803566103469720 \times 10^{-53}$ s.m^{-1}.(rad.s^{-1})$^{-3}$ $p_4 = 1.910115270652648 \times 10^{-68}$ s.m^{-1}.(rad.s^{-1})$^{-4}$
Non linearity	$n_2 = 1.1 \times 10^{-20}$ m^2/W
Surface mode	None in the range [1520 - 1605 nm]

Chapter B2

Toward Raman-free four-wave mixing

In this chapter, the first section presents how the LF-HCPCF provides low loss, Raman-free spectral zones in the selected telecom transmission band where photon pairs can be generated through FWM. This is demonstrated through a study of the spectral density map of the source. In a second section, the setup we have implemented to detect the photon pairs is described and its limitations are discussed.

2.1 Computed Spectral Density Map

The knowledge of the propagation constant of the fiber $\beta_1(\omega)$ through the OLCI characterisation allows to calculate the phase mismatch $\Delta\beta$.

We have seen previously (see section A.2.5) that the spectral density map is an approximated spectral probability density of photon-pair wavelengths. This 2D map is useful to qualitatively visualize the signal/idler wavelength that can be generated for a given pump wavelength.

$$\text{SDM}(\omega_p, \Delta\omega) = \text{sinc}\Big((2\beta(\omega_p) - \beta(\omega_p + \Delta\omega) - \beta(\omega_p - \Delta\omega))\frac{\text{L}}{2}\Big) \tag{B2.1}$$

with $\Delta\omega = \omega_{p0} - \omega_i = \omega_s - \omega_{p0}$ the frequency difference between pump and idler or signal.

a) Raman-free spectral zone

In Figure B2.1, the simulated SDM of the LF-HCPCF as a function of pump wavelength and of $\Delta\lambda_{s,i} = \lambda_{s,i} - \lambda_p$ is shown. With such a convention, positive $\Delta\lambda$ are related to the idler wavelength whereas negative $\Delta\lambda$ are related to the signal wavelength. The map is symmetric with respect to the horizontal axis since signal and idler are generated symmetrically to the pump[1]. The central red zone ($\Delta\lambda = 0$) corresponds to the degenerated case where signal and idler have the same frequency as the pump (modulational instability). We have already mentioned in section A.2.5 that such configuration makes it experimentally difficult to separate the photon pairs from the pump. We are rather interested in the quasi-parabolic parts with a larger wavelength separation between pump, signal and idler photons (see Fig. B2.2). We recall that the parabola part starts dissociating from the central zone at the position of the ZDW at 1552 nm.
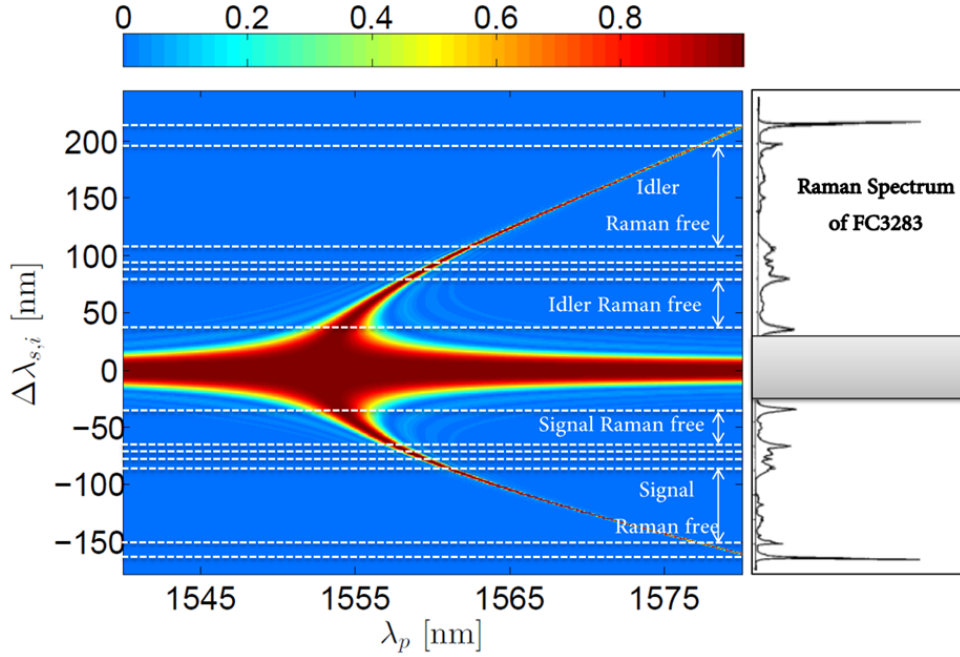

Fig. B2.1: *Left: Spectral density map ($|SDM|^2$) of the LF-HCPCF FWM as a function of the pump wavelength λ_p and the relative signal or idler wavelength $\Delta\lambda_{s,i} = \lambda_{s,i} - \lambda_p$. The white dashed lines give the position of the Raman lines. Right: Raman spectrum of the FC3283 reproduced for this liquid with permission from [59]. The gray rectangle corresponds to a zone with no available data.*

The position of the principal and secondary Raman lines of the liquid are superimposed on the SDM with white dashed lines. In order to generate photon pairs which are not contaminated by Raman-scattering noise, -*Raman-free photons*, one has to consider spectral ranges which are not crossed by the Raman lines. In particular, two Raman-free spectral ranges are

---

[1] signal and idler are created symmetrically when considering the frequencies ($\omega_{s,i} = \omega_p \pm \Delta\omega$). We choose this wavelength representation for its more familiar orders of magnitude. This explains why values on the y-axis are not strictly symmetric.
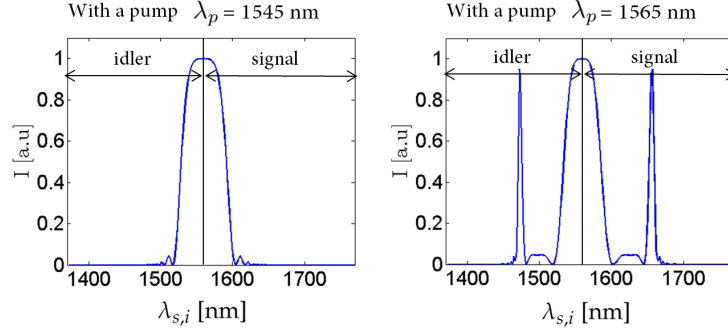
Fig. B2.2: *Computed signal and idler generated spectrum in the modulation instability regime (left) and four-wave mixing regime (right) for λ_p = 1545 nm and 1565 nm, respectively. While, modulation instability regime is limited to broad parametric generation around the pump, FWM allows to generate narrow and well separated signal and idler wavelengths. Note that these spectrum are obtained by vertical slicing of the SDM at the corresponding λ_p.*

easily identifiable (see Table B2.1).

Tab. B2.1: Combination of wavelengths associated with the generation of photon-pairs devoid of Raman-scattering. Note that the signal wavelength range is voluntary reversed (from higher to lower) in order to respect its association with pump and idler.

	Raman-free zone I	Raman-free zone II
$\lambda_p \in$	[1554 - 1557 nm]	[1561 - 1576 nm]
$\lambda_i \in$	[1592 - 1630 nm]	[1665 - 1781 nm]
$\lambda_s \in$	[1518 - 1490 nm]	[1469 - 1413 nm]

b) Experimental considerations

From an experimental point of view, this two dimensional plot is really useful to choose the experimental parameters. This choice may take into account the amount of Raman noise, the telecom channel in which signal and idler are created, etc. For this purpose it is also convenient to add the experimental limitations on the map in order to easily determine the working points which are worth considering. Let us first consider the fiber-related intrinsic limitation:

- **fiber transmission window:** The first limitation is the finite fiber transmission width. If signal and idler are generated outside the fiber transmission band, they experience high loss and are unlikely to exit the fiber. Qualitatively, the transmission window can be inferred from the finite difference frequency domain simulation. Indeed, the spectral range for which the fundamental mode does not couple with the cladding gives an approximation of fiber transmission window which is estimated to be [1440 - 1740] nm (see Fig.

B2.3.a).

Moreover, we may add the following experimental limitations due to the equipment currently available in the laboratory:

- **pump tunability:** In our experimental setup, we use telecom femtosecond fiber laser (Pritel) which is tunable over $\lambda_p = 1540$ - 1564 nm, limiting the possible configurations.

- **detector efficiency:** Another important limitation arises from SPDs detection efficiency (ID-220, ID Quantique). The detectors exhibit about 20 % detection efficiency in the range 1200-1600 nm, but the efficiency quickly drops beyond this range (see Fig. B2.3.b). Such limitations put constraints on the detection of the idler photon. Note that this limitation can be overcome by using other SPDs, in particular superconducting SPDs generally exhibit an increased detection range of 400-2500 nm.
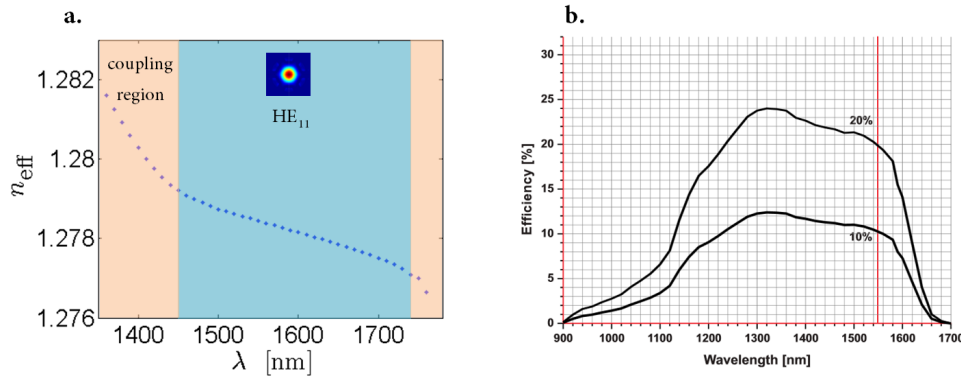
Fig. B2.3: *a. Simulated effective index (FDFD) of the filled-fiber. The blue region corresponds to the spectral region for which the fondamental mode does not couple to cladding modes. b. SPDs detector efficiency for two possible configurations. The red curve correspond to $\lambda = 1550$ nm. Beyond 1600 nm the efficiency quickly drops. Source ID Quantique*

A new SDM taking these experimental limitations into account is shown in Figure B2.4. Among the two Raman-free ranges presented above, only one, featuring closer signal and idler wavelength to the pump, is experimentally accessible under our experimental constrains.

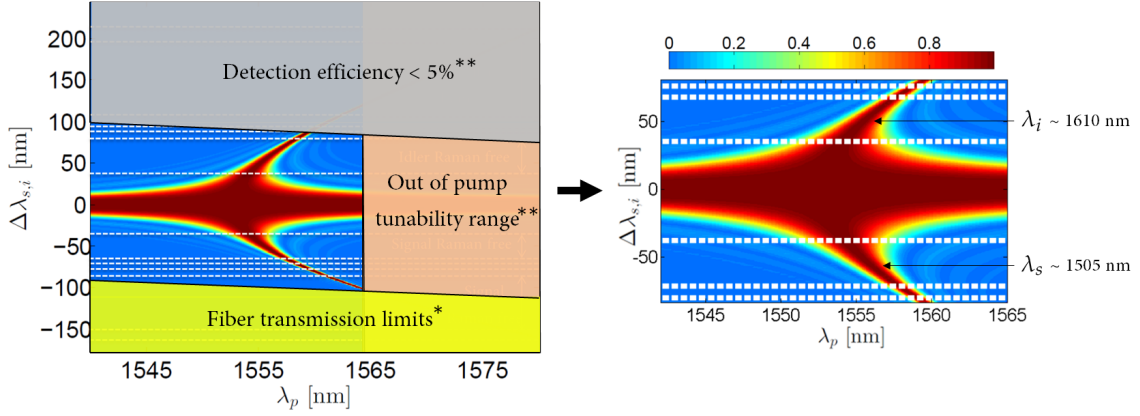**Fig. B2.4:** *Spectral density map while taking experimental constrains into consideration. The white dashed lines give the position of the Raman noise. *Intrinsic fiber limit **Limits due to our experimental equipments*

2.2 Experimental setup and filtering

Our experimental setup to characterise photon-pair generation is shown in Fig. B2.5. A telecom fiber laser (Pritel) provides picosecond pulses centered at a wavelength λ_p tunable in the C-band (1535-1565 nm) with a fixed repetition rate $f_p = 100$ MHz. An afocal system controls the size of the beam waist. The pump pulses are sent on a grating followed by a pinhole in order to filter out any residual fluorescence or Raman scattered photons that may have been generated in the laser delivery fiber. It is of the utmost importance to filter all the noise present at signal and idler wavelengths prior the injection in the fiber, because after the fiber, such noise could not be distinguished from the parametric photons. A half-wave plate (HWP) allows the polarization of the pump to be aligned on one of the axes of the fiber. Around 3.5 mW of pump power is injected into the 1 meter long LF-HCPCF (10 mW with a coupling efficiency of ∼ 35%). In the fiber core, the spontaneous FWM process may occur and lead to the generation of a photon pair which co-propagates with the pump.

Prior the detection with single photon detectors (SPD), the signal and idler photons must be isolated from the pump. On the one hand, since few mW of pump are injected in the fiber, at a repetition rate of $\Gamma \sim 100$ MHz, the number of pump photons per pulse is:

$$N_{pump} = \frac{P_{out}}{\hbar \omega_p \times \Gamma} \approx 10^8 \, photons/pulse \tag{B2.2}$$

On the other hand, we are working in a regime where at most one photon pair is generated per pulse in order to avoid multipair events. Thus, a filtering of at least 90 dB of the pump is required to be able to extract a photon pair.
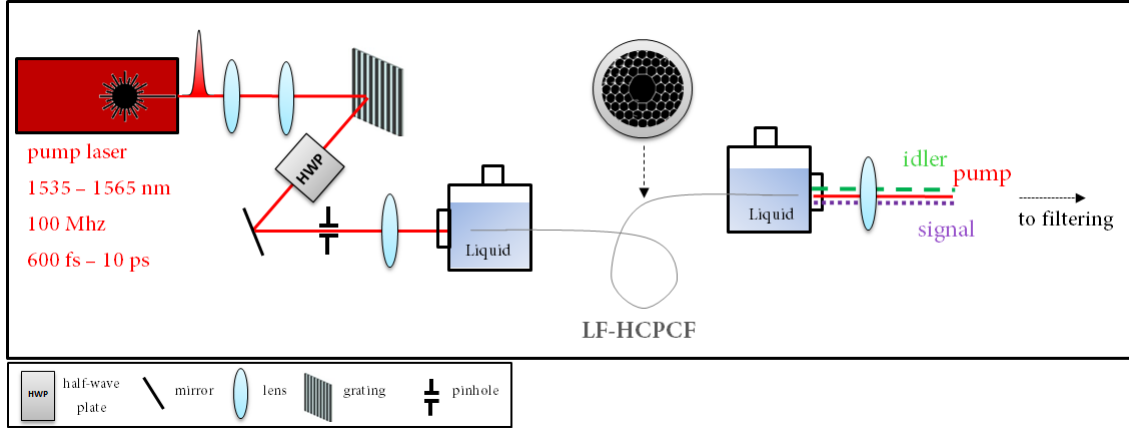
Fig. B2.5: *Experimental setup for photon pair generation.*

Several degrees of freedom can be used to filter the signal and idler from the pump and from background noise:

- **polarization:** since the fiber birefringence is negligible[2], the FWM phase matching function ϕ is the same whether considering photon pairs generated with the same polarization as the pump (co-polarized phase matching) or with a perpendicular polarization (cross polarized phase matching). The occurence probability of generating cross polarized photons is nine times lower than the co-polarized parametric photons[3]. Nevertheless, in the cross polarised configuration, the photon-pairs can be separated from the pump using a polariser.

- **frequency:** using gratings or prisms, the signal and idler can be spatially isolated from the pump.

- **time delay:** signal and idler photons being always created simultaneously, it is a good approximation to consider that the two detectors click with a constant delay corresponding to the optical paths difference between signal and idler arms. The pair detection that do not correspond to this delay can be discarded as they do not correspond to signal-idler coincidence. This is particularly useful to eliminate background noise. As opposed to the polarization and spectral filtering, such technique is applied after detection, as a *post-selection*.

In practice, these three strategies are implemented simultaneously for an efficient filtering.

---

[2] due to the geometrical symmetry
[3] due to a lower number of degenerate components in the nonlinear susceptibilty [96]

a) Free-space filtering

At the fiber output, a half-wave plate and a PBS allow to choose either co- or cross-polarized signal and idler (see Fig. B2.6). Selecting the cross-polarized allows a first step of pump filtering of ~20 dB. Then, a diffraction grating spatially separates the pump, signal and idler. The pump is sent to a beam block. Signal and idler each go through a second grating for improved filtering. Indeed, as gratings are not perfect, a small part of the pump may be scattered in the directions of both detection paths. The second grating allows to significantly reduce the number of these scattered photons. The three transmission gratings (T-940-C, LightSmyth) have 940 lines/mm. Their diffraction efficiency is around 94 % for both polarizations. Finally, the parametric photons are collected with two microscope objectives. Two id220 free-running InGaAs Single Photon Detectors (SPDs) are then used for detection.
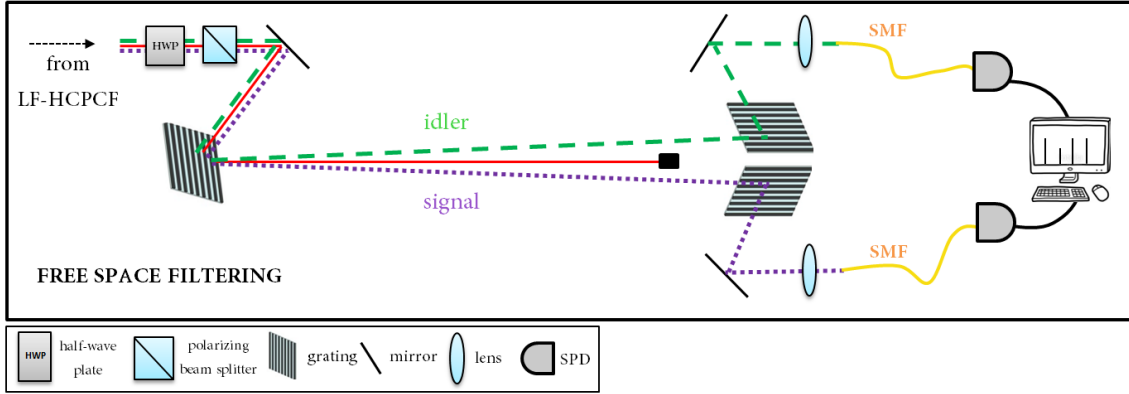

Fig. B2.6: *Setup of the free-space filtering configurations with three identical diffraction gratings.*

In practice, the major disadvantage of using gratings for isolating photon pairs is the alignment of the signal and idler paths. Each pump wavelength is associated to a couple λ_s and λ_i at which photon pair generation is expected. The direction of the beams after the gratings being wavelength dependent, the axis of the signal and idler arms must be aligned before each measurements (λ_s, λ_i pair). A CW tunable laser tuned at λ_s and λ_i is used for the preliminary alignment. Consequently, the filtering is strongly limited by the alignment laser tunability range, putting stringent limitation on signal and idler wavelengths that can be detected. In our case, we use a CW laser (T-100, Yenista) with tunability of $1525 - 1562$ nm. The two major problems arising from these considerations are:

- the Raman-free range is no longer accessible in this configuration

- the filtering is more delicate, both because the spectral separation is narrow and because the signal and idler are generated within the spectral gain of Erbium where the pump laser emits some fluorescence.

That is why we explore another filtering technique where no preliminary alignment step is required. It is based on telecom fiber filtering.

b)   Fibered filtering

Thanks to the development of spectral multiplexing and demultiplexing techniques in today's telecom networks, a very large range of cost-effective[4] fibered filters is available. They are characterized by their channel width and channel spacing and can be divided into three categories:

-   Wavelength Division Multiplexer (WDM)

-   Coarse Wavelength Division Multiplexer (CWDM)

-   Dense Wavelength Division Multiplexer (DWDM)

The given wavelengths positions and spacing are standardized by the so-called International Telecommunication Union (ITU) grids (ITU-CWDM and ITU-DWDM). Table B2.2 sums up the main characteristics of commercial telecom channel products.

Tab. B2.2: Standard commercial parameters of the Normal-, Coarse- and Dense-demutiplexing. Note that in the case of DWDM, 50 GHz and 200 GHz versions also exist.

	WDM	CWDM	DWDM
number of channels	2	16	40
spacing between channel	240 nm	20 nm	100 GHz ($\sim$ 0.8 nm)
$\lambda_{\min}$	1310 nm	1271 nm	1519.48 nm
$\lambda_{\max}$	1550 nm	1611 nm	1577.03 nm

Since the signal and idler Raman-free photon wavelengths are expected around: $\lambda_s = 1505$ nm / $\lambda_i = 1610$ nm, we choose CWDM filters (Senko) that cover this spectral range. It consists of passive add/drop filters with one input and two output ports. They transmit a certain wavelength $\lambda_k \pm 6.5$ nm at the first exit port, and reflect all others wavelength $\bar{\lambda_k}$ at the second one[5].

Figure B2.7 describes this alternative experimental filtering setup. It starts with the same polarization filtering as in the free-space configuration (HWP + PBS). In principle this may be done with fibered optical elements (Paddle Polarization Controllers + Fused PBS), yet it is much preferable to do it in free-space: indeed, if the LF-HCPCF allows to generate Raman-free photons, it is equally important not to generate any Raman contamination during the filtering

---

[4] < 30$ per CWDM filter

[5] instead of this 1x2 (input x output) single channel component, 1x4 channels to 1x16 channels demultiplexer also exist in order to separate different wavelengths with only one device.

step. Coupling the strong pump directly after the LF-HCPCF into fibers would risk generating Raman-scattering noise. Therefore, a first step of free-space filtering allows to makes sure that a negligible amount of pump power interacts with silica.

After the polarization filtering, the remaining pump together with the signal and idler are coupled into a fiber and goes through a three step spectral filtering. First, a filter centered at λ_p allows to reject the pump while keeping all the other wavelengths. Then, a second filter at λ_i separates the signal from the idler in two arms. Finally, further filters are used in both arms for improved filtering at λ_s and λ_i, respectively. In overall, assuming F as the filter response, the idler wavelength go through $F(\bar{\lambda}_p) \times F(\lambda_i) \times F(\lambda_i)$ and signal through $F(\bar{\lambda}_p) \times F(\bar{\lambda}_i) \times F(\lambda_s) \times F(\lambda_s)$. According to the specifications, the isolation for the transmitted port $F(\lambda_k)$ and for the reflected port $F(\bar{\lambda}_k)$ are > 40 dB and > 13 dB, respectively per filter. Thus, a pump isolation of > 90 dB is expected (> 93 dB for the idler and > 106 dB for the signal).

Insertion loss equals 0.7 dB per filters, such that the total fiber filtering loss is estimated to 3 dB[6] (excluding the $\approx$ 40% coupling when injecting in the first fiber).
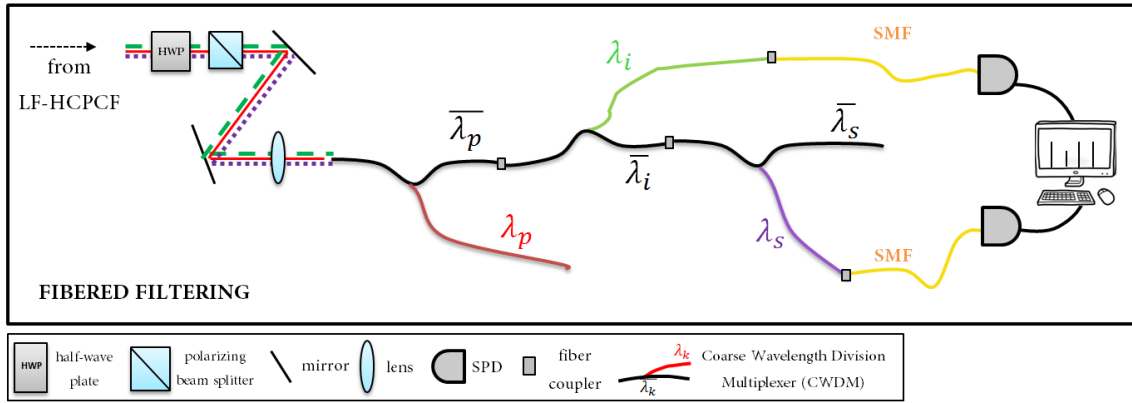

Fig. B2.7: *Setup of the fibered filtering scenario with CWDM.*

In the case of the commercially available fibered filtering, the alignment issue is solved with the constraint of the ITU grid. We designate as $[s1, s2, s3]$ and $[i1, i2, i3]$, the possible CWDM used for filtering signal and idler and p for the pump. Since the photon pairs are created symmetrically to the pump central frequency, the chosen signal and idler CWDM must generally be of the type $[s_x, i_x]$ with x = 1, 2 or 3. Unfortunately, CWDM channels are defined by equal spacings in wavelength[7] and not in frequency. This means that for increased separation from the pump, the two parametric photons are not strictly generated in two symmetric CWDM channels. For instance, with a pump at λ_p = 1557 nm, the signal is generated at $\sim$ 1490 nm in the center of s3, however its idler sibling is generated at $\sim$ 1630 nm which is outside of i3.

Figure B2.8 shows a comparison between the free-space and the fibered filtering strategies.

---

[6] this can be futher reduced by splicing the different fibers together to avoid transition connectors

[7] in contrast with DWDM

For both techniques, the wavelength that can be selected are highlighted with coloured rectangles superimposed on the spectral density map.
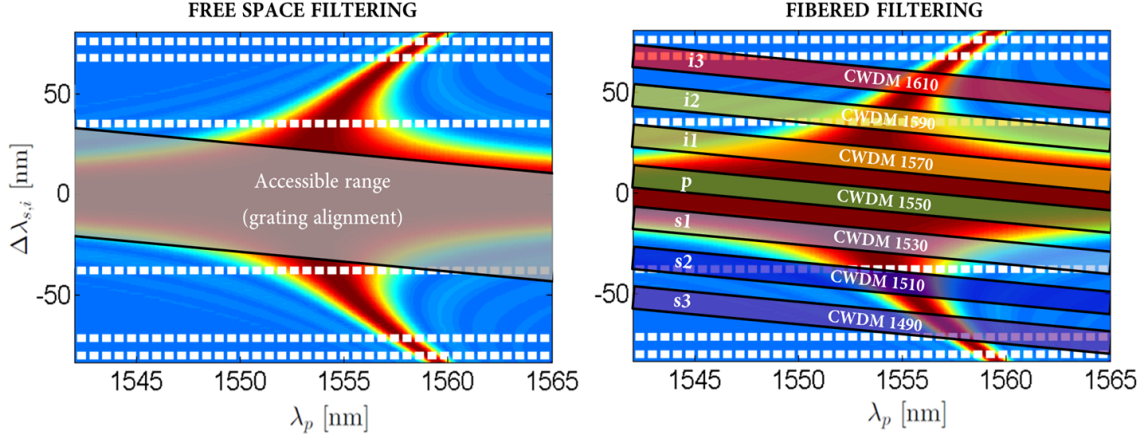

Fig. B2.8: *Spectral density map showing the frequency signal and idler frequencies that can be filtered depending on the chosen experimental scheme. While for the free-space filtering, the signal and idler can be chosen freely in a narrow band (the C band), in the case of the fibered filtering a larger spectral range is accessible at the cost of fixed channels.*

Tab. B2.3: Comparison of the two implemented filtering strategies.

	Gratings Filtering	CWDM Filtering
Accessible λ_s, λ_i	[1527-1562]	1490; 1510; 1530; 1550; 1570; 1590; 1610
Detection Bandwidth	0.3 nm	13 nm
Alignement	Yes	No

c) Discussion and Perspectives

Despite the good pump isolation, both filtering setups do not allow the characterization of photon pair generation in a satisfactory and reproducible fashion. Nevertheless, this non-completion can be attributed to our experimental setup limitations rather than to the source itself.

The free-space filtering with gratings has already proven its worth in past work [25, 29] at the condition that the spectral separation between the pair and the pump is not too narrow[8]. At present, our C-band CW laser limits the spectral separation to an upper bound of ~ 10 nm.

[8] in the work [29] the separation is estimated to ~ 30 nm (60 times the pump width) with a pump in the infrared.

Therefore, a CW tunable laser covering the telecom S-band (1460-1530 nm) and L-band (1565-1625 nm) would be useful to greatly extend our measurement range.

Alternatively, in order to improve the fibered filtering, the 13 nm detection bandwidth of CWDM may be too broad, letting too much noise go to the detectors. It would be worth trying a narrower filtering bandwidth, with either S- and L-band DWDM or with tunable filters which are much more costly solutions than CWDM[9].

Conclusion

We have shown that the choice of the liquid allows to engineer both linear and non linear properties of a LF-HCPCF and more specifically, the ZDW position, the nonlinear coefficient and the Raman free zones. In this way, the phase-matching wavelength range of the four wave mixing process and the photon pair generation efficiency can be optimized with respect to the Raman line position.

For a given commercial fiber, we have identified at least one liquid that satisfies all requirements toward the realization of a LF-HCPCF Raman free photon pair source, with a ZDW in the desired telecom range, and a nonlinear coefficient comparable to the one of silica. All the elements of a low SNR fibered photon pair source at telecom wavelength, fully operating at room temperature are therefore gathered.

---

[9] tunable filter > 1000 $ whereas CWDM < 30 $

Part C

Raman-free photon-pair generation and spectral correlations engineering in Gas-filled IC fiber

Part C of the manuscript is devoted to the second hollow-core source we have designed based on a gas-filled inhibited coupling fiber. In the first chapter we show how this second type of hollow-core fiber allows to design a source with tailored spectral correlations. In the second chapter, experimental characterization of the JSI of the source in the stimulated regime is performed while varying various parameters of both the fiber (length, gas pressure, pulse shaping, etc.) and the pump beam (central wavelength, spectral width, spectral phase). Finally, the characterisation of the source in the photon-pair regime is presented in the third chapter.

This second project is done in collaboration with Charles Fabry and XLIM laboratories. The tested fiber is an "in-house" HCPCF from XLIM.

Chapter C1: Spectral correlation engineering and fiber design

Chapter C2: Joint Spectral Intensity tomography

Chapter C3: Raman-free photon-pair generation

Chapter C1

Spectral correlation engineering and fiber design

   This first chapter describes the usefulness of *spectral-correlation engineering* (i.e. the ability to control the JSI shape) in view of quantum information applications. We first discuss the requirements in terms of dispersion to achieve this goal. This leads to the introduction of the second type of hollow-core fiber: the inhibited coupling fiber, and we demonstrate that it intrinsically exhibits dispersion properties that allow spectral correlation engineering. An analytical model, which allows to link the parameters of the fiber/filling medium combination (fiber inner radius, silica strut thickness, gas pressure, temperature) to its optical properties (dispersion, loss, nonlinearity, etc), is presented and discussed further in the chapter. Finally, the model is used to identify a fiber design exhibiting a factorable JSI that can be used as a heralded-single photon source.

1.1   Introduction to spectral-correlation engineering

Photon-pairs, whether generated through SPDC or FWM, are one of the backbone resources in the field of quantum information. Among the numerous applications, they are useful in linear optical quantum computation [97], quantum cryptography [98], quantum communication [99], teleportation [100], entanglement swapping [101]. Many of these applications require

a large number of photons in a pure state with high visibility Hong-Ou-Mandel interferences [102].

Standard parametric sources often generate two photons sharing undesired spatial and spectral entanglement. As described in chapter A.2.2, such entanglement results in individual photons being in a mixed state, which limits the visibility of interference between single photons from different sources. Therefore, it is essential to build sources that allow to easily control the spectral correlation of the generated pairs. Spatial entanglement can be suppressed by using a guided-source such as fibers or waveguides. However, avoiding the spectral correlations requires more stringent designs [36] as detailed hereafter.

a)   Filtering strategy versus Source engineering

One way to overcome spectral correlations is to use a narrow-band spectral filtering to select a factorable region of the JSA [103, 104]. However, this approach has one significant drawback: the filter reduces the number of usable photons. This approach forces a trade-off between purity and brightness [44] the narrower the filter, the higher the purity but the lower the number of photons reaching the detectors. This can be seen easily in Fig. C1.1. For instance, starting from a given non-engineered source of single photon purity P = 30 % (Fig. C1.1 top right hand side), 50 % purity is obtained at the cost of removing 27 % of the generated photons and 95 % purity is obtained at the cost of removing 85% of the generated photons.

In general, this approach, whether sacrificing either purity or brightness, is not scalable to large-scale quantum information applications, requiring high rates of pure photons. In contrast, perfect interference visibility between photons from distinct sources can be achieved without resorting to filtering if the photons are directly produced in a factorable state[1]. This is the motivation behind the *spectral correlation engineering* of parametric sources [36]. We have seen previously (see chapter A.2.3) that such a state is obtainable provided that the source dispersion enables a group-velocity matching between pump, signal and idler frequencies. Theoretical and experimental works have shown how this is achievable in crystals [39, 105, 106, 107], in chip-based sources [47, 108] and solid-core fibers [10, 34, 109, 110, 111]. In the following, we present a strategy to attain this goal in hollow-core fiber media.

b)   What about photonic-bandgap hollow-core fiber ?

The dispersion profile of PGB-HCPCF is generally not compatible with correlation engineering. As we have seen previously (see section B.1.1) it exhibits a monotonically decreasing "S-shape" dispersion associated with a parabolic inverse group-velocity (β_1) as shown in Fig. C1.2. This

---

[1] even the sidelobes of the *sinc* can be filtered with a very limited impact on the brightness (<2%)

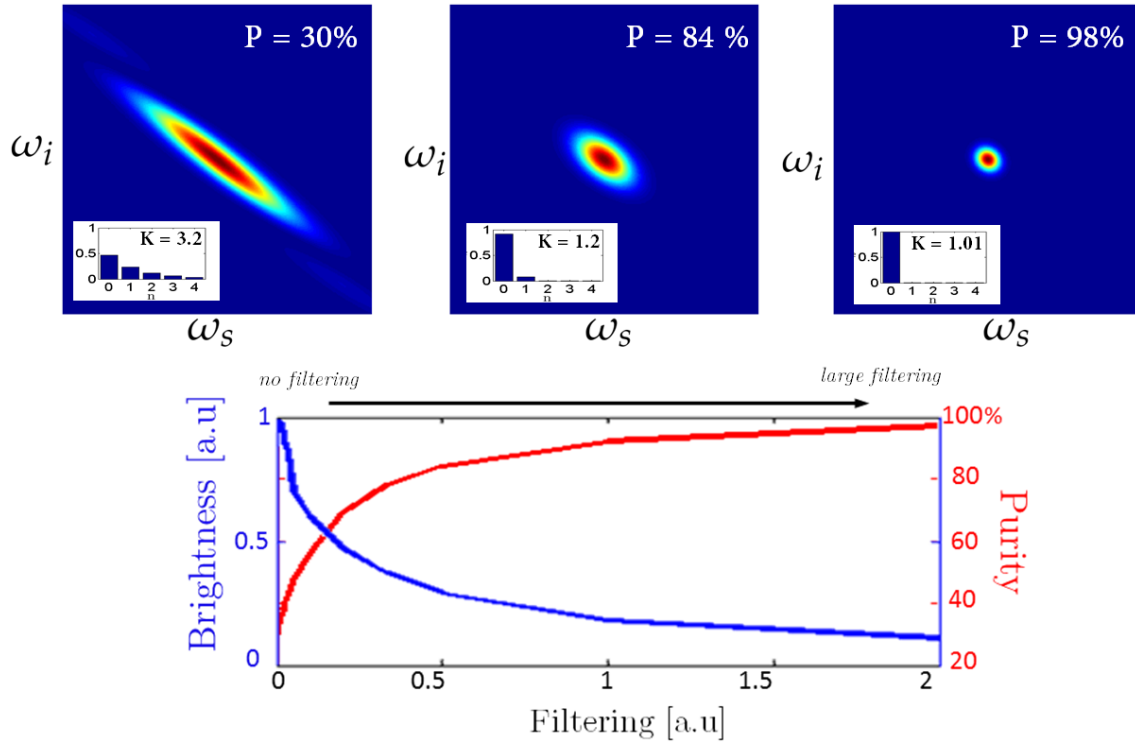**Fig. C1.1:** *Top: Simulation of a JSI and associated Schmidt decomposition with increasing filtering. The white number corresponds to the single photon purity. The simulation considered Gaussian filter applied on both signal and idler frequencies. Bottom: Corresponding trade-off between purity and brightness as a function of the amount of filtering (= $\frac{1}{\sigma}$ with σ an arbitrary filtering width.)*

means that in typical PBG-HCPCF, there is only one ZDW, which, by definition, is a local minimum of the β_1 curve. And, as the FWM process requires the pump wavelength to be close to a ZDW, it restrains β_{1p} to be close to a minimum (Fig. C1.2.b) such that $\beta_{1s} > \beta_{1p}$ and $\beta_{1i} > \beta_{1p}$. Consequently the conditions for obtaining a factorable state are not fulfilled[2].
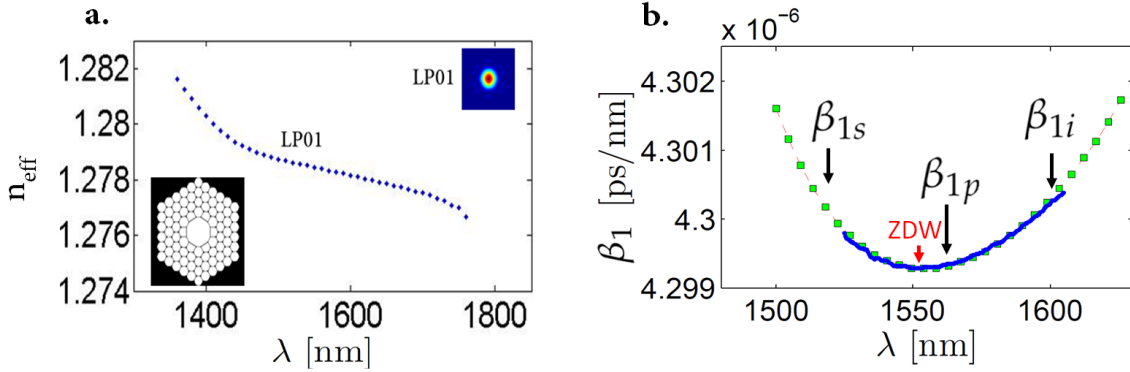

Fig. C1.2: *a. Simulated effective index obtained with FDFD simulation (PBG-HCPCF from Part B). b. Inverse group velocity as a function of wavelength. The green square correspond to FDFD simulation and the blue lines to the OLCI measurement.*

We perform simulations in order to find fiber designs compatible with group-velocity matching. The key is to look for fiber exhibiting a non-monotonic dispersion (presence of several ZDWs) since it has been demonstrated that it allows the generation of a much larger variety of spectral correlations and in particular of factorable states [34, 110]. Let us demonstrate that a non-monotonic profile can be achieved thanks to surface modes.

As discussed precedently (see section B.1.3), a common issue with PBG-HCPCF is the presence of surface modes that couple to the fundamental mode. Since they increase the loss [90, 112] and limit the usable bandwidth [23], surface modes are generally unwanted and number of studies have been carried out in order to avoid their presence in the transmission bandwidth[3] [90, 115, 116]. However, beside these detrimental effects, the presence of surface modes also results in splitting the bandgap into several bands, each with their own ZDW. As an illustration, Fig. C1.3 shows the result of FDFD simulation of a fiber design exhibiting 3 bands because of 2 surface modes which couple to the fundamental mode at ~ 1480 nm and 1600 nm. The simulation uses the same design than Fig. C1.2 but with a 40 % widening of the silica ring delimiting the core (see inset). In such a multiband dispersion profile, FWM can occur with pump, signal and idler spread out in three different band as shown in Fig. C1.3.b. In such a case, β_{1p} can remains near a ZDW without the restriction that β_{1s} and β_{1i} have higher value than β_{1p}. With

---

[2]we recall that the conditions are that either the inverse group velocity of the pump equals one of the parametric photon (asymmetric group-velocity matching: $\beta_{1p} = \beta_{1s}$ or $\beta_{1p} = \beta_{1s}$) or that it is the arithmetic average of the inverse group velocity of signal and idler photon (symmetric group-velocity matching: $2\beta_{1p} = \beta_{1s} + \beta_{1,i}$

[3]a common strategy is to lower the thickness of the silica ring around the core [113, 114] which results in "pushing away" the surface modes outside the bandgap

this restriction lifted, one can access a variety of group-velocity relation between pump, signal and idler such as $\beta_{1p} = \beta_{1s}$ as illustrated in this figure [117].
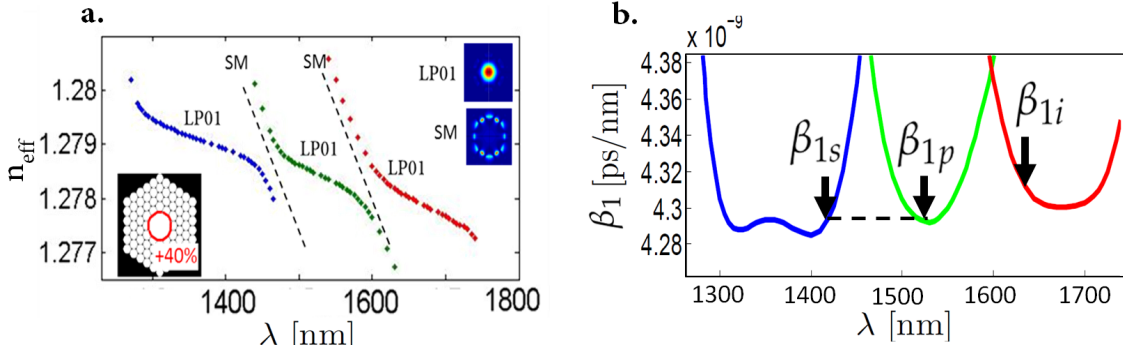

Fig. C1.3: *a. FDFD simulation with a 40 % increased of the core thickness b. Corresponding simulated inverse group velocity as a function of wavelength.*

However, the idea to purposely add SM to obtain non-monotonic dispersion profile is in opposition with the global trend in the fiber community to get rid of these surface modes. Therefore, even-though multiband dispersion profile in PBG has been demonstrated through surface mode couplings [90, 114, 22] or even through double bandgap structure [77], it remains experimentally challenging to have a precise control on this multiband behaviour yet. With this in mind, we have chosen to use the second type of hollow-core fiber *the inhibited-coupling fiber* [4]. As we will see, these fibers intrinsically exhibit a multiband dispersion profile making them suitable for spectral correlation engineering. This study is done in the framework of a collaboration with Fetah Benabid from XLIM laboratory who designed the first inhibited-coupling fiber in 2002 [72, 73], the so-called kagome fiber, and whose group (GPPMM) detains state of the art hollow-core fiber fabrication facilities and know-how. Prior to giving an explanation of the guidance mechanism of inhibited coupling HCPCF, let us first present its main distinctive features compared to PBG-HCPCF.

1.2 Comparison between PBG and IC

As a result of their different guidance nature, PBG and IC exhibit differences in their dimensions (i.e. core diameter, pitch, thickness of the silica web) and optical properties (i.e transmission bandwidth, loss, dispersion, etc). Figure C1.4 presents an intuitive picture of these distinctions while Table C1.1 gives a more quantitative comparison.

---

[4] in the literature, inhibited-coupling HCPCF is sometimes associated to the ARROW terminology (anti-resonance reflecting optical waveguide) or anti-resonant hollow core fibers. For more details please refer to [118]. Moreover, it provides extended explanations on the different hollow-core guidance mechanisms and a review of the different applications

The main differences are:

- IC span an extremely large transmission bandwidth (several octaves) from the far infrared to the UV.

- Unlike standard PBG which are generally composed of a unique "S-shape" dispersion profile, IC intrinsically display a dispersion composed of several S-shape wide bands separated by non-guiding highly dispersive narrow bands.

- The mean group velocity dispersion in the guided ranges is generally much lower in IC than in PBG (around two orders of magnitude lower).
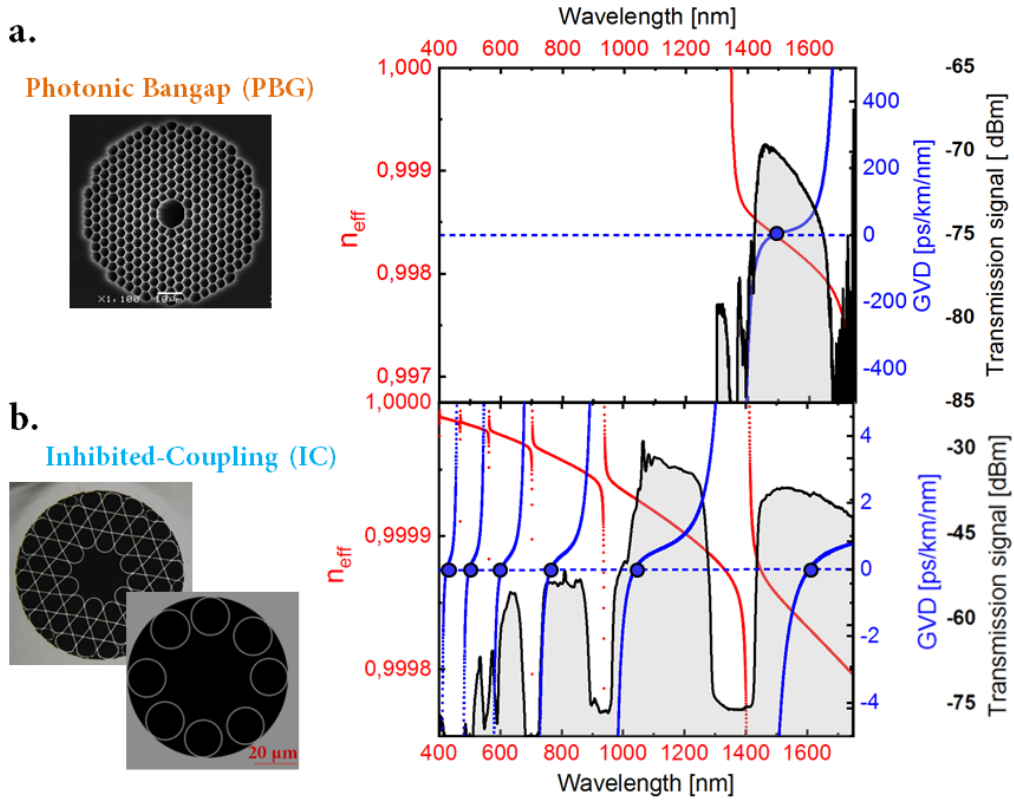

Fig. C1.4: *a. PBG fiber and b. IC fiber cross sections and their optical properties. The effective index is plotted in red, the group-velocity dispersion in blue and the transmission in dark lines. The blue dots give the position of the zero-dispersion wavelengths.*

a) A different cladding design

The properties of IC are a direct consequence of their guidance mechanism. Unlike the PBG fiber that can guide only wavelengths that are close to the periodicity[5] of the cladding, IC fibers

---

[5] in fact, the periodicity is not a necessary condition but more a mathematical convenience for applying the Bloch theorem (more details in [118].

Tab. C1.1: Features comparison between photonic bandgap and inhibited coupling HCPCF

	PBG	IC
	Optical parameter	
mean field diameter (MFD)	4-15 μm	15-95 μm
loss [dB/km]	1.2-25 @1550 nm 50-100 @1 μm 1000 @500 nm	10-50 @1550 nm 8.5-20 @1 μm 10-20 @500 nm
bandwidth	50-200 nm	>1 μm
dispersion in guided ranges [ps/km/nm]	10-300	3-10
typical polarisation maintenance (PER)	15-20 dB	15-20 dB
numerical aperture (NA)	0.1-0.2	0.01-0.05
optical overlap with silica cladding	0.1-1 %	0.001-0.01 %
	Geometrical parameter	
core diameter	5-20 μm	15-100 μm
strut thickness	100-200 nm	250-3000 nm

does not possess a bandgap [73]. The guidance is based on a photonic analogue of the bound state within a continuum established within the field of solid-state quantum physics [119, 120], where a quantum state remains localised into a given mode even though it coexists with a continuum of scattering modes. Concerning inhibited-coupling fiber, the bound state is the core mode whereas the continuum is formed by cladding modes. In other words, the core modes and the cladding modes coexist without being coupled to one another. As we will see, this non-coupling is due either to their small spatial overlap or to their strong effective index mismatch [121].

core mode   *air cladding mode*   *silica cladding mode*
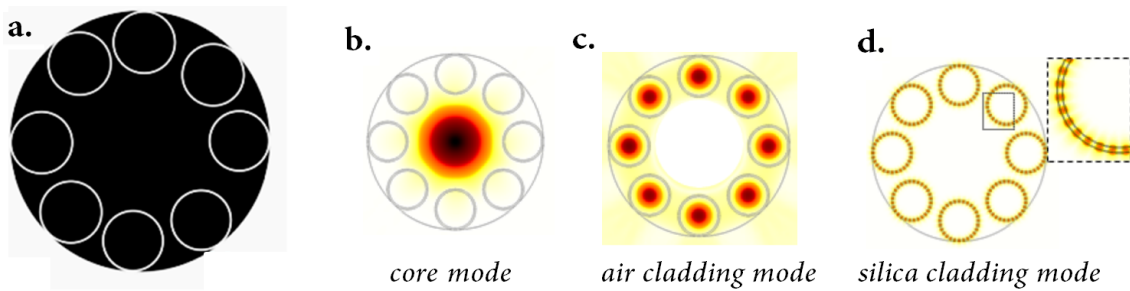
Fig. C1.5: *Example of IC fiber geometry and examples of associated core and cladding modes [122].*

In practice, IC fiber geometries are designed in such a way that the silica cladding modes (for instance Fig. C1.5.d) exhibit a much faster transverse field oscillation than the core modes [73]. The cladding (here composed of tubes) exhibits a round and smooth shape but at a much

smaller scale than the core size, forcing a faster transverse field oscillation [6]. This is in contrast to PBG fiber which have many sharp bends and nodes (i.e. intersection of silica struts) in the core vicinity. Such a smooth structure allows to get rid of silica-cladding mode with slow transverse field oscillation that could possibly have coupled to the core modes[7]. Actually, they do couple at some specific wavelengths denominated as *resonances.* These resonances are responsible for the multiband behaviour of IC-fiber and thus, play a central role for the spectral-correlation engineering as we will see. In the next section, we will determine the wavelengths for which there are such resonant couplings.

Moreover, regarding air-cladding modes, although they have a slow transverse field oscillation (Fig. C1.5.c), they do not couple with the core mode because they do not spatially overlap and exhibit different effective index due to the lower size of the tubes.

b)   Resonances with the silica tubes

Let us consider the IC fiber geometry of Fig. C1.5. Because it has a simple structure, the wavelengths for which there is a strong coupling between core mode and silica-cladding modes can be determined easily. It occurs when the core modes and silica-cladding mode have identical transverse and longitudinal wavevector ($\beta_{\text{tube}} = \beta_{\text{core}}$).
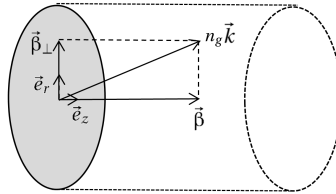

Fig. C1.6: *Illustration of the conventions used for the propagation vectors.*

For the sake of this calculation, let us first describe the core and cladding modes wavectors. For a given mode X travelling in a medium of index n_g, the wavevector can be written as:

$$(n_g k)^2 = \beta_X^2 + \beta_{X,\perp}^2 \tag{C1.1}$$

where $k = \frac{2\pi}{\lambda}$, β_X is the projection along the z-axis and $\beta_{X,\perp}$ the transverse component (see Fig. C1.6).

The Core mode. On the one hand, the longitudinal wavevector β_{core} of the fundamental

---

[6] see for instance the emergence of hypo-cycloid core contour [123].

[7] opposingly, "nodes" in the claddind tend to favour highly localised mode with a slow transverse field oscillation

mode in the fiber[8] (HE_{11}) can be approximated by [124, 125]:

$$\beta_{core}^2 = (n_{air}k)^2 - \beta_{core,\perp}^2 \tag{C1.2a}$$

$$\approx k^2 - \frac{j^2}{R^2} \tag{C1.2b}$$

where j = 2.405 is the first zero of the 1st Bessel function. Please note that this is true in the assumption that the fiber radius R is much larger than λ.

The silica-cladding mode. On the other hand the longitudinal wavevector β_{tube} of the mode localized within the silica of the tube constituting the cladding is given by:

$$\beta_{tube}^2 = (n_{si}k)^2 - \beta_{tube,\perp}^2 \tag{C1.3a}$$

$$= (n_{si}k)^2 - (\beta_r^2 + \beta_\theta^2) \tag{C1.3b}$$

where β has been decomposed in the cylindrical coordinates system. These tube modes can be described as $HE_{m,l}$ such that the transverse components are [126]:

$$\beta_r = (l-1)\frac{\pi}{t} \tag{C1.4}$$

$$\beta_\theta = \frac{m}{2R_t} \tag{C1.5}$$

where t is the silica strut thickness, R_t the tube radius, l the radial- and m the azimuthal-mode number, respectively. Figure C1.7 shows examples of field distributions in one tube of the cladding.

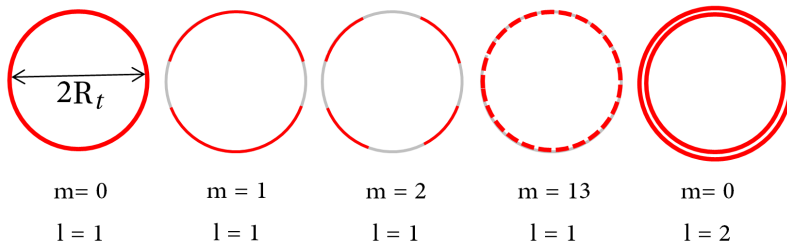| 2R_t | | | | |
| m= 0 | m = 1 | m = 2 | m = 13 | m= 0 |
| l = 1 | l = 1 | l = 1 | l = 1 | l = 2 |

Fig. C1.7: *Examples of tube modes designated by their radial (l) and azimuthal (m) mode number. In practice, the silica-cladding modes are spread over all the tubes of the cladding.*

---

[8]more generally, a $HE_{m,n}$ mode is described by : $\beta_{core}^2 \approx k^2 - \frac{j_{m-1,n}^2}{R^2}$ with $j_{m,n}$ the nth root of the mth Bessel function

The core and silica-cladding modes are longitudinally phase-matched when:

$$\beta_{\text{tube}} = \beta_{\text{core}} \tag{C1.6a}$$

$$(n_{si}k)^2 - \left((l-1)\frac{\pi}{t}\right)^2 - \left(\frac{m}{2R_t}\right)^2 = k^2 - \frac{j^2}{R^2} \tag{C1.6b}$$

$$\left((l-1)\frac{\pi}{t}\right)^2 + \left(\frac{m}{2R_t}\right)^2 = \frac{2\pi}{\lambda^2}(n_{si}^2 - 1) + \frac{j^2}{R^2} \tag{C1.6c}$$

Considering the case of wavelengths much smaller than the radius of the tube ($\lambda \ll R$), the longitudinal phase-matching identity can be simplified to:

$$\left((l-1)\frac{\pi}{t}\right)^2 + \left(\frac{m}{2R_t}\right) = \frac{2\pi}{\lambda^2}(n_{si}^2 - 1) \tag{C1.7}$$

The two modes couple to each other if they are also transversely phase-matched. This occurs when the silica mode azimuthal number m equals the one of the core mode [127]. Thus, for the fundamental mode ($m = 0$), the transverse and longitudinal phase-matching condition can be written as:

$$\left((l-1)\frac{\pi}{t}\right)^2 = \frac{2\pi}{\lambda^2}(n_{si}^2 - 1) \tag{C1.8}$$

This identity can be written in the form:

$$\boxed{\lambda_{l-1} = \frac{2t}{l-1}\sqrt{n_{si}^2 - 1}} \tag{C1.9}$$

where we recall that l is an integer.

Therefore, a strong hybridization between core mode and cladding modes is expected at wavelengths λ_l. These resonances correspond to the narrow regions in Fig. C1.4 with high loss and diverging dispersion.

c) Density of states

With this in mind, let us compare the density of photonic states of an IC fiber to the one of a PBG (see Fig. C1.8). The horizontal axis $k\Lambda$ of the IC diagram is normalised relatively to the resonant condition $k\Lambda = (2t/\lambda)\sqrt{n_{si}^2 - 1}$ whereas for the PBG diagram it is normalised by $k\Lambda$ with Λ being the pitch of the 2D crystal.

Firstly, one can notice that unlike PBG, the IC effective index diagram exhibits no bandgap but a quasi-continuum of propagating modes, as mentioned above. In other words, there is no region in the density of state which is free of cladding modes. Nevertheless, in IC, two types of

cladding modes can be distinguished (as seen in Fig. C1.5) (i) modes lying in the silica cladding which are identifiable by their steep dispersion (grey vertical lines) and (ii) modes lying in air with a flat dispersion below the air light line (horizontal dashed line). The air modes can either correspond to core modes (yellow) or air-cladding mode lying within the tubes (dark horizontal line).

Secondly, despite they cross each other in the density of states curves, the core mode does not hybridize with cladding mode[9], except in the vicinity of the resonance where $k\Lambda \sim 1$.
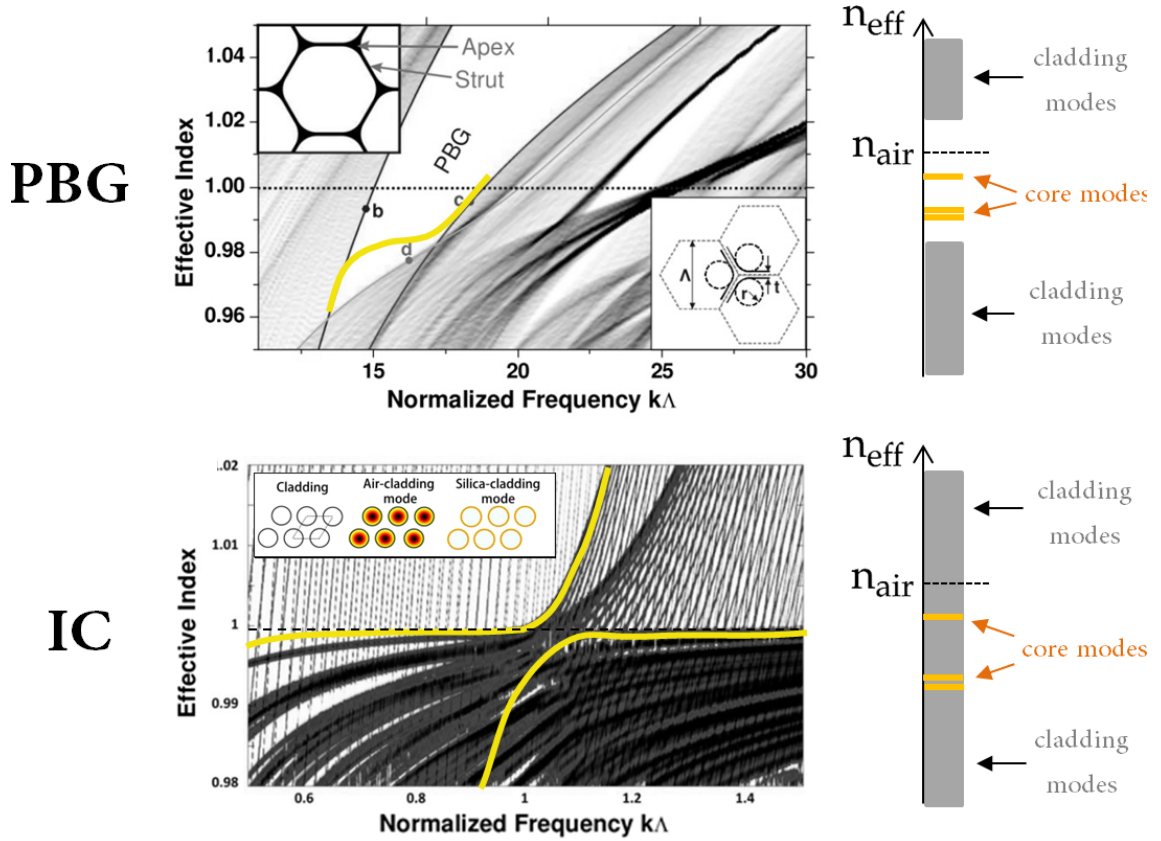

Fig. C1.8: *Comparison between density of photonic states for the cladding structure (grey) and core mode (yellow) in PBG and IC fiber. The core mode is an illustration and does not corresponds to actual computed data. As opposed to PBG where the core modes lie in a region void of cladding mode (the bandgap), IC core modes are cohabiting with a region filled with cladding mode. The two density of photonic states are reproduced from [77, 121].*

Thus, PBG and IC rely on two different strategies to guide light in the core. PBG fibers are designed in such a way that a core mode exists in a region free of cladding mode. Thus, the core

---

[9] more precisely, such a diagram considers an infinite cladding structure without defect/core. Nevertheless, one can observe that, except in the vicinity of the resonances, there is an absence of hybridization between the air cladding modes and the silica cladding modes. Since core modes have similar dispersion to air-cladding mode, it gives a strong intuition about the coupling inhibition between the core modes and the silica cladding modes.

mode cannot leak out because there is no cladding mode to couple to. Alternatively, IC rely on engineering the core and cladding modal content in such a way that they do not couple [118].

d) Variety of inhibited-coupling designs

As opposed to PBG, the cladding modes in IC fibers are very localized with little interaction with their close neighbouring guiding sites. This has two main consequences:

- it can be shown [121] that, in first approximation, this dispersion diagram is independent from the lattice geometrical arrangement (change of pitch, of pattern or of lattice structure, see for instance Fig. C1.9). This is why our mathematical derivation (cf section C.1.2.b) describing the coupling resonances in a tubular IC fiber can be extended to others IC geometries.

- the first sites around the core are sufficient to compose the cladding [73]. Interestingly, the cladding structure of IC fibers has gradually simplified. Figure C1.9 explicitely shows this trend from its first design (kagome-like) in 2002 [72] composed of an extended lattice, to lighter and lighter cladding such as the Tubular fiber [128] composed of a single layer of tubes around the core.
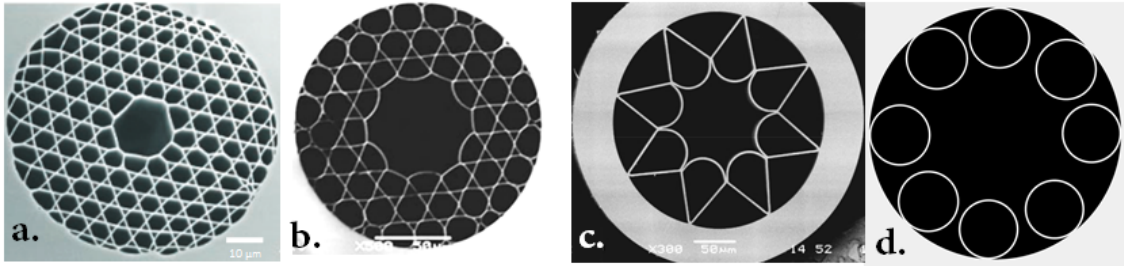

Fig. C1.9: *SEM images of different types of inhibited-coupling fibers classed by historical order **a.** Kagome (2002, [72]), **b.** Kagome with hypocycloid shaped core structure (2011, [129]), **c.** Hollow-core with ice-cream-cone shape capillary in the cladding (2012, [130]) **d.** Tubular fiber designed by XLIM used in this work .*

Moreover, it is also remarkable to observe how the evolution of the design has eliminated all the nodes and sharp angles present in the cladding[10] in order to inhibit the existence of cladding mode with a slow transverse oscillation. This is particularly the case with the latest design, the tubular (Fig. C1.9.d) which does not exhibit any nodes in its cladding structure[11].

As opposed to PBG fiber where we used FDFD simulations to infer the relation between

---

[10]in particular in the core vicinity

[11]even at the junctions where the tubes are attached, the almost perfect round structure of the tube makes this intersection relatively small

the geometrical parameters of the fiber and its dispersion properties, IC fibers can be well described by an analytical model. In the following section we will detail this model and show how it can be used to predict the phase-matching and spectral correlations.

1.3 IC fiber analytical model

An analytical model was recently given to describe the effective index of a $\mathrm{HE}_{m,n}$ mode tube-type hollow core fiber filled with a gas [131]:

$$n_{\mathrm{eff}} = n_{gas} - \frac{j_{m-1,n}^2}{2k_0^2 n_{gas} \mathrm{R}^2} - \frac{j_{m-1,n}^2}{k_0^3 n_{gas}^2 \mathrm{R}^3} \frac{\cot\left[\Psi(t)\right]}{\sqrt{\epsilon-1}} \frac{\epsilon+1}{2} \qquad \text{(C1.10)}$$

with : $\Psi(t) = k_0\, t\sqrt{n_{si}^2 - n_{gas}^2}$, R the fiber radius, $\epsilon = n_{si}^2/n_{gas}^2$, $j_{m,n}$ the nth root of the mth Bessel function, t the silica strut thickness, n_{gas} the gas refractive index and n_{si} the glass refractive index.

Simulations and experimental observations have shown that such a tube-type model can provide an accurate description of IC-fibers [132]. It is quite remarkable that, **regardless of the complexity of the cladding geometry, the dispersion can be inferred with high accuracy only by considering two of its geometrical parameters: (i) the core radius** R **describing the overall dispersion and (ii) the silica strut thickness** t **describing the resonances**. Potentially, the core radius may be a few percent underestimated when extrapolating an IC fiber to a tube-type [133].

For instance, despite their apparent geometrical differences, if a Kagome-like and a Tubular-like IC fiber (see Fig. C1.10) have the same radius R and silica strut thickness t, they will exhibit very close dispersion. This approximation holds because IC fibers are commonly used in the regime where $\lambda << \mathrm{R}$ and because the guided field is concentrated in the core region so that the evolution of the effective index is, in first approximation, independent of the cladding design around the core, whether it is a tube, 8 tubes or a kagome-lattice. On the contrary, loss is very sensitive to cladding geometry [134]. For this reason, the analytical model describing the loss in tube-type fiber [131] cannot be extrapolated to IC fibers that generally exhibit loss that is several orders of magnitude lower than a tube-type hollow core.

Let us describe in more details the different terms of Eq. (C1.10). The expression can be split in two parts, i) the slowly varying contribution n_{mean} and ii) the fast evolving part related to the resonances n_{discont} such that $n_{\mathrm{eff}} = n_{\mathrm{mean}} + n_{\mathrm{discont}}$. Figure C1.11 shows an example illustrating the contributions of the two terms in the analytical model.

Moreover, for simplicity, only the fundamental mode HE_{11} is considered in the following. Thus,
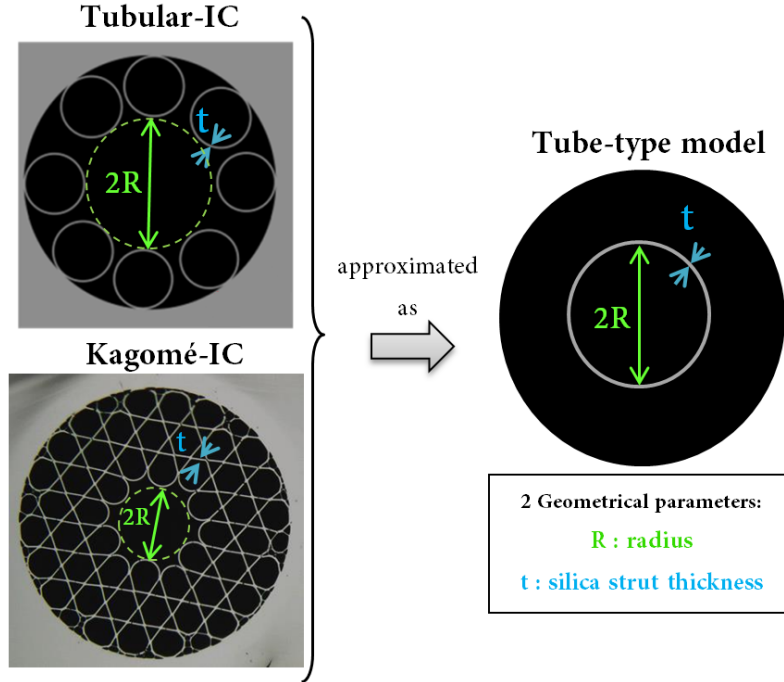
Fig. C1.10: *IC fiber dispersion, independently from the cladding geometry, can be described by a tube-type model. Only two geometrical parameters are required, the fiber radius* R *and the silica strut thickness* t.

$j_{m-1,n}$ is replaced by j with $j = j_{0,1} \approx 2.405$

$$n_{\text{eff}} = \underbrace{n_{gas} - \frac{j^2}{2k_0^2 n_{gas}\text{R}^2}}_{n_{\text{mean}}} - \underbrace{\frac{j^2}{k_0^3 n_{gas}^2 \text{R}^3} \frac{\cot\left[\Psi(t)\right]}{\sqrt{\epsilon-1}} \frac{\epsilon+1}{2}}_{n_{\text{discont}}} \tag{C1.11}$$

a) Mean dispersion

Medium and Guide dispersion

The slowly varying contribution of the effective index is described by the first two terms of Eq. (C1.11) depending on gas refractive index and fiber core radius. Note that these two terms, taken individually, correspond to the well established formula given by *Marcatili et al.* [124] describing a hollow waveguide with a perfectly reflecting boundary.

The mean dispersion results from a competition between the *medium dispersion* which is here
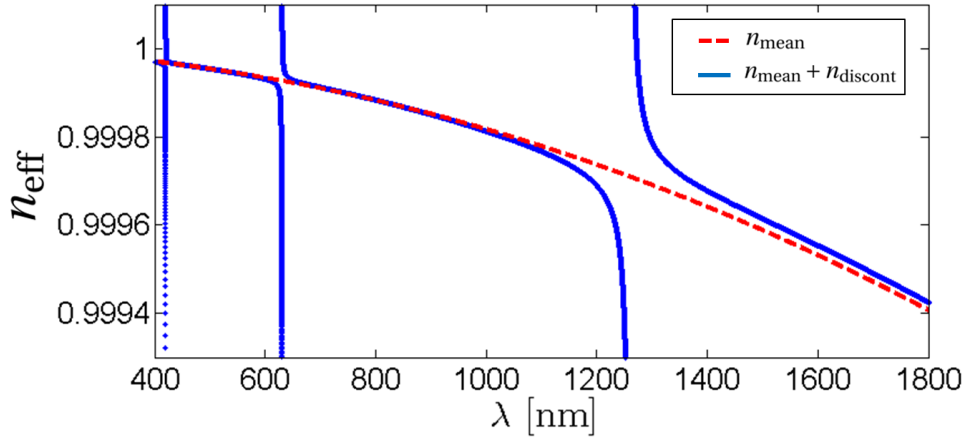
Fig. C1.11: *Effective index of an empty 20 µm radius fiber with strut thickness t = 600 nm. The red dashed line corresponds to the slowly varying contribution (n_{mean}), when neglecting the effect of resonances. The blue curve gives the dispersion predicted by the analytical model ($n_{eff} = n_{mean} + n_{discont}$) including the resonances.*

the gas, and the *guide dispersion* which is a geometrical effect[12]:

$$n_{\text{mean}} = n_{gas} - \frac{j^2}{2k_0^2 n_{gas} R^2} \tag{C1.12a}$$

$$= 1 + \underbrace{(n_{gas} - 1)}_{\text{medium dispersion}} - \underbrace{\frac{j^2}{2k_0^2 n_{gas} R^2}}_{\text{guide dispersion}} \tag{C1.12b}$$

The guide dispersion mostly depends on the radius ($\propto -\frac{\lambda^2}{R^2}$), the smaller the radius, the steeper the dispersion. Figure C1.12, right hand side, presents the empty guide dispersion for three different radiuses.

Although a gas is generally a low dispersive medium, the contribution of the material dispersion is not negligible since the guide dispersion may be also quite remarkably low (especially in the case of large core) when compared to standard silica core waveguide. The dispersion of several gas (xenon, argon and neon) at standard temperature and pressure is shown in Fig. C1.12, left hand side. The heavier the atomic weight of the gas constituents, the higher the dispersion.

Depending on the fiber radius and gas used, the relative weight of medium and guide dispersion can largely vary. Nevertheless, in general, at longer wavelength, the overall dispersion tends to be governed by the guide whereas at lower wavelength the gas is predominant[13] as it

---

[12] as it can be seen in Eq. (C1.12b), the guide and medium dispersion are not strictly decoupled since the guide dispersion depends on n_{gas}, however this dependence is negligible.

[13] intuitively, at lower wavelength ($\lambda \ll R$), light do not "see" the core walls and only experiences the medium.
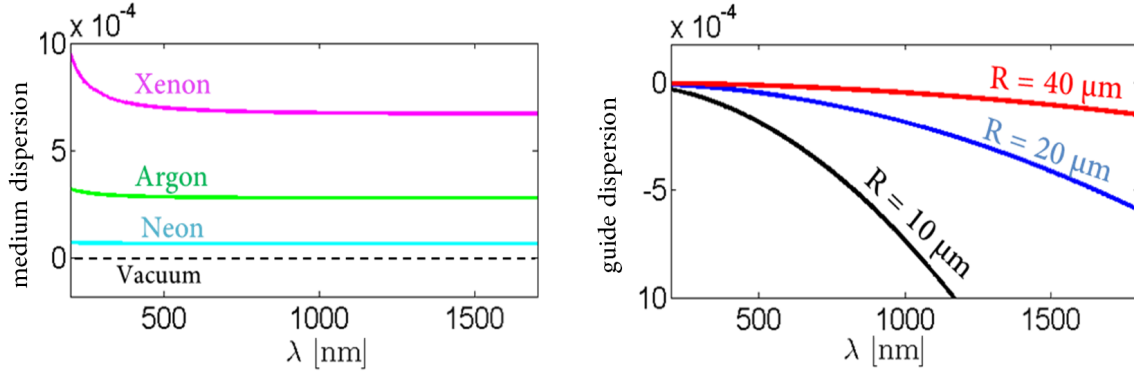
Fig. C1.12: *Left: medium dispersion for 1 bar of xenon (magenta curve), argon (green) and neon (cyan). Right: empty guide dispersion for a radius of 10 µm (black), 20 µm (blue) and 40 µm (red). Medium and guide dispersion are defined by Eq. C1.12b.*

can be seen in Fig. C1.12.

Temperature and Pressure

Temperature and most notably pressure are interesting parameters to use from a practical point of view. In contrast to the fiber geometrical parameters which are fixed once the fiber is designed, **the temperature and the pressure offer the possibility of an active control over the dispersion as well as over the consequent phase-matching condition of the four-wave mixing.** The refractive index of the gas at temperature T and pressure P can be extrapolated from the general Sellmeier equation at standard temperature and pressure conditions (T_0, P_0) using:

$$n_{\text{gas}}(\lambda, P, T) \approx \sqrt{1 + (n_{\text{gas}}^2(\lambda, P_0, T_0) - 1).\frac{P}{P_0}.\frac{T_0}{T}} \qquad \text{(C1.13)}$$

This equation shows that, pressure and temperature have similar influences but with opposite directions. Increasing the pressure/decreasing the temperature makes the gas more dispersive. Moreover, the temperature has less influence than pressure (since $T_0 \sim 273$ K whereas $P_0 \sim 1$ bar). Figure C1.13.a shows the influence of pressure and temperature modifications, and, indeed shows that it is mostly impacting lower wavelengths where the gas dispersion is predominant (see discussion above).

The position of the mean ZDW[14] can be shifted with pressure or temperature modification (see Fig. C1.13.b). A practical implementation of such a control will be presented in the experimental results (see section C.2.3).

---

[14] herein we focus on the mean dispersion and do not yet consider the effect of the resonances on the dispersion
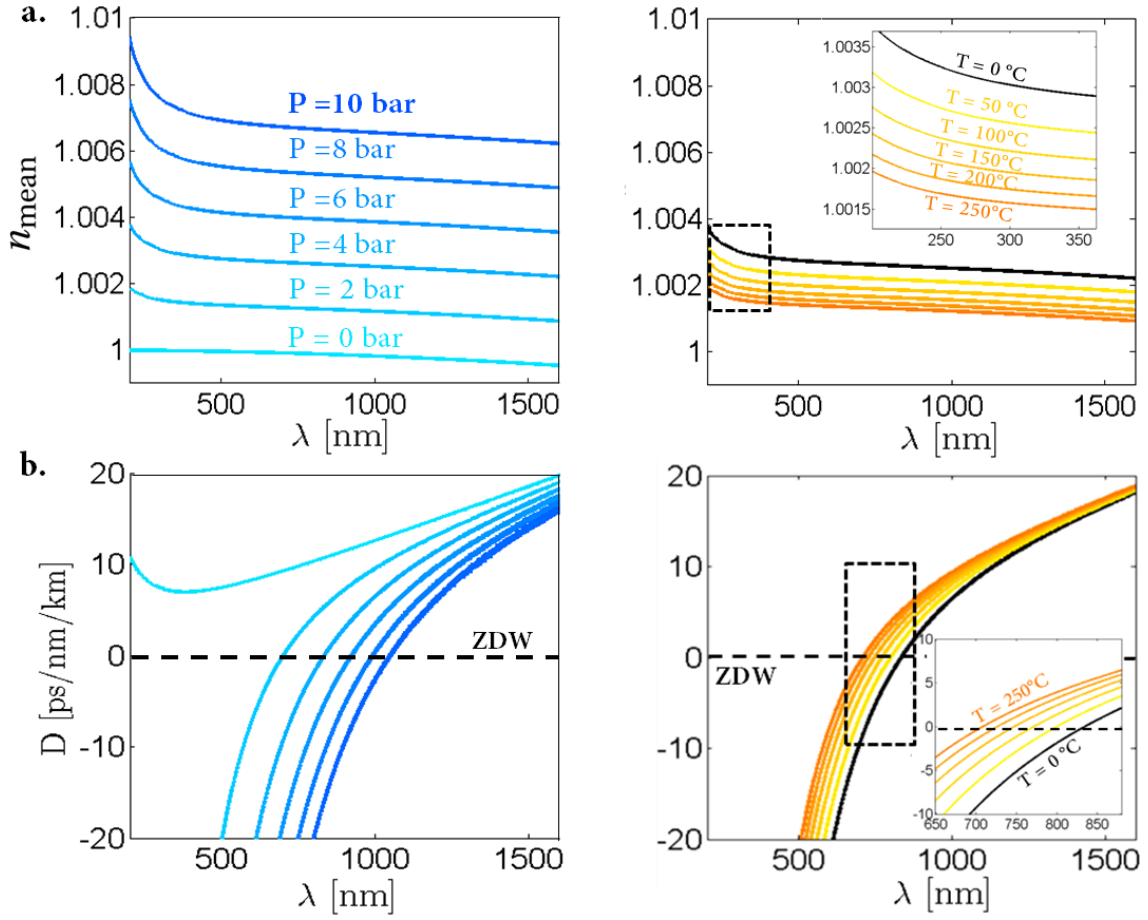
Fig. C1.13: *a.* *Left: Mean effective index at different pressures of xenon in a fiber of 20 μm radius at T =
273 K. Right: Same fiber design with a fixed pressure of 4 bar of xenon and for different temperatures.*
b. *Corresponding group velocity dispersion (D = -$\frac{2\pi c}{\lambda^2} \frac{d\beta}{d\omega^2}$).*

b)   Resonances

Let us now consider the third and last term of Eq. (C1.11) introducing the resonances with the
silica struts:

$$n_{\text{discont}} = -\frac{j^2}{k_0^3 n_{gas}^2 R^3} \frac{\cot\left[\Psi(t)\right]}{\sqrt{\epsilon-1}} \frac{\epsilon+1}{2} \tag{C1.14}$$

This term is significant only when the cotangent function diverges, that is, when $\Psi(t) = m\pi$
with m an integer. Since $\Psi(t) = k_0 \, t\sqrt{n_{si}^2 - n_{gas}^2}$, this occurs when:

$$\lambda_m = \frac{2t}{m}\sqrt{n_{si}^2 - n_{gas}^2} \tag{C1.15}$$

which corresponds to the position of the resonances we found in Eq. (C1.9) when describ-
ing the wavelengths at which a strong coupling exists between the core mode and the silica

cladding modes[15].

Equation (C1.15) shows that the position of the resonances depends on the refractive index of the filling medium. This is useful for sensing application as for instance in [122]. In our case, since $n_{gas}^2 \sim 1$, it can be simplified into $\lambda_m \approx \frac{2t}{m}\sqrt{n_{si}^2 - 1}$. Thus, we will assume that the position of the discontinuities solely depends on the silica strut thickness t.

Figure C1.14 shows the dispersion of IC-fibers calculated from Eq. (C1.10) with different values of t. For a small t value, the dispersion is free of discontinuities in the usual transmission range of such fiber which covers visible to infrared wavelength. It is useful to note that, when considering a fiber with a parameter t, the first resonance (i.e. the highest wavelength resonance) is roughly at $\lambda_1 \approx 2t$. For instance, a fiber with silica strut thickness $t = 200$ nm has its first discontinuity in the blue at 420 nm while the others are at lower wavelength in the UV region. As t increases, the discontinuities are red-shifted such that more and more discontinuities are present in this visible/IR spectral region, forming a multiband dispersion profile. As a matter of fact, most fibers in the literature have silica strut thickness in the range $t \in [250-3000]$ nm. Therefore, when designing the fiber **the number and position of the bands, and consequently the number of ZDW can be well controlled by adjusting the silica strut thickness parameter**. Table C1.2 gives examples of resonance positions for the different fiber designs of Fig. C1.14.

Tab. C1.2: The six first resonances as a function of the silica strut thicknesses. The numbers in bold character correspond to resonances which appear in Fig. C1.14. As t increases, the resonances are shifted from the UV to the infrared.

	λ_1 [nm]	λ_2 [nm]	λ_3 [nm]	λ_4 [nm]	λ_5 [nm]	λ_6 [nm]
$t = 200$ nm	420	210	140	105	84	70
$t = 400$ nm	**840**	420	280	210	168	140
$t = 800$ nm	**1680**	**840**	**560**	420	336	280
$t = 1600$ nm	3360	**1680**	**1120**	**840**	**672**	**560**

The next section describes the link between the multiband behaviour and the possibility to access photon-pair with tailored spectral properties.

---

[15] except that we were considering an empty cladding, such that $n_{gas} = 1$.
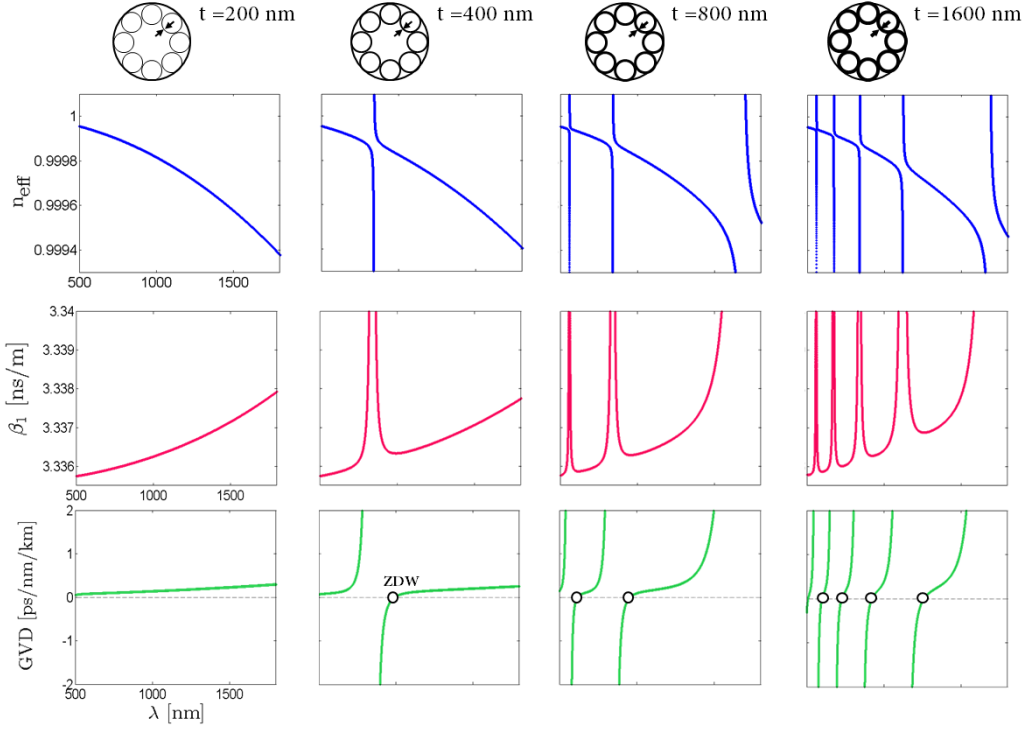
Fig. C1.14: *Effective index, inverse group velocity (β_1) and group velocity dispersion (GVD) of an air-filled 20 μm radius fiber for different silica strut thicknesses. As the silica strut becomes thicker, the number of resonances increases and the dispersion is becoming more and more multiband. The white dots represent the zero dispersion wavelengths.*

1.4 Multiband FWM - Spectral correlation engineering

Since they modify the dispersion, the resonances play a crucial role in the phase-matching. This is illustrated in Fig.C1.15 showing examples of spectral density map. We recall that the spectral density map gives the wavelength of the generated photons as a function of the pump wavelength. We have superimposed the corresponding angle θ of the phase matching. For comparison purposes, we have plotted the simulation results with (right hand side) and without[16] (left hand side) taking into account the resonances in the dispersion. Two observations can be made:

- if the resonances are neglected, the SDM is composed of a unique branch denoted (S) whereas when the resonances are incorporated, several branches exist ((S'), (M1) and (M2)). The branches (S) and (S') are very similar, corresponding to a *singleband* FWM, where the pump and the parametric photons lie in the same band (see second row of Fig.C1.15). Thus, the most significant difference is the phase-matching branches (M1) and (M2) (λ_p in the range [650-750] and [950-1200] nm, respectively). These branches

---

[16] such simulation would also describes a fiber whose silica strut thickness is really thin, typically t <200 nm, where all the discontinuities are in the UV region or below

correspond to a *multiband* FWM; either the signal (M1) or the idler (M2) can be in a different band from the pump.

- one can observe that whenever pump, signal and idler are within the same band ((S) or (S')), the phase matching angle θ mainly varies from −30° to −60°, thus corresponding to correlated JSA whatever the pump wavelength[17]. In contrast, when considering the multiband FWM, it exhibits a much larger range of phase-matching angle, which vary from −90° to 90°. Therefore, in this multiband FWM, all three factorable states (i.e. θ = 0°, θ = 45°, θ = 90°) become theoretically accessible. In this example a multiband FWM described by (M1) favours a group velocity matching $\beta_{1p} = \beta_{1i}$ whereas (M2) favours $\beta_{1p} = \beta_{1s}$.
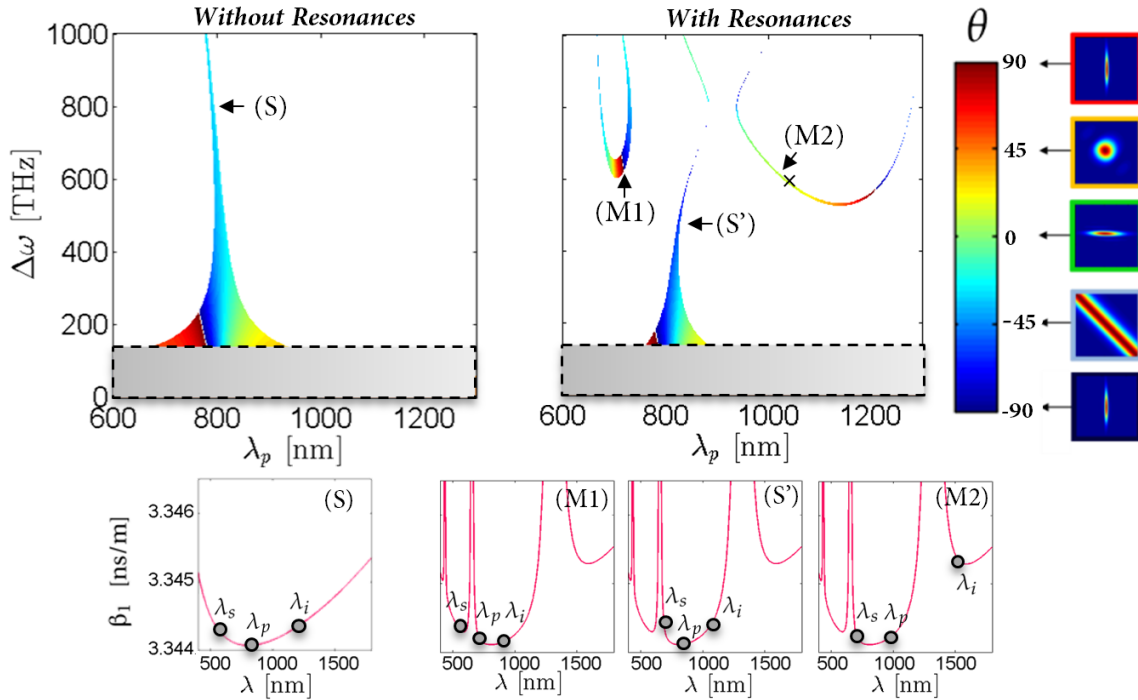

Fig. C1.15: *Top: Simulation comparing the FWM spectral density map with and without neglecting the effect of resonances in the dispersion. The parameters used are the one of the fiber experimentally used (R = 22 μm, t = 630 nm, and P = 3.5 bar of xenon). The y-axis corresponds to the gap between pump and signal/idler frequencies $\Delta\omega = |\omega_p - \omega_{s/i}|$. The color gives an additional information about the angle θ of the phase matching function. (S) and (S') correspond to a singleband FWM whereas (M1) and (M2) correspond to a multiband FWM. The black cross describes our experimental configuration (λ_p = 1030 nm). The grey region corresponds to FWM where signal and idler are generated close to the pump wavelength making their filtering quite difficult. Note that the lines have been thickened for improved visibility. Bottom: Corresponding group velocity relations.*

---

[17] there are some exceptions if the parametric photons are generated very close to the pump but in that case they are difficult to separate from the pump.

Consequently, the multiband dispersion profiles provide an unprecedentedly large control parameter-space in setting the FWM wavelengths (i.e. pump, signal and idler). **By positioning the three involved wavelengths either in the same band (singleband FWM) or in different bands (multiband FWM), one can control the group-velocity relation between them to generate various photon-pair states, from correlated to factorable.**

In the following, we use the analytical model to identify a fiber design that exhibits a multiband FWM and which is compatible with our experimental environment (laser, gas, fibers available).

1.5 Design of the gas-filled source

Among the numerous possibilities of fiber geometries, the design of the fiber has been chosen such that:

- CONDITION 1: **It allows a multiband FWM**

- CONDITION 2: **The idler photon is generated in the telecom band**

- CONDITION 3: **The source is Raman-free**

The experimental parameters span a four dimensional space defined by {R, t, gas choice, gas pressure}. In practice, temperature is also a parameter but since it has the same effect as pressure, it can be discarded. Thanks to the description of the model, we know that it is responsible for the resonance positions whereas the radius and the gas allow to manipulate the mean dispersion to which the phase matching is related.

a) Setting the resonances between pump and signal/idler

Our pump laser wavelength is infrared ($\lambda_p = 1030$ nm) and as we want the idler photon to be in the telecom range ($\lambda_i \sim 1550$ nm), hence, the signal is expected around $\lambda_s \sim 770$ nm due to energy conservation. Thus, in order to have a resonance in between the pump wavelength and one of the parametric photon, it is required to have either a resonance around ~ 1300 nm (in between pump and idler) or at ~ 900 nm (in between pump and signal).

As previously discussed, the position of the resonances of an IC fiber is given by $\lambda_m = \frac{2t}{m}\sqrt{1.45^2 - 1}$. By rearranging this equation, one can easily find which are the compatible silica strut thicknesses giving rise to a resonance at either 900 or 1300 nm. Figure C1.16 presents a non-exhaustive list of possible silica strut thickness parameters associated with a multiband profile with resonances at these wavelengths.
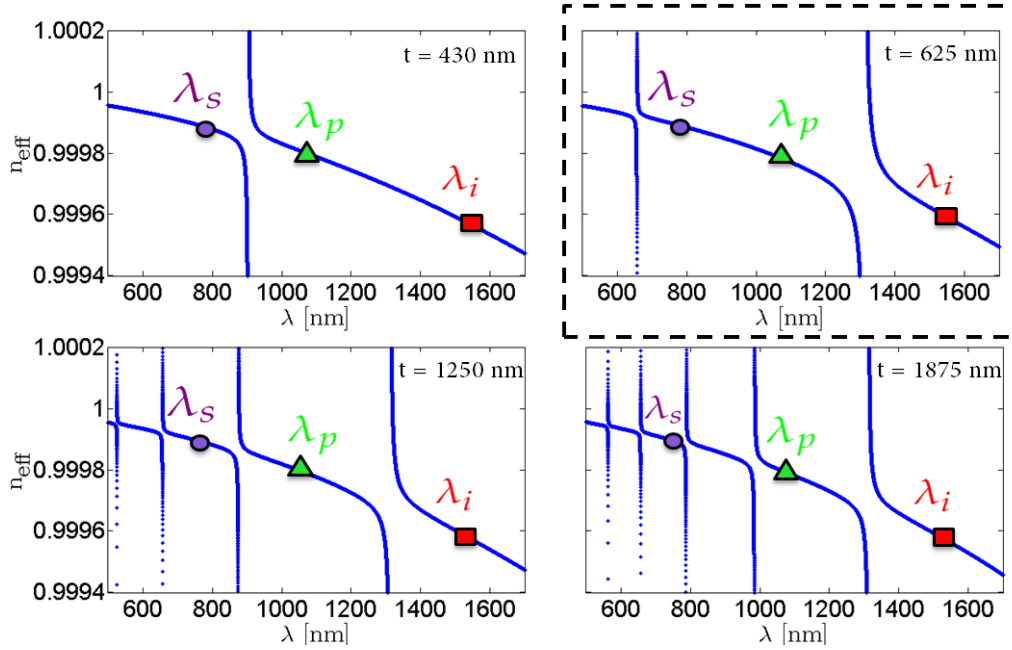
Fig. C1.16: *Different configurations exhibiting a resonance in between one parametric photon (either signal or idler) and the pump wavelength. The dashed rectangle designates the design chosen for the experiment. The other parameters used in the simulations which have no influence on the resonances are set to R = 20 µm, and $n_{gas} = 1$.*

b)   Noble gas for Raman-free generation

As far as the gas choice is concerned, in principle, many gases can be used. The only requirement is to apply the same strategy as we used in part B, consisting in avoiding a spectral overlap between Raman-scattering and FWM.

Nevertheless, working with noble gases (Fig. C1.17) makes the situation much simpler. Being mononatomic, they are completely devoid of Raman-scattering noise [24, 135] (see section B.3.1). Argon and xenon belong to this family and since they were already available in the laboratory facility, we naturally opted for these. Their respective refractive indices are (Sellmeier equation):

$$n_{\text{xenon}} = 1 + \frac{0.00322869}{46.301 - \lambda^{-2}} + \frac{0.00355393}{59.578 - \lambda^{-2}} + \frac{0.0606764}{112.74 - \lambda^{-2}} \tag{C1.16}$$

$$n_{\text{argon}} = 1 + \frac{2.50141 \times 10^{-3}}{91.012 - \lambda^{-2}} + \frac{5.00283 \times 10^{-4}}{87.892 - \lambda^{-2}} + \frac{5.22343 \times 10^{-2}}{214.02 - \lambda^{-2}} \tag{C1.17}$$

with λ in µm.

Fig. C1.17: *The different noble gases and their atomic number. The higher the atomic number, the higher the non-linearity. Note that radon is radioactive.*

c)   Phase matching condition

In addition to the multiband dispersion, the configuration must also fulfil the phase-matching condition between the involved wavelengths. The analytical model describing the dispersion is used to find the fiber configurations that satisfies $2\beta(\lambda_p) = \beta(\lambda_s) + \beta(\lambda_i)$ at these specific wavelength. As the parameter t is already constrained to a set of values (with a small tolerance) for positioning the resonances, we are left with two free parameters: radius[18] and gas pressure.

Figure C1.18 shows the results of simulations for different t values (associated with a multiband dispersion, see Fig. C1.16). Despite some exceptions[19] for any given core radius value, pressure can be found where a FWM involving the wavelength of interest is achieved. For instance, a fiber defined by (R = 40 μm; $t = 430$ nm) fulfils the required phase-matching when filled with either 3 bar of Xe or 16 bar of Ar. **For almost any fiber geometry (core radius R and t fixed), tuning the pressure to the right value enables a four-wave mixing.**

d)   Nonlinearity

Another main tendency that can be deduced from Fig. C1.18 is that the lower the radius, the higher the gas pressure required to achieve phase matching. We have seen previously (see Eq. (A2.3)) that the number of generated photon-pairs N_{pair} is proportional to the square of the nonlinear index of the gas n_2, and inversely proportional to the power fourth of the fiber radius.

$$N_{pair} \propto \left(\frac{n_2}{R^2}\right)^2 \tag{C1.18}$$

Moreover, a gas nonlinearity is linearly proportional [20] to its pressure such that:

$$N_{pair} \propto \left(\frac{P}{R^2}\right)^2 \tag{C1.19}$$

Therefore, the fact that lower radius requires stronger pressure for achieving the phase-matching has a strong beneficial effect to increase the nonlinearity. Although they are both

---

[18] in practice, there are some limitations in the fiber drawing process. For instance if one desires a thin silica strut thickness, then it is generally easier to aim a small radius than a large one.

[19] for instance (R < 12 μm; $t = 625$ nm) exhibits no phase-matching solution or alternatively (R = 20 μm; $t = 1875$) has non-unique solutions with a phase-matching at both 16 bar or 30 bar of xenon.

[20] except at very high pressure (> 50 bar) where the gas may enters a supercritical regime [135, 136]
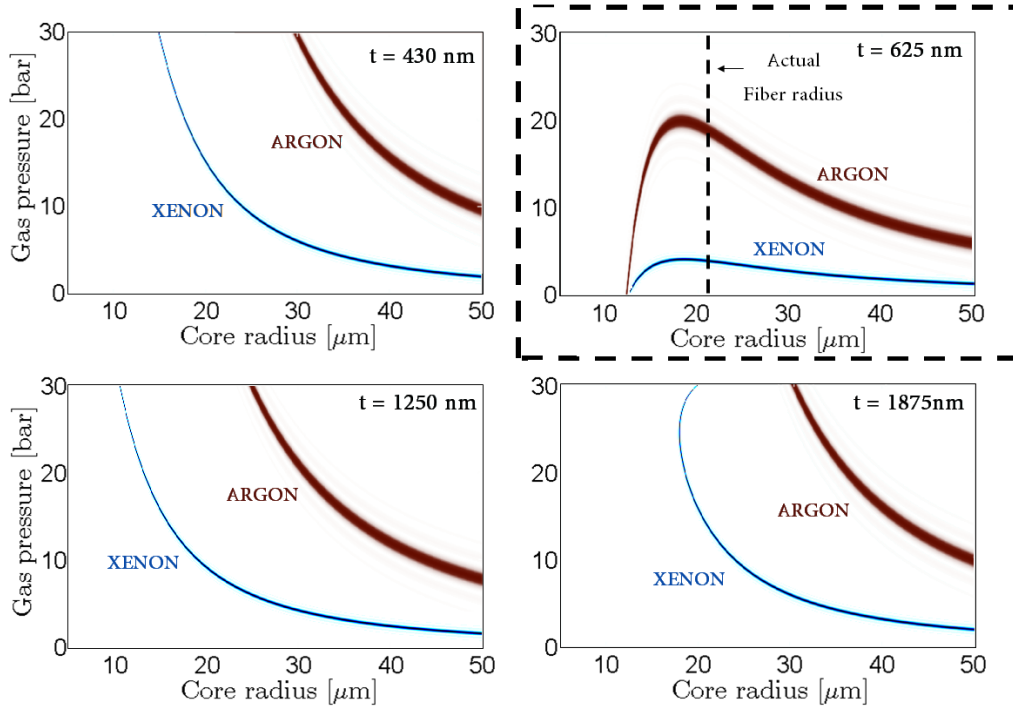
Fig. C1.18: *Combinations of radius and gas pressure (either xenon or argon) allowing to obtain a phase matching between the pump at 1030 nm, an idler photon at 1550 nm and a signal photon at ~ 770 nm. The simulations are done for a fixed parameter t given in the top right corner and temperature of 300 K. The dashed lines indicate the fiber design we will used in the following.*

solutions to our phase-matching requirements, a source with parameters (R = 15 μm; t = 430 nm; P = 30 bar of Xe) is expected to have 5000 times higher brightness[21] than one with (R = 40 μm; t = 430 nm; P = 3 bar of Xe).

For xenon and argon, the nonlinearity is $n_2 = 9.2\,10^{-23}$ and $0.8\,10^{-23}\,\mathrm{m}^2/\mathrm{W/bar}$, respectively.

e)   Propagation Loss

Propagation losses also increase with decreasing core radius (R^{-4} for IC-tubular and R^{-3} for IC-kagome fiber [134]) which forces a compromise between loss and brightness. With a radius around tens of micrometers, the losses are remarkably low ($\approx 10-100$ dB/km) at a central wavelength in a given transmission band but they increase rapidly as the wavelength approaches a band-edge. None of the involved wavelengths λ_p, λ_s, λ_i should therefore be too close to a discontinuity, which must be taken into account in the fiber design in order to enable efficient FWM.

---

[21] 100 times more due to the higher pressure, and 50 times more due to the smaller core
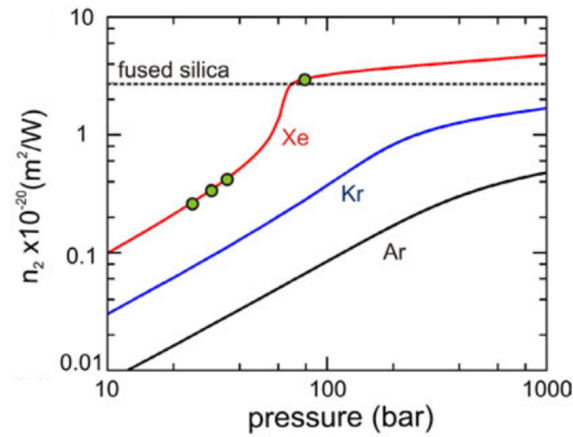
Fig. C1.19: *Dependence of the gas nonlinearity n_2 with pressure at 293 K for xenon, krypton and argon. The nonlinearity of fused silica is included for comparison. Above 58 bar, xenon becomes a supercritical fluid which explains the change of behavior. The plot is extracted from [136]*

The influences of the different parameters on the source properties are summarized in Table C1.3.

Tab. C1.3: Summary of the different parameter influence.

Silica strut thickness t	sets the resonance positions (Eq. C1.15)
Radius R	related to the mean dispersion (Eq. C1.12b) nonlinearity $N_{pair} \propto 1/R^4$ modal content (number of modes increases with R) losses $\propto 1/R^3$ (Kagome) or $1/R^4$ (Tubular)
Gas nature	related to the mean dispersion (Eq. C1.12b) absence of Raman-scattering in noble gas
Gas pressure P	active parameters for achieving phase-matching nonlinearity $N_{pair} \propto P^2$

1.6 Chosen design

For the experimental implementation an IC tubular composed of 8 tubes, with strut thickness $t = 625 \pm 20$ nm, has been chosen. The inner core fiber radius of 22 ± 1 μm offers a good trade-off between loss and generation efficiency. A cross-section of the fiber is shown in Fig. C1.20.a.

Its main optical properties are described in Fig. C1.20.b-f. The low transmission around 650 nm and 1300 nm confirms the expected positions of the resonances. As a result, signal and pump are indeed in a different band from the idler. According to the simulation given below (Fig. C1.20.e), the phase-matching between the infrared pump and an idler photon in the telecom is achieved when filled with either ~ 4 bar Xe or ~ 18 bar of Ar. The associated inverse-group velocities (β_1) at 4 bar of Xe is computed in Fig. C1.20.d. This multiband FWM is fulfilling $\beta_{1,s} < \beta_{1,p} < \beta_{1,i}$ which is the first requirement to obtain a factorable state[22].
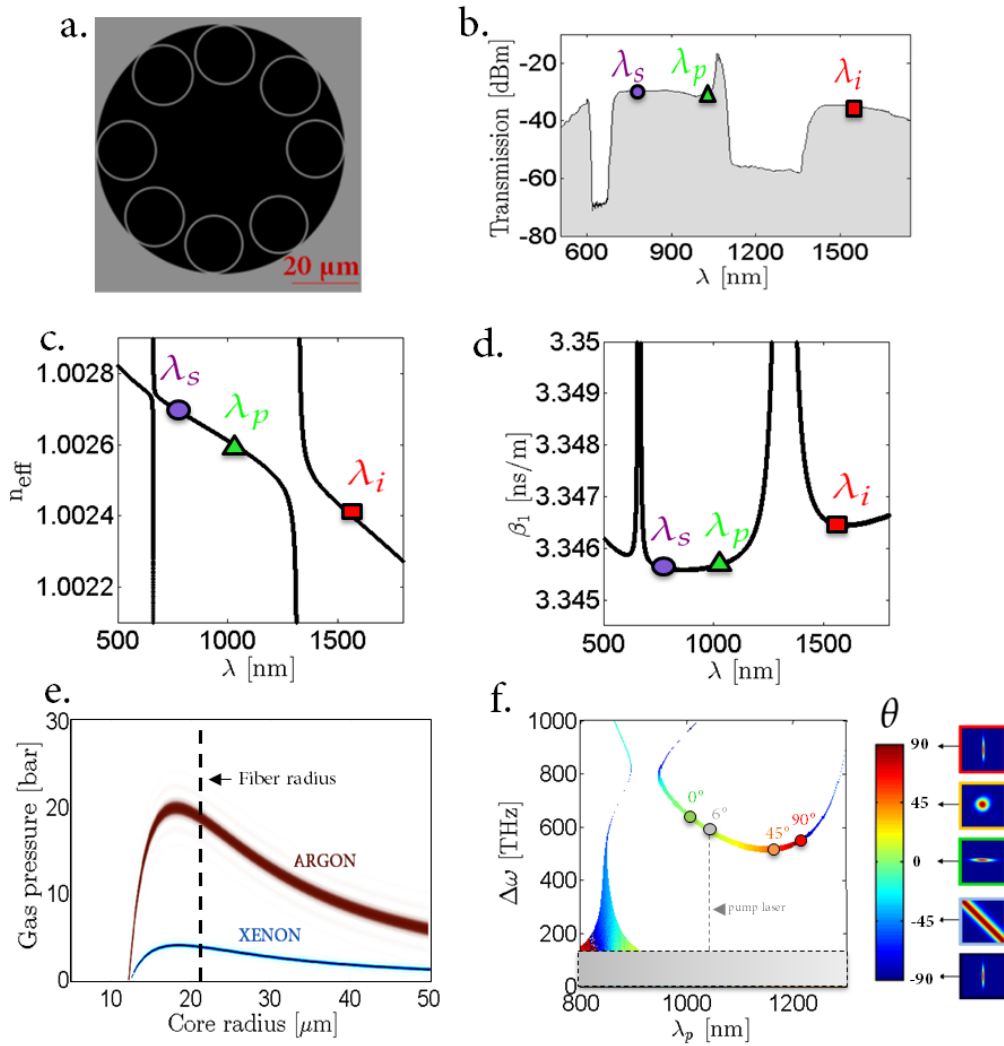
Fig. C1.20: *a. Fiber cross section. b. Recorded transmission with a supercontinuum source clearly showing the multiband behavior. Note that the peak at 1050 nm is a measurement artefact due to the supercontinuum pump. c. Simulated effective refractive index, d. inverse group velocity when filled with 4 bar of Xe at 300 K, e. Phase-matching condition as a function of pressure (silica strut thickness of t = 625 nm) and f. Computed SDM*

---

[22] as described in Section C.2.3 the second requirement is a condition that link the fiber length to the spectral width of the laser

Conclusion

This chapter described the guidance mechanism of inhibited coupling fiber and an analytical model that links the fiber parameters to its dispersion. It is noteworthy that this very simple model involves only three design parameters, namely fiber core diameter, strut thickness and gas refractive index without adjustable parameter whatsoever. A detailed description of the influence of each of these parameters on the four-wave mixing properties has been given.

The model allows to predict that gas-filled hollow-core fibers provides a versatile platform for FWM generation of photon-pair states. In particular, we show how the intrinsic multiband dispersion of IC fibers can be exploited to access multiband FWM and, therefore, to tailor the photon-pair spectral correlations.

We have designed a fibered photon-pair source compatible with our pump laser at 1030 nm with the further advantage of (i) allowing the generation of spectrally factorable state (ii) being Raman-free and (iii) generating the idler wavelength at telecom wavelength and the signal in the range of atomic transitions and Silicon single photon detectors. The next step is the experimental confirmation of these promising predictions and the next chapter describes the Joint Spectral Intensity tomography characterization that we have implemented.

Table C1.4 summarizes the different fiber parameters.

Tab. C1.4: Summary of the parameters of the designed GF-HCPCF

Inhibited-coupling fiber filled with 3.5 bar of xenon	
Length	$L_{\text{fiber}} = 1$ m
Fiber radius	$R \sim 22\,\mu m$
Mean Field Diameter	$MFD \sim 34.5\,\mu m$
Gas linear refractive index	$n_{\text{gas}} - 1 = 6.9 10^{-4}$
Zero Dispersion Wavelengths	$\lambda_{\text{ZDW}} \approx [1588, 741, 480, ...]$ nm (@0 bar) $\lambda_{\text{ZDW}} \approx [1592, 830, 600, ...]$ nm (@3.5 bar)
Mean Dispersion (when filled)	$\beta(\omega) = \sum_{k=0}^{6} p_k \omega^k$ $p_0 = -4.7253552831760 \times 10^3$ m^{-1} $p_1 = 3.348057042450029 \times 10^{-9}$ m^{-1}.(rad.s^{-1})$^{-1}$ $p_2 = -2.800594014367931 \times 10^{-27}$ m^{-1}.(rad.s^{-1})$^{-2}$ $p_3 = 9.071092214869253 \times 10^{-43}$ m^{-1}.(rad.s^{-1})$^{-3}$ $p_4 = -1.591068992461979 \times 10^{-58}$ m^{-1}.(rad.s^{-1})$^{-4}$ $p_5 = 1.523372019192271 \times 10^{-74}$ m^{-1}.(rad.s^{-1})$^{-5}$ $p_6 = -5.889602718617450 \times 10^{-91}$ m^{-1}.(rad.s^{-1})$^{-6}$
Resonances	[1312 nm, 660, 440, ...]
Non linearity	$n_2 = 3.2 10^{-22}$ m^2/W (@3.5 bar)

Chapter C2

Joint Spectral Intensity tomography

This chapter is dedicated to the measurement of the joint spectral intensity. We first introduce the *stimulated emission tomography* technique which allows a fast and highly resolved measurement of the JSI. Then, we use this technique to measure the JSI of the gas-filled IC-HCPCF. More specifically, we study how the JSI can be manipulated by varying parameters related to the medium, such as the gas pressure or the fiber length. Finally, we detail how the JSI can be also tailored by modifying the pump beam spectral properties (central wavelength, FWHM, chirp) thanks to a pulse-shaper.

2.1 JSA characterization techniques

There are many different approaches[1] to measure the joint spectral properties of photon pairs [137]. The most direct measurement would be to record signal and idler frequencies over a large number of successive events in order to infer the probability distribution, it is difficult in practice as single photon detectors do not resolve frequency. Historically, one of the first technique is the spectrally resolved coincidence counting [39, 138] which uses monochromators before the signal and idler SPDs. The monochromator consists of a grating followed by a slit whose position determines the selected frequency window. In this configuration, the number of coincidences recorded on the SPDs gives one pixel of the two dimensional JSI. To reconstruct

---

[1] See [137] for a description and comparison of the different techniques (spectrally coincidence counting, single-photon spectrograph, diagonal Fourier transform, etc).

the entire JSI, one has to repeat the measurements with all possible combinations of ω_s, ω_i by moving one slit while keeping the other fixed and vice versa. However, this technique is quite unpractical since the rate at which coincidences are observed is very low, even for bright sources [137].

Among all the existing techniques for characterizing the spectral correlations, one of the most efficient and with the highest resolution is the Stimulated Emission Tomography (SET) [139, 140]. It relies on an equivalence between the phase-matching of the spontaneous process and its corresponding stimulated process (Fig. C2.1). Typically the resolution can reach 100 x 100 pm (signal x idler) [139, 140] with acquisition time of only a few minutes.
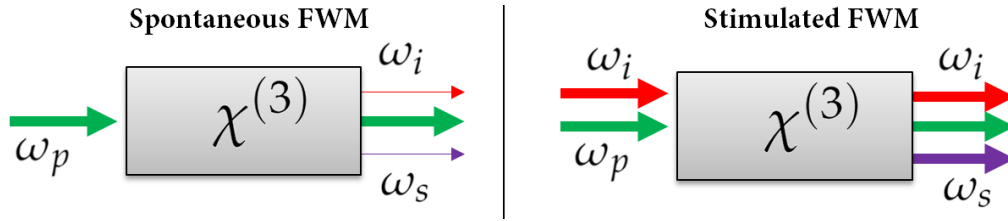

Fig. C2.1: *Comparison between Spontaneous and stimulated four-wave mixing processes. In the spontaneous regime, only the pump field is injected and generates signal and idler photons from vacuum fluctuations. In the stimulated regime, a second field at signal or idler wavelength is injected along with the pump. The thickness of the arrows are relative to the intensities.*

The underlying assumption is that the JSI in the stimulated regime is an amplified version[2] of the JSI in the spontaneous regime (see Eq.C2.1). The amplification factor is approxilmately equal to the average photon number N_{seed} of the coherent seed [139]:

$$JSI_{stim} \approx N_{seed} \times JSI_{spont} \qquad (C2.1)$$

Thus, working in the stimulated regime provides an increased signal-to-noise ratio by several orders of magnitude. Thus, the main advantage is that SET allows replacing the single photon detectors with fast and spectrally resolved classical detectors (spectrometer, optical spectrum analyser) provided an additional laser is used at signal or idler wavelength to seed the process. Nevertheless, to guarantee the equivalence between spontaneous and stimulated JSI, one has to make sure that the variation of the stimulated generated signal power remains linear with seed power [137, 140, 141] (i.e small parametric gain regime).

More precisely, SET tomography requires a seed laser which is tunable and whose spectrum is much narrower than the pump. It can be equally used either to stimulate signal or idler photon. When the seed is at idler (signal) frequency, each recorded spectrum gives one horizontal

---

[2] more precisely, one has also to consider the modal content. Indeed only the mode (e.g. polarisation, spatial mode) of the seed is amplified.

(vertical) slice of the JSI. By tuning the seed, different slices can be recorded in order to do a full tomography of the state (see Fig. C2.2).
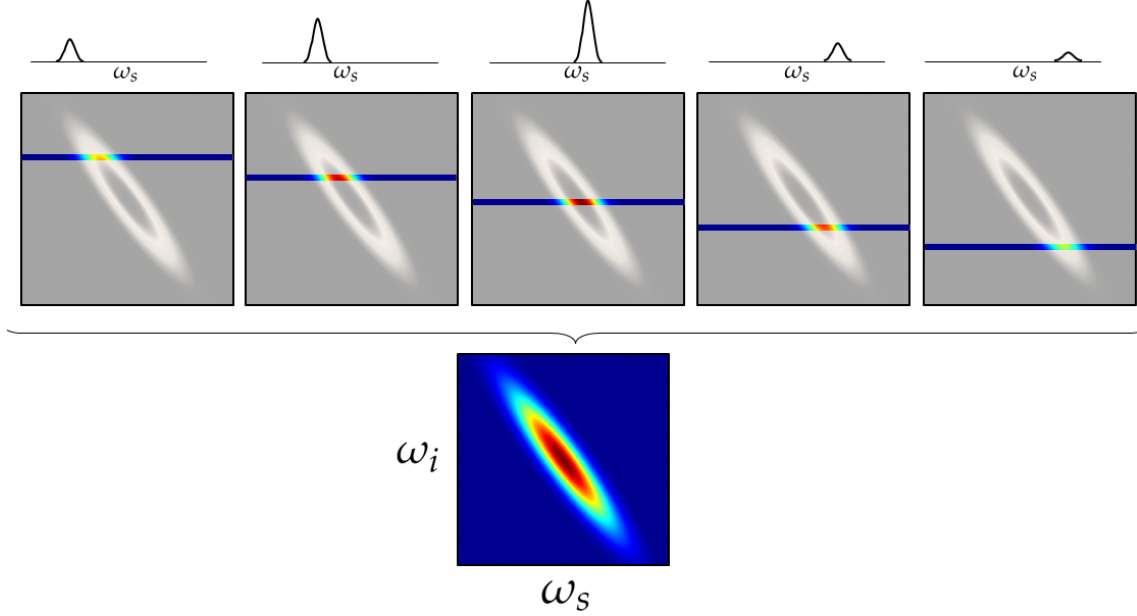

Fig. C2.2: *Principle of the JSI reconstruction with SET. For each value of seed frequency the corresponding spectrum of the signal is recorded. These spectra correspond to an horizontal slice of the JSI. Adding all the slices numerically allows to reconstruct the JSI. Note that the different slices must be normalized by the seed power coupled in the fiber.*

Standard SET, as most tomography techniques, measures only the joint spectral intensity without accessing the phase. The ability to measure the joint spectral phase may be useful as signal and idler can exhibit entanglement in their phase, especially in the case of complex temporally elongated pump pulse. In this context, SET can be extended to also measure the joint spectral phase, as demonstrated in [142]. Nevertheless, if the pump pulse is Fourier transform-limited, it is generally accepted that measuring the intensity is enough [137].

2.2   Experimental tomography setup

Our SET experimental characterization setup is shown in Figure C2.3. Both pump and seed lasers are fibered. We use an Ytterbium pulsed pump laser (Satsuma, Amplitude Systems) at λ_p = 1030 nm with 280 fs pulse duration at 2 MHz pulse repetition rate and the average pump power injected in the HCPCF is 60 mW. The seed laser used to stimulate the FWM is a continuous-wave Erbium laser tunable from λ_i = 1530 nm to 1560 nm (T100, Yenista). The seed power injected in the IC-HC-fiber is around[3] 100 mW, which corresponds to a power of 50

---

[3] in later experiment, the configuration is P_{pump} = 260 mW and P_{seed} = 10 mW

nW effectively involved in the FWM process[4] because of the duty cycle of the pump. Both laser polarizations can be controlled independently with two halfwave plates (HWP).

The fiber ends are inserted into gas-cells (see inset) with a pressure monitoring and glass windows for optical power injection. Injected into one of the cells, the gas fills the fiber core and an equilibrium between the two gas cells is obtained within less than an hour. At the fiber output, the generated signal at $\omega_s = 2\omega_p - \omega_i$ is filtered with dichroic mirrors (DM) and sent to a spectrometer (SILVER-Nova StellarNet). The seed power is monitored so that any power change when tuning ω_i can be captured and to normalize the data of the various slices.

Note that the spectrometer is preliminary aligned thanks to the generation of a supercontinuum. In fact, the repetition rate of the pump laser is lowered to 200 kHz and the average power is set to ~ 1 W in order to obtain ~ μJ pulses. With such energy and the high nonlinearity of xenon, the pulses generate a supercontinuum within the gas-filled fiber covering all the spectrum from the infrared to the UV. At the fiber output, a first dichroic mirror DM2 extracts the wavelength range 690-810 nm from the supercontinuum which can be used to align the different optical elements before the spectrometer. There are two additional DM2, not shown in Fig.C2.3 and a lens to couple to the spectrometer in free space.
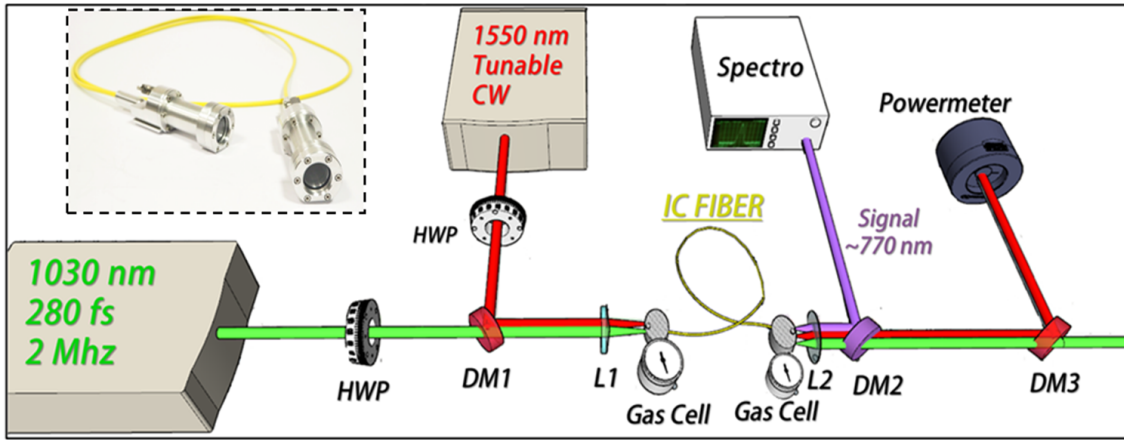
Fig. C2.3: *Experimental setup for the stimulated emission tomography. Pump, signal and idler are represented in green, violet and red, respectively. The inset shows a photo of the gas cells and fiber.*

By progressively increasing the pressure, one can find the pressure value that allows pump and seed to interact in a stimulated FWM. With the seed at 1550 nm, the phase-matching is achieved with 3.4 bar of xenon. At such pressure, a strong signal around 770 nm is recorded on the spectrometer (see Fig. C2.4.a).

Moreover, in order to make sure that our measurements would be valid in the spontaneous

---

[4] which means ~ 10^5 photons per pump pulses which is much smaller than the typical $\approx 10^9$ photos/pulse of the pump.

regime, the power dependence of the power generated at signal frequency has been measured as a function of pump power and seed power. Figure C2.4 shows the results confirming the linear dependence versus seed power and quadratic dependence versus pump power, thus validating that our experimental results are transferable to the spontaneous regime [137, 140, 141].
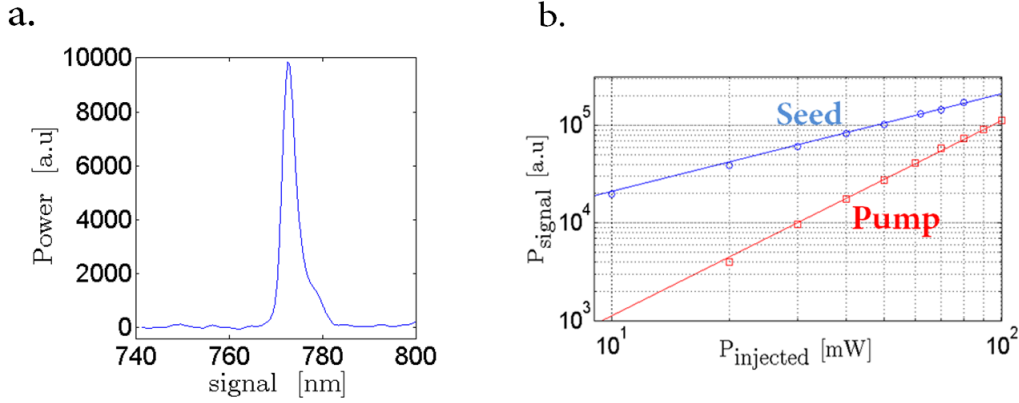

Fig. C2.4: *a. Recorded signal spectrum while the fiber is filled with 3.4 bar of Xe and with the seed laser at 1545 nm. b. Power generated at the signal frequency as a function of the seed power (blue dots) and of the pump power (red squares) at the fiber output obtained by integrating the spectrum measured with the spectrometer. The solid lines correspond to a perfect linear and quadratic dependence (log scale).*

Once the FWM is obtained by setting the right pressure inside the fiber, one can sweep the seed laser frequency to record different spectra (slices of the JSI) in order to reconstruct the full JSI of the source.

In the following, we reconstruct the JSI of the gas-filled fiber for different experimental parameters. We remind that the JSA is the combination between, on the one hand the energy conservation function (associated to the pump), and on the other hand the phase matching function (associated to the medium). We focus first on parameters associated to the phase-matching function (fiber length, gas pressure) as described in the next section.

2.3 Experimental JSI (Phase Matching Engineering)

a) Length variation

Let us begin by performing the tomography for different fiber lengths. The measurement is performed for a length of one meter and then repeated for shorter and shorter sections of the same fiber. Figure C2.5 shows a comparison between experimental and simulated JSI as well as the associated Schmidt number for fiber lengths going from 40 to 100 cm for the fiber filled with 3.4 bar of xenon. With 1 meter, the phase matching function (red dashed lines) and the energy conservation function (blue dashed lines) have about the same width, resulting in an almost

round JSA. As the fiber becomes shorter, the width of the phase matching function broadens ($\Delta\phi \propto \frac{1}{L}$, see section B.2.1) such that the JSI stretches along the anti-diagonal. Intuitively, as the fiber length decreases, the momentum conservation is more and more relaxed such that the FWM becomes more and more constrained through energy conservation, which bears the correlations. **By simply reducing the fiber length, the bi-photon JSI changes from the shape of a nearly separable states into that of a correlated state.** This can be seen on the associated Schmidt decomposition: as the length reduces, the Schmidt number increases. In the current setup, the minimum fiber length is limited to around 30 cm, mostly due to the size of the two gas cells.

The lobe-shaped region in the top right corner of the JSI profile is attributed to the non perfect Gaussian spectral shape of the pump laser pulses. Such shape may be due to residual self-phase modulation taking place within the pump laser[5] and could be removed using appropriate filters prior to the HCPCF or pulse shaping techniques. The parameters used in the simulation are $t = 630$ nm, $R_{eff} = 22$ μm and P = 3.4 bar. The Sellmeier equations of xenon is given in Eq. C1.17.

b) Pressure Variation

The effect of pressure variation on the phase-matching function (and thus of the JSA) is twofold:

Firstly, as pressure increases, the signal and idler fulfilling the phase matching condition are further and further apart from the pump central frequency. Using the same fiber, this effect is demonstrated by characterizing the JSI of the source as a function of gas pressure, for two different gases, argon and xenon. For instance, we measure that changing the xenon pressure from 3.00 bar to 3.65 bar shifts the idler wavelength from 1531 to 1551 nm and the signal wavelength from 776 to 771 nm. Similarly, the same effect is observable with argon when the pressure is modified from 14 to 17 bar. The experimental results are described in Fig. C2.6. As the pressure increases, the JSI moves along the anti-diagonal which means that signal wavelength is blue-shifted and idler wavelength is red-shifted. A linearization of the measured data gives a sensitivity of $\Delta\omega = 27.4$ Thz/bar in Xe and 5.6 Thz/bar in Ar, which is two orders of magnitude higher than the sensitivity reported in a recent work on temperature tuning in solid core fibers (0.1 Thz/°C) [143]. Moreover, the gas can be chosen depending on the desired sensitivity. For instance, xenon is a good option for high sensitivity whereas neon is more suitable for low sensitivity. Figure C2.7.a shows a comparison between the effect of xenon, argon and neon filling in this HCPCF.

---

[5] a modulation is observed in the laser datasheet. Note that this defect will disappear later on after a change of laser.
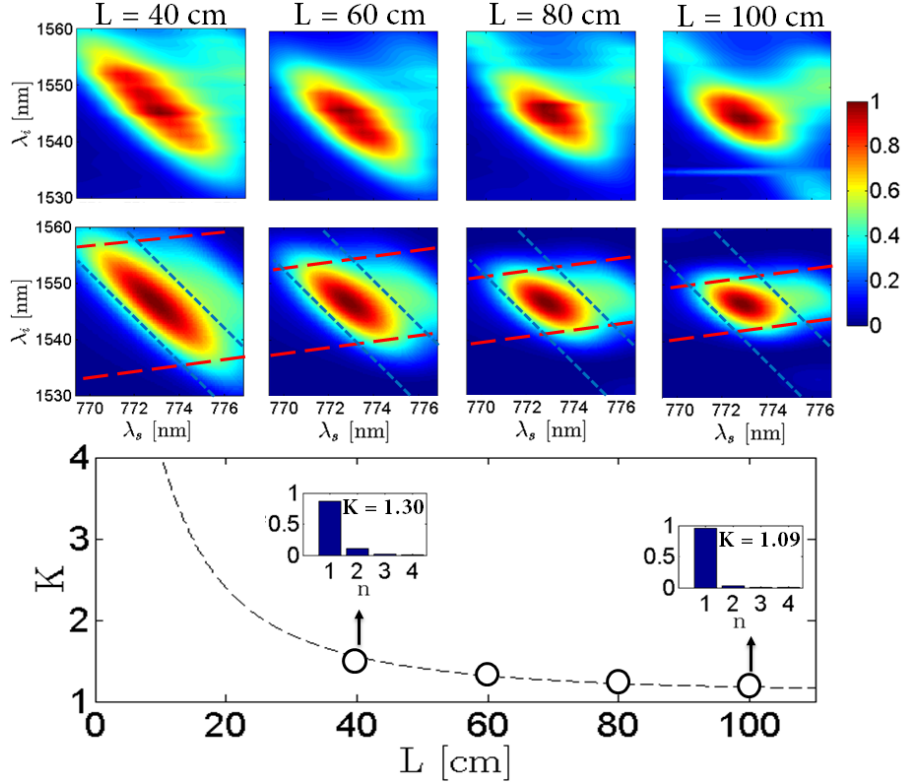
Fig. C2.5: *Top, comparison between experimental (1st row) and simulated (2nd row) JSI for different fiber lengths when filled with 3.4 bar of Xe. The red dashed lines delimit the phase-matching function φ whereas the narrow blue ones delimit the energy conservation function. The simulation takes into account a modulation in the Gaussian shape of the pump laser spectrum to reproduces the residual side lobe. Bottom, corresponding Schmidt number and Schmidt decomposition (assuming no phase correlations).*

Secondly, the simulation also predicts that changing the pressure slightly rotates the angle θ of the phase matching. In our experimental configuration (λ_p = 1030 nm and P = 3.4 bar), the phase matching angle is expected to rotate by around ~ 6° per bar of xenon. However, our measurement range is still too restricted to observe such an effect, due to the limited seed laser wavelength tunability.

Both effects of the rotation of phase-matching angle θ and the shift of the JSI occur simultaneously. Adjusting θ can be used, for instance, to fine-tune the purity of a heralded single photon source. Alternatively, the signal/idler wavelength tuning is useful for instance to aim at a specific telecom channel or atomic transition. Nevertheless, if one wants to tune the wavelength of one photon while keeping the angle constant or vice-versa, it is possible to decouple the two effects by changing the pump wavelength. Figure C2.7.b presents an example of the large range of angles θ that can be obtained while generating an idler photon at 1550 nm.
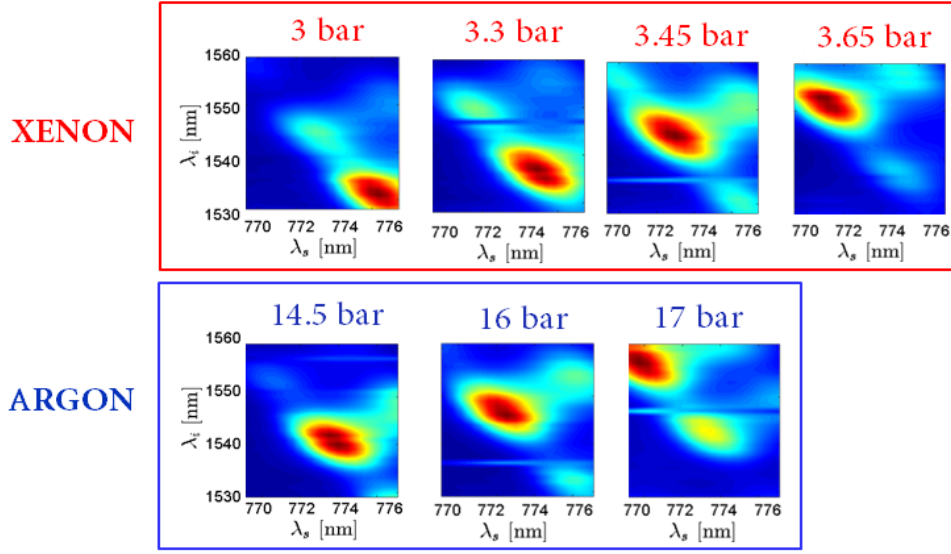
130

Fig. C2.6: *JSI as a function of gas pressure when filled with xenon and argon. Changing the pressure allows to shift the JSA along the anti-diagonal. The fiber length is 1 meter.*
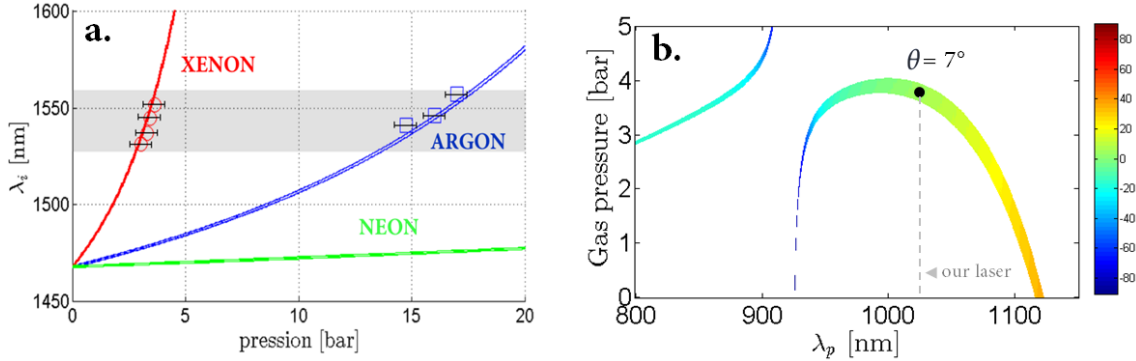
Fig. C2.7: *a. Central position of the JSI idler wavelength as a function of gas pressure, for xenon (red circles) and argon (blue squares) and comparison with the simulation. The measurement range shaded in gray was limited by the tunability of the seed laser. b. Possible configurations of gas pressure and pump laser leading to the generation of an idler photon at 1550 nm. The numerous possibilities exhibit different phase matching angles θ described by the color index. Note that the lines have been thickened for improved visibility.*

As we have seen that for our given HCPCF, the sensitivities of the shift of the JSA depend on the choice of gas. Nevertheless, it is noteworthy that it also depends on the fiber geometry. As discussed earlier (see section C.1.3) the dispersion results from two contributions, the gas dispersion on the one side, which is pressure- and temperature-dependent, and the guide dispersion on the other side. Thus, depending on the weight of one relative to the other, the mean dispersion is more or less sensitive to a change of gas refractive index. For instance, fibers with large core have a lower waveguide dispersion. Consequently they will be more sensitive to a

change of gas refractive index, caused by a pressure modification. Alternatively, smaller core or fiber filled with light atomic weight gases, will be less sensitive to a change of gas refractive index as the waveguide dispersion will be predominant. This is an example of the numerous possibilities offered by gas-filled HCPCF.

As a result, we have seen how the JSA could be engineered through the phase-matching function ϕ. We want to show in the next section that it can also be tailored by modifying the energy conservation function $\alpha(\omega_s, \omega_i)$. This can be accomplished with pulse-shaping techniques which are well established in the field of ultrafast optics [144]. They allow to tailor both temporal and spectral shape of our pump pulses. Let us first introduce the pulse-shaper devices.

2.4 Pulse shaping

a) Definition

A short pulse is most often represented by its spectral amplitude A(ω) and phase φ(ω) such that: $E(\omega) = A(\omega)e^{i\varphi(\omega)}$. A pulse shaper is a device allowing to modify these features.

$$E_{in}(t) \quad \boxed{\begin{array}{c} \text{Pulse} \\ \text{Shaper} \\ M(\omega) \end{array}} \quad E_{out}(t) = M(t) * E_{in}(t)$$

$$E_{in}(\omega) \qquad\qquad E_{out}(\omega) = M(\omega) \times E_{in}(\omega)$$
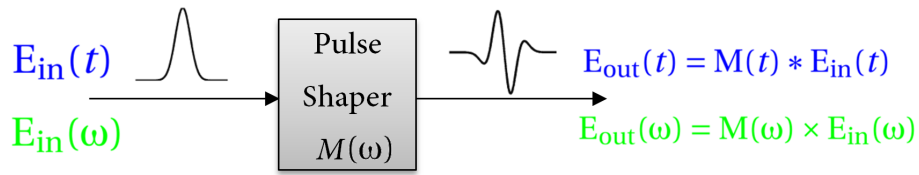
Fig. C2.8: *Principle of pulse shaper techniques allowing to modify the temporal and spectral profile to an arbitrary shape.*

The two most common technologies of arbitrary pulse shaping are[6]:

- the **'4f-line'** which most often consists of a spatial light modulator (SLM) inserted into the Fourier plane. It is achieved by a first grating spatially diffracting the different spectral components of the pulse which are then focused with a lens on different pixels of a SLM. Being spatially separated on the SLM, each frequency can be addressed individually with an arbitrary phase or optical density in order to shape the pulse. Finally, after the SLM, a second combination of lens and grating allows the recombination of the frequencies into a single collimated beam (see Fig. C2.9.a) .

- the **AOPDF** : acousto-optic programmable dispersive filter (also called Dazzler). It relies on a longitudinal interaction between the optical pulse and an acoustic wave propagating in a birefringent crystal [145, 146]. The optical pulse is initially propagating along the

---

[6] for a complete review see [144]

fast polarisation ordinary axis of the crystal. The pump is diffracted onto the slow axis of the crystal whenever the optical frequency ω fulfills a phase-matching of the form: $\vec{k}_{\text{slow}}(\omega) = \vec{k}_{\text{ac}}(\omega_{\text{ac}}) + \vec{k}_{\text{fast}}(\omega)$ where 'ac' denotes the acoustic wave and 'slow' and 'fast' denote the wavevector along the fast and slow axis of the crystal [144]. In practice acoustic wave is polychromatic with a frequency that is varying along the crystal. In this configuration, each spectral component of the pump is switched to the slow axis at different positions in the crystal. As the group velocities of the fast and slow axis are different, one gets a different arrival time at the output of the crystal for each wavelengths (see Fig. C2.9.b). Thus, by controlling the acoustic wave spectral content, one can modify the phase relations between the different optical wavelength constituents of the diffracted beam. Moreover, the amplitude of the wavelength constituents can be also adjusted by controlling the acoustic wave intensity and therefore the diffraction efficiency. With a control of its amplitude and its phase, the diffracted beam can be shaped to any arbitrary form.

Both systems have their advantages depending on the targetted applications. AOPDF may exhibit a lower attenuation and a higher damage threshold and '4f-line' has a better resolution. The main differences between the two systems are the temporal synchronization and the mask setting time.

AOPDF requires to temporally synchronize the optical and acoustic pulses so that they interact at the same position within the crystal from pulse to pulse. Since the generation of acoustic wave is of the order of the kHz (up to[7] 100 kHz), this constraints on the pump pulses repetition rate. In fact, in the regime where the pump repetition rate is fast (~ MHz) compared to the repetition rate of the acoustic wave, AOPDF can possibly be used without synchronisation with a limited impact on the pulse to pulse reproducibility.

An advantage of '4f-line' is that, once oriented, the liquid crystals mask in the SLM do not need to be changed [144]. Thus, for a given mask, since there is no need for synchronisation, the pump repetition rate is not limited. Yet, a limitation arises when one wants to change the mask from pulse to pulse. Since SLM have a really slow response time (~ 60 Hz), the repetition rate would be highly limited .

In the end, when choosing between one pulse shaper device or another, one has to consider, in addition to the global performances (see for instance Table C2.1), the repetition rate of the laser and whether the mask has to be changed from pulse to pulse.

---

[7] fastest commercial product from Fastlite

Tab. C2.1: Comparison between a commercial '4f-line' (Finisar) and AOPDF (FastLite) pulse shapers.

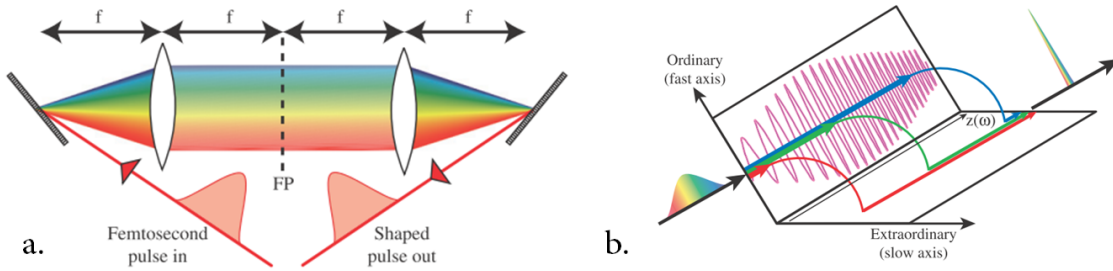|	'4f-line'	AOPDF
Resolution	0.1 nm	0.5 nm
Maximum Attenuation	25 dB	45 dB
Damage threshold	500 mW	4 W
Setting time	<500 ms	3 ms
Repetition rate	N.A (stationary)	kHz

Fig. C2.9: *Principle of **a.** the '4f-line' and **b.** the acousto-optic programmable dispersive filer (AOPDF). FP designates the Fourier plane, where the SLM is inserted. Sketchs from [144].*

b) Adapt in the experimental setup

In order to shape the pump spectral properties, an AOPDF (HR-1030, FastLite) is added at the pump laser output[8]. In our case, we have decided to work with AOPDF since it was already available in our laboratory facility. The new setup is shown in Figure C2.10. Prior the AOPDF, a half wave plate aligns the pump polarization with the fast axis of the crystal. The acoustic wave inside the crystal is created by a RF-generator. The shape of the acoustic wave is computer driven, allowing both the amplitude and phase of the pump spectrum to be controlled. Moreover, a few minor changes have been implemented in the setup[9].

An example of measured spectrum (raw data) recorded in this new configuration is shown in Fig C2.11. With a couple of dichroic mirrors (DM2, DM3), the pump is eliminated below the noise level of the spectrometer.

---

[8] note that aligning the AOPDF is quite straightforward and can be realized with minor modification of the setup in only a few hours.

[9] for practical reasons, the pump laser is changed to the same model with 250 fs pulses instead of 280 fs previously and the spectrometer to a HR4000-Ocean Optics (instead of the StellarNet).
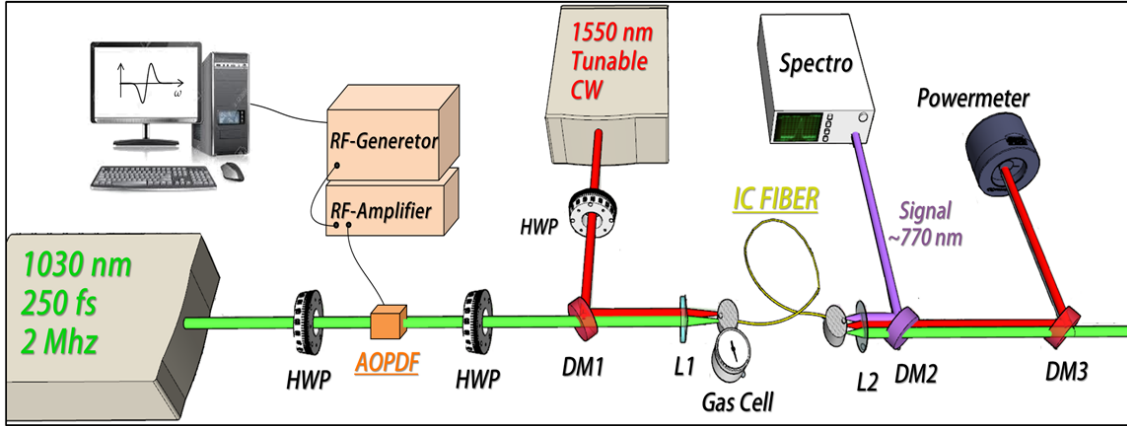
Fig. C2.10: *New experimental setup allowing to control the pump temporal and spectral properties.*
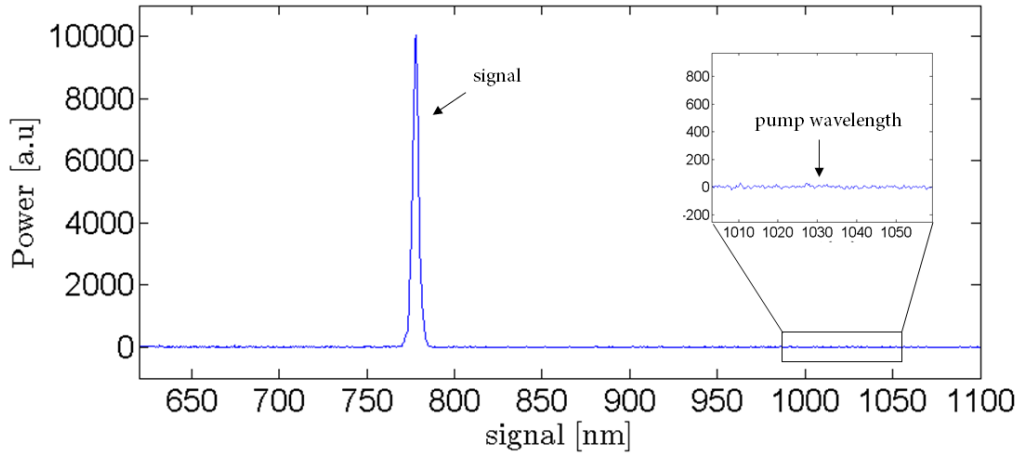
Fig. C2.11: *Example of raw data recorded by the spectrometer. The seed is not present since the spectrometer is insensitive to telecom wavelengths. Here the pump power is set to* P_{pump} *= 650 mW and the seed to* P_{seed} *= 10 mW*

2.5   Experimental JSI (Pump spectrum Engineering)

Let assume than the pump is described by a Gaussian, then, the pump spectrum is described by three features, (i) the central frequency, (ii) the spectral amplitude and (iii) the spectral phase:

$$E_L(\omega) = E_0 \, e^{\frac{-(\omega - \omega_L)^2}{2\sigma_L^2}} \, e^{i\varphi_L(\omega)} \tag{C2.2}$$

Thanks to the pulse shaper, the laser central frequency ω_L, the spectral width σ_p and the

phase can all be mapped to a new value.

Laser pulse $E_L \rightarrow$ **Shaped pulse** E_p

$$\sigma_L \rightarrow \sigma \qquad (\text{with } \sigma < \sigma_L)$$

$$\omega_L \rightarrow \omega_p$$

$$\varphi_L(\omega) \rightarrow \varphi(\omega)$$

We remind that the energy conservation function is the convolution of the pump with itself. For a Gaussian of width σ and mean μ, the autocorrelation remains a Gaussian whose width is $\sigma_{E*E} = \sqrt{2}\sigma$ and mean $\mu_{E*E} = 2\mu$. Therefore, considering a transform limited pump of the form $E_p(\omega) = E_0 e^{-(\omega - \omega_p)^2/2\sigma^2}$, the energy conservation function is given by:

$$\alpha_{\mathbf{FT}}(\omega_s, \omega_i) = [E_p * E_p](\omega_s + \omega_i) \qquad \text{(C2.3a)}$$

$$= \int d\omega \, E_p(\omega) E_p(\omega_s + \omega_i - \omega) \qquad \text{(C2.3b)}$$

$$= \sqrt{\pi}\sigma E_0^2 \, e^{-\frac{(\omega_s + \omega_i - 2\omega_p)^2}{4\sigma^2}} \qquad \text{(C2.3c)}$$

With the AOPDF programmed to shape a Gaussian, we performed JSI tomographies for different bandwidths σ, different central frequencies ω_p and different phases.

a) Pump width variation

We have seen previously that the amount of spectral entanglement is related to the ratio between the energy conservation width $\Delta\alpha$ and the phase matching width $\Delta\Phi$ (see section A.2.1). In this context, we have already experimentally demonstrated how $\Delta\Phi$ can be varied with the fiber length in order to change the shape of the JSI from separable to correlated (Fig C2.5). Alternatively, one can also control the energy conservation width $\Delta\alpha = \sqrt{2}\sigma$ with the pulse shaper for that same purpose.

Since the new spectral shape $E_p(\omega)$ is extracted from spectrum $E_L(\omega)$, the shaped width can only be equal or smaller than the one of the laser ($\sigma \leq \sigma_L$) as illustrated in Figure C2.12. Several JSI tomographies are performed for increasing values of σ. The experimental JSI are shown in the first row of Fig. C2.13. All other parameters (fiber length, pressure, central frequency) are kept constant. The second row shows the corresponding simulated JSI, where the energy conservation and phase matching are superimposed in red and blue dashed lines, respectively.

For $\sigma = 1.7$ nm, the energy conservation width is narrower than the phase matching width
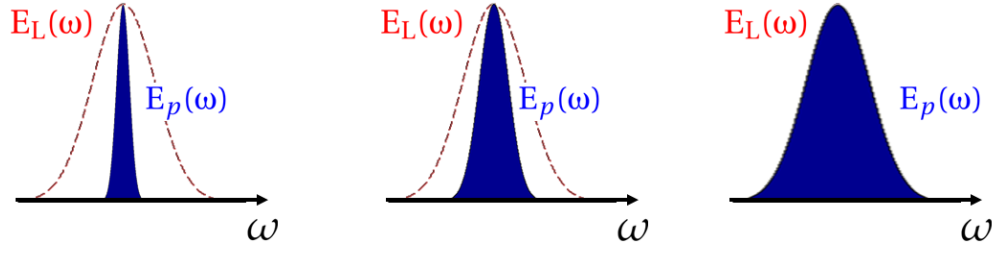
Fig. C2.12: *Example of shaped spectra $E_p(\omega)$ (filed blue curve) with different widths σ. The initial pump laser spectrum $E_L(\omega)$ is represented by dashed red lines.*
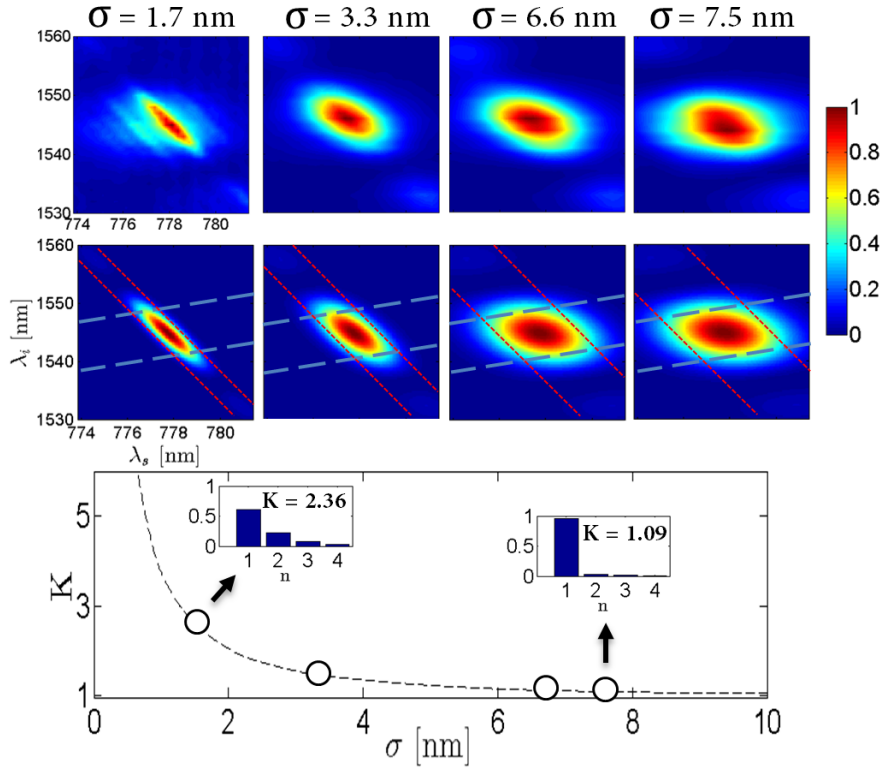
Fig. C2.13: *Top, comparison between experimental (1st row) and simulated (2nd row) JSI for different values of pump spectral width. The other parameters are fixed ($L = 1$ m, $P = 3.4$ bar of xenon, $\lambda_p = 1033.5$). The blue lines delimit the phase-matching function whereas the red lines delimit the energy conservation function. Bottom, corresponding Schmidt number and Schmidt decomposition (assuming no phase correlation).*

($\Delta\alpha < \Delta\Phi$) resulting in an elliptic JSI along the anti-diagonal. Such a form is a signature of spectral correlations[10]. This is confirmed by computing the associated Schmidt number which is estimated to be K = 2.36. As σ increases, the JSI morphs into a more and more circular shape, thus approaching a factorable state. Again, this is confirmed with the Schmidt number which, in this configuration, is close to unity (K = 1 $\rightarrow$ factorable).

---

[10] more precisely, correlations with negative sign (anti-correlation) since the ellipse is along the antidiagonal defined by $\omega_s - \omega_i$

This effect is similar to what was observed when changing the fiber length. From a practical point of view, changing σ has the advantage of being reversible as opposed to a change of length.

Note that the rebounds that can be observed on the experimental JSI when σ = 1.7 nm are attributed to the pulse shaper. When the width of the desired profile approaches the pulse shaper resolution, such oscillations can be observed.

b) Central wavelength variation

Let us now consider the effect of varying the pump central frequency. In principle, one could use a tunable pump laser. Since our pump laser central frequency is fixed (at λ_p = 1033 nm), we use the pulse shaper to map it to a new value. When the width of the shaped pulse is much narrower than the laser width ($\sigma << \sigma_p$), the pulse shaper can be used to change the position of the central frequency (see Fig. C2.14). However such a change comes at a cost- the further apart the new central frequency, the lower the intensity.

Fig. C2.14: *Example of shaped spectra* $E_p(\omega)$ *(filled blue curve) with different central frequencies. The initial pump laser spectrum* $E_L(\omega)$ *is represented by dashed red lines.*
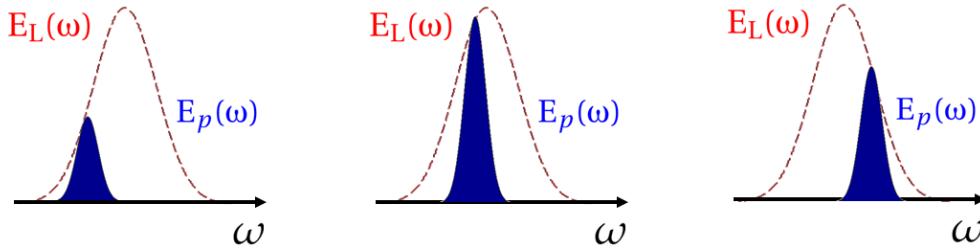
In terms of JSI, changing λ_p is equivalent to moving the energy conservation function along the diagonal in the $\{\lambda_s, \lambda_i\}$ plane (cf section A.2.1). Since the JSI is the intersection of α and Φ, if α is shifted, the JSI is consequently also shifted.
Figure C2.15 shows the comparison between experimental and simulated spectra. The loss of intensity while moving away from the central frequency of the laser is not clearly visible since each recorded JSI is normalised to its own maximum[11]. While λ_{p0} increases, the JSI shifts towards the top right corner.

It is noteworthy that such shift happens with a different direction from what was observed with the pressure tuning (see section C.2.3). When changing λ_p the JSI is shifted along the direction of the phase matching (represented by blue dashed lines), whereas with the pressure

---

[11] however one can observe that for the largest separation (λ_{p0} = 1029 or 1037 nm), the background noise is much more significant since the signal is lower.
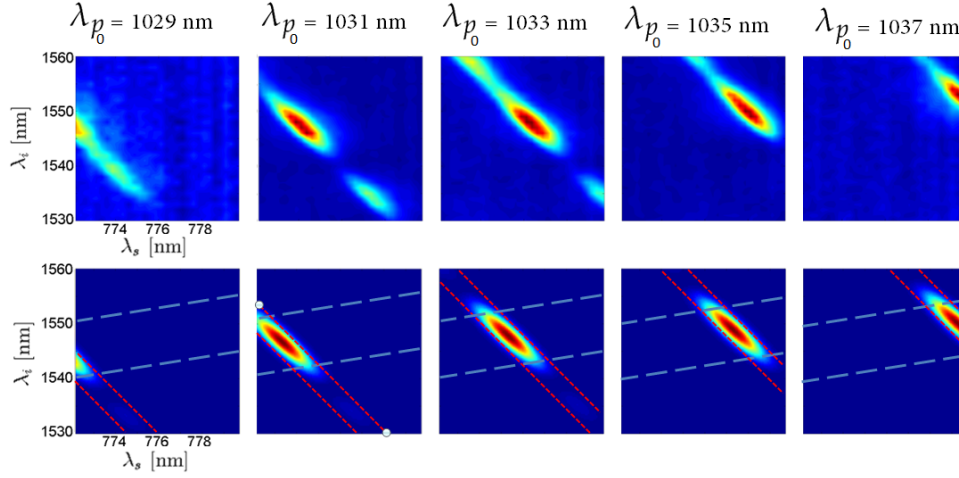
Fig. C2.15: *Influence of a change of central pump wavelength on the JSI. The other parameters are fixed (L = 1 m, P = 3.4 bar, ...).*

variation, the JSI is shifted along the direction of the energy conservation (narrow red dashed lines). **Therefore, by tuning either the pressure and/or λ_p, one can actively move the JSI in two different directions of the 2D plane, meaning that, in principle, any position can be attained.**

Moreover, one can see that the JSIs of Fig. C2.15 exhibit some side lobes along the antidiagonal direction which are stronger than the expected rebounds of the sinc function[12]. We notice that their presence is related to the bending of the fiber. Indeed, by curving or stressing the fiber, the dispersion of the fiber can be slightly change and produce other phase-matching conditions resulting in sidelobes in the JSI [147].

As a result, both the shape and the position of the JSI can be controlled by tailoring the amplitude of the pump with the pulse shaper. The control can be further extended by tailoring the pump phase.

c) Phase variation - Chirp

Until now, we have considered a flat phase (a Fourier transform limited pulse). Let us now study the more general case of an elongated pulse (chirped pulse). As described in section A.2.4, the chirp is also important to take into account since it can induce temporal correlations between signal and idler.

---

[12]this can also be noticed in Fig. C2.6

A chirped pulse is described by:

$$E_p(\omega) = E_0 \, e^{-\frac{(\omega-\omega_p)^2}{2\sigma^2}} \, \underbrace{e^{i\frac{C}{2}(\omega-\omega_p)^2}}_{\text{chirp}} \tag{C2.4}$$

where C quantifies the amount of chirp (C = 0 $\rightarrow$ Fourier transform limited pulse, |C| >0 $\rightarrow$ elongated pulse). In practice C can be modified experimentally either with the pulse shaper or as an internal parameter within the laser. It can have either positive or negative values.
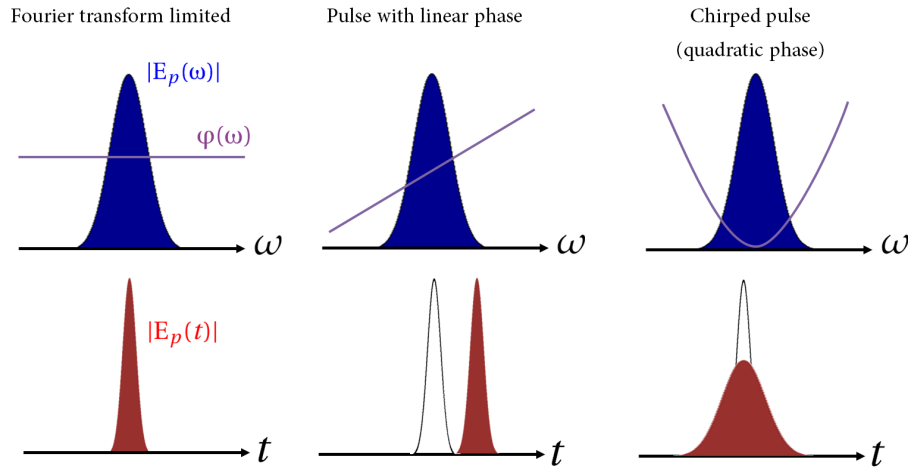
Fig. C2.16: *The first row presents the spectral intensity (blue) and phase (purple) and the second one, the associated temporal intensity (red). Whereas a spectral linear phase delays the pulse with no modification of its shape, a spectrally chirped pulse has an elongated temporal width compared to the Fourier-transform limited case.*

With such a chirped pulse, the associated energy conservation function is given by[13]:

$$\alpha(\omega_s, \omega_i) = \frac{\sqrt{\pi}E_0^2}{\sqrt{\frac{1}{\sigma^2} - iC}} \, e^{-\frac{(\omega_s+\omega_i-2\omega_p)^2}{4\sigma^2}} \, e^{i\frac{C}{4}(\omega_s+\omega_i-2\omega_p)^2} \tag{C2.5}$$

This result can be compared to the Fourier transform limited pump case (Eq. (C2.3c)) such that:

$$\alpha(\omega_s, \omega_i) = \frac{\alpha_{\mathbf{FT}}(\omega_s, \omega_i)}{\sqrt{1 - i\sigma^2 C}} \, e^{i\frac{C}{4}(\omega_s+\omega_i-2\omega_p)^2} \tag{C2.6}$$

And, consequently, since the phase-matching function $\phi(\omega_s, \omega_i)$ remains unchanged whether a chirp is added to the pulse or not, the JSA is:

$$F(\omega_s, \omega_i) = \frac{F_{\mathbf{FT}}(\omega_s, \omega_i)}{\sqrt{1 - i\sigma^2 C}} \, e^{i\frac{C}{4}(\omega_s+\omega_i-2\omega_p)^2} \tag{C2.7}$$

---

[13]the calculation is easily performed by replacing $\frac{1}{\sigma^2}$ in the non-chirped case by $\frac{1}{\sigma^2} - iC$

CHAPTER C2. JOINT SPECTRAL INTENSITY TOMOGRAPHY

where $F_{\mathbf{FT}}(\omega_s, \omega_i) = \alpha_{\mathbf{FT}}(\omega_s, \omega_i) \times \Phi(\omega_s, \omega_i)$ is the JSA when pumped with a Fourier transform limited Gaussian pulse.

Looking at Eq. (C2.7), two distinctions with the Fourier transform limited are to be seen: Firstly, the JSA is decreased by a factor $\sqrt{1 - i\sigma^2 C}$. **This means that the magnitude of the JSA drops with increasing chirp.** Thus, the Fourier transform limited case (C = 0) is the one exhibiting the highest efficiency. In terms of intensity, the JSI is decreased by a factor: $|\sqrt{1 - i\sigma^2 C}|^2 = \sqrt{1 + \sigma^4 C^2}$. This is verified experimentally as shown in Fig. C2.17 where a horizontal slice of the JSI of the source is represented for increasing value of chirp. The chirp[14] is controlled by an internal parameter of the laser. Starting from the maximum value obtained at (C = 0), adding a positive or negative chirp reduces the peak intensity for a constant pulse energy. **Interestingly, such simple measurement allows to estimate the amount of chirp of the pump pulse at the fiber input[15].** For instance, if one wants to avoid any chirp, maximising the measured signal allows to eliminate the chirp, regardless of whether it comes from the laser or from optical elements before the fiber (mirrors, waveplate, PBS). This effect is inherent to FWM as a consequence of the autocorrelation of the pump. It does not occur in SPDC process (whose energy conservation function is directly related to the pump spectrum and not to the autocorrelation of the pump).
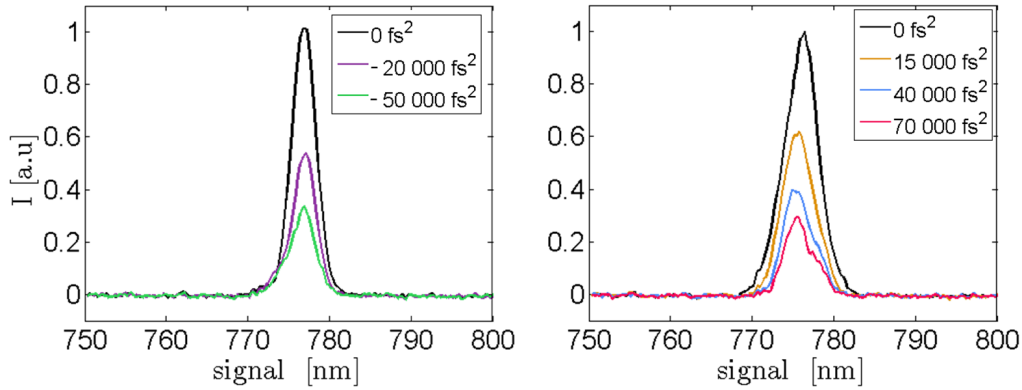
Fig. C2.17: *Measured spectra at the fiber output as a function of chirp. Left, negative chirp and right, positive chirp. The other parameters are fixed (L = 1 m, P = 3.4 bar).*

Secondly, the term $e^{i\frac{C}{4}(\omega_s + \omega_i - 2\omega_p)^2}$ in Eq. (C2.7) is a signature of spectral phase correlation between signal and idler (see section A.2.4). To represent these correlations, one possibility is to visualize the phase of the JSA (until now we have only represented the modulus of the JSA |F|). Alternatively, one can also consider representing the JTA (= **FT**(JSA)). Indeed, the phase

---

[14] more specifically, the parameter allows to control the temporal pulse width (at fixed spectrum).
[15] providing a calibration step

correlations in the spectral domain correspond to amplitude correlations in the temporal domain. Figure C2.18 shows simulations of the JTA of our source for different chirp values. As the chirp increases, the JTA morphs into an ellipse along the diagonal. This means that signal and idler temporal properties become more and more correlated. Note that the JSA shape remains unchanged (shown in Fig. C2.18.c) whatever the chirp (only the phase changes and the mean magnitude).
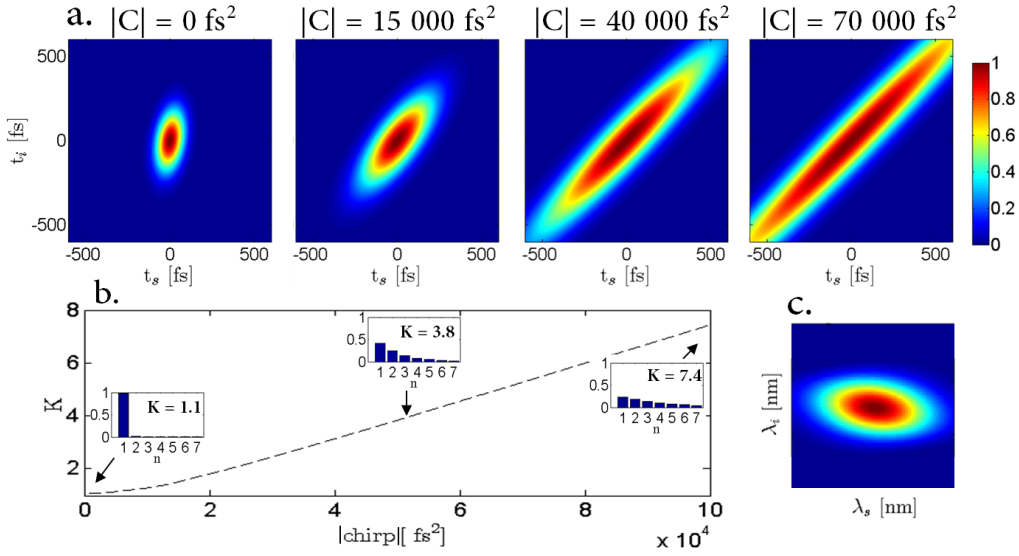
Fig. C2.18: *a. Simulated JTA ($\tilde{F}$) for different chirp values. The other parameters are fixed (L = 1 m, P = 3.4 bar, ...). For simplicity, the sidelobes of the sinc have been neglected. b. Schmidt number as a function of chirp. c. Corresponding JSA modulus (|F|).*

From an exprimental point of view, our current experimental setup only measured the JSI. Thus the phase information is lost and it is not possible to directly measure neither the phase of the JSA nor the JTA. Yet, they can be indirectly deduced from the measurement of the chirp (Fig. C2.17) and from the simulation. In practice, it would be possible to improve the tomography setup such that it is phase-sensitive as shown in [142] [16].

---

[16] in this alternative setup [142], the seed is not anymore coming from a different laser, but directly from the pump laser

Summary of the results and Conclusion

In this chapter, the experimental results obtained with noble gases validate both the model and the concept of JSI manipulation.

A large dynamic control of the JSA has been experimentally demonstrated. To our knowledge this is the first demonstration of a two dimensional shift of the JSA (either along α or along Φ) and over more than $\Delta\omega = 17\text{TH}z$. Moreover, the widths $\Delta\alpha$ and $\Delta\Phi$ can be independently tailored with the pump spectral width and the fiber length. In particular, changing the ratio $\Delta\alpha/\Delta\Phi$ allows to control the amount of spectral amplitude correlations. Finally, the chirp allows to tailor the spectral phase correlations.
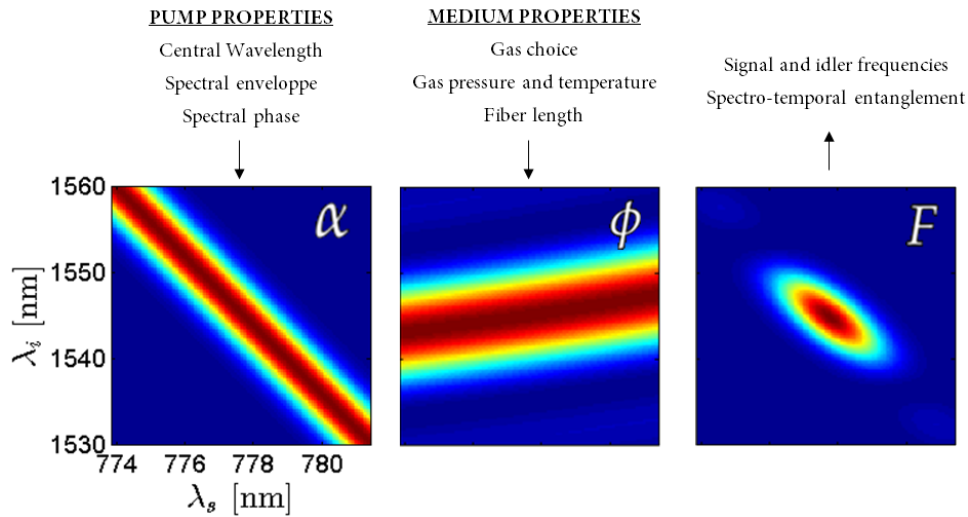
Fig. C2.19: *Summary of the links between the experimental parameters and the JSA.*

Tab. C2.2: Impacts of the different experimental parameters.

Controlling the JSI position	
pressure tuning	shifts JSI along the direction of α
central Wavelength tuning	shifts JSI along the direction of Φ
Controlling the Correlations	
fiber length	modifies the spectral correlations (amplitude)
pump spectral width	modifies the spectral correlations (amplitude)
chirp	modifies the spectral correlations (phase)

Chapter C3

Raman-free photon-pair generation

In this chapter, we present the characterization of the source in the spontaneous regime. By performing count and coincidence detections, the brightness (i.e. the number of generated photon-pairs per unit of time) and the signal to noise ratio of the source are experimentally measured.

3.1 Experimental setup

As opposed to the stimulated emission tomography setup (Fig. C2.10), in the spontaneous regime, the process is not seeded anymore. Thus, in the following experiments, the continuous seed laser is removed and the spectrometer is replaced by single photon detectors. Moreover, in the photon-pair regime, since a single photon-pair must be extracted from an intense pulse containing $\sim 10^{10}$ photons, an efficient filtering of the pump must be implemented. In this source, the wide spectral gap ($\Delta v \sim 100$ THz) between the pump, signal and idler frequencies makes the experiment much easier than with the source described in Part B as standard optics can be efficiently used (in particular dichroic mirrors and bandpass filters) to efficiently suppress the pump and extract the parametric photons with relatively low loss. Furthermore, due to the equivalence between the phase-matching conditions in spontaneous and stimulated regime, the experimental configuration that was used in the stimulated regime is a good starting point to perform the measurement in the photon-pair regime.

The new setup is described in Fig. C3.1. The Ytterbium laser (Satsuma, Amplitude Systems)

144

at λ_p = 1033 nm delivering 230 fs pulses sends pulses inside the gas-filled HCPCF. Prior to the fiber, a half-wave plate controls the laser polarisation. At the fiber output, the signal and idler are separated thanks to a set of 3 dichroic mirrors, together with one broadband filter (short-pass and longpass filter for the signal and idler arm respectively) and one bandpass filter (10 nm width for the signal and 12 nm for the idler) on each arm. Each photon is injected into a singlemode fiber and sent toward single photon detectors. Since signal and idler wavelengths are not in the same frequency range, the two detectors are different. In general, detectors at telecom wavelength exhibit much poorer performances than their visible counterparts. That is why the idler detector which is a free-running InGaAs/InP SPD (ID230, ID quantique) has dark counts of the order of 2.1 kHz and ∼ 20 % detection efficiency whereas the signal detector which is a Si SPD (SPCM-AQ4C, PerkinElmer) has dark counts around 0.1 kHz and detection efficiency of the order of ∼ 60 %. Finally the TTL signals from detectors are sent to a time-tagging and correlation measurement device.
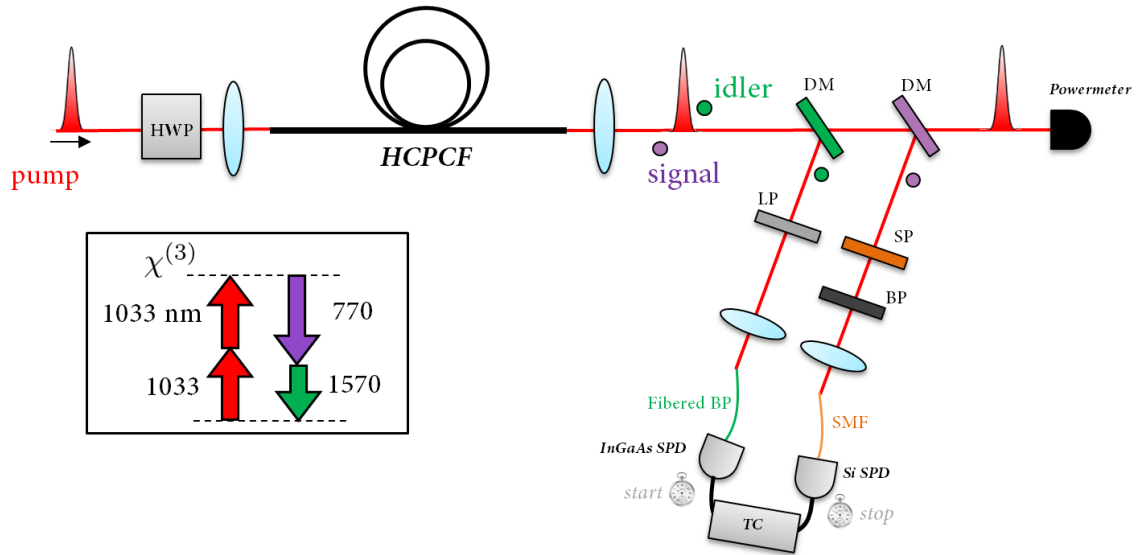
Fig. C3.1: *Experimental setup for count and coincidence measurement of the photon pairs. HWP: half-wave plate, DM: Dichroic mirror, LP: Longpass filter, SP: Shortpass filter BP: Bandpass filter, SPD: Single photon detector, TC: Time-correlated counting.*

In such experiment, it is important to address the trade-off between letting the maximum amount of photon-pair reaching the detectors and filtering the noise. With that in mind, the position of the JSA has been fine-tuned through gas pressure (to ∼ 4.1 bar) in order to reache an optimised position at the center of the two bandpass filters as shown in Fig. C3.2. This is an illustration of how useful the control of the JSA position can be in practice. Note that in this fiber, a pseudo pressure equilibrium is reached so quickly (few seconds) that gas pressure can be tuned actively to optimise the detected signal. This must be due to the large size of the core and the cladding tubes, favouring a good transfer of the gas through the fiber.
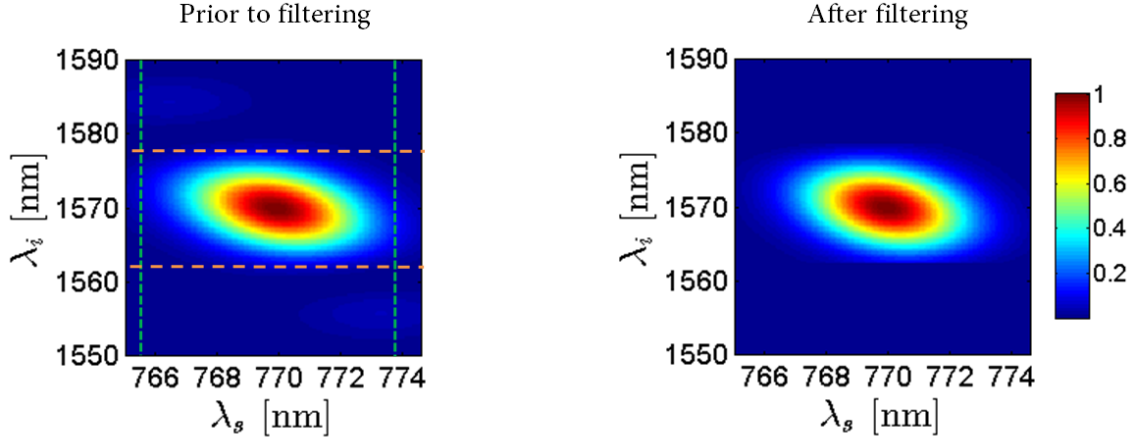
Fig. C3.2: *Left: simulated JSI at the fiber output prior to filtering. Right: simulated JSA taking into account the cropping due to the different filters. The dashed lines represent the two bandpass filters, green for the signal (Gaussian filter centered at 770 nm with 10 nm FWHM) and orange for the idler (Rectangular filter centered at 1570 nm of 14 nm width).*

3.2 Count measurements

A first characterization is to measure the number of counts reaching each detector. The recorded signal may be a combination of several events: the dark-counts, unfiltered photons from the pump, Raman-scattered photon and the parametric photons. These different events can be distinguished from each other through their power dependence. The parametric photons evolve quadratically with pump power, whereas the Raman-scattered photons or pump scattered photons, evolve linearly and the dark counts do not depend on pump power. Thus, by fitting the evolution of the number of counts as a function of the injected pump power P, one can evaluate the different contributions:

$$Counts = a + b\mathrm{P} + c\mathrm{P}^2 \tag{C3.1}$$

with:

$$a = \text{Dark Count contribution}$$
$$b = \text{Raman-scattering + Pump diffusion contribution}$$
$$c = \text{Four-wave mixing photon contribution}$$

Experimentally, on both signal and idler arms the results show a clear quadratic component indicating that photon-pairs are produced (see Fig. C3.3). **To our knowledge, this is the first demonstration of single photon-pair generation in a gas-filled HCPCF.**

Figure C3.3 shows the signal and idler counts as a function of power in linear and log scale.

146
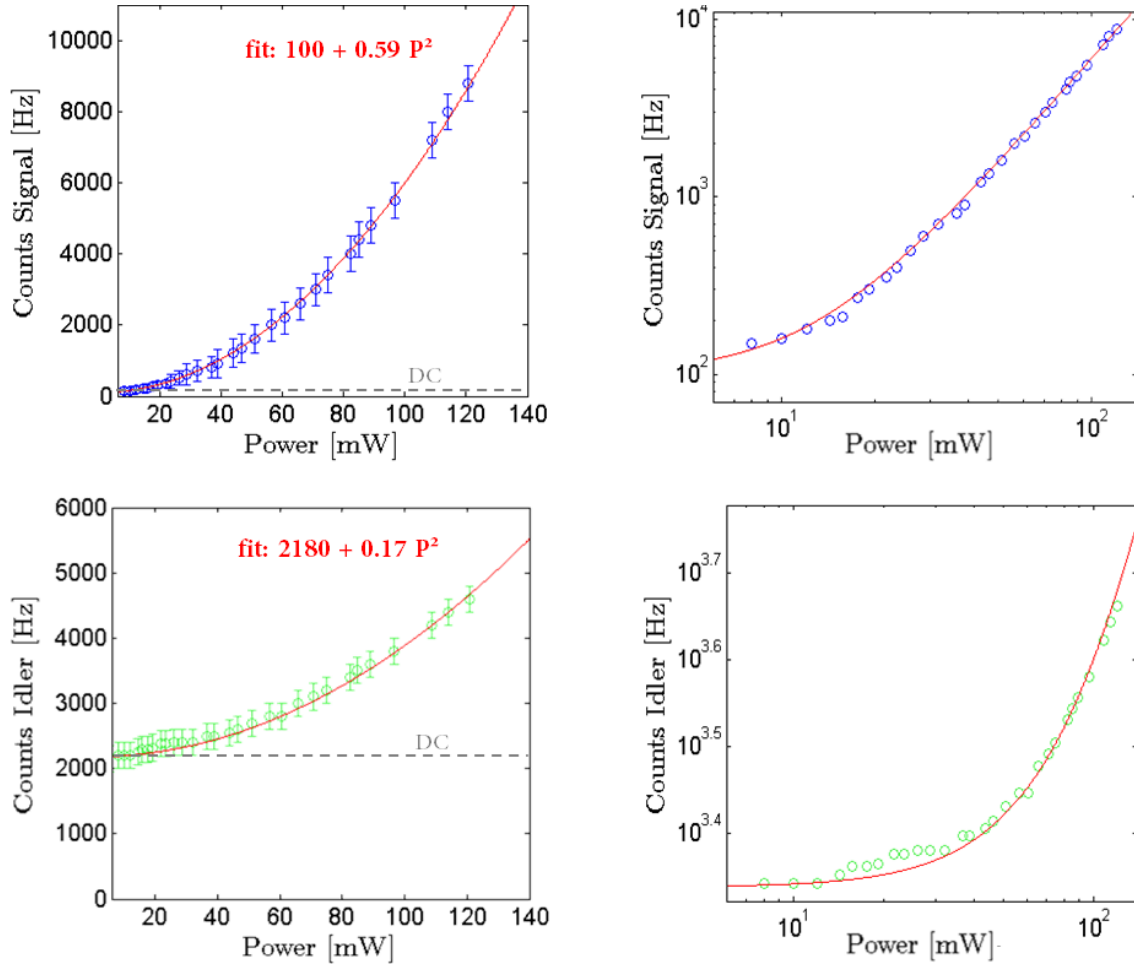
Fig. C3.3: *Raw detected signal counts as a function of pump power in linear (left) and log scale (right). The red lines correspond to a quadratic fit without linear component (fit = a + c P²). DC: dark counts*

The results are compared with a perfectly quadratic polynomial of the form:

SIGNAL	IDLER
$a_s = 100\,\text{Hz}$	$a_i = 2180\,\text{Hz}$
$b_s = 0\,\text{Hz/mW}$	$b_i = 0\,\text{Hz/mW}$
$c_s = 0.59\,\text{Hz/mW}^2$	$c_i = 0.17\,\text{Hz/mW}^2$

A much lower number of photons are recorded on the idler side due to the lower detection efficiency of the telecom SPD. Also, the telecom SPD is much noisier.

Raman-free generation

The absence of linear contribution is a very remarkable result. This means that there is no residual pump diffusion, and, more importantly, no detectable Raman-scattering[1]. As previously discussed (see chapter A3) in such a source, the optical mode within the fiber is only interacting with xenon which, as a noble gas, exhibits no Raman-scattering. Even the minute fraction of the optical mode overlapping with silica (estimated to be $< 10^{-3}$ % with simulation) would exhibit a very low level of Raman-scattering due to the huge spectral gap between the pump and the parametric photon frequencies. Indeed the most significant Raman line is below 40 THz with a peak located at 13.2 THz whereas the parametric photons are separated by ~ 100 THz from the pump.

Thus, to our knowledge, this is the first demonstration of Raman-free photon-pair generation within a fiber architecture. This is of most interest since Raman-scattering has been the main limitations of fiber photon-pair source.

Brightness

Let us now discuss the brightness of the source. It is related to the quadratic coefficient c. The detected photons are either dark counts or parametric photons:

$$C_s = DC_s + N_s \tag{C3.2}$$
$$C_i = DC_s + N_i$$

with $N_x = c_x P^2$, with $x = s, i$, corresponding to the detected parametric photons.

Therefore, in order to estimate the number of detected parametric photons, one simply has to subtract the dark counts to the detected counts. This is only true because of the absence of linear noise.

In theory, the intrinsic *generated* number of parametric signal and idler photons should be the same since they are always created by pairs. However, in practice, N_s and N_i differ from each other because of the different overall transmission in each arm. They are related to the number of pairs N_{pair} by the equations:

$$N_s = T_s N_{pair} \tag{C3.3}$$
$$N_i = T_i N_{pair}$$

where T_x is the overall transmission on arm x, taking into account optical loss and detectors

---

[1] in the following, whenever we mention the absence of RS, we implicitly also include the absence of pump diffusion

quantum efficiencies.

Thus, knowing the overall transmission on each arm, one can infer the intrinsic brightness of the source N_{pair}. On the signal arm, from the output of the fiber to the detector, the optical transmission (optical losses + coupling efficiency) are measured to be $\eta_{l,s} \approx 60$ %, to which we must add loss on the bandpass filter ($\eta_{BP,s} \approx 50\%$) and the detector quantum efficiency ($\eta_{QE,s} \approx 60$ %). This estimation of the loss is done by injecting light from a continuous wave laser at either 780 nm and 1560 nm inside the HCPCF and to measure the power after each optical component. In the end, the signal photon has an overall transmission of $T_s = 18$ % ($T_s = \eta_{l,s} \times \eta_{BP,s} \times \eta_{QE,s}$) and the idler photon has $T_i = 6$ % chance of being detected ($\eta_{l,i} \approx 0.4$; $\eta_{BP,i} \approx 0.8$; $\eta_{QE,i} \approx 0.2$)). Therefore we obtain:

$$N_{pair} = \frac{N_s}{T_s} \approx 1.66 \times 10^{-4} \text{ pairs/impulsion (@10 mW)} \tag{C3.4}$$

$$N_{pair} = \frac{N_i}{T_i} \approx 1.41 \times 10^{-4} \text{ pairs/impulsion (@10 mW)}$$

which is the same order of magnitude.

This experimental result can be compared to the expected brightness of the source. In Chapter A2 we have seen that the probability to generate a pair at ω_s, ω_i is given by (Eq. A2.4b):

$$\text{Proba}(\omega_s, \omega_i) = |\kappa|^2 F(\omega_s, \omega_i)^2 \tag{C3.5}$$

Such that the estimated number of generated photon-pair in the spectral range defined by the bandpass filter $f_s(\omega_s); f_i(\omega_i)$ is:

$$N_{pair}^{(simu)} = f_{rep} \iint |\kappa|^2 F(\omega_s, \omega_i)^2 f_s(\omega_s) f_i(\omega_i) \, d\omega_s \, d\omega_i \tag{C3.6}$$

$$\approx 20 \times 10^{-4} \text{ pairs/impulsion (@10 mW)} \tag{C3.7}$$

with f_{rep} the pump laser repetition rate.

The experimental results are one order of magnitude lower than the simulation. Apart from the fact that the model may contains some errors (missing constant, etc.), this difference may be attributed to defects in the fiber structure, either due to the fiber bending or to inhomogeneities in the microstructuration which have the effect of reducing the overall effective interaction length of the four-wave mixing process. We recall that effect of inhomogeneities was already observed in section C.2.5 on the measured JSI. In fact, a strong decrease of the brightness attributed to inhomogeneities has been observed in the HCPCF photon-pair source previously

reported [2] [29, 148].

It is noteworthy that the brightness can be increased very easily (by ~ two orders of magnitude) by using a pump laser with higher repetition rate[3].

3.3 Coincidence measurements

In this section the temporal correlations between the recorded events is studied. In particular, as opposed to photons from the noise, the signal and idler photons are simultaneously created and therefore they reach the detectors with a constant delay. The information of the temporal delay between detection events can be obtained thanks to the Time-Tagger (see Fig. C3.1). It associates each detector click to a certain time of detection thanks to its internal clock. Figure C3.4 shows an example of recorded histogram depicting the number of detected events as a function of difference in arrival time of the two SPD's electrical output within a 15 µs window.
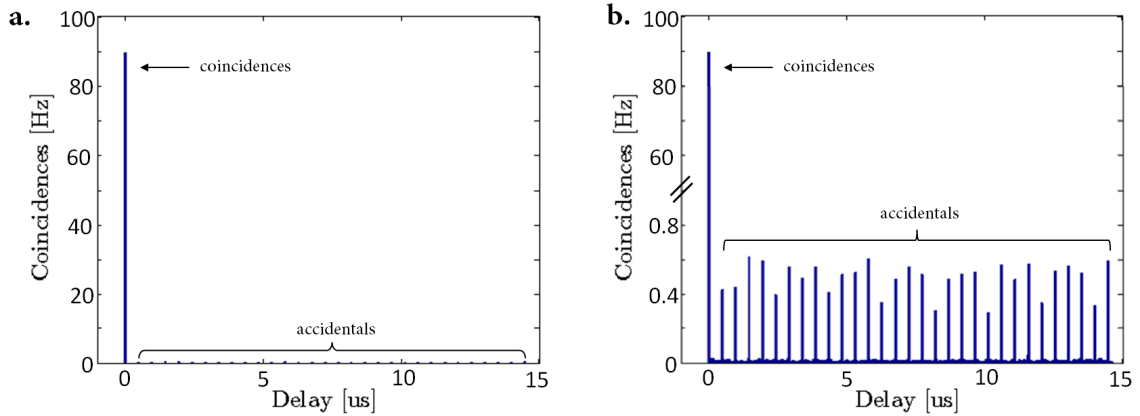
Fig. C3.4: *a. Measured temporal correlations histogram while pumping the HCPCF with P = 60 mW and with a pressure of xenon of 4.1 bar. The bin width in the histogram is 1.4 ns. b. Same histogram with a splited y-axis to show the accidentals. Herein,* $N_{coinc} = 90$, $N_{acc} = 0.5$ *and* $N_{unco} = 6.7\,10^{-3}$ *Hz*

The histogram shows a large predominance of a peak at zero delay, meaning that most of the time, the two detectors click simultaneously. This is a clear signature of photon-pair generation.

Indeed, in such a histogram three different physical quantities can be distinguished:

---

[2] three orders of magnitude decrease was observed between simulation and measurement in liquid-filled PBG-HCPCF of [29]. Moreover, the effects of inhomogeneities are abundantly discussed in the thesis of Thibault Harlé [148]

[3]instead of our 2 MHz, many lasers exhibit 100 MHz - 1GHz repetition rate

- The *coincidences* (N_{coinc}) which is the number of simultaneous detections. It quantifies the events where a signal and an idler from the same pair are being detected (= true coincidences). In fact, a fraction of this peak is also due to "false coincidences" where photons from the noise (Raman, unfiltered pump or DC) give a simultaneous detection with either another photon from the noise or with a parametric photon.

- The secondary peaks are called *accidentals* (N_{acc}). They correspond either to the detections of unpaired signal and idler (parametric photon which has lost its sibling) or detection with a Raman-scattered photon or unfiltered pump photon. These peaks are separated by 500 ns corresponding to our 2 MHz repetition rate of the laser.

- The *uncorrelated* events (N_{unco}) which correspond to the detection between a dark count and another photon (either parametric, Raman or DC). They are not temporally correlated to the pump pulses, in other words they are not related to the pulse repetition rate. These events are distributed on all the bins of the histogram (including the coincidences and accidentals bins).

Figure C3.5 and Table C3.1 provide a description of these different possible detection events and of their power dependence.
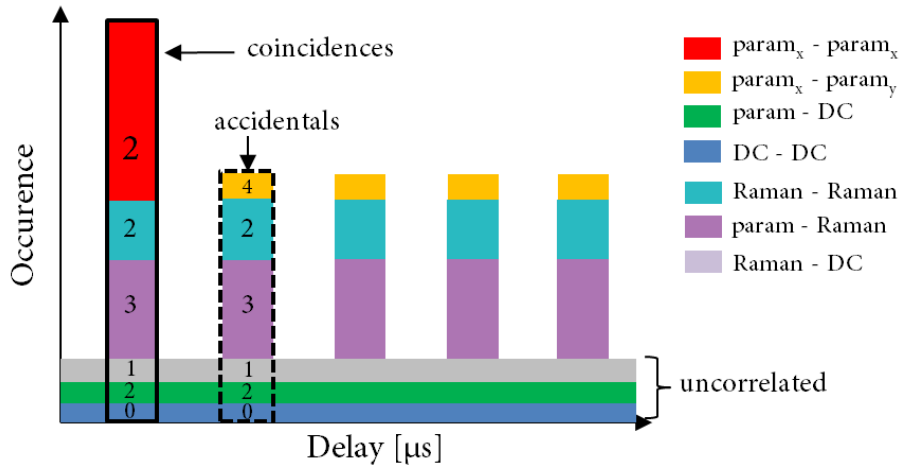
Fig. C3.5: *Schematic coincidence histogram of standard fiber-based photon-pair sources. The intensity of the peaks are arbitrary. The number designates the power dependence ($i \rightarrow P^i$).*

As for the count measurements, a study of the power dependence of these three different physical quantities allows to separate the contributions of four-wave mixing, Raman-scattering and DC. First, one can see that the coincidences evolve quadratically with pump power. No third order power dependence (related to Raman-parametric coincidence) can be detected. This is a further proof of the absence of Raman-scattering noise in such media. Moreover, in

Tab. C3.1: Different types of detections events and their characteristics.

Type	Denomination	Power dependence	Temporal position in the histogram
Photons from the same pair	$N_{param\_x-param\_x}$	P^2	Main peak
Photons from different pair	$N_{param\_x-param\_y}$	P^4	Secondary peaks
Photon from a pair and DC	$N_{param-DC}$	P^2	Continuous distribution
DC-DC	N_{DC-DC}	Constant	Continuous distribution
Additional events in presence of Raman-scattering			
Raman and parametric	$N_{param-Raman}$	P^3	Main and secondary peaks
Raman and Raman	$N_{Raman-Raman}$	P^2	Main and secondary peaks
Raman - DC	$N_{Raman-DC}$	P	Continuous distribution

the case of multiple pair generation, the peak would exhibit a power fourth dependence corresponding to the detection of signal and idler from different pairs but here such events are negligible.

Second, the accidentals exhibit a power four dependence: since the detection of the two photons from different pairs are independent events, their probabilities are multiplied. Here also, the absence of third power dependence due to the conjoint detection of a parametric photon (quadratic) and a Raman-scattered photon (linear), is a further proof that RS is negligible.

Finally, the uncorrelated detections also exhibit a quadratic behaviour plus a constant. These events are due to coincidences between a dark-count (constant) and a parametric photon (quadratic) and the constant is due to DC-DC (once again, without linear dependence due to Raman-scattering).

As a result, the reading of the temporal correlation histogram (such as C3.4) of our source devoid of Raman-scattering, is much simpler compared to the case with RS (Fig. C3.5) as shown in Fig. C3.7 .

Coincidence to Accidental Ratio

A standard measure of the quality of a photon-pair source is to look at the coincidence to accidental ratio (CAR). We recall that this number is defined as the ratio between the main peak and the average of the secondary peaks:

$$CAR = \frac{N_{coinc}}{N_{acc}} \tag{C3.8}$$
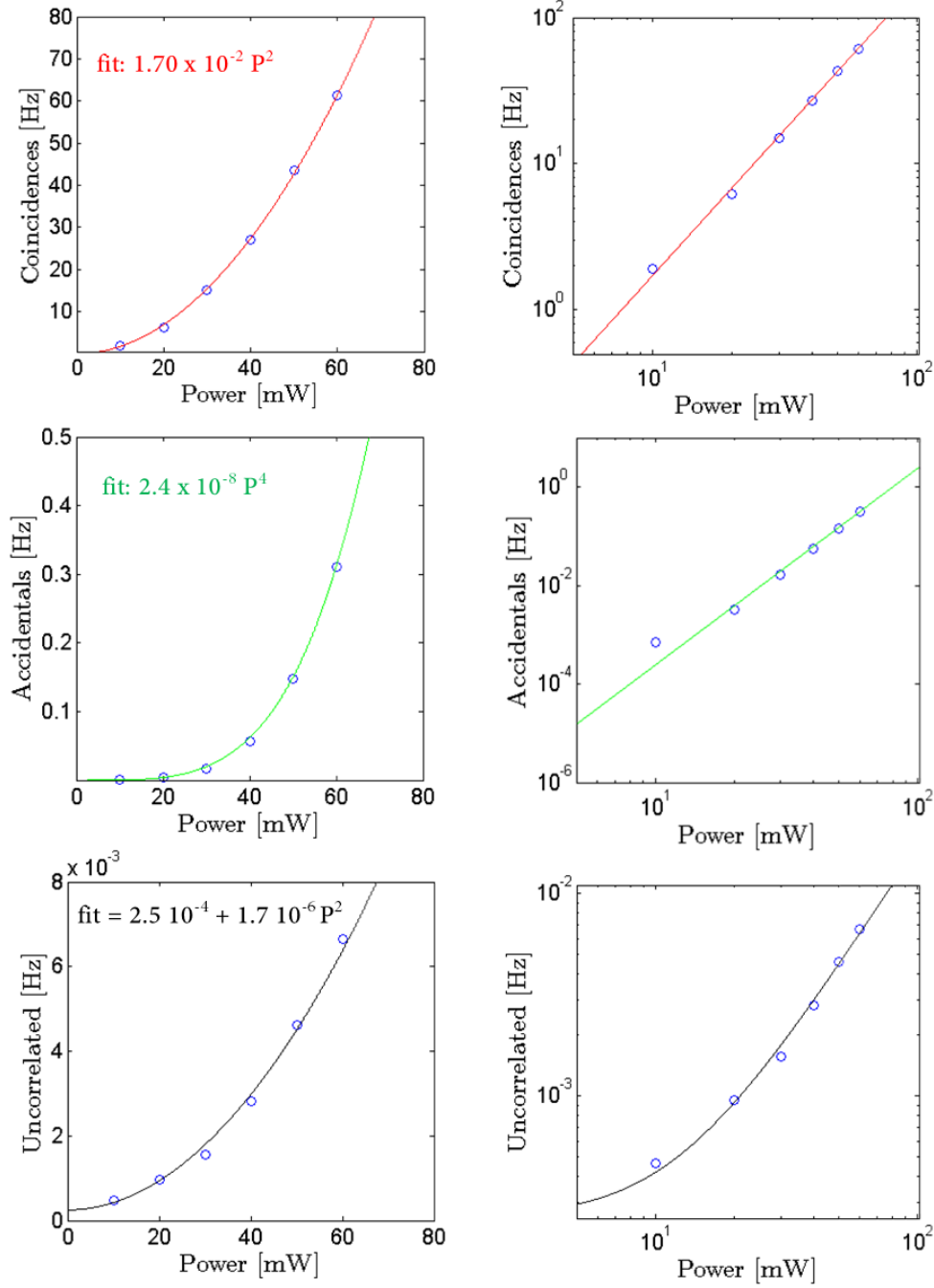
Fig. C3.6: *First row, true coincidences (N$_{coinc}$), second row, accidentals (N$_{acc}$) and third row, uncorrelated (N$_{unco}$), as a function of pump power in linear (left) and log (right) scale. The coloured lines correspond to the polynomial fit.*

In absence of RS, the CAR is simply described by:

$$CAR = \frac{N_{param\_x\text{-}param\_x} + N_{param\text{-}DC} + N_{DC\text{-}DC}}{N_{param\_x\text{-}param\_y} + N_{param\text{-}DC} + N_{DC\text{-}DC}} \tag{C3.9}$$
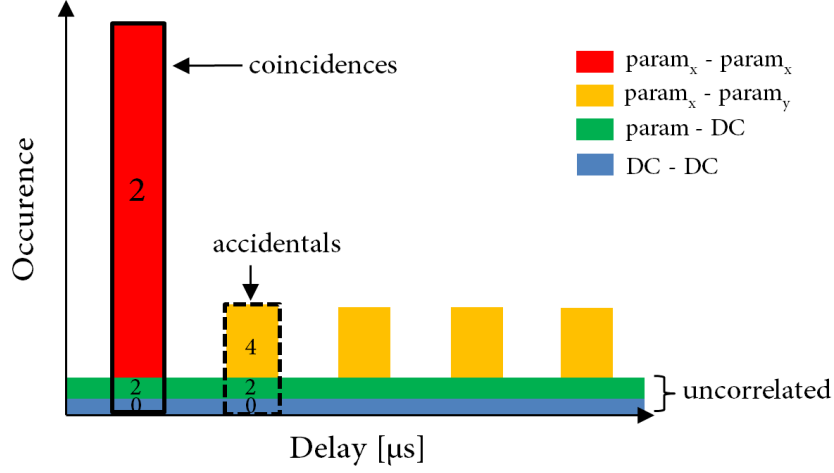
Fig. C3.7: *Schematic coincidences histogram of our HCPCF photon-pair sources. Compared to the standard case (Fig. C3.5), the histogram is less contaminated by the loss.*

where each term is described in Tab. C3.1.

In the regime where the DC have a much lower probability of occurrence than the parametric photon[4], the CAR can be approximated by:

$$\text{CAR} \approx \frac{N_{\text{param\_x-param\_x}}}{N_{\text{param\_x-param\_y}}} \tag{C3.10}$$

In this regime, the CAR is only limited by unpaired parametric photons. As described above, the rate of unpaired parametric photons grows much more rapidly ($\propto P^4$) than true coincidences ($\propto P^2$). More precisely, the number of true coincidences is given by the number of generated photon-pairs (N_{pair}) multiplied by the probability to detect both photons:

$$N_{\text{param\_x-param\_x}} = T_s T_i N_{\text{pair}} \tag{C3.11}$$

whereas for the coincidences of unpaired parametric photons, the probability is given by:

$$N_{\text{param\_x-param\_y}} = T_s(1 - T_i)N_{\text{pair}} \times T_i(1 - T_s)N_{\text{pair}} \tag{C3.12a}$$

$$= T_s T_i(1 - T_s)(1 - T_i)N_{\text{pair}}^2 \tag{C3.12b}$$

where we recall that T_x is the overall transmission on arm x, taking into account optical loss and detectors quantum efficiencies.

---

[4]typically in our setup this is achieved for P > 20 mW

Thus, for our source, the CAR is given by:

$$\text{CAR} \approx \frac{1}{(1 - \text{T}_s)(1 - \text{T}_i)\text{N}_{\text{pair}}} \tag{C3.13}$$

Since the number of photon-pairs evolves quadratically with the pump power, the higher the power, the lower the CAR. This trend is confirmed experimentally as shown in Fig. C3.8, where the measured CAR is given as a function of pump power. Indeed, when decreasing the pump power from P= 60 to 15 mW, the CAR increases until it reaches a plateau around 10 mW. As the power decreases, the DC coincidences become less and less negligible compared to photon-pairs and below 10 mW, DC-DC coincidences cause the CAR to decrease, until the limit where CAR → $\text{N}_{\text{DC-DC}}/\text{N}_{\text{DC-DC}}$ = 1. Experimentally, the CAR reaches really high values, up to 2750 at 10 mW. **It is noteworthy that, to our knowledge, this is the best CAR reported in any fiber architecture. This result is the completion of our original motivation to have a Raman-free medium that would exhibit a high signal to noise ratio at room temperature.** Moreover this value is currently only limited by the detectors (efficiency and dark counts), allowing possibility for large improvements.
In comparison, Table C3.2 shows the best CAR reported in different fiber architecures, namely, solid-core photonic crystal fiber, cooled-down dispersion shifted fiber or hollow-core fiber.

Moreover, one can see that the highest point at 10 mW in Fig. C3.8 is slightly detuned from the overall trend. This is due to experimental limits of the setup. At low power, the number of accidentals reaches such low values ($\approx$ 2 events/hour) that it requires really long integration times to get enough statistics. At 10 mW, the number of accidentals could be overestimated, explaining this detuning.

Tab. C3.2: Comparison of different fiber photon-pair sources. Note that the brightness corresponds to the one obtained in the regime of the best CAR. DSF: dispersion shifted fiber; PCF: silica-core photonic crystal fiber; HCPCF: hollow-core photonic crystal fiber. SPD: single photon detector, S-SPD: superconducting single photon detector. *only limited by the detectors

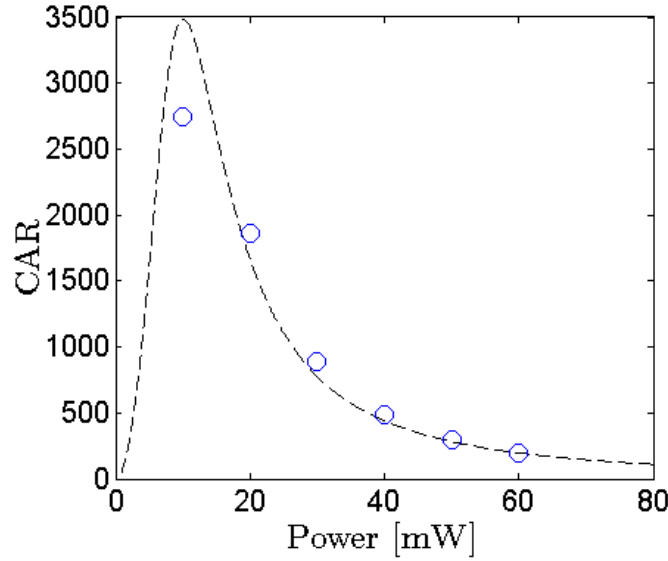| Strategy	Fiber type	Temperature	Detectors	Best CAR reported	Raw Brightness pairs/pulse	Refs.
Cryogenic cooling	DSF	4 K 300 K	S-SPD	1300 10	10^{-5}	[149]
Large detuning	PCF	300 K	SPD	1000	10^{-6}	[61]
Hollow-core	HCPCF	300 K	SPD	63	10^{-4}	[25]
Hollow-core	HCPCF	300 K	SPD	>2700*	10^{-6}	**This work**

Fig. C3.8: *Measured CAR as a function of pump power (blue dots). The best CAR equals 2740. The integration time does not exceed one hour per point. The dashed lines are obtained by computing the CAR with the polynomial fit parameters of Fig. C3.6.*

Discussion on the signal to noise ratio

In most experiments, the CAR is a good approximation of the signal to noise ratio (SNR). As shown in Fig. C3.9.a, in the case of standard fibered photon-pair source (presenting some Raman-scattering or pump diffusion), the main peak of the histogram contains both signal and noise, whereas the secondary peaks gives the noise (almost[5] the same amount as in the main peak). Thus, in that case, dividing the number of occurrences in the main peak, by the ones in the secondary peaks legitimately measures the signal to noise ratio.

However, in our Raman-free configuration, one can argue that the CAR may no longer be a good approximation of the SNR, giving at best a strong underestimation. Most quantum applications post-select the coincidence events and discard all the others. Such applications will be only limited by the amount of noise in the coincidence peak. Therefore, considering the secondary peak as an estimation of the amount of noise[6] may not be relevant in this case where the noise contribution to the central peak is significantly lower (see Fig. C3.9.b).

For these reasons, we propose a second evaluation of the SNR of our source defined by the

---

[5] a small fraction due to detections of two unpaired-parametric photons is not present in the main peak

[6] moreover, the secondary peaks which are here mostly composed of the detection of two unpaired parametric photons are not really related to an intrinsic source of noise but rather a consequence of loss in the setup (see Eq. C3.12b and Eq. C3.13).
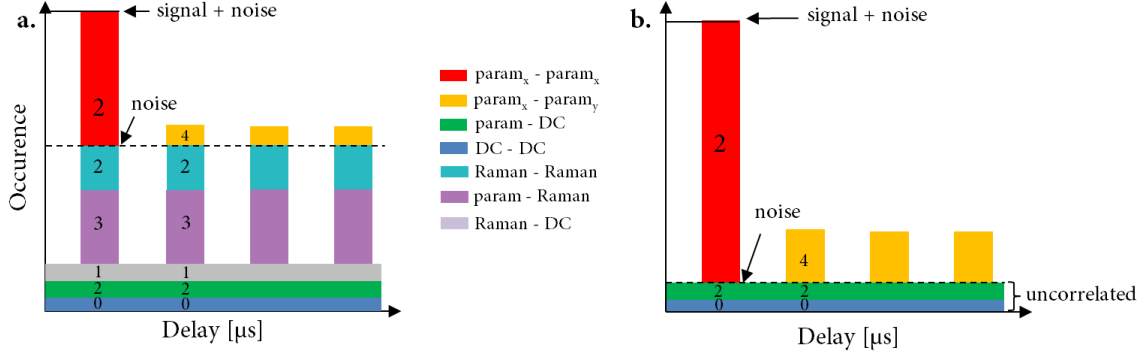
Fig. C3.9: *Signal and noise distribution in **a.** a standard fiber-based architecture and **b.** our HCPCF. In the former, the CAR (ratio between the main peak and secondary peak) gives a good approximation of the SNR whereas in the latter it is not the case.*

ratio of coincidences and uncorrelated:

$$\text{SNR} = \frac{\text{N}_\text{coinc}}{\text{N}_\text{unco}} \tag{C3.14a}$$

$$= \frac{\text{N}_\text{param\_x-param\_x} + \text{N}_\text{param-DC} + \text{N}_\text{DC-DC}}{\text{N}_\text{param-DC} + \text{N}_\text{DC-DC}} \tag{C3.14b}$$

Similarly, in the regime where DC-DC are negligible, one can write:

$$\text{SNR} \approx \frac{\text{N}_\text{param\_x-param\_x} + \text{N}_\text{param-DC}}{\text{N}_\text{param-DC}} \tag{C3.15}$$

which does not depend on the pump power since all terms share the same quadratic power dependence.

Figure C3.10 describes the SNR of our source. At low power, the SNR and the CAR exhibit the same behaviour, limited by the DC-DC coincidences. However, unlike the CAR, the SNR does not decrease with pump power but converges toward a constant of around ≈ 9000 (as expected from Eq. C3.15). This is quite a radical change. **If one considers this as the legitimate signal to noise ratio, then it is fair to say that the SNR of our source is not decreasing with pump power**[7].

In comparison, in a standard silica-core fiber source the SNR would decreased due to the presence of Raman-parametric coincidences ($\propto P^3$) which increase faster than the true coincidences (quadratic). In sources limited by Raman-scattering SNR $\approx$ CAR.

---

[7]At some point, the SNR will start decreasing due to double pair generation that brings noise terms proportional to P^4. For instance, above 250 mW, double-pair events are not negligible since the probability of generating a photon-pair pair per pulse is p=0.1 (and 0.01 at $\sim$ 80 mW). And the probability of generating a double pair is given by $\approx p^2/2$ [150]
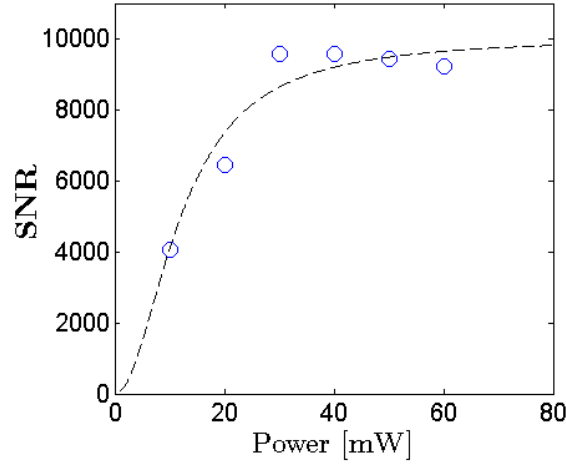
Fig. C3.10: *Experimental SNR (blue dots). The fit (dashed lines) is computed using the polynamial fit of Fig. C3.6*

3.4 Spectral tunability through gas-pressure

We also check that, as in the case of stimulated regime (see section C.2.3), the signal and idler frequencies can be controlled through pressure tuning. Using a set of different filters, we look for the pressure which maximizes the number of counts reaching the idler SPD as a function of the different filter central frequencies (6 fiber CWDM filters from 1510 to 1610 separated by 20 nm step). The results are in good agreement with what was obtained using the stimulated emission tomography (see Fig. C2.7) and with simulation, as shown in Fig. C3.11.
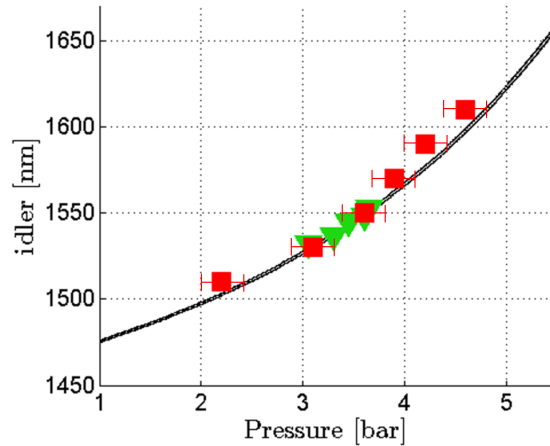
Fig. C3.11: *Measured idler frequency as a function of gas pressure (xenon) in the spontaneous regime (red squares), using the stimulated emission tomography (green triangle). The dark line corresponds to a simulation with fiber parameters: t = 628 nm; r = 22 μm. The measurement range of the stimulated emission tomography was limited by the seed laser tunability.*

CONCLUSION & PERSPECTIVES

Despite the ubiquitous usage of hollow-core photonic cristal fibers in a large and diverse range of fields (nonlinear optic, metrology, atom optics, plasma physics, etc.), it has been only recently that their potential for quantum information became apparent. The present PhD thesis is a contribution to the latter. Particularly, it focuses on one of the main driving subjects in the field of quantum information which is the generation of single photons and/or entangled photons. The results of the present work are twofold:

On the one hand, we have demonstrated that the "*hollow-core attribute*" allows to get rid of the Raman-scattering noise which is known to be the main limitation of photon-pair source based on silica-core fibers. Thanks to this specificity, we have designed a liquid-filled photonic bandgap hollow-core fiber that satisfy all requirements toward the realization of a Raman-free photon-pair source in the telecom range. We showed that the phase matching wavelength range of the four-wave mixing process can be optimised with respect to the Raman line position. Moreover, a second fiber was designed, based on a gas-filled inhibited-coupling HCPCF, in which we demonstrate the first fibered Raman-free photon-pair generation. The source sets the current state-of-the-art signal to noise ratio among all fiber architectures, thanks to the hollow-core and the large spectral separation between pump and parametric photons. The coincidence to accidental ratio reaches value up to 2700 and is currently only limited by the detectors and losses.

On the other hand, we have shown that the "*photonic-crystal fiber attribute*" offers tremendous possibilities to control the medium properties (dispersion, nonlinearity, modal content, optical loss, birefringence). For instance, the filling medium and fiber can be chosen such that the source exhibits a transmission window and a zero dispersion wavelength in a given spectral range (here telecom C-band) as demonstrated in Part B. The fiber dispersion can also be controlled in order to engineer the generated photon-pair state. In particular, we have demonstrated in Part C how the multiband property of IC fibers can be exploited to access various JSA shapes corresponding to spectrally correlated or factorable photon-pair states. In view of quantum information applications (heralded single photon source), we have used this property when designing our gas-filled inhibited-coupling fiber such that is generates factorable

159

photon-pairs at benchmark frequencies (telecom and visible).

In essence, the unprecedented signal to noise ratio, the spectral versatility of the source, as well as all the advantages associated to fiber (room temperature, alignment-free, robustness, compatibility with fiber-network) make this fiber a serious competitor in photon-pair sources.

PERSPECTIVES

The results obtained here and the versatility of gas-filled HCPCF pave the way to a number of possible experiments. Further characterisations of the photon-pair source are currently performed in order to study the photon-pair statistics. Moreover, in the course of my PhD, I ave also identified other uses of the fiber that would benefit from the Raman-free behaviour or the spectral versatility. These different perspectives are described in the following.

Photon statistics

Under-going work investigates the photon statistics of the source. As it is based on a spontaneous parametric process, there is a non-zero probability of generating multiple photon pairs from a single pump pulse. Alternatively, noise in the setup can also lead to "false" detection events. The amount of these unwanted detections can be characterised by measuring the heralded second order correlation function $g_H^{(2)}$ [151, 152]. It consists in dividing one of the detection arm (here the idler), with a 50:50 beam splitter and to measure the number of coincidences that occur between the single-photon detectors at the two output ports, while a signal photon was preliminary detected (see Fig. C3.12.a). More precisely, the heralded second order correlation function is given by:

$$g_H^{(2)} = \frac{N_s N_{si_1 i_2}}{N_{si_1} N_{si_2}} \tag{C3.16}$$

with $N_{si_1 i_2}$ the number of tri-coincidences, N_s the number of signal counts and N_{si_x} the number of coincidences between the signal and one of the idler detectors (x = 1,2).

In practice, a value of $g_H^{(2)} < 1$ is a signature that most often there is no more than a single pair, and the lower the value, the closer it is to "an ideal" photon-pair source. If they were only single photon-pair (signal and idler), no tri-coincidences ($N_{si_1 i_2}$) could be detected and $g_H^{(2)} = 0$. Figure C3.12.b shows the evolution of $g_H^{(2)}$ as a function of power. As the power decreases, the probability of generating multiple pairs becomes more and more negligible such that $g_H^{(2)}$ decreases.

Moreover, the exact same setup can be used to measure the single photon-purity (and thus
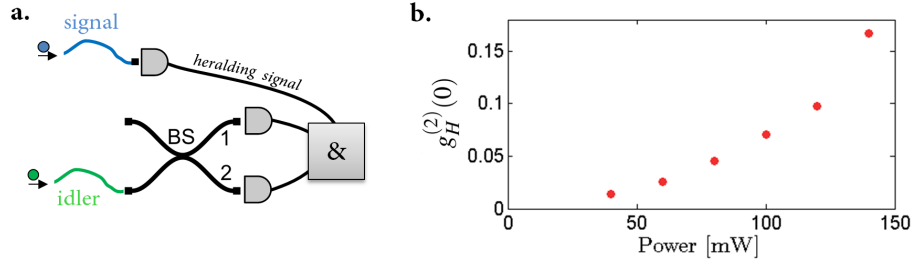
Fig. C3.12: *a. Experimental layout for measuring $g_H^{(2)}$. b. Preliminary experimental result for the measure of $g_H^{(2)}$. At 40 mW, $g_H^{(2)} \approx 0.01$.*

the Schmidt number), provided that the signal it no longer used as a heralding signal. This measurement is called the unheralded second order coherence (see more details in [137, 153]). In the short term, the single-photon purity will be experimentally measured while varying the different experimental parameters (pump FWHM, chirp, gas pressure, etc.) and compared to the results obtained with the stimulated emission tomography setup (chapter C2)

Toward classical and quantum signal propagation in the same device

Raman-scattering is not only an issue in the context of photon-pair generation. In order to develop a scalable approach to quantum information it is important to make fiber network compatible with both classical and quantum information protocols. In principle, the world-wide fiber network can be used either for sending classical or quantum information, however it is much challenging to multiplex classical and quantum information [4]. One of the reason is that the classical signals produce Raman-scattering which will outnumber the quantum signal [154]. A hollow-core fiber network may not have this limitation.

In practice, the promising possibility of a quantum/classical cohabitation within hollow-core fiber could be tested with only minor changes in the experimental setup we have implemented. As shown in Fig. C3.13, by injecting a spectrally filtered[8] telecom pulse inside the HCPCF, it would be possible to check whether a classical and quantum signals can copropagate in a hollow-core fiber without Raman-scattering noise contamination. This would be a major step toward practical quantum information protocols.

Toward pulsed temporal-mode encodings

We have seen previously how controlling the joint-spectral amplitude allows to tailor the signal and idler frequencies (position of the JSA) and their spectral correlations (shape of the JSA). In fact, our experimental apparatus could also allow to change the time-frequency modal contents. We recall that the time-frequency modes of the photon-pair state is given by the Schmidt

---

[8]the erbium gain of the laser should be well filtered
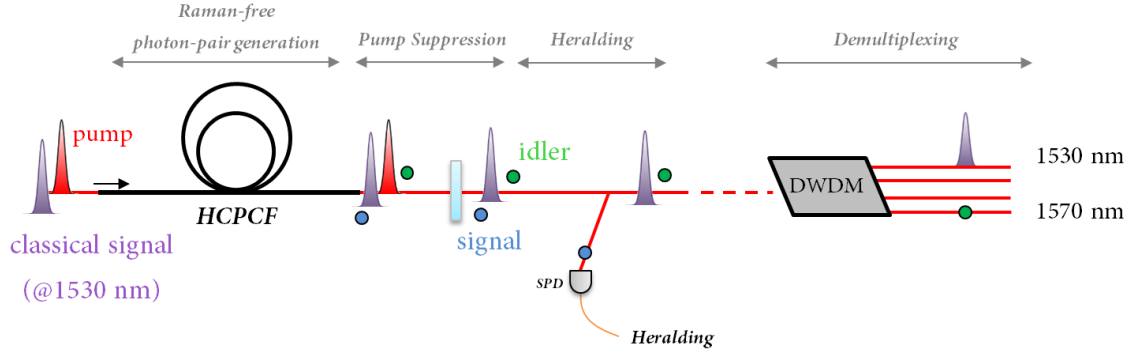
Fig. C3.13: *Experiment to test the propagation of a classical data pulse with a quantum signal generated in another telecom channel.*

decomposition (see section C.2.2):

$$|\psi_{pair}\rangle = \iint d\omega_s \, d\omega_i F(\omega_s, \omega_i) \, |0, 0\rangle \tag{C3.17}$$

$$= \sum_{n=0}^{\infty} \sqrt{c_n} \, |S_n, I_n\rangle \tag{C3.18}$$

where $\hat{S}_k^\dagger |0\rangle = |S_k\rangle$, $\hat{I}_k^\dagger |0\rangle = |I_k\rangle$.

Until now, we have only considered either factorable state of the form: $|S_0, I_0\rangle$ or correlated state of the form $\sum_0^\infty \sqrt{c_n} \, |S_n, I_n\rangle$ with c_n monotonously decreasing $c_0 > c_1 > c_2 > ... > c_n$. As a consequence, the propagation modes of the photons of the pair were essentially the fundamental modes S_0 and I_0; the first letter of the TM alphabet (assumed to be a Gaussian).
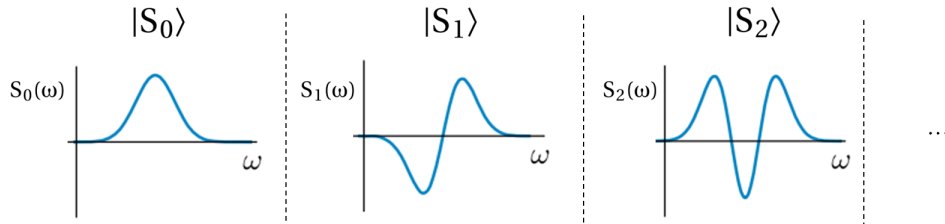
Fig. C3.14: *The first three signal time-frequency modes.*

However, if one wants to use the TM mode as an encoding basis [40, 48, 49], it is important to be able to access the other letters of the alphabet[9]. This is possible thanks to the pulse-shaper. As shown in Fig. C3.15, in the specific case of asymmetric group-velocity matching (here $\theta = 0°$), engineering the energy conservation function results in manipulating the signal frequency-mode. In other words, it is possible to access state of the form $|S_j, I_0\rangle$ ($j \in \mathbb{N}$) where the idler photon is in the fundamental mode and the signal in an arbitrary mode. Inversely, an

---

[9] we recall that time-frequency modes span an infinitely large countable basis

asymetric group-velocity matching of $\theta = 90°$ allows to manipulate the idler while keeping the signal in the fundamental mode [105].
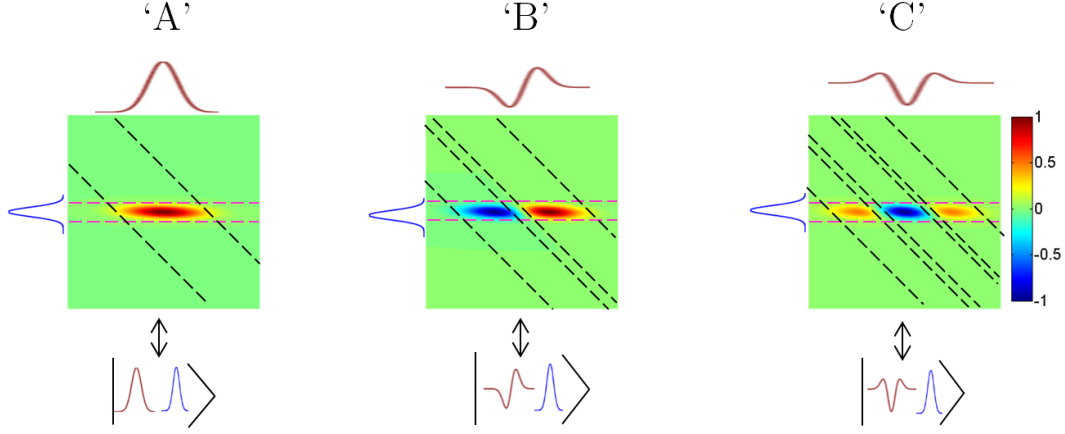
Fig. C3.15: *In a source engineered medium (here $\theta = 0$ and $\Delta\phi < \Delta\alpha$), the signal photon map to any state of the TM alphabet by modifying the pump shape. Energy conservation (black dashed lines). Phase-matching (pink dashed lines)*

With a phase-matching angle of $\theta = 6°$, our photon-pair source is in a configuration corresponding to Fig. C3.15 and would allow to modify the signal time-frequency mode. A preliminary work in order to control the TM alphabet is described here. Using the pulse-shaper device, we can modify the pump spectrum and as a consequence, the energy conservation function. It is noteworthy that the relation between the desired signal time-frequency mode and the pump shape which is required to obtain such a mode is not direct. Indeed, we have seen that, in the case of FWM[10], the energy conservation is not strictly the pump spectrum but its autocorrelation. Thus, in order to encode a given $\left| S_j \right\rangle$ on the signal, one has to shape the pump spectrum with a function whose autocorrelation is the function S_j. For instance, a pump spectrum with a square shape will generate a signal whose spectrum is triangular (= autocorrelation of a square). We have experimentally demonstrated this effect and the results are shown in Fig. C3.16.

Spontaneous Photon triplet generation

With a large transmission bandwidth spanning from the UV to the infrared, inhibited-coupling HCPCF may provide a suitable tool for photon-triplet generation through third order spontaneous parametric down conversion (TOSPDC). It is another $\chi^{(3)}$ nonlinear effect where one pump photon at ω_p gives rise to three photons at ω_r, ω_s and ω_i (satisfying the energy conservation $\omega_p = \omega_r + \omega_s + \omega_i$ and phase matching $\beta(\omega_p) = \beta(\omega_r) + \beta(\omega_s) + \beta(\omega_i)$) (see Fig. C3.17). To our knowledge, this effect has never been observed in any medium in the spontaneous regime.

---

[10]as opposed to SPDC where energy conservation is directly related to the pump spectrum
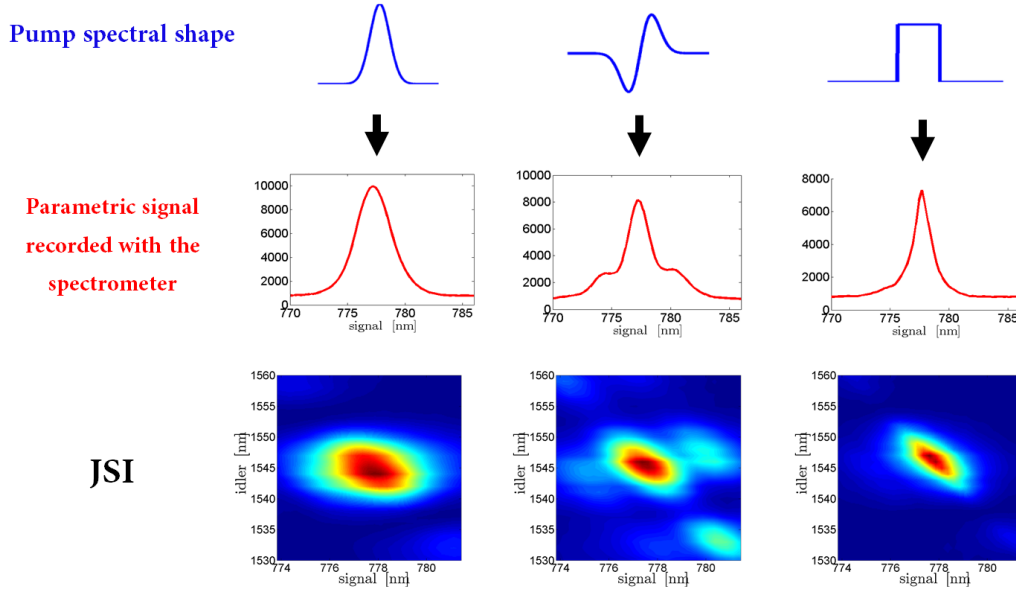
Fig. C3.16: *Top the spectral mask sent to the AOPDF. Bottom The corresponding spectrum recorded with the spectrometer at signal wavelength (horizontal slice of the JSI) and corresponding measured JSI*
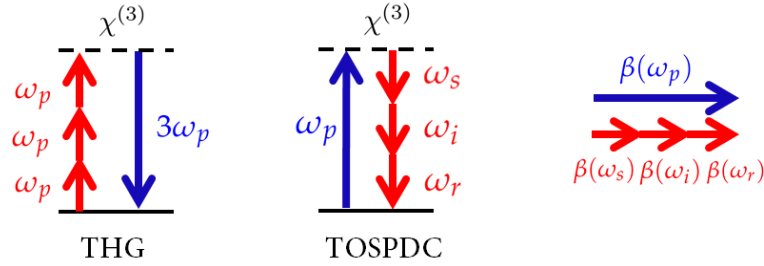
Fig. C3.17: *Energy diagram of third harmonic generation (THG), triplet generation (TOSPDC) and corresponding phase-matching.*

Photon triplets have been the focus of a large number of studies as they can lead to the generation of the so-called Greenberger–Horne–Zeilinger [155] (GHZ) tripartite maximally entangled state $\left| \psi \right\rangle = \frac{1}{\sqrt{2}}(\left|000\right\rangle + \left|111\right\rangle))$, which is an important resource both from a fundamental and a practical viewpoint [156].

The inverse process, third-harmonic generation (THG) is a first step toward the generation of photon-triplet since it shares almost[11] the same phase-matching condition than TOSPDC (i.e. $n(\lambda) = n(3\lambda)$) [157]. The third harmonic has been obtained in IC-fiber [158] thanks to an intermodal phase-matching. Indeed, chromatic dispersion usually prevents a phase-matching allowing the generation of photons-triplet sharing the same spatial mode as the pump. However a phase-matching can be obtained between $n(3\lambda)$ in the fundamental mode and $n(\lambda)$ in

---

[11] the self-phase matching contribution ($\propto \gamma P$) is not the same for THG and TOSPDC

a higher order mode (HE_{13} or higher). Moreover, as for FWM, the phase-matched frequencies can be controlled actively with the gas pressure. Fig. C3.18 shows that the fiber design we used to generate photon-pair would also allows the generation of HE_{11} photon-triplet in the telecom range when pumped by a HE_{13} mode at $\lambda_p \approx 500$ nm.
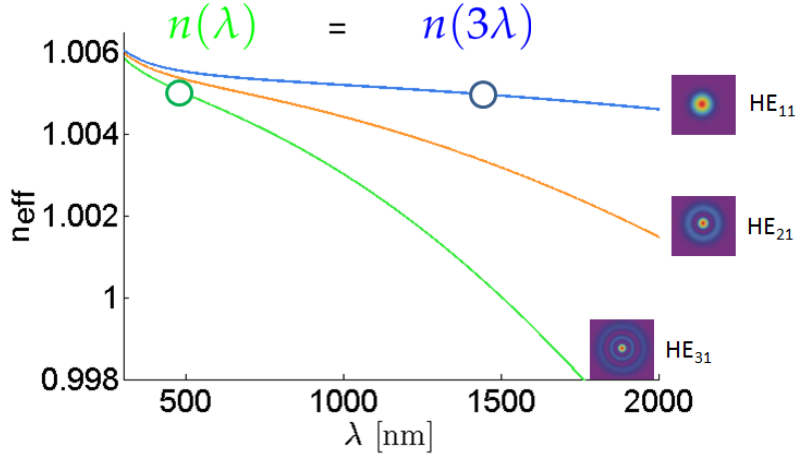
Fig. C3.18: *Computed intermodal phase-matching for photon-triplet generation. For clarity, the resonances has been removed. The photon triplet would be in the fundamental mode and the pump in a HE_{13}. Fiber paramaters: r = 20 μm, P = 8 bar of Xenon.*

With the large range of optimization parameters in the fiber structure and fluid, we have done preliminary calculations indicating that it would be possible to observe triplets within a few hours integration time, using the best available single photon detectors, and thanks to the absence of Raman-scattering in the used fiber.

Appendix

I SDM calculation

This appendix details the calculation of the SDM which is introduced in section A.2.5. The SDM gives a simplified calculation of the biphoton wavefunction in the case of degenerated monochromatic pump. We recall that in the general case, the biphoton wavefunction is:

$$\left| \psi_{pair} \right\rangle = \kappa \int dt \int dz \iint d\omega_s \, d\omega_i E_{p1}^{(+)}(z,t) E_{p2}^{(+)}(z,t) e^{-i\left(\beta(\omega_s)+\beta(\omega_i)\right)z - i\left(\omega_s+\omega_i\right)t} \left| \omega_s, \omega_i \right\rangle \quad \text{(C3.19)}$$

Considering degenerated monochromatic pump:

$$\mathrm{E}_{p1}^{(+)}(z,t) = \mathrm{E}_{p2}^{(+)}(z,t) = e^{i(\beta(\omega_{p0})z - \omega_{p0}t)} + c.c$$

The equations becomes

$$\left| \psi_{pair} \right\rangle = \kappa \int dt \int dz \iint d\omega_s \, d\omega_i e^{i(2\beta(\omega_{p0})z - 2\omega_{p0}t)} e^{-i\left(\beta(\omega_s)+\beta(\omega_i)\right)z - i\left(\omega_s+\omega_i\right)t} \left| \omega_s, \omega_i \right\rangle \quad \text{(C3.20a)}$$

$$= \kappa \int dt \int dz \iint d\omega_s \, d\omega_i e^{i(2\beta(\omega_{p0})-\beta(\omega_s)-\beta(\omega_i))z} e^{-i(2\omega_{p0}-\omega_s-\omega_i)t} \left| \omega_s, \omega_i \right\rangle \quad \text{(C3.20b)}$$

Space and Time Integral

$$\int dz \, e^{i(2\beta(\omega_{p0})-\beta(\omega_s)-\beta(\omega_i))z} \quad \rightarrow \quad \text{sinc}\left(2\beta(\omega_{p0})-\beta(\omega_s)-\beta(\omega_i)\right) \quad \text{(C3.21)}$$

$$\int dt \, e^{-i(2\omega_{p0}-\omega_s-\omega_i)t} \quad \rightarrow \quad \delta\left(\omega_s+\omega_i-2\omega_{p0}\right) \quad \text{(C3.22)}$$

Such that:

$$\left| \psi_{pair} \right\rangle = \kappa \iint d\omega_s \, d\omega_i \, \text{sinc}\left(2\beta(\omega_{p0})-\beta(\omega_s)-\beta(\omega_i)\right) \delta\left(\omega_s+\omega_i-2\omega_{p0}\right) \left| \omega_s, \omega_i \right\rangle \quad \text{(C3.23a)}$$

$$= \kappa \int d\omega_s \, \text{sinc}\left(2\beta(\omega_{p0})-\beta(\omega_s)-\beta(2\omega_{p0}-\omega_s)\right) \left| \omega_s, 2\omega_{p0}-\omega_s \right\rangle \quad \text{(C3.23b)}$$

Applying the change of variable:

$$\omega_s \rightarrow \omega_{p0} + \Delta\omega$$
$$d\omega_s \rightarrow d(\Delta\omega)$$

We obtain:

$$\left| \psi_{pair} \right\rangle = \kappa \int d(\Delta\omega) \quad \text{SDM}(\omega_{p0}, \Delta\omega) \quad \left| \omega_{p0}+\Delta\omega, \omega_{p0}-\Delta\omega \right\rangle \quad \text{(C3.24)}$$

$$\boxed{\text{SDM}(\omega_{p0}, \Delta\omega) = \text{sinc}\left(2\beta(\omega_{p0})-\beta(\omega_{p0}+\Delta\omega)-\beta(\omega_{p0}-\Delta\omega)\right)} \quad \text{(C3.25)}$$

II Spectral phase correlation

In this appendix, we show that constant and linear spectral phase does not incorporate any temporal correlations (i.e does not modify the shape of the JTA).

Let us consider a pulse of the form:

$$\mathrm{E}_p(\omega) = \mathrm{E}_0 \, e^{-\frac{(\omega - \omega_p)^2}{2\sigma^2}} \, e^{i\varphi(\omega)} \tag{C3.26}$$

with:

$$\varphi(\omega) \approx \varphi_0^{(0)} + (\omega - \omega_0)\varphi_0^{(1)} + \frac{1}{2}(\omega - \omega_0)^2 \varphi_0^{(2)} \tag{C3.27}$$

For simplicity, we only consider the first three terms and neglect higher order terms:

$$\mathrm{E}_p(\omega) = \mathrm{E}_0 \, e^{-\frac{(\omega - \omega_p)^2}{2\sigma^2}} \, e^{i(\varphi_0^{(0)} + (\omega - \omega_p)\varphi_0^{(1)} + \frac{1}{2}(\omega - \omega_p)^2 \varphi_0^{(2)})} \tag{C3.28}$$

In the temporal domain, the pulse is given by:

$$\mathrm{E}_p(t) = \mathbf{FT}(\mathrm{E}_p(\omega)) \tag{C3.29a}$$

$$= \mathbf{FT}(\mathrm{E}_0 \, e^{-\frac{(\omega - \omega_p)^2}{2\sigma^2}}) * e^{i\varphi_0^{(0)}} * \mathbf{FT}(e^{i(\omega - \omega_p)\varphi_0^{(1)}}) * \mathbf{FT}(e^{i\frac{1}{2}(\omega - \omega_p)^2 \varphi_0^{(2)}}) \tag{C3.29b}$$

$$= \mathrm{E}_{p,\mathbf{FT}}(t) * \underbrace{e^{i\varphi_0^{(0)}}}_{\text{phase}} * \underbrace{\delta(t + \varphi_0^{(1)}) e^{-i\varphi_0^{(1)}\omega_p}}_{\text{delay}} * \underbrace{e^{-i\frac{t^2}{2\varphi_0^{(2)}}} e^{i\omega_p t}(-i\varphi_0^{(2)})^{-1/2}}_{\text{broadening}} \tag{C3.29c}$$

where $\mathrm{E}_{p,\mathbf{FT}}(t)$ is the Fourier transform pulse when no phase is applied ($\varphi = 0$).

In comparison to the Fourier transform pulse, there is three additional terms depending on $\varphi_0^{(0)}, \varphi_0^{(1)}$ and $\varphi_0^{(2)}$, respectively. The term $e^{i\varphi_0^{(0)}}$ is a global phase. The convolution with $\delta(t + \varphi_0^{(1)}) e^{-i\varphi_0^{(1)}\omega_p}$ corresponds to incorporating a temporal delay. Since, neither $\varphi_0^{(0)}$ and nor $\varphi_0^{(1)}$ distort the temporal amplitude profile of the pulse, such spectral phase components have no effect on the overall on the time-frequency correlations.

This is why, in the manuscript, we did not consider these terms, and have only considered the quadratic chirp ($\varphi_0^{(2)}$) which causes a broadening of the temporal profile and thus changes the shape of the JTA (see section A.2.4 for theory and section C.2.5 for experimental results).

III   Articles

In the following pages we include the papers reporting on the work presented in this doctoral thesis:

1. *"Active engineering of four-wave mixing spectral entanglement in multiband hollow-core fiber"* demonstrates theoretically and experimentally how the multiband properties of inhibited coupling fiber allows to engineer the spectral correlations of the photon-pairs. Using a stimulated emission tomography on the fiber presented in Part C, we obtain various joint spectral intensity profiles, from factorable to entangled.

2. *"Raman-tailored photonic crystal fiber for telecom band photon-pair generation"* describes the liquid-filled photonic bandgag HCPCF presented in Part B of the manuscript. In particular we demonstrate how the choice of liquid allows to control the transmission band and the position of the ZDW. We also discuss the presence of Raman-free spectral range at telecom wavelength where a FWM can be obtained.

3. *"Tailoring modal properties of inhibited-coupling guiding fibers by cladding modification"* descibes how the modal content can be modified by changes in the fiber cladding and in particular the number and position of the tubes. More specifically, we present two fibers with different cladding structures which favor propagation of LP_{11} and LP_{21} modes, respectively.

Other papers are currently in preparation about the Raman-free generation of photon-pairs and about the various joint-spectral amplitude profiles that have been obtained in the gas-filled HCPCF.

Active engineering of four-wave mixing spectral correlations in multiband hollow-core fibers

M. Cordier,[1] A. Orieux,[2] B. Debord,[3,4] F. Gérome,[3,4] A. Gorse,[4] M. Chafer,[3,4] E. Diamanti,[2] P. Delaye,[5] F. Benabid,[3,4] and I. Zaquine[1,*]

[1]*Laboratoire de Traitement et Communication de l'Information, Télécom ParisTech, Université Paris-Saclay, 75013 Paris, France*
[2]*Laboratoire d'Informatique de Paris 6, CNRS, Sorbonne Université, 75005 Paris, France*
[3]*GPPMM Group, XLIM Research Institute, CNRS UMR 7252, Université de Limoges, Limoges, France*
[4]*GLOphotonics S.A.S., 123 avenue Albert Thomas, Limoges, France*
[5]*Laboratoire Charles Fabry, Institut d'Optique Graduate School, CNRS, Université Paris-Saclay, 91127 Palaiseau cedex, France*
[*]*isabelle.zaquine@telecom-paristech.fr*

Abstract: We demonstrate theoretically and experimentally a high level of control of the four-wave mixing process in an inert gas–filled inhibited-coupling guiding hollow-core photonic crystal fiber. The specific multiple-branch dispersion profile in such fibers allows both correlated and separable bi-photon states to be produced. By controlling the choice of gas and its pressure and the fiber length, we experimentally generate various joint spectral intensity profiles in a stimulated regime that is transferable to the spontaneous regime. The generated profiles may cover both spectrally separable and correlated bi-photon states and feature frequency tuning over tens of THz, demonstrating a large dynamic control that will be very useful when implemented in the spontaneous regime as a photon pair source.

1. Introduction

Entanglement is a key resource in quantum information and strong effort has been made to increase the Hilbert space dimension of the generated quantum states either through the number of particles involved or through the generation of qudits with dimension $d \gg 2$ [1–5]. However, in some applications, it is required to go against this trend and to look for separable states. This is particularly driven by the requirement to generate pure states, through heralding from multipartite states. One emblematic example is a heralded single photon source based on parametric photon pair generation. The purity of the heralded photon can be obtained only if the entanglement in all degrees of freedom (spatial, polarization, spectral) is removed between the photon and its heralding twin [6, 7]. In other terms, the photon-pair state must be engineered into a separable state. While removing spatial and polarization entanglement can be easily achieved, the suppression of spectral correlations is generally challenging. It requires stringent conditions on the optical nonlinear process and more specifically on the phase-matching condition. This is exemplified with bulk crystals, commonly used in photon pair generation, and the limited wavelength range where the required conditions can be satisfied [7]. Integrated sources offer more flexibility in engineering the spectral entanglement at specific wavelengths, for instance by designing the poling period of the waveguide [8] or the microstructuration in photonic crystal fiber [9, 10]. Within this context, tuning the photon pairs phase-matched frequencies has been reported using temperature control of a photonic chip [11], or fiber [12]. Furthermore, promising results have been obtained using modulation instability in gas-filled hollow-core photonic crystal fibers, where the amount of spectral correlations of bright twin beams was controlled through gas pressure, chirp and length tuning [13]. Such a source has the further advantage of being

devoid of Raman scattering noise thanks to the use of noble gas. However, modulation instability requires a strong self-phase modulation in order to generate signal and idler whose spectra are not overlapping with the pump spectrum [14]. We therefore have chosen to use four-wave mixing (FWM) where signal and idler can be well separated from the pump in a low gain regime, making it suited for spectral engineering in the photon pair regime [15].

We propose the first demonstration of spectral correlation engineering through a four-wave mixing involving multiple transmission bands of the fiber. The given medium is a gas-filled inhibited-coupling (IC) guiding hollow-core photonic crystal fiber (HCPCF) with controllable dispersion and optical nonlinearity. We used this feature to generate various joint spectral intensity (JSI) profiles, thus indicating the possibility to produce various degrees of spectral correlations. This is a first experimental step toward a versatile fibered and Raman-free photon-pair source.

2. Spectral entanglement

The bi-photon state produced by spontaneous four-wave mixing (SFWM) in an optical fiber of length L is given below using a standard perturbative approach [16]:

$$\left|\psi_{pair}\right\rangle = \kappa \int \int d\omega_s d\omega_i F(\omega_s, \omega_i) \, \hat{a}_s^\dagger(\omega_s) \, \hat{b}_i^\dagger(\omega_i) \left|0, 0\right\rangle \tag{1}$$

Here the quantity κ is a normalizing constant, $\hat{a}_s^\dagger$ and $\hat{b}_i^\dagger$ are the monochromatic creation operators of the two photons s and i of the photon pair and $F(\omega_s, \omega_i)$ is the joint spectral amplitude function (JSA) describing the spectral properties of the generated photon pair. This function can be approximated as the product of the energy conservation function $\alpha(\omega_s, \omega_i)$ and the phase matching function $\phi(\omega_s, \omega_i)$: $F(\omega_s, \omega_i) \approx \alpha(\omega_s, \omega_i) \, \phi(\omega_s, \omega_i)$.

In FWM with degenerate pump, the energy conservation function is defined as the autoconvolution of the pump spectral amplitude $\alpha = [A * A](\omega_s + \omega_i)$ with $A(\omega)$ usually described by a Gaussian function of width σ. The phase matching function is given by:

$$\phi = \mathrm{sinc}\left[\Delta k_{\mathrm{lin}}(\omega_s, \omega_i)\frac{L}{2}\right] \times \exp\left[i\Delta k_{\mathrm{lin}}(\omega_s, \omega_i)\frac{L}{2}\right], \tag{2}$$

where Δk_{lin} is a first order Taylor expansion of the wavevector mismatch between the photon pair and the pump photon. It is performed around the perfect phase matched frequencies ω_s^0, ω_i^0 and ω_p^0:

$$\Delta k_{\mathrm{lin}}(\omega_s, \omega_i) = (\omega_s - \omega_s^0).(\beta_{1p} - \beta_{1s}) + (\omega_i - \omega_i^0).(\beta_{1p} - \beta_{1i}),$$

where $\beta_{1\mu} = \frac{dk}{d\omega}\big|_{\omega_\mu^0}$ is the inverse group velocity. The spectral correlations can be displayed graphically by mapping F in the (ω_s, ω_i) space as shown in Fig. 1. The energy conservation function α exhibits spectral anti-correlation (Fig 1, left). The shape of the phase matching function can either compensate or reinforce this anti-correlation, depending on its width $\Delta\phi = 1/(L\sqrt{0.096 \times ((\beta_{1p} - \beta_{1s})^2 + (\beta_{1p} - \beta_{1i})^2)})$ and angle $\theta = -\arctan(\frac{\beta_{1p}-\beta_{1s}}{\beta_{1p}-\beta_{1i}})$.

In fact, the JSA profile, chiefly described by θ, $\Delta\alpha$ and $\Delta\phi$, is a direct signature of how the photon-pair states are correlated, as illustrated in Table 1 where we can distinguish two families. The first one comprises factorable states where the signal and idler photons, being spectrally independent, are in a product state. It has been shown [7] that this state can take the form of three distinctive JSA geometry profiles forming a circle or an ellipse along either the horizontal or the vertical axis, each corresponding to a specific phase relationship between the photon pair and the pump. The second family of states that can be identified by JSA profiles relates to what is commonly referred to as correlated states. In such a scenario signal and idler photons are
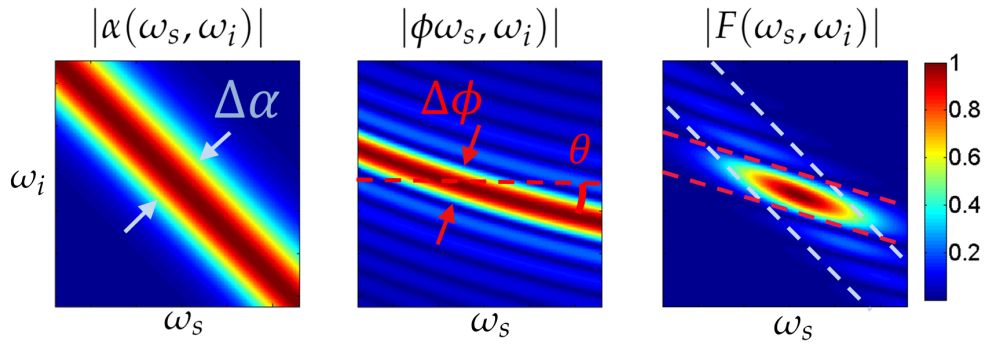
Fig. 1. From left to right: absolute value of the energy conservation function α, the phase matching function ϕ and corresponding joint spectral amplitude in the case of a Gaussian pump in an unengineered medium.

spectrally entangled. A representative JSA of such states is shown on the right hand side panel of Table 1. Here, the JSA typically shows a tilted ellipse profile.

These various degrees of spectral entanglement can be described in a more quantitative way by using the Schmidt decomposition of the JSA, which consists in finding the two sets of orthonormal functions $S_n(\omega_s)$ and $I_n(\omega_i)$ respectively depending only on signal and idler frequency [6]: $F(\omega_s, \omega_i) = \sum_{n=0}^{\infty} \sqrt{c_n} S_n(\omega_s) I_n(\omega_i)$. Substituting into Eq. (1), we obtain:

$$\left| \psi_{pair} \right\rangle = \sum_{n=0}^{\infty} \sqrt{c_n} \, \hat{A}_n^\dagger \, \hat{B}_n^\dagger \left| 0, 0 \right\rangle, \tag{3}$$

where $\hat{A}_n^\dagger = \int d\omega_s S_n(\omega_s) \hat{a}_s^\dagger(\omega_s)$ and $\hat{B}_n^\dagger = \int d\omega_i I_n(\omega_s) \hat{b}_i^\dagger(\omega_i)$ define the temporal modes creation operators. The coefficients c_n are real normalized scalars.
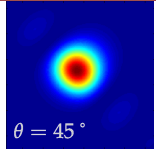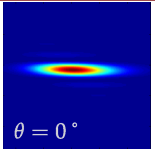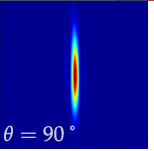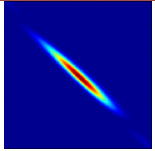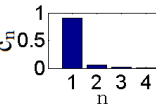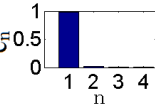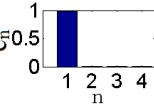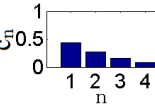
By definition, a factorable state corresponds to the case where there is only one non-zero element in the decomposition so that $\left| \psi_{pair} \right\rangle = \left| A_0 \right\rangle \left| B_0 \right\rangle$ implies spectral independence between signal and idler photons. We also define the mean number of excited modes by the Schmidt number : $K = \frac{1}{\sum_n c_n^2}$. $K = 1$ for a factorable state and $K > 1$ for a correlated state.

These photon-pair states, being spectrally factorable or entangled, are all useful in quantum technology (QT) applications. For example, correlated states are essential in security of quantum key distribution [17], whilst factorable states are the backbone in heralded single photon sources. Furthermore, the temporal mode basis of the signal and idler presented above can be used as an encoding basis in a high dimension Hilbert space [5]. For example, by controlling the Schmidt decomposition one can address the different qudit states of each photon of the pair and tailor the entanglement between these two qudits. A large range of control parameters is required in order to achieve that in a dynamic way with a given source, and we demonstrate here that hollow-core fibers provide the ideal platform for that purpose.

3. Dispersion and group velocity matching conditions in hollow-core fibers

HCPCFs are an exceptional tool for light and fluid-phase interactions thanks to their ability to micro-confine together light and fluids within small modal areas and over interaction lengths that can reach up to kilometers with extremely low optical losses. Furthermore, with a judicious choice of the gas and HCPCF design, gas-filled HCPCFs have been shown to be excellent and versatile platforms for nonlinear and quantum optics [18, 19], with optical nonlinearity and dispersion that can be highly tailored.

Table 1. **Sets of conditions required to obtain either factorable or correlated pair states. Each set defines i) a relation between the group-velocities of pump, signal and idler photons which in turn determines the angle θ ii) a relation between medium length and pump bandwidth.**

Factorable			Correlated
$2\beta_{1p} = \beta_{1s} + \beta_{1i}$	$\beta_{1p} = \beta_{1s}$	$\beta_{1p} = \beta_{1i}$	$\beta_{1p} < \beta_{1s,i}$
$\Delta\phi = \Delta\alpha$	$\Delta\phi << \Delta\alpha$	$\Delta\phi << \Delta\alpha$	-
$\theta = 45°$	$\theta = 0°$	$\theta = 90°$	

Among the numerous existing fiber designs, we use Inhibited-Coupling guiding HCPCF whose guidance mechanism relies on a principle akin to bound or quasi-bound state in a continuum [20]. In practice, this is achieved by engineering the fiber microstructure such that the coupling between the cladding mode continuum and the core mode is strongly inhibited. Such fiber are sometimes called ARROW [21] in the literature; we refer the reader to [22] for the detailed differences between IC and ARROW. Figure 2 shows a micrograph of our tubular IC-HCPCF and its transmission and dispersion spectra.

IC-HCPCF intrinsically exhibit several bands in their transmission bandwidth spanning from the deep infrared to the UV (see Fig. 2). The corresponding multiple zero-dispersion wavelengths (ZDW) give rise to a large variety of phase-matching and group velocity relations.

An analytical model was recently given to describe the effective index of a $HE_{m,n}$ mode inside
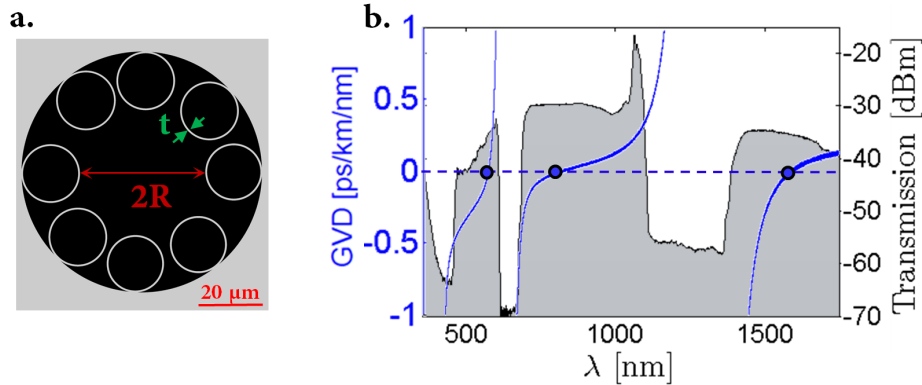
Fig. 2. (a) Fiber cross section (R = 20 μm, $t \approx 630$ nm) and (b) its optical properties. The group-velocity dispersion (blue) is computed with the analytical model whereas the black curve gives the transmitted power for a fiber length of 6.5 m pumped with a super-continuum source. The circles give the position of the zero-dispersion wavelengths. The high peak in the transmission at 1064 nm is a measurement artifact due to the super-continuum pump.

a tube-type hollow core fiber [23]:

$$n_{\text{eff}} = n_{gas} - \frac{j_{m-1,n}^2}{2k_0^2 n_{gas} R^2} - \frac{j_{m-1,n}^2}{k_0^3 n_{gas}^2 R^3} \cdot \frac{\cot\left[\Psi(t)\right]}{\sqrt{\epsilon-1}} \cdot \frac{\epsilon+1}{2},$$

(4)

with : $\Psi(t) = k_0\, t\sqrt{n_{si}^2 - n_{gas}^2}$, R the fiber radius, $\epsilon = n_{si}^2/n_{gas}^2$, $j_{m,n}$ the n$^{\text{th}}$ root of the m$^{\text{th}}$ Bessel function J, t the silica strut thickness and n_{si} the glass refractive index. Simulations and experimental observations have shown that such a tube-type model can provide an accurate description of IC-fiber dispersion [24], provided an effective fiber core radius R_{eff} is used, that is slightly larger than the actual one [25]. Moreover, as long as $\lambda << R$ the evolution of the effective index is, in first approximation, independent of the cladding design around the core. IC fibers can therefore exhibit very close dispersion profiles despite their apparent geometrical difference (i.e tubular lattice, kagome lattice), as long as they have the same radius and silica strut thickness. However, as losses strongly depend on the cladding geometry [26], this simple tube-type model is not suited to infer fiber losses.

The slowly varying contribution of the effective index is described by the first two terms of Eq. (4) depending on gas dispersion and fiber core radius only. The third term introduces the resonances with the silica struts. The positions of these narrow non-guiding regions depend on silica strut thickness t and correspond to $\Psi(t) = l\pi$ with l integer. This defines a set of wavelengths $\lambda_l = \frac{2t}{l}\sqrt{n_{si}^2 - n_{gas}^2}$ where the fiber dispersion is divergent.

Figure 3 shows the dispersion of IC-fibers calculated from Eq. (4) with different silica strut thicknesses t but same radius. For a small t value, the discontinuities λ_l are mostly concentrated in the UV region, such that in the visible and infrared spectral window, the dispersion profile is mainly composed of one transmission band denoted I. As t increases, the discontinuities are red-shifted, forming a more and more multiband dispersion structure (additional bands denoted II, III, ...). The number and position of the bands and ZDWs can therefore be controlled when designing the fiber.

Such multiband dispersion profiles provide an unprecedentedly large control parameter-space in setting the FWM wavelengths (i.e. pump, signal and idler). For example by positioning the three involved wavelengths either in the same band (singleband FWM) or in different bands (multiband FWM), one can control the phase relation between them to span the different bi-photon quantum states mentioned previously. This is illustrated in Fig. 4 where we plot the FWM spectral density map giving both the wavelength of the generated photon and the angle θ of the phase matching as a function of the pump wavelength. The top left hand side corresponds to a simulation neglecting the resonances in the dispersion. In such a case, the phase matching angle θ mainly varies from $-30°$ to $-60°$, thus corresponding to correlated JSA whatever the pump wavelength. In contrast, if the resonances are incorporated in the simulation (Fig. 4 top right hand side), it exhibits a much more diversified phase-matching possibilities. More specifically, new FWM phase matching are available for λ_p in the range [650-750] and [950-1200] nm corresponding to multiband FWM with either signal (M1) or idler (M2) situated in a different dispersion band than the pump (see the bottom insets). In such a multiband configuration, others relations between β_{1p}, β_{1s} and β_{1i} become possible allowing various angles θ. For instance, due to the relative positions of the band between one another (related to the gas pressure), a multiband FWM described by (M1) favours a group velocity matching $\beta_{1p} = \beta_{1i}$ whereas (M2) favours $\beta_{1p} = \beta_{1s}$. Thanks to such multiband FWM, all three factorable states (i.e. $\theta = 0°$, $\theta = 45°$, $\theta = 90°$) become theoretically accessible. To our knowledge, this is the first demonstration that HC-PCF dispersion can be tailored to engineer such a large range of bi-photon quantum states.

The core radius R must also be chosen carefully as it is related to multiple properties, mainly: losses, generation efficiency and modal contents. The FWM generation efficiency varies as R^{-4} which favors a small radius but the general losses also increase with decreasing core radius (R^{-4})
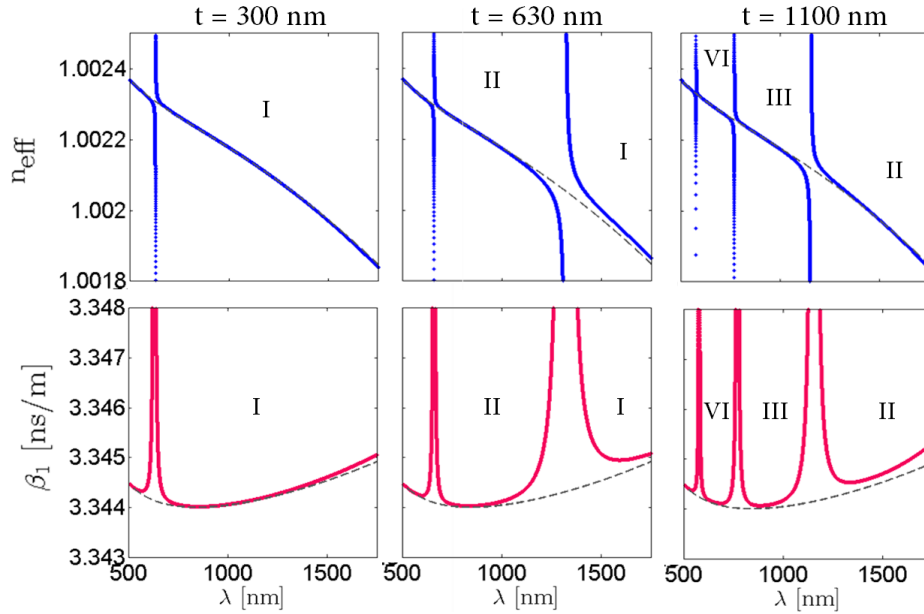
Fig. 3. Top: Effective index and bottom: inverse group velocity β_1 in a IC fiber filled with Xenon (3.5 bar) with a radius of 22 μm for three different silica strut thickness. The Roman numbers to the different bands separated by discontinuities. The gray dashed lines correspond to the dispersion when neglecting the resonances (neglecting last term of Eq. (4)).

which forces a compromise [26]. In such fibers, with a radius around tens of micrometers, the losses are remarkably low ($\approx 10 - 100$ dB/km) at a central wavelength in the band but they increase rapidly as the wavelength approaches a band-edge. None of the involved wavelengths λ_p, λ_s, λ_i should therefore be too close to any discontinuity, which must be taken into account in the fiber design in order to enable efficient FWM. Finally, this type of fiber is usually a few-mode fiber but it can behave as single mode with a careful coupling (Fig. 5(c)).

4. Tomography of the JSI in IC-HCPCF

In order to test our model experimentally we chose a tubular IC-HCPCF composed of 8 tubes with strut thickness $t = 630 \pm 20$ nm. Its 22 ± 1 μm effective core radius offers a good trade-off between losses, generation efficiency and modal content, as explained above. Cross-section and losses are given in Fig. 2 and the simulated phase matching is shown in Fig. 4 right hand side. The fiber design was chosen to exploit a multiband FWM while operating at convenient wavelengths. Indeed, the pump wavelength is set at 1030 nm which is commercially very common. Similarly, the idler wavelength lies at telecom wavelength range, while the signal wavelength is in the range of atomic transitions and Silicon single photon detectors. Nevertheless, using Eq. (4), one can reach any wavelength combination that fulfill energy conservation. Finally the fiber exhibits a polarization extinction ratio of ~ 30 dB.

We use stimulated emission tomography technique (SET) to reconstruct the JSI (= $|JSA|^2$) [27]. Among the existing techniques, SET allows replacing the single photon detectors with fast and spectrally resolved classical detectors provided an additional laser is used at signal or idler wavelength to seed the process. The equivalence of the JSI between spontaneous and stimulated regime is valid only if the variation of the stimulated generated signal power remains linear
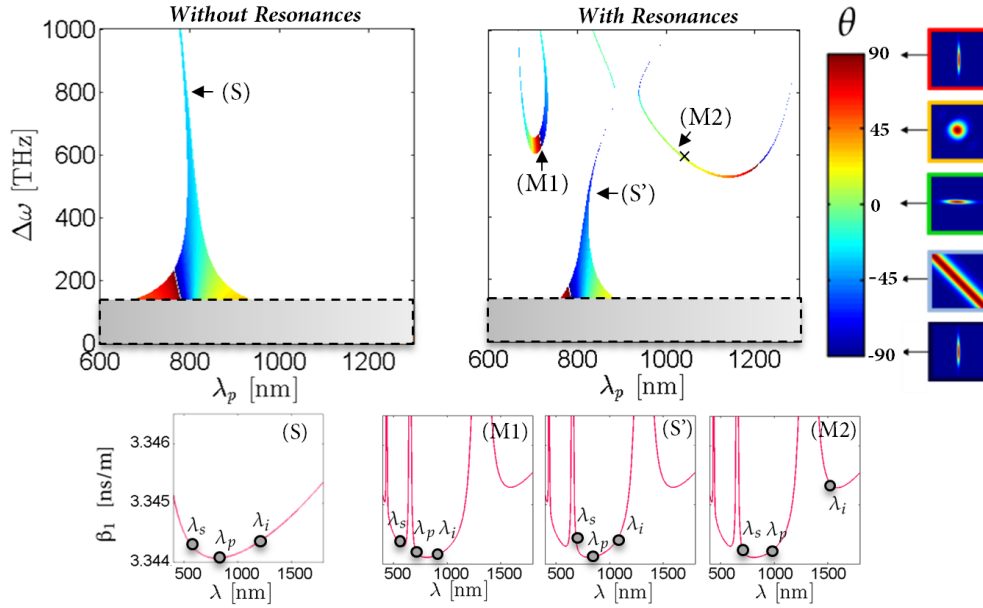
Fig. 4. Top: Simulation comparing the FWM spectral density map with and without neglecting the effect of resonances in the dispersion. The parameters used are the one of our fiber (R = 22 μm, t = 630 nm, and P = 3.5 bar of Xe). The y-axis corresponds to the gap between pump and signal/idler frequencies $\Delta\omega = |\omega_p - \omega_{s/i}|$. The color gives an additional information about the angle θ of the phase matching function. (S) and (S') correspond to a singleband FWM whereas (M1) and (M2) correspond to a multiband FWM. The black cross describes our experimental configuration (λ_p = 1030 nm). The grey region corresponds to FWM where signal and idler are generated too close to the pump wavelength. Note that the lines have been thickened for improved visibility. Bottom: Corresponding group velocity relations.

with seed power [28, 29] (i.e small parametric gain regime). The underlying assumption is that the JSI in the stimulated regime is an amplified version of the JSI in the spontaneous regime; the amplification factor is equal to the average photon number N_{seed} of the coherent seed: $\text{JSI}_{\text{stim}} \approx N_{\text{seed}} \cdot \text{JSI}_{\text{spont}}$.

Our SET experimental characterization setup is shown in Fig. 5. We use a pulsed pump laser (Satsuma, Amplitude Systems) at λ_p = 1030 nm with 280 fs pulse duration at 2 MHz pulse repetition rate and the average pump power injected in the HCPCF is 60 mW. The seed laser (T100, Yenista) is a continuous-wave laser tunable from λ_i = 1530 nm to 1560 nm. The seed power injected in the IC-HC-fiber is around 100 mW, which corresponds to an average power of 50 nW that is effectively involved in the FWM process because of the duty cycle of the pump. Both laser polarizations can be controlled independently with two halfwave plates (HWP). The two fiber ends are inserted into gas-cells with a pressure monitoring and glass windows for optical power injection. Injected into one of the cells, the gas fills the fiber (core and cladding) and an equilibrium between the two gas cells is obtained within less than an hour. At the fiber output, the generated signal at $\omega_s = 2\omega_p - \omega_i$ is filtered with dichroic mirrors and sent to a spectrometer (SILVER-Nova Stellar). For a given seed frequency ω_i, the recorded spectrum gives one horizontal slice of the JSI. The full JSI is composed of all the recorded spectra obtained by sweeping the seed wavelength. The seed power is monitored in order to take into account any power change when tuning ω_i and to normalize the slices. The power dependence of the
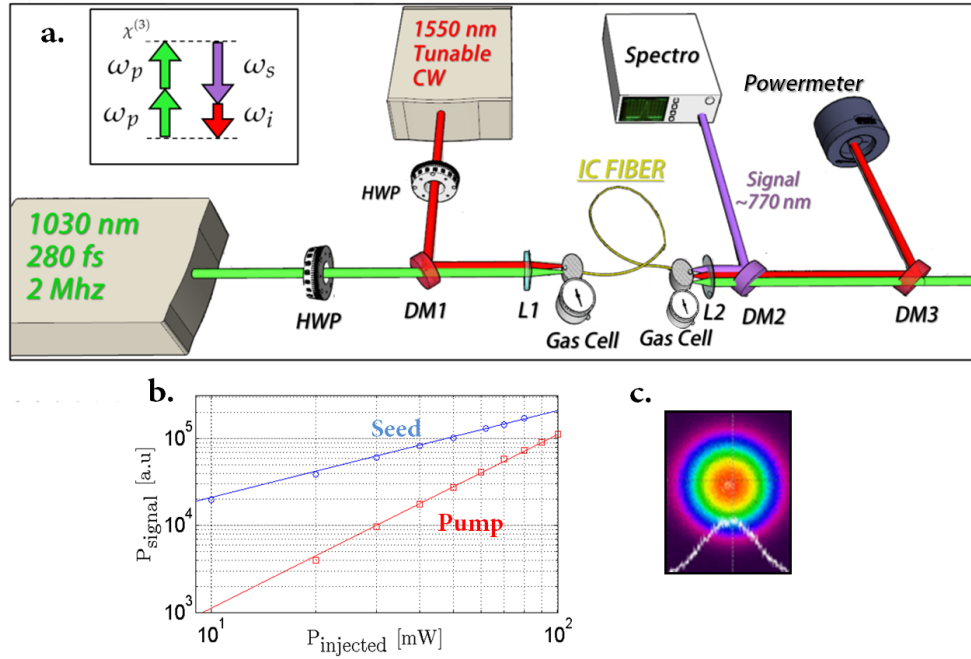
Fig. 5. (a) Experimental setup for the stimulated emission tomography. HWP: half-wave plate, L: lens, DM: Dichroic Mirror. (b) Power generated at the signal frequency as a function of the seed power (blue dots) and of the pump power (red squares), measured at the fiber output. The solid lines correspond to a perfect linear and quadratic dependence (log scale). (c) Measured spatial profile at the fiber output at pump frequency.

power generated at signal frequency as a function of pump power and seed power was measured. Figure 5(b) shows the results confirming the linear dependence versus seed power and quadratic dependence versus pump power, thus validating that our experimental results are transferable to the spontaneous regime [28–30]. Moreover, due to the low nonlinearity, self and cross-phase modulation are here negligible.

Figure 6 illustrates how, by simply changing the fiber length, the bi-photon JSI morphs from the shape of highly correlated states into that of nearly separable states. The figure shows a comparison between experimental and theoretically simulated JSI for fiber lengths going from 40 to 100 cm for the fiber filled with 3.4 bar of xenon as well as the associated Schmidt number K (since simulations assume a flat phase, it is actually a lower bound of K). With a length of 1 meter, the phase matching function and the energy conservation function have about the same width, resulting in an almost factorable state. Decreasing the length implies an increase of the phase matching function width $\Delta\phi$, which gives an increasingly correlated JSI. In the current setup, the minimum fiber length is limited to around 30 cm, mostly due to the size of the two gas cells. The lobe-shaped region in the top right corner of the JSI profile is attributed to the non perfect Gaussian spectral shape of the pump laser pulses. Such shape is due to residual self-phase modulation taking place within the laser and which could be removed using appropriate filters or pulse shaping techniques. The parameters used in the simulation are $t = 630$ nm, $R_{\text{eff}} = 22$ μm and $P = 3.4$ bar.
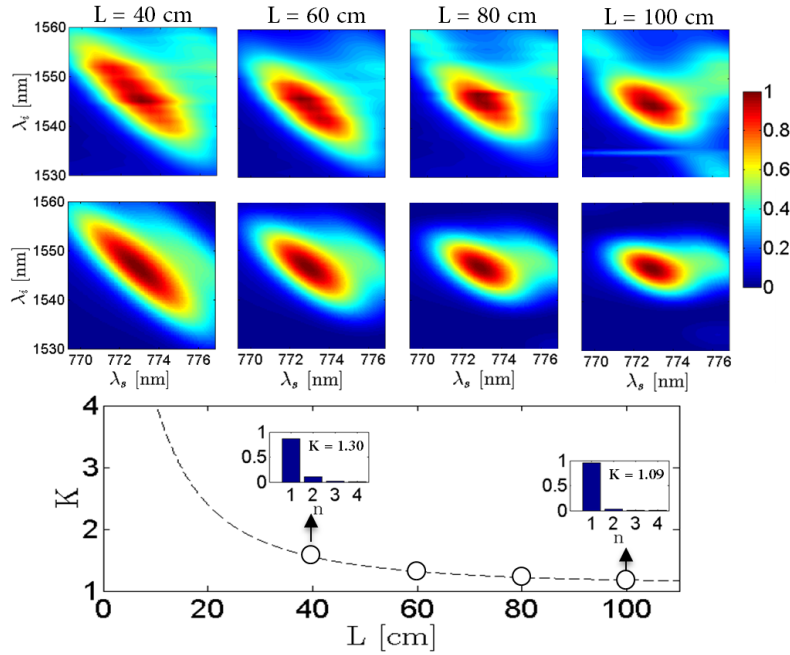
Fig. 6. Top, comparison between experimental (1st row) and simulated (2nd row) JSI for different fiber lengths when filled with 3.4 bar of Xe. The simulation takes into account a modulation in the Gaussian shape of the pump laser spectrum. Bottom, corresponding Schmidt number and Schmidt decomposition (assuming a flat phase).

5. Active tunability of the JSI

An extended control of the spectral properties is possible through the filling gas. Gas temperature and, more notably, pressure can be used to actively impact the dispersion and nonlinear response. The refractive index of the gas at temperature T and pressure P can be extrapolated from the general Sellmeier equation at standard temperature and pressure conditions (T_0, P_0) using:

$$n_{\text{gaz}}(\lambda, P, T) \approx \sqrt{1 + (n_{\text{gaz}}^2(\lambda, P_0, T_0) - 1).\frac{P}{P_0}.\frac{T_0}{T}} \tag{5}$$

The overall dispersion in Eq. (4) results from a competition between the gas dispersion on one side, which is pressure- and temperature-dependent, and the guide dispersion on the other side. Thus, depending on the weight of one relative to the other, the overall dispersion is more or less sensitive to a change of gas refractive index. For instance, fibers with large core have a lower waveguide dispersion. Consequently they will be more sensitive to a change of gas refractive index, caused by a pressure modification. Alternatively, smaller core or fiber filled with light atomic weight gases, will be less sensitive to a change of gas refractive index as the waveguide dispersion will be predominant.

Using the same fiber, we demonstrate this effect by characterizing the JSI of the source as a function of gas pressure, for two different gases, namely argon and xenon (see Fig. 7). Noble gases have been chosen because they are devoid of Raman scattering [31, 32], which eliminates the usual main source of noise in fibered photon-pair generation. The Sellmeier equations of xenon and argon are taken from [33, 34] and their non-linear indices are $n_2 = 9.2 \ 10^{-23}$ and 0.8 10^{-23} m²/W/bar, respectively [35].
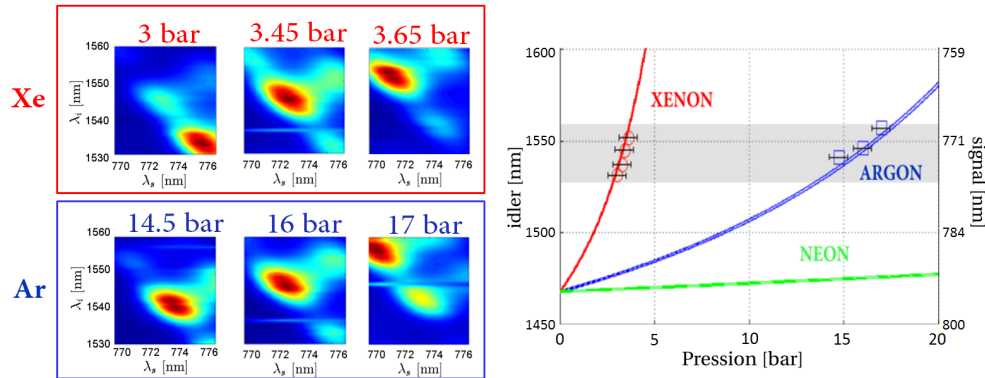
Fig. 7. Left: JSI as a function of gas pressure when filled with xenon and argon Right: Central position of the JSI idler wavelength as a function of gas pressure, for xenon (red circles) and argon (blue squares) and comparison with the simulation. The measurement range in shaded gray was limited by the tunability of the seed laser.

Increasing the pressure has two effects. Firstly, the signal and idler are generated further apart from the pump. For instance, we measured that changing the pressure from 3 bar to 3.65 bar of xenon shifts the idler wavelength from 1531 to 1551 nm and the signal wavelength from 776 to 771 nm. The recorded frequency tuning over $\Delta\omega = 17$ THz is only limited by the tunability of our seed laser. A linearization of the measured data gives a sensitivity of $\Delta\omega = 27.4$ THz/bar in Xe and 5.6 THz/bar in Ar, which can be compared with recent work on temperature tuning in solid core fibers where the reported sensitivity is 0.1 THz/°C [12]. Pressure tuning has the advantages of being compatible with long fibers and free of Raman noise as well as offering both high or low sensitivity according to the gas choice. Secondly, simulation also predicts that changing the pressure slightly rotates the angle θ of the phase matching of $\sim 6°$per bar of xenon. Adjusting θ can be used, for instance to fine-tune the purity of a heralded single photon source whereas wavelength tuning can be used for instance to aim at a specific telecom channel or atomic transition. With a tunable pump laser, it is also possible to tune the wavelength of one photon while keeping the angle constant and vice-versa.

6. Conclusion

In this paper, we demonstrate that FWM in gas-filled hollow-core fibers provides a versatile platform for generating and manipulating photon-pair states. In particular we show how the intrinsic multiband dispersion of IC fibers can be exploited to access multiband FWM and therefore various JSI shapes corresponding to spectrally factorable or correlated photon pair states. In the case of inhibited-coupling fiber, we present a model relating fiber design, filling medium and dispersion properties to allow for the design of specific fibers for given quantum information applications. It is noteworthy that this very simple model involves only three design parameters, namely fiber core diameter, strut thickness and gas refractive index without adjustable parameter whatsoever.

The experimental results obtained with noble gases validate both the model and the concept of JSI manipulation. A near-factorable JSI is experimentally demonstrated with signal and idler at visible and telecom wavelengths respectively. The effect of fiber length variation on the degree of spectral entanglement as well as the dynamic tuning of the signal and idler wavelength over 17 THz through gas pressure are in perfect agreement with the simulations. Future work will investigate the tailoring of the pump spectral properties with a pulse-shaper for an improved control of the spectral correlations as well as characterizing of the source in the photon pair

regime. Note that, for this off-the-shelf fiber design and a pump of 1 mW, the generation efficiency is expected to be on the order of 10^{-5} pairs/pulse in the spontaneous regime [36]. Furthermore, we believe that using multiband FWM to access tailored spectral correlations can be extended to other media such as for instance sequence of coupled micro-ring resonators [37, 38].

Funding

Acknowledgments

References

1. X.-L. Wang, L.-K. Chen, W. Li, H.-L. Huang, C. Liu, C. Chen, Y.-H. Luo, Z.-E. Su, D. Wu, Z.-D. Li, Y. Hu, X. Jiang, C.-Z. Peng, L. Li, N.-L. Liu, Y.-A. Chen, C.-Y. Lu, and J.-W. Pan, "Experimental ten-photon entanglement," Phys. Rev. Lett. **117**, 210502 (2016).
2. A. Mair, A. Vaziri, G. Weihs, and A. Zeilinger, "Entanglement of the orbital angular momentum states of photons," Nature **412**, 313 (2001).
3. M. Krenn, M. Huber, R. Fickler, R. Lapkiewicz, S. Ramelow, and A. Zeilinger, "Generation and confirmation of a (100× 100)-dimensional entangled quantum system," Proc. Natl. Acad. Sci. U.S.A. **111**, 6243–6247 (2014).
4. M. Malik, M. Erhard, M. Huber, M. Krenn, R. Fickler, and A. Zeilinger, "Multi-photon entanglement in high dimensions," Nat. Photonics **10**, 248 (2016).
5. B. Brecht, D. V. Reddy, C. Silberhorn, and M. Raymer, "Photon temporal modes: a complete framework for quantum information science," Phys. Rev. X **5**, 041017 (2015).
6. C. Law, I. Walmsley, and J. Eberly, "Continuous frequency entanglement: effective finite hilbert space and entropy control," Phys. Rev. Lett. **84**, 5304 (2000).
7. W. P. Grice, A. B. U'Ren, and I. A. Walmsley, "Eliminating frequency and space-time correlations in multiphoton states," Phys. Rev. A **64**, 063815 (2001).
8. A. Eckstein, A. Christ, P. J. Mosley, and C. Silberhorn, "Highly efficient single-pass source of pulsed single-mode twin beams of light," Phys. Rev. Lett. **106**, 013603 (2011).
9. O. Cohen, J. S. Lundeen, B. J. Smith, G. Puentes, P. J. Mosley, and I. A. Walmsley, "Tailored photon-pair generation in optical fibers," Phys. Rev. Lett. **102**, 123603 (2009).
10. C. Söller, B. Brecht, P. J. Mosley, L. Y. Zang, A. Podlipensky, N. Y. Joly, P. S. J. Russell, and C. Silberhorn, "Bridging visible and telecom wavelengths with a single-mode broadband photon pair source," Phys. Rev. A **81**, 031801 (2010).
11. R. Kumar, J. R. Ong, M. Savanier, and S. Mookherjea, "Controlling the spectrum of photons generated on a silicon nanophotonic chip," Nat. Comm. **5**, 5489 (2014).
12. E. Ortiz-Ricardo, C. Bertoni-Ocampo, Z. Ibarra-Borja, R. Ramirez-Alarcon, D. Cruz-Delgado, H. Cruz-Ramirez, K. Garay-Palmett, and A. U'Ren, "Spectral tunability of two-photon states generated by spontaneous four-wave mixing: fibre tapering, temperature variation and longitudinal stress," Quantum Sci. Technol. **2**, 034015 (2017).
13. M. Finger, N. Joly, P. S. J. Russell, and M. Chekhova, "Characterization and shaping of the time-frequency schmidt mode spectrum of bright twin beams generated in gas-filled hollow-core photonic crystal fibers," Phys. Rev. A **95**, 053814 (2017).
14. M. A. Finger, T. S. Iskhakov, N. Y. Joly, M. V. Chekhova, and P. S. J. Russell, "Raman-free, noble-gas-filled photonic-crystal fiber source for ultrafast, very bright twin-beam squeezed vacuum," Phys. Rev. Lett. **115**, 143602 (2015).
15. W. J. Wadsworth, N. Joly, J. C. Knight, T. A. Birks, F. Biancalana, and P. S. J. Russell, "Supercontinuum and four-wave mixing with q-switched pulses in endlessly single-mode photonic crystal fibres," Opt. Express **12**, 299–309 (2004).
16. K. Garay-Palmett, H. J. McGuinness, O. Cohen, J. S. Lundeen, R. Rangel-Rojo, A. B. U'ren, M. G. Raymer, C. J. McKinstrie, S. Radic, and I. A. Walmsley, "Photon pair-state preparation with tailored spectral properties by spontaneous four-wave mixing in photonic-crystal fiber," Opt. Express **15**, 14870–14886 (2007).
17. N. J. Cerf, M. Bourennane, A. Karlsson, and N. Gisin, "Security of quantum key distribution using d-level systems," Phys. Rev. Lett. **88**, 127902 (2002).
18. F. Benabid and P. Roberts, "Linear and nonlinear optical properties of hollow core photonic crystal fiber," J. Mod. Opt. **58**, 87–124 (2011).
19. P. S. J. Russell, P. Hölzer, W. Chang, A. Abdolvand, and J. Travers, "Hollow-core photonic crystal fibres for gas-based nonlinear optics," Nat. Photonics **8**, 278 (2014).
20. F. Couny, F. Benabid, P. Roberts, P. Light, and M. Raymer, "Generation and photonic guidance of multi-octave optical-frequency combs," Science **318**, 1118–1121 (2007).
21. N. Litchinitser, A. Abeeluck, C. Headley, and B. Eggleton, "Antiresonant reflecting photonic crystal optical waveguides," Opt. Lett. **27**, 1592–1594 (2002).

22. B. Debord, A. Amsanpally, M. Chafer, A. Baz, M. Maurel, J. Blondy, E. Hugonnot, F. Scol, L. Vincetti, F. Gérôme, and F. Benabid, "Ultralow transmission loss in inhibited-coupling guiding hollow fibers," Optica **4**, 209–217 (2017).
23. M. Zeisberger and M. A. Schmidt, "Analytic model for the complex effective index of the leaky modes of tube-type anti-resonant hollow core fibers," Sci. Rep. **7**, 11761 (2017).
24. M. Zeisberger, A. Hartung, and M. Schmidt, "Understanding dispersion of revolver-type anti-resonant hollow core fibers," Fibers **6**, 68 (2018).
25. B. Debord, M. Alharbi, T. Bradley, C. Fourcade-Dutin, Y. Wang, L. Vincetti, F. Gérôme, and F. Benabid, "Hypocycloid-shaped hollow-core photonic crystal fiber part i: Arc curvature effect on confinement loss," Opt. Express **21**, 28597–28608 (2013).
26. L. Vincetti, "Empirical formulas for calculating loss in hollow core tube lattice fibers," Opt. Express **24**, 10313–10325 (2016).
27. M. Liscidini and J. Sipe, "Stimulated emission tomography," Phys. Rev. Lett. **111**, 193602 (2013).
28. B. Fang, O. Cohen, M. Liscidini, J. E. Sipe, and V. O. Lorenz, "Fast and highly resolved capture of the joint spectral density of photon pairs," Optica **1**, 281–284 (2014).
29. K. Zielnicki, K. Garay-Palmett, D. Cruz-Delgado, H. Cruz-Ramirez, M. F. O'Boyle, B. Fang, V. O. Lorenz, A. B. U'Ren, and P. G. Kwiat, "Joint spectral characterization of photon-pair sources," J. Mod. Opt. **65**, 1141–1160 (2018).
30. A. Eckstein, G. Boucher, A. Lemaître, P. Filloux, I. Favero, G. Leo, J. E. Sipe, M. Liscidini, and S. Ducci, "High-resolution spectral characterization of two photon states via classical measurements," Laser Photonics Rev. **8**, L76–L80 (2014).
31. M. Azhar, G. Wong, W. Chang, N. Joly, and P. S. J. Russell, "Raman-free nonlinear optical effects in high pressure gas-filled hollow core pcf," Opt. Express **21**, 4405–4410 (2013).
32. K. Lynch-Klarup, E. Mondloch, M. Raymer, D. Arrestier, F. Gérôme, and F. Benabid, "Supercritical xenon-filled hollow-core photonic bandgap fiber," Opt. Express **21**, 13726–13732 (2013).
33. A. Hitachi, V. Chepel, M. I. Lopes, and V. N. Solovov, "New approach to the calculation of the refractive index of liquid and solid xenon," J. Chem. Phys. **123**, 234508 (2005).
34. A. Bideau-Mehu, Y. Guern, R. Abjean, and A. Johannin-Gilles, "Measurement of refractive indices of neon, argon, krypton and xenon in the 253.7–140.4 nm wavelength range. dispersion relations and estimated oscillator strengths of the resonance lines," J. Quant. Spectrosc. Radiat. Transf. **25**, 395–402 (1981).
35. M. Azhar, N. Joly, J. Travers, and P. S. J. Russell, "Nonlinear optics in xe-filled hollow-core pcf in high pressure and supercritical regimes," Appl. Phys. B **112**, 457–460 (2013).
36. M. Barbier, I. Zaquine, and P. Delaye, "Spontaneous four-wave mixing in liquid-core fibers: towards fibered raman-free correlated photon sources," New J. Phys. **17**, 053031 (2015).
37. J. E. Heebner, P. Chak, S. Pereira, J. E. Sipe, and R. W. Boyd, "Distributed and localized feedback in microresonator sequences for linear and nonlinear optics," J. Opt. Soc. Am. B **21**, 1818–1832 (2004).
38. J. Notaros, J. Mower, M. Heuck, C. Lupo, N. C. Harris, G. R. Steinbrecher, D. Bunandar, T. Baehr-Jones, M. Hochberg, S. Lloyd, and D. Englund, "Programmable dispersion on a photonic integrated circuit for classical and quantum applications," Opt. Express **25**, 21275–21285 (2017).

Optics Letters

Raman-tailored photonic crystal fiber for telecom band photon-pair generation

M. Cordier,[1] A. Orieux,[1,2,3] R. Gabet,[1] T. Harlé,[4] N. Dubreuil,[4] E. Diamanti,[2]
P. Delaye,[4] and I. Zaquine[1,*]

[1]*Laboratoire de Traitement et Communication de l'Information, Télécom ParisTech, Université Paris-Saclay, 75013 Paris, France*
[2]*Laboratoire d'Informatique de Paris 6, CNRS, Université Pierre et Marie Curie, Sorbonne Universités, 75005 Paris, France*
[3]*Institut de Recherche en Informatique Fondamentale, CNRS, Université Paris Diderot, Sorbonne Paris Cité, 75013 Paris, France*
[4]*Laboratoire Charles Fabry, Institut d'Optique Graduate School, CNRS, Université Paris-Saclay, 91127 Palaiseau cedex, France*
*Corresponding author: isabelle.zaquine@telecom-paristech.fr

We report on the experimental characterization of a novel nonlinear liquid-filled hollow-core photonic crystal fiber for the generation of photon pairs at a telecommunication wavelength through spontaneous four-wave mixing (SFWM). We show that the optimization procedure in view of this application links the choice of the nonlinear liquid to the design parameters of the fiber, and we give an example of such an optimization at telecom wavelengths. Combining the modeling of the fiber and classical characterization techniques at these wavelengths, we identify for the chosen fiber and liquid combination SFWM phase-matching frequency ranges with no Raman scattering noise contamination. This is a first step toward obtaining a telecom band fibered photon-pair source with a high signal-to-noise ratio. © 2017 Optical Society of America

Photon pairs that can give rise to either entanglement or to heralded single photons are a basic resource for quantum information protocols for quantum communications or linear optics quantum computation. Recent achievements in entangled photon pair sources are mainly based on the second-order nonlinear process of spontaneous parametric downconversion (SPDC) in bulk crystals [1,2], and in waveguides [3]. The third-order process of spontaneous four-wave mixing (SFWM) in fibers, however, is an interesting alternative toward integration in future quantum communication networks. Indeed, glass fibers are widely investigated for various nonlinear applications [4]. They can exhibit very low absorption, strong confinement over long distance, and high nonlinearities according to the chosen glass. Moreover, the various design parameters in microstructured fibers allow for precise engineering of their propagation characteristics, including for instance dispersion. Among the third-order nonlinear processes associated with propagation in glass fibers, one can cite not only parametric processes

such as third-harmonic generation or four-wave mixing that can generate new frequencies in the medium if the phase-matching condition is satisfied, but also inelastic scattering processes involving vibrational excitation modes of the medium such as Raman scattering. Due to the amorphous nature of glass, Raman scattering does not give rise to discrete lines, but to a continuous broadband spectrum. This can be very useful for realizing broadband amplifiers [5], but quite deleterious for quantum optics applications such as photon pair generation where Raman photons give rise to uncorrelated photon noise that cannot be filtered [6,7]. The resulting signal to noise ratio (SNR) limitation is an important issue for the practical use of such sources for quantum information.

In order to combine high nonlinearity with a discrete line Raman spectrum, the amorphous propagation medium can be replaced by a crystalline medium [8,9], a liquid [10], or even a gas [11]. In this last case, Raman noise can be totally eliminated when using noble gases, and nonlinearity can be obtained at the cost of very high pressure conditions in the fiber.

A very practical solution is to use liquid-filled hollow-core photonic crystal fibers (LF-HC-PCF). They have been investigated either for designing Raman wavelength converters [12–15] or, conversely, to show that the Raman lines can be avoided in order to produce high SNR photon pairs through SFWM. A near infrared LF-HC-PCF photon pair source was recently reported, exhibiting a three-order-of-magnitude suppression of the Raman noise [10].

In this Letter, we detail the influence of the liquid on the guiding properties of the hollow-core photonic crystal fiber, and we show how the optimization of the microstructured fiber and liquid combination can provide low loss, Raman-free spectral zones in the selected telecom transmission band where photon pairs can be generated through FWM by satisfying the phase-matching condition. Avoiding the spectral overlap of the two nonlinear processes can lead to a substantial increase of the SNR of the pair generation. We demonstrate the first nonlinear LF-HC-PCF with a transmission band and a zero dispersion wavelength (ZDW) in the telecom wavelength range as a first step toward a Raman-free photon pair source at such

wavelengths. Prior to the description of the performed experimental characterizations, we give a modeling of the changes in the linear optical properties of the fiber induced by the liquid filling. These investigations show the strong links between fiber and liquid parameters that must be taken into account in order to satisfy all the requirements of a photon pair source.

The properties of the empty fiber and the choice of the liquid are related through the mapping of the transmission band of the filled fiber to the target SFWM phase-matching range. The ZDW is the reference wavelength around which the phase-matching condition can be satisfied. It should be ideally situated close to the middle of the transmission band in order to obtain a broad range of possible signal and idler wavelength pairs, which can be calculated from the dispersion properties of the filled fiber. The choice of the liquid is also constrained by its nonlinear coefficient, which determines the pair generation efficiency and its low absorption losses in the telecom range. Therefore, LF-HC-PCFs provide a very versatile platform, allowing the engineering of linear and nonlinear properties through both fiber microstructure design and liquid optimization. This Letter is based on the use of commercial fibers and focused on the choice of the best associated liquid.

On the practical side, both core and cladding are filled with the chosen liquid: by placing both ends of the fiber in tanks, the fiber automatically gets filled through capillarity. Liquids with relatively low viscosity (1 mPa.s) will therefore be selected in order to limit the fiber-filling process duration. The non-toxicity (or low toxicity) of the liquid is also taken into account. In this fully filled fiber, the photonic bandgap guiding property is conserved, despite the reduced index contrast between the glass part and the filled holes [16]. Any characteristic wavelength λ_{empty} of the transmission band of the empty fiber is shifted to λ_{filled} in the following way, where the refractive index of a medium is noted n_{medium} [15,16]:

$$\lambda_{\text{filled}} = \lambda_{\text{empty}} \sqrt{\frac{n_{\text{silica}}^2 - n_{\text{liquid}}^2}{n_{\text{silica}}^2 - n_{\text{air}}^2}}. \tag{1}$$

To operate near the telecom wavelength of 1.55 μm, the empty PCF transmission must be centered well beyond 1.55 μm. We have chosen two commercial fibers (NKT Photonics) with transmission bands centered on 2.3 μm (called Fiber A) and 2 μm (called Fiber B). Equation (1) provides a first estimation of the liquid refractive index range (1.25–1.29) in order to shift the transmission window to the telecom band. Fluorocarbon liquids can be used with the further advantage of a low absorption in this range. In order to predict precisely the dispersion properties of the filled fiber, we investigated numerically the impact of the filling on the transmission window for various combinations of fibers and liquids. The finite-difference frequency-domain (FDFD) simulations [17] are based on a reconstructed fiber geometry. The parameters are directly extracted from SEM images of the fiber (see Fig. 1). It is noteworthy that the parameters of pentagons and hexagons around the core are slightly different from the rest of the cladding, as shown in Ref. [18]. The limited precision in fiber parameter extraction and the uncertainty of the exact refractive index value of the liquid at telecom wavelength contribute to an error on the absolute position of the ZDW. We can estimate an upper bound of ±30 nm to this error that mostly corresponds
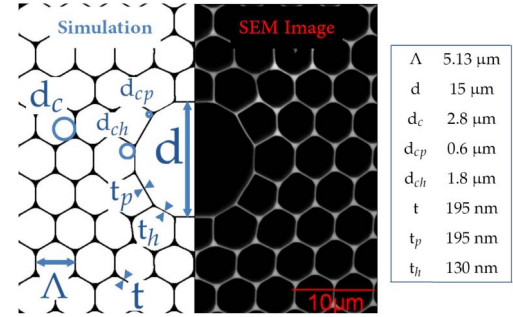

Fig. 1. Scanning electron microscope image of the microstructured region of fiber A (right part of the image) and the reconstructed geometry used for the simulation (left part), with the reconstruction parameters in the table: pitch Λ, core diameter d, diameter of the round corners of the cladding hexagons d_c, diameters of the cladding pentagons d_{cp} and hexagons d_{ch} neighboring the fiber core, cladding thickness t and cladding thickness around the fiber core t_p and t_h.

to a global shift of the group velocity dispersion (GVD) curve with no impact on the curvature. Moreover, in the case of fluorocarbon liquids selected in this Letter, we have checked that the liquid dispersion can be neglected compared to the waveguide dispersion.

Figure 2 shows the FDFD simulation results of the three tested combinations. We plot a relative refractive index, subtracting n_{zdw} (index value at the ZDW), to allow for an easier comparison of the ZDWs in the three cases.

The dispersion of the three simulated fibers has been characterized by optical low-coherence interferometry (OLCI): the interferometer experimental setup is described in Fig. 1 of Ref. [19]. The measured interferogram allows the calculation of the complex transmittivity from which the GVD of each transmitted mode is derived. Table 1 summarizes the three tested fiber characteristics. Only the fiber filled with FC3283 (perfluorotripropylamine, $C_9F_{21}N$) with a refractive index of 1.28 exhibits a ZDW close to 1.55 μm, thus satisfying the requirement for a photon pair source in the C-band. For this fiber/liquid combination, the measured inverse group-velocity β_1 of the fundamental mode is shown in Fig. 3 and compared with the simulation. The measured ZDW is 1.552 μm ± 3 nm. The FDFD simulated curve is in perfect agreement with the OLCI measurement of GVD.
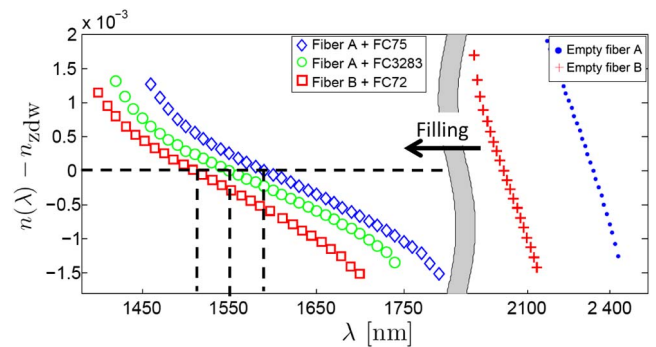

Fig. 2. Calculated effective index of the fundamental mode as a function of the wavelength. Note that the subtracted n_{zdw} has a different value for the three curves.

Table 1. Optical Properties for Different Fiber/Liquid Combinations[a]

Fiber	Liquid	n_{liquid}	ZDW (nm)
A (HC2300)	FC3283	1.28	1552
A (HC2300)	FC75	1.27	1592
B (HC2000)	FC72	1.25	≈1510
[10] (HC1550PM)	Acetone d6	1.36	896

[a]The 3M references FCxxx have been used for the fluorocarbon liquids. The NKT reference HCxxxx gives an approximate idea of the position of the transmission band of the empty fiber, and the ZDW of the filled fiber has been measured with OLCI. The configuration of Ref. [10] is also included for comparison.

This technique also gives access to the dispersion of higher propagation modes which can highlight coupling between different guided modes. We are especially interested in trying to avoid surface modes that can induce anti-crossing with the fundamental mode [21]. In such a case, the guided mode would then be a combination of the fundamental mode and a surface mode, with a higher overlap with the silica structure therefore inducing more losses, dispersion, and Raman noise. We have checked that the chosen fiber-liquid combination does not exhibit such an anti-crossing in a 100 nm wide window around the ZDW where the photon pairs will be generated.

The nonlinearity of the LF-HC-PCF is also an important parameter for the optimization of the SNR of the photon pair generation. Because we use the fundamental propagation mode with a low overlap with the silica structure, it is determined solely by the nonlinear index of the liquid. We measure the nonlinear index of the FC3283 through self-phase modulation (SPM) broadening of square spectrum pulses, using the setup described in Ref. [22]. The transmission spectra measured for increasing incident power are shown in the left graph of Fig. 4. Whereas the spectrum at low power exhibits a square shape, a symmetric spectral broadening is observed for increasing power, characterizing the SPM induced by an optical Kerr effect. By comparing with simulated spectra, the nonlinear phase shift $\Phi_{NL} = n_2 \frac{2\pi L}{A_{eff}\lambda} P_{peak}$ can be derived from the measured spectral broadening, with n_2 being the nonlinear refractive index, L being the fiber length, A_{eff} being the effective area, λ being the wavelength, and P_{peak} being the peak power injected in the fiber mode. The square spectral shape of the pump pulses
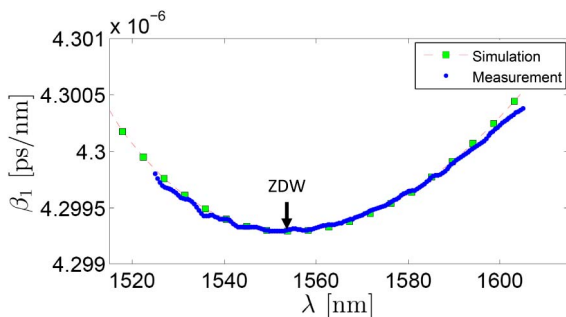

Fig. 3. Inverse group velocity of the fundamental mode for the Fiber A/FC3283 combination (1) measured with OLCI (blue dots) and (2) calculated with the FDFD simulation (green squares). The index of the liquid is adjusted to 1.283 instead of the reported value of 1.281 measured in the visible range [20].
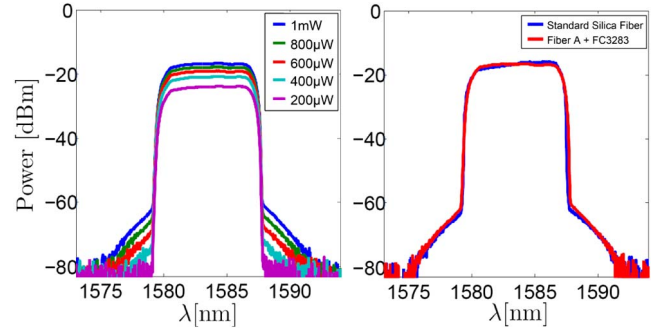

Fig. 4. Laser delivers 1.1 ps pulses (close to Fourier transform) with a 50 MHz repetition rate; the peak power is 18 W for 1 mW average power. Left, spectra of the square wave pulse generator transmitted by the fiber for different levels of injected power; right, a comparison between the fiber under study and a standard polarization-maintaining fiber.

offers an improved sensitivity in measuring low nonlinear phase shifts. The lowest nonlinear phase shift observed at 400 μW (see the pedestals on the spectra) is about 4 mrad. A nonlinear phase shift of $\Phi_{NL} = 10$ mrad is obtained for an average power of 1 mW in the LF-HC-PCF. This measured value is of the order of the one obtained with a polarization-maintaining silica fiber of the same length (Fig. 4). Taking into account the experimental parameters and the characteristics of the fiber ($A_{eff} = 95$ μm^2, $L = 1$ m), this leads to an estimated nonlinearity of the chosen liquid FC3283 $n_2 = 1.1 \times 10^{-20}$ m^2/W. This nonlinear coefficient, together with experimental parameters depending on the chosen setup, will determine the conversion efficiency of the SFWM process in this LF-HC-PCF.

It is noteworthy that nonlinearities as large as two orders of magnitude higher than silica can be obtained with other liquids, such as carbon disulfide (hence, giving rise to a four order-of-magnitude increase in the SFWM efficiency). These high nonlinearities are often associated with a high refractive index, thus requiring the use of fibers with glass index higher than silica. Higher index glass HC-PCFs have been reported [23,24], but they remain more difficult to obtain than silica HC-PCF.

From the classical linear and nonlinear characterization presented in the previous part and from the Raman spectrum of the FC3283 (see Fig. 5), we can predict the SFWM phase-matching curve of the fiber and identify Raman-free zones for the photon pair generation. In the case of SFWM with degenerate pumps, signal and idler frequencies are constrained by the energy $2\omega_p = \omega_s + \omega_i$ and momentum conservation $2\beta(\omega_p) = \beta(\omega_s) + \beta(\omega_i)$, where $\omega_{p,s,i}$ and $\beta(\omega_{p,s,i})$, respectively, refer to the frequencies and wavevector of the pump, signal, and idler photons [4]. We define the phase-matching function $F(\omega_{p0}, \Delta\omega)$ as

$$F = \text{sinc}^2\left((2\beta(\omega_{p0}) - \beta(\omega_{p0} + \Delta\omega) - \beta(\omega_{p0} - \Delta\omega))\frac{L}{2}\right), \quad \textbf{(2)}$$

with L being the fiber length and $\Delta\omega = \omega_{p0} - \omega_i = \omega_s - \omega_{p0}$ being the frequency difference between the pump and idler or signal and pump.

The phase-matching function F, calculated in the case of a strict energy conservation for a pump frequency ω_{p0}, can also be
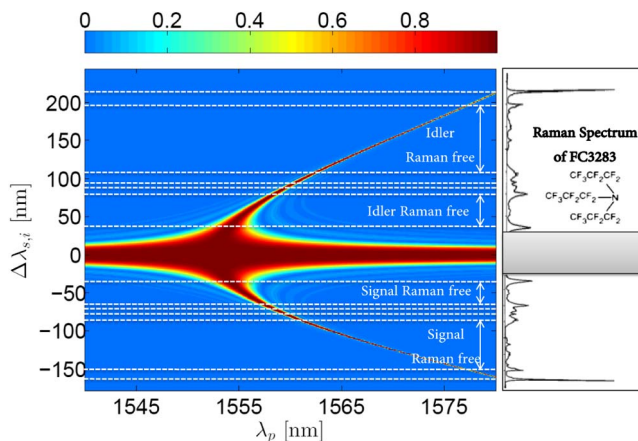
Fig. 5. Left, calculated probability density spectrum F of emission of the pairs through SFWM and Raman lines (white dashed lines) as a function of the pump wavelength λ_p and the relative signal or idler wavelength $\Delta\lambda_{s,i} = \lambda_{s,i} - \lambda_p$. Right, Raman spectrum of the chosen fluorocarbon liquid perfluorotripropylamine, $C_9F_{21}N$, FC3283, reproduced with permission from [25].

seen as a normalized probability density spectrum of photon pair emission in the LF-HC-PCF. Its dependence with pump wavelength and relative signal or idler wavelength is shown in Fig. 5. This two-dimensional plot allows us to choose the experimental parameters: in the central red zone corresponding to degeneracy of the signal and idler wavelengths, it is difficult to separate the photon pairs from the pump. We are rather interested in the quasi-parabolic parts on both sides with a large wavelength separation between the signal and idler photons. The superimposition of the Raman lines of the liquid on this map shows the pump spectral ranges for which signal and idler photons can be generated away from the Raman noise.

We have shown that the choice of the liquid allows us to engineer both linear and non linear properties of a LF-HC-PCF and, more specifically, the ZDW position, the nonlinear coefficient, and the Raman-free zones. In this way, the phase-matching wavelength range of the four-wave mixing process and the photon pair generation efficiency can be optimized with respect to the Raman line position. For a given commercial fiber, we have identified at least one liquid that satisfies all requirements toward the realization of a LF-HC-PCF Raman-free photon pair source, with a ZDW in the desired telecom range and a nonlinear coefficient comparable to what is obtained with silica. Therefore, all the elements of a high SNR fibered photon pair source at telecom wavelength, fully operating at room temperature, are gathered. Moreover, the engineering of nonlinearity and spectral correlation of the signal and idler photons could be further improved using a fiber especially designed for this purpose. With the possibility to design specific fibers and to use various glass and liquid media, the investigation of such a versatile fiber medium at telecom wavelength can give rise not only to high quality sources, but also to a variety of devices and, therefore, have a large impact on quantum communication network development.

REFERENCES

1. M. Giustina, M. A. Versteegh, S. Wengerowsky, J. Handsteiner, A. Hochrainer, K. Phelan, F. Steinlechner, J. Kofler, J.-Å. Larsson, C. Abellán, W. Amaya, V. Pruneri, M. W. Mitchell, J. B. T. Gerrits, A. E. Lita, L. K. Shalm, S. W. Nam, T. Scheidl, R. Ursin, B. Wittmann, and A. Zeilinger, Phys. Rev. Lett. **115**, 250401 (2015).
2. L. K. Shalm, E. Meyer-Scott, B. G. Christensen, P. Bierhorst, M. A. Wayne, M. J. Stevens, T. Gerrits, S. Glancy, D. R. Hamel, M. S. Allman, K. J. Coakley, S. D. Dyer, C. Hodge, A. E. Lita, V. B. Verma, C. Lambrocco, E. Tortorici, A. L. Migdall, Y. Zhang, D. R. Kumor, W. H. Farr, F. Marsili, M. D. Shaw, J. A. Stern, C. Abellán, W. Amaya, V. Pruneri, T. Jennewein, M. W. Mitchell, P. G. Kwiat, J. C. Bienfang, R. P. Mirin, E. Knill, and S. W. Nam, Phys. Rev. Lett. **115**, 250402 (2015).
3. O. Alibart, V. D'Auria, M. De Micheli, F. Doutre, F. Kaiser, L. Labonté, T. Lunghi, E. Picholle, and S. Tanzilli, J. Opt. **18**, 104001 (2016).
4. G. P. Agrawal, *Nonlinear Fiber Optics* (Academic, 2007).
5. J. Bromage, J. Lightwave Technol. **22**, 79 (2004).
6. J. Fulconis, O. Alibart, W. Wadsworth, P. St.J. Russell, and J. Rarity, Opt. Express **13**, 7572 (2005).
7. Q. Lin, F. Yaman, and G. P. Agrawal, Phys. Rev. A **75**, 023803 (2007).
8. Q. Lin and G. P. Agrawal, Opt. Lett. **31**, 3140 (2006).
9. I. Agha, M. Davanço, B. Thurston, and K. Srinivasan, Opt. Lett. **37**, 2997 (2012).
10. M. Barbier, I. Zaquine, and P. Delaye, New J. Phys. **17**, 053031 (2015).
11. F. Benabid and P. Roberts, J. Mod. Opt. **58**, 87 (2011).
12. S. Lebrun, P. Delaye, R. Frey, and G. Roosen, Opt. Lett. **32**, 337 (2007).
13. M. C. Phan Huy, A. Baron, S. Lebrun, R. Frey, and P. Delaye, J. Opt. Soc. Am. B **27**, 1886 (2010).
14. S. Lebrun, C. Buy, P. Delaye, R. Frey, G. Pauliat, and G. Roosen, J. Nonlinear Opt. Phys. Mater. **19**, 101 (2010).
15. S. Lebrun, M. C. Phan Huy, P. Delaye, and G. Pauliat, Proc. SPIE **10021**, 1002104 (2016).
16. G. Antonopoulos, F. Benabid, T. Birks, D. Bird, J. Knight, and P. St.J. Russell, Opt. Express **14**, 3000 (2006).
17. A. B. Fallahkhair, K. S. Li, and T. E. Murphy, J. Lightwave Technol. **26**, 1423 (2008).
18. K. Z. Aghaie, M. J. Digonnet, and S. Fan, J. Lightwave Technol. **31**, 1015 (2013).
19. R. Gabet, P. Hamel, Y. Jaouën, A.-F. Obaton, V. Lanticq, and G. Debarge, J. Lightwave Technol. **27**, 3021 (2009).
20. W. Hasi, Z. Lu, S. Gong, S. Liu, Q. Li, and W. He, Appl. Opt. **47**, 1010 (2008).
21. J. A. West, C. M. Smith, N. F. Borrelli, D. C. Allan, and K. W. Koch, Opt. Express **12**, 1485 (2004).
22. S. Serna, J. Oden, M. Hanna, C. Caer, X. Le Roux, C. Sauvan, P. Delaye, E. Cassan, and N. Dubreuil, Opt. Express **23**, 29964 (2015).
23. F. Désévédavy, G. Renversez, J. Troles, P. Houizot, L. Brilland, I. Vasilief, Q. Coulombier, N. Traynor, F. Smektala, and J.-L. Adam, Opt. Mater. **32**, 1532 (2010).
24. X. Jiang, T. Euser, A. Abdolvand, F. Babic, F. Tani, N. Joly, J. Travers, and P. St.J. Russell, Opt. Express **19**, 15438 (2011).
25. V. S. Gorelik, A. V. Chervyakov, L. I. Zlobina, and O. N. Sharts, Proc. SPIE **3855**, 16 (1999).

SCIENTIFIC REP♦RTS

OPEN

Tailoring modal properties of inhibited-coupling guiding fibers by cladding modification

Jonas H. Osório [1], Matthieu Chafer[1,2], Benoît Debord[1,2], Fabio Giovanardi[3], Martin Cordier[4], Martin Maurel[1,2], Frédéric Delahaye[1,2], Foued Amrani[1,2], Luca Vincetti [3], Frédéric Gérôme[1,2] & Fetah Benabid[1,2]

Understanding cladding properties is crucial for designing microstructured optical fibers. This is particularly acute for Inhibited-Coupling guiding fibers because of the reliance of their core guidance on the core and cladding mode-field overlap integral. Consequently, careful planning of the fiber cladding parameters allows obtaining fibers with optimized characteristics such as low loss and broad transmission bandwidth. In this manuscript, we report on how one can tailor the modal properties of hollow-core photonic crystal fibers by adequately modifying the fiber cladding. We show that the alteration of the position of the tubular fibers cladding tubes can alter the loss hierarchy of the modes in these fibers, and exhibit salient polarization propriety. In this context, we present two fibers with different cladding structures which favor propagation of higher order core modes – namely LP_{11} and LP_{21} modes. Additionally, we provide discussions on mode transformations in these fibers and show that one can obtain uncommon intensity and polarization profiles at the fiber output. This allows the fiber to act as a mode intensity and polarization shaper. We envisage this novel concept can be useful for a variety of applications such as hollow core fiber based atom optics, atom-surface physics, sensing and nonlinear optics.

Intense efforts have been devoted to hollow-core photonic crystal fiber (HCPCF) research since its first proposal in 1995[1]. In the latest years, HCPCFs have revealed themselves as a great platform for the understanding of the waveguiding mechanisms and as an excellent tool for addressing diverse applications needs.

HCPCF can guide light by photonic bandgap (PBG)[1] or Inhibited-Coupling (IC)[2] mechanisms. In PBG guiding fibers, and similarly to total-internal reflection fibers, the coupling of the core mode to the cladding is forbidden because the cladding modal spectrum is void from any propagation mode at the core guided-mode effective index-frequency space[1]. Otherwise, in IC guiding fibers, the core and cladding modes coupling is robustly minimized by having a strong mismatch in their transverse spatial phases and a small spatial overlap between their fields[2]. In this context, the confinement loss (CL) in IC fibers, in contrast with PBG ones, is strongly dependent on the core contour characteristics. This observation motivated the introduction of the hypocycloid-core contour (*i.e.* negative curvature) in 2010[3,4], which allowed to attain a dramatic reduction in the transmission losses in IC guiding HCPCFs.

Thus, a great interest was observed on the development of HCPCFs with hypocycloid-shaped cores and, in particular, on the study of single-ring tubular lattice (SR-TL) HCPCF[5]. The growing interest in this sort of fibers has been motivated by their noteworthy properties, which encompass a cladding geometric simplicity combined with the absence of connecting nodes, and allows obtaining, by virtue of IC criteria, ultralow-loss and broad spectral transmission bandwidth[6]. In this framework, research papers have been published on the optimization of SR-TL HCPCF design to reduce confinement and bend losses[6–8], to study their modal content and to achieve single-mode operation[6,9–11]. Additionally, one can find in the literature a set of investigations on the use of such fibers in applied fields as in mid-IR lasers[12], generation of single-cycle pulses[13], and sensing[14].

[1]GPPMM Group, XLIM Research Institute, CNRS UMR 7252, University of Limoges, Limoges, France. [2]GLOphotonics S.A.S., 1 avenue d'Ester, Ester Technopôle, Limoges, France. [3]Department of Engineering "Enzo Ferrari", University of Modena and Reggio Emilia, 41125, Modena, Italy. [4]Laboratoire de Traitement et Communication de l'Information, Télécom ParisTech, Université Paris-Saclay, 75013, Paris, France. Correspondence and requests for materials should be addressed to F.B. (email: f.benabid@xlim.fr)

SR-TL HCPCFs transmit light by IC guiding[2]. In SR-TL HCPCFs, the lattice tubes define an hypocycloid core contour, which lowers the spatial overlap between core and cladding modes. Additionally, it is endowed with a silica microstructure which is void of structural nodes (which support low azimuthal number modes and disfavor IC guidance)[6].

As in SR-TL HCPCFs the core contour is demarcated by the tubes that forms the fiber cladding, the definition of their geometric parameters are of great importance for designing the fiber properties. For instance, by adequately choosing the diameter, the thickness and the number of tubes in the cladding, the researcher can design fibers with different core sizes, predict the spectral location of the transmission bands and the losses levels which are suitable for the desired application[6,15].

Here, in a different fashion, we study and demonstrate that the alteration of the azimuthal position of the cladding tubes can favor the propagation of higher order core modes, *i.e.*, by adequately choosing the spacing of selected cladding tubes, it is possible to tailor the fiber modal properties and alter the loss hierarchy of the modes in the fiber. To achieve this goal, we used the findings of the detailed study on the Poynting vector in the transverse plane of SR-TL HCPCF available in[6], which concluded that the power leakage through the spacing between the lattice tubes is strongly increased when this spacing between them is enlarged.

Thus, here, we explore this concept both theoretically and experimentally by studying and developing two tubular fibers whose lowest loss modes are the LP_{11} and LP_{21}, instead of the LP_{01}. We believe that such control feature on the mode loss hierarchy is unprecedented in optical fiber.

Additionally, we present experiments on mode transformations in these fibers with modified cladding structures. We show that interesting output intensity profiles can be obtained. In particular, for one of the studied fibers, the superposition of LP_{01} and LP_{11} modes entails an LP_{11}-like intensity profile in the fiber output with unusual orthogonal polarization sites. Remarkably, if the input light polarization is conveniently adjusted, these orthogonal polarization regions can be individually or simultaneously excited. We envisage that these properties can be useful for atom optics and sensing experiments.

Simulation Results

Figure 1 summarizes numerical simulation results for three SR-TL HCPCFs fiber designs (FD). The first FD (see top left of the panel Fiber Design #0 of Fig. 1a) is a SR-TL HCPCF with 10 tubes and constant spacing between the tubes, used here as a reference to study the properties of the novel designs proposed in the following. The second FD consists of a cladding with 8 tubes and two larger gaps defining an angle of 180° between them (Fiber Design #1) and a third fiber with 8 tubes and four larger gaps apart 90° with respect to each other (Fiber Design #2). The fibers have same core diameter (45 μm) and same tubes sizes (outer diameter D = 15 μm and thickness t = 750 nm). FD #1 is obtained from FD #0 structure by simply removing two tubes on the horizontal axis. The obtained larger gaps measure 20.2 μm. FD #2, in turn, has the same number of tubes than FD #1 but a different azimuthal distribution of the same. Thus, in FD #2, we obtain two pairs of larger gaps, one along the horizontal direction and the other along the vertical one. The larger gaps in FD #2 are narrower than in FD #1 and they measure 12.3 μm.

In Fig. 1, each of the FD panels shows the fiber structure transverse profile (top left), its effective index (top right), and the CL spectrum of the most representative core modes that can be guided through the fibers – namely the LP_{01}, LP_{11} and LP_{21} modes (medium of the panel). The intensity profiles of these modes are shown in the bottom left. The bottom right of the panel shows the corresponding Poynting vector transverse component. It is noteworthy that TE_{01}-like, TM_{01}-like and HE_{21}-like modes were found in the simulations of FD #0 and FD #2 due to its 10-fold and 4-fold symmetry, respectively. However, in FD #1, owing to its 2-fold symmetry, LP_{11}-like modes were obtained in the simulations. In order to have homogeneous results between the different fibers under test, we choose to analyze LP-like mode profiles and adopt the LP notation for simplicity. Within this context, the LP_{11}-like modes profiles for FD #0 and FD #2 were obtained by a suitable superposition of the TE_{01}-like, TM_{01}-like and HE_{21}-like modes found in the simulations[16]. Additionally, as LP modes with same azimuthal number can exhibit different field distributions, here we define as LP_{11a} the mode with the two lobes along the vertical direction and as LP_{11b} the mode having the two lobes along the horizontal one. Moreover, it is true that for each field distribution there are two different polarizations. Since the numerical results show a weak dependence on the polarization in the investigated fibers, we emphasize that we only consider the vertically polarized LP-like modes in our analyses for simplicity.

The effective indices plots show comparable dispersion curves for the three FD. In contrast, the plots for the CL reveal that the alteration of the azimuthal position of the cladding tubes in the fiber structure allows changing the modes losses hierarchy. For FD #0, as expected, the simulation results show that the LP_{01} is the core mode with lowest CL figures (with losses around 3.6 dB/km at 1000 nm), followed by the higher order modes. Instead, we see that, for FD #1, the inclusion of larger gaps between the tubes at 180° enhances more than two decades the CL for the fundamental mode LP_{01} and for the modes LP_{11b}, while keeping low impact in the CL of the LP_{11a} and LP_{21} modes. It entails that, for FD #1, the mode with lowest loss is the LP_{11a} mode, whose CL is calculated to be 33 dB/km at 1000 nm – not so different than the loss of the same mode in FD #0 (12 dB/km).

In this context, it is also remarkable that FD #1 geometry entails very different loss figures among the modes of LP_{11} family. It is noteworthy that the LP_{11a} mode, which has the zero electric field line separating the two lobes passing through the larger gaps, exhibits much lower losses than the LP_{11b}, which has the zero line passing through a narrower gap. The larger gaps between the cladding tubes in the horizontal direction causes the LP_{11b} mode field to spread towards the silica jacket, which strongly deteriorates its confinement and highly increases its loss from 11 dB/km to 16500 dB/km at 1000 nm. Also, the LP_{21} mode has the zero line passing through the larger gaps and, thus, shows a weak dependence on them. At 1000 nm, its CL passes from 70 dB/km in FD #0 to 360 dB/km in FD #1. Finally, it is worthy observing in Fig. 1 that the larger gaps in the FD #1 cladding enhances the difference
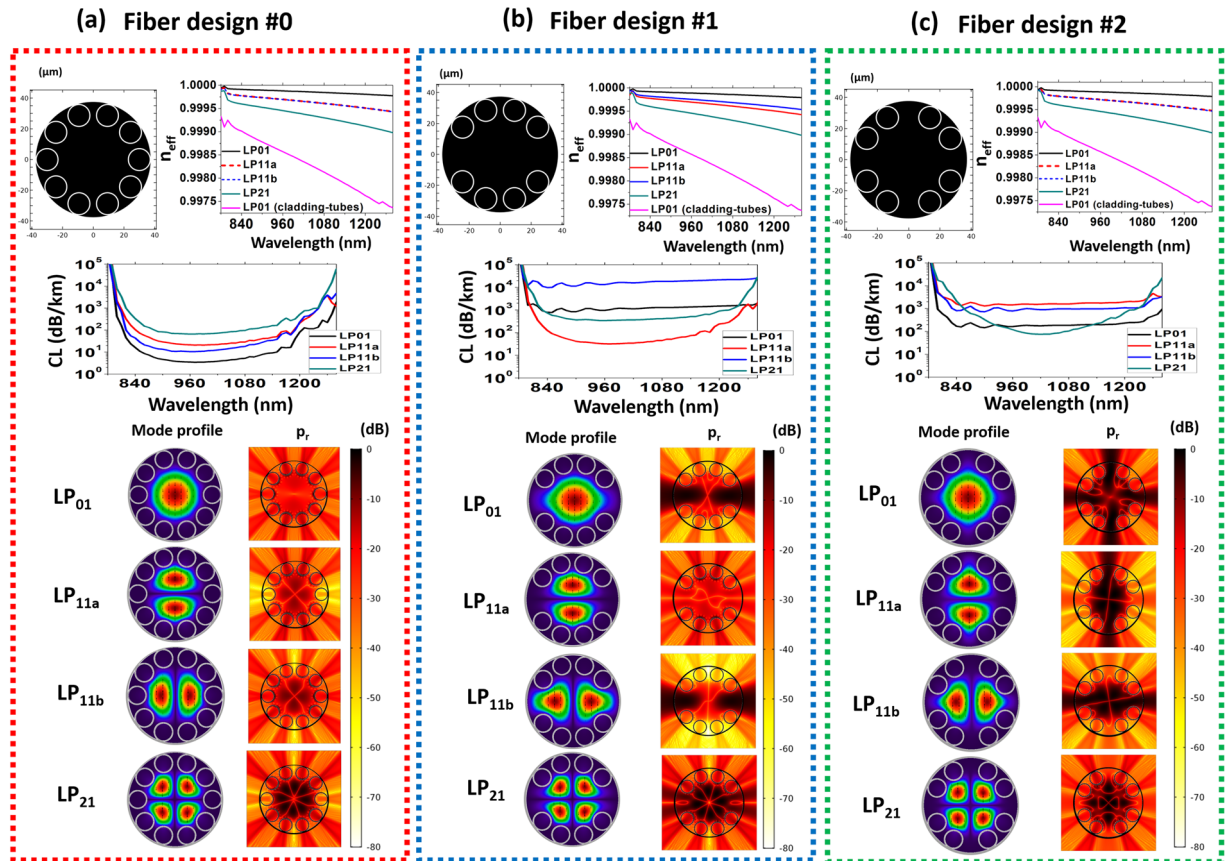
Figure 1. Schematic diagram for the cross sections of the studied fibers; plots for the effective refractive index (n_{eff}) and CL as a function of the wavelength for LP$_{01}$ (black curve), LP$_{11a}$ (red curve), LP$_{11b}$ (blue curve) and LP$_{21}$ (green curve); mode profiles and color map for the radial component of the Poynting vector (p_r – in logarithmic scale, at the wavelength of 1000 nm) for LP$_{01}$, LP$_{11a}$, LP$_{11b}$ and LP$_{21}$. (**a**) Fiber design #0: tubular fiber with identical gap between the lattice tubes. (**b**) Fiber design #1: tubular fiber with two bigger gaps at 180°; (**c**) Fiber design #2: tubular fiber with four bigger gaps at 90°. In the effective refractive index plots, the cladding tubes HE$_{11}$ (LP$_{01}$) dispersion (pink curves) is shown for comparison.

between the effective refractive indexes of LP$_{11a}$ and LP$_{11b}$ modes. At 1000 nm, the difference between their effective refractive indices is 7×10^{-5}.

Furthermore, by observing in Fig. 1 the FD #2 figures, we can observe that the addition of four larger gaps defining an angle of 90° between each other again allows to change the modes losses hierarchy. For this fiber, the inclusion of the bigger gaps at 90° deteriorates the losses of the LP$_{11}$ mode, causing the modes with lowest losses to be the LP$_{21}$ and LP$_{01}$ modes. In particular, at 1000 nm, the mode with the lowest loss is the LP$_{21}$ one with CL around 80 dB/km.

The explanation of how the alteration of the azimuthal position of the cladding tubes can modify the modes losses hierarchy is centered on the fact that the power leakage through the spacing between the cladding tubes is strongly increased when this spacing is larger[6]. To address this point, we calculated the power flux along the fiber radial direction for the most representative modes guided through the fibers. The density of power flowing along the radial direction is accounted by the normalized radial component of the Poynting vector, p_r, given by Eq. (1), where $\vec{E}$ and $\vec{H}$ are the electric and magnetic fields of the mode, $\hat{r}$ is the radial unit vector, and p_z the maximum value of the longitudinal component of the Poynting vector[6]. The results of these simulations are shown in Fig. 1, where p_r (at the wavelength of 1000 nm) is plotted in logarithm scale.

$$p_r = \frac{1}{2p_z} \vec{E} \times \vec{H^*} \cdot \hat{r}$$

(1)

It is seen that, for FD #0, the main channel for mode leakage is the direction along the lattice tubes instead of the gaps between the same. For the mode LP$_{01}$, the electric field distribution does not depend on the azimuthal angle. This results in a symmetric p_r distribution on the fiber cross-section plane. Conversely, the modes with non-zero azimuthal number exhibit one or more zero lines in the electric field distribution. For these modes, the p_r distributions show that the flux along these zero electric field lines is significantly lower. For the mode LP$_{11a}$,
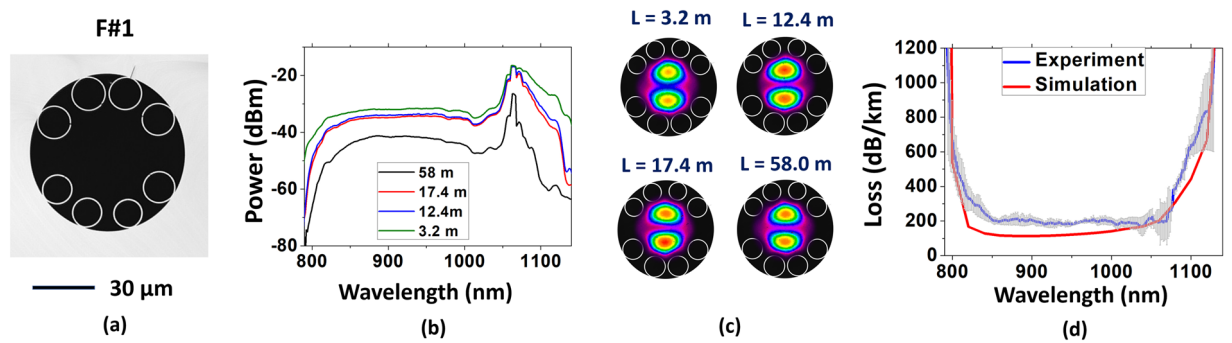
Figure 2. (**a**) Cross section of the fiber with two bigger gaps at 180° (F#1), (**b**) the transmitted spectra and (**c**) the near field profiles for different lengths. (**d**) Measured loss for the LP_{11} mode (blue line) together with the simulated CL (red line).
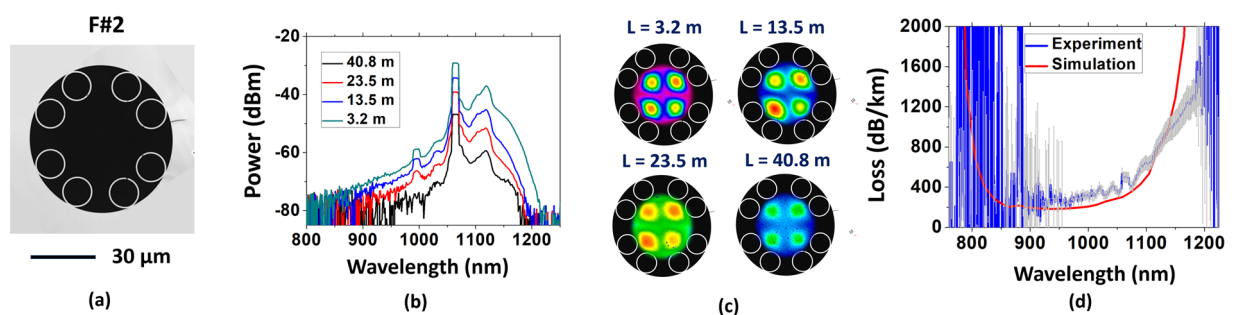

Figure 3. (**a**) Cross section of the fiber with four bigger gaps at 90° (F#2), (**b**) the transmitted spectra and (**c**) the near field profiles for different lengths. (**d**) Measured loss for the LP_{21} mode (blue line) together with the simulated CL (red line).

this corresponds to the horizontal axis and, for LP_{11b}, to the vertical direction. For the mode LP_{21}, zero electric field lines exist along horizontal and vertical directions.

In FD #1, the larger spacing between the lattice tubes in the horizontal direction causes the gap between the tubes to be the main channel for power leakage of LP_{01} and LP_{11b}. In fact, by comparing CL figures of FD #0 and FD #1 we can observe that the CL of LP_{01} and LP_{11b} significantly increase whereas the variation for the CL of LP_{11a} and LP_{21} is much weaker. As a consequence of that, in FD #1, the LP_{11a} mode becomes the lowest loss one. This property is confirmed by the results of FD #2. In this case, the only mode having zero electric field lines along the direction of the two pairs of larger gaps (and, thus, low p_r along these directions) is the LP_{21} mode. Therefore, it exhibits the lowest CL in this fiber (around 1000 nm wavelength).

To stress that the change in the modes loss hierarchy in these fibers is due to the modification in the fiber cladding rather than any resonant coupling of the core modes to the cladding, we provide in Fig. 1 the dispersion curve for the fundamental mode of the cladding tubes (pink line). We see there is a great difference between the core modes effective refractive indexes and the effective refractive index of the fundamental mode in the cladding tubes, which excludes the possibility of resonant coupling between them.

Ergo, we can observe that the CL hierarchy of the fiber modes can be effectively tailored by working on the tubular fibers cladding unit-cell. In this approach, we take into account the field distributions of the core modes and strategically enlarge selected gaps between the cladding tubes in order to favor the propagation of higher order modes.

Fiber Fabrication and Loss Measurement

To experimentally study the results attained in the simulations, we performed the fabrication of two different fibers, which reproduced the characteristics of the ones studied in the last section (Figs 2a and 3a show their cross sections). The fibers were fabricated by using stack-and-draw technique. Here, we refer to the fabricated fibers as F#1 and F#2 to avoid confusion with the simulated ones. F#1 structure has larger gaps between the tubes defining an angle of 180° between them. F#2 has, instead, larger gaps at 90° between each other. The larger gaps between the tubes in F#1 measure (17.0 ± 0.2) μm while the smaller ones measure (4 ± 1) μm. In F#2, the larger gaps between the lattice tubes measure (9.2 ± 0.8) μm and the smaller ones (3.4 ± 0.4) μm.

Cutback measurements were performed in order to account for LP_{11} and LP_{21} losses in F#1 and F#2 respectively. To achieve this, we optimized the input coupling conditions to obtain the LP_{11} and LP_{21} profiles at the fibers output before performing the cutback. It was done by both offsetting the input beam from the fiber center and/ or by conveniently tilting it. Figure 2b show the transmitted spectra through F#1 for different fiber lengths. For each fiber length, the output beam profile is recorded to ensure that only the mode of interest is excited. Figure 2c
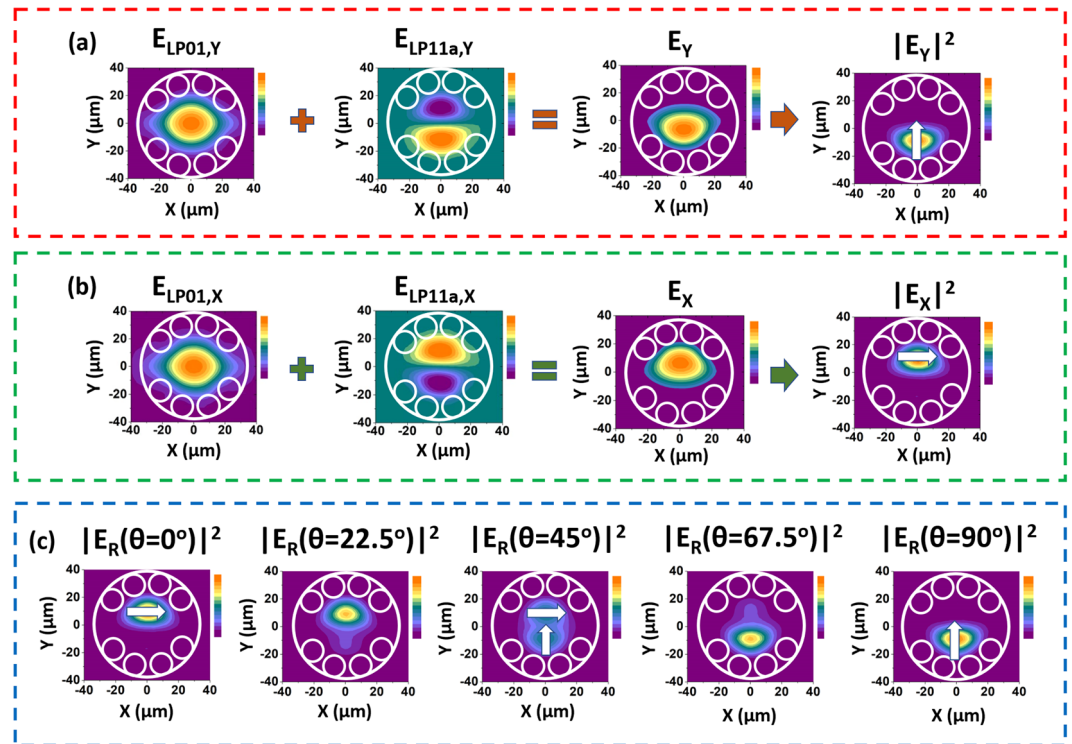
Figure 4. (**a**) Electric field profiles of $LP_{01,Y}$, $LP_{11a,Y}$, and of the superposition of these modes in FD #1 ($E_{LP01,Y}$, $E_{LP11a,Y}$ and E_Y). $|E_Y|^2$ stands for the intensity profile. (**b**) Electric field profiles of $LP_{01,X}$, $LP_{11a,X}$, and of the superposition of these modes in FD #1 ($E_{LP01,X}$, $E_{LP11a,X}$ and E_X). $|E_X|^2$ stands for the intensity profile. (**c**) Resultant intensity profile for the superposition of the LP_{01} and LP_{11a} modes as a function of the input polarization angle (θ). Arrows represent the electric field.

shows the reconstructed near field profiles for the spectra presented in Fig. 2b. Here, the camera images were superposed to the fiber cross section to help visualization. The results shown in Fig. 2c readily demonstrate that the measured loss (Fig. 2d, blue line) stands for the LP_{11} mode loss in F#1, measured to be 200 dB/km for wavelengths around 1000 nm. Also, it is shown in Fig. 2d the CL for LP_{11} which was simulated from a model based of the fiber microscopy image (red line). A good agreement is seen between simulated and experimental results.

Analogously, Fig. 3b show the transmitted spectra through F#2 for different fiber lengths when the fiber output was that of the LP_{21} mode (near field profiles available in Fig. 3c, with camera images superposed to the fiber cross section to help visualization). The measured loss for the LP_{21} mode in F#2 was accounted as 300 dB/km for wavelengths around 1000 nm (Fig. 3d). Similarly to F#1, the simulated CL for LP_{21} mode in F#2 (red line) compares well with the measured results. It is noteworthy that it is the first time that exciting selectively LP_{11} or LP_{21} over such long section of fiber of this type is reported.

Mode Transformations In Modified Cladding Fibers

Although the tubular fibers with modified cladding we study herein can favor the propagation of higher order modes and change the modes losses hierarchy in the fibers, we can, by adequately tuning the coupling conditions, excite combinations of the modes supported by the fiber structure. Indeed, we could, by conveniently tuning the light launching conditions, obtain LP_{01}-like and LP_{11}-like mode profiles in F#1 output, and LP_{01}-like, LP_{11}-like, and LP_{21}-like mode profiles in F#2 output. The observation of these mode profiles is consistent to the modal content of F#1 and F#2 measured using spectral and spatial imaging technique (S^2 technique)[17], which detected that LP_{01} and LP_{11} contributions in F#1 output and LP_{01}, LP_{11} and LP_{21} contributions in F#2 output.

In this section, we show that owing to the possibility to excite combinations of these modes on one hand and, on the other, due to their particular polarization properties, we can generate interesting output intensity profiles with unusual intensity profile and polarization distributions. The fiber, thus, acts as a mode intensity and polarization shaper.

As an example, we investigated the superposition of LP_{01} and LP_{11a} modes in FD #1 to illustrate the fiber intensity and polarization shaping capability. Figure 4a,b show the simulated electric field distributions of vertically and horizontally polarized LP_{01} and LP_{11a} modes ($E_{LP01,Y}$, $E_{LP01,X}$, $E_{LP11a,Y}$ and $E_{LP11a,X}$), and the electric field and intensity profile which results from their superposition (E_Y, E_X, $|E_Y|^2$ and $|E_X|^2$), calculated according to Eq. (2) and Eq. (3). In Eqs (2) and (3), α, β, γ, and δ are constants that account for the contributions of the $LP_{01,Y}$, $LP_{11a,Y}$, $LP_{01,X}$ and $LP_{11a,X}$ modes to the output profile. The E_Y, E_X, $|E_Y|^2$ and $|E_X|^2$ profiles shown in Fig. 4 were calculated for $\alpha = 0.75$, $\beta = 0.25$, $\gamma = 0.75$, and $\delta = 0.25$.
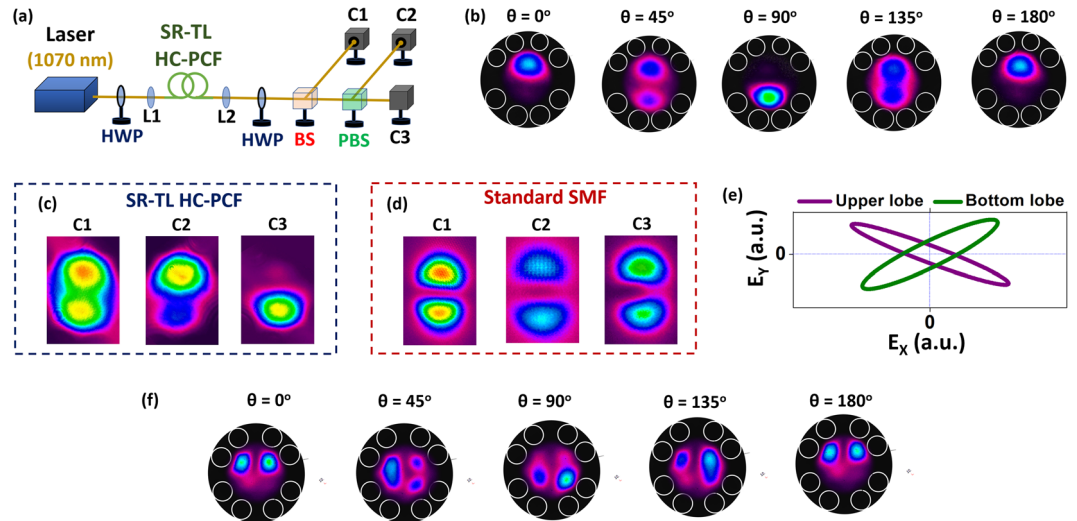
Figure 5. (**a**) Experimental setup for the mode transformations characterizations. HWP: half-wave plate; L1 and L2: lenses; BS: beam splitter; PBS: polarizing beam splitter; C1, C2 and C3: CCD cameras. (**b**) Output intensity profile of F#1 measured in C1 for different input polarization angles. Output intensity profiles measured in C1, C2 and C3 for (**c**) F#1 and for (**d**) a standard telecom optical fiber. (**e**) Polarization ellipses from polarimeter data for upper and bottom lobes in the LP_{11}-like profile of F#1 output. (**f**) Output intensity profile of F#2 measured in C1 for different input polarization angles. In (**b,f**) the camera images were superposed to the fiber cross section for better visualization.

$$E_Y = \alpha\, E_{LP01,Y} + \beta\, E_{LP11a,Y} \tag{2}$$

$$E_X = \gamma\, E_{LP01,X} + \delta\, E_{LP11a,X} \tag{3}$$

In Fig. 4a, we observe that a y-polarized lobe at the bottom half of the core can be obtained if vertically polarized light is launched into the fiber. Otherwise, Fig. 4b shows that, if horizontally polarized light is coupled into the fiber, an x-polarized lobe at the upper half of the core is obtained.

An interesting outcome of the above properties is seen when we examine a beam with such modal content after passing through a polarizer which axes are defined by an angle θ with respect to the horizontal plane. The resulting intensity is given by Eq. (4):

$$|E_R(\theta)|^2 = [(\gamma\, E_{LP01,X} + \delta\, E_{LP11a,X})\cos\theta]^2 + [(\alpha\, E_{LP01,Y} + \beta\, E_{LP11a,Y})\sin\theta]^2 \tag{4}$$

Figure 4c shows the intensity profiles for different θ values (obtained by using α = 0.75, β = 0.25, γ = 0.75, and δ = 0.25). It is observed that, as the polarization angle is changed, the output intensity profile is altered so that a LP_{11}-like mode profile with unusual orthogonal polarization regions can be obtained when θ = 45°. This is remarkable and very different from the usual electric field configuration of a LP_{11} mode output, whose electric field orientation at the lobes are parallel. When θ = 0° and θ = 90°, we obtain, respectively, the x- and y-polarized lobes at the upper and bottom halves of the core, which is consistent to Fig. 4a,b results.

The experimental demonstration of this intensity spatial-mode shaping principle was carried for both F#1 and F#2, and it is shown in Fig. 5. The setup employed (Fig. 5a) uses a diode laser at 1070 nm to couple into the fiber under test, CCD cameras (C1, C2 and C3) for beam profile recording, and polarizing optical components to control the beam polarization at fiber input and at the different output ports.

Figure 5b presents the output LP_{11}-like intensity profiles measured in C1 for different input polarization angles (θ) for a 3.6 m long F#1 (the camera images were superposed to the fiber cross section to help visualization). We observe that, consistently with the simulations shown in Fig. 4c, the alteration of the input light polarization allows obtaining the bottom lobe, the upper lobe or both lobes in the fiber output. Additionally, Fig. 5c exhibits that, for the situation in which the fiber output has the two-lobed LP_{11}-like profile (observed in C1), the detected profiles in C2 and C3 are that of the upper and bottom lobes respectively. As C2 and C3 are placed at different ports of the PBS, we conclude that the lobes in the output profile of the F#1 have orthogonal polarization states, as the simulations have predicted. For comparison, we show in Fig. 5d the profiles detected in C1, C2 and C3 when F#1 is replaced by a 1 m long standard telecom fiber (singlemode at 1550 nm, but which supports few modes at 1070 nm). The procedure for LP_{11} excitation in the telecom fiber was the same than the one performed to couple the higher order modes in the tubular fibers – the input beam was conveniently offset and tilted to obtain the desirable output profile. As expected, the lobes of the LP_{11} mode in the telecom fiber have parallel polarization direction and, therefore, the mode profile is not split by the PBS. The property of having an LP_{11}-like output profile with orthogonal polarization sites is, therefore, remarkable and very particular to the tubular fiber design we study herein.

Additionally, we measured, by replacing C1 by a polarimeter, the polarization state of each lobe in F#1 output profile individually. It was done by selectively blocking the LP_{11}-like profile lobes and launching the resulting light into the polarimeter. Figure 5e shows the polarization ellipses measured in the polarimeter for both lobes. The ellipticity (ε) of the polarization ellipses was measured as 0.15 and 0.21 for the upper and bottom lobe respectively. The crossed orientation of the polarization ellipses shown in Fig. 5e confirms that the lobes in F#1 output intensity profile have indeed mutually orthogonal polarization states.

Furthermore, we show in Fig. 5f that it is also possible to tune the output intensity profile shape when using F#2. For this one, we see that the rotation of the input polarization angle (θ) allows to obtain two lobes at the bottom or at the upper part of the core at the fiber output, which, once again, is very distinctive. By simply rotating the polarization angle, we can obtain a variety of intensity profile such as ones with two and three lobes.

Conclusion

In conclusion, we theoretically and experimentally investigated the properties of IC guiding tubular fibers with modified cladding structures. A strategic modification of the azimuthal position of the tubular fiber cladding tubes allows altering the mode losses hierarchy in these fibers. To study this new concept, we studied two novel fibers with modified cladding structures, which favored the propagation of LP_{11} and LP_{21} modes. In addition, we showed that it is possible to work on the combinations of the modes in the fibers with modified cladding in order to obtain interesting intensity and polarization profiles at the fiber output. We believe that this concept will be useful for new experiments in HCPCF based sensing, atom optics, atom-surface interaction and nonlinear optics. For example, in alkali atom filled HCPCF experiments such as the ones reported in[1], the ability to excite the atoms with such intensity profiles could be useful to assess the contribution of the atom-surface interaction compared to a Gaussian-like profile. Also, the capability to excite selectively such polarization dependent modes would open the control parameter space in nonlinear optical experiments. Furthermore, it should also be said that the loss levels reported here could be reduced if a cladding structure with lower confinement loss such as nested cladding tubes is used[7]. Finally, the results reported herein reinforce the idea that a deep understanding of the fiber cladding is key for designing IC guiding optical fibers with the desired characteristics and performances.

Data Availability

The data that support the findings of this study are available from the corresponding author upon reasonable request.

References

1. Birks, T. A., Roberts, P. J., Russell, P. S. J., Atkin, D. M. & Shepherd, T. J. Full 2-D photonic bandgaps in silica/air structures. *Electronics Letters* **31**, 1941–1943 (1995).
2. Couny, F., Benabid, F., Roberts, P. J., Light, P. S. & Raymer, M. G. Generation and photonic guidance of multi-octave optical-frequency combs. *Science* **318**, 1118–1121 (2007).
3. Wang, Y. Couny, F., Roberts, P. J. & Benabid, F. Low loss broadband transmission in optimized core-shape Kagome hollow-core PCF. In *Conference on Lasers and Electro-Optics* (OSA, 2010), paper CPDB4.
4. Wang, Y. Y., Wheeler, N. V., Couny, F., Roberts, P. J. & Benabid, F. Low loss broadband transmission in hypocycloid-core Kagome hollow-core photonic crystal fiber. *Optics Letters* **36**, 669–671 (2011).
5. Pryamikov, A. D. *et al*. Demonstration of a waveguide regime for a silica hollow-core microstructured optical fiber with a negative curvature of the core boundary in the spectral region >3.5 μm. *Optics Express* **19**, 1441–1448 (2011).
6. Debord, B. *et al*. Ultralow transmission loss in inhibited-coupling guiding hollow fibers. *Optica* **4**, 209–217 (2017).
7. Belardi, W. & Knight, J. Hollow antiresonant fibers with reduced attenuation. *Optics Letters* **39**, 1853–1856 (2014).
8. Frosz, M. H., Roth, P., Günendi, M. C. & Russell, P. S. J. Analytical formulation for the bend loss in single-ring hollow-core photonic crystal fibers. *Photonics Research* **5**, 81–91 (2017).
9. Newkirk, A. V. *et al*. Modal analysis of antiresonant hollow core fibers using S² imaging. *Optics Letters* **41**, 3277–3280 (2016).
10. Uebel, P. *et al*. Broadband robustly single-mode hollow-core PCF by resonant filtering of higher-order modes. *Optics Letters* **41**, 1961–1964 (2016).
11. Edavalath, N. N. *et al*. Higher-order mode suppression in twisted single-ring hollow-core photonic crystal fibers. *Optics Letters* **42**(11), 2074–2077 (2017).
12. Hassan, M. R. A., Yu, F., Wadsworth, W. J. & Knight, J. C. Cavity-based mid-IR fiber gas laser pumped by a diode laser. *Optica* **3**, 218–221 (2016).
13. Balciunas, T. *et al*. A strong-field driver in the single-cycle regime based on self-compression in a kagome fibre. *Nature Communications* **6**, 6117, https://doi.org/10.1038/ncomms7117 (2015).
14. Giovanardi, F., Cucinotta, A. & Vincetti, L. Inhibited coupling guiding hollow fibers for label-free DNA detection. *Optics Express* **25**, 26215–26220 (2017).
15. Vincetti, L. Empirical formulas for calculating loss in hollow core tube lattice fibers. *Optics Express* **24**, 10313–10325 (2016).
16. Marcatili, E. & Schmeltzer, R. Hollow metallic and dielectric waveguides for long distance optical transmission and lasers. *Bell. Syst. Tech.* **43**, 1783–1809 (1964).
17. Nicholson, J. W., Yablon, A. D., Ramachandran, S. & Ghalmi, S. Spatially and spectrally resolved imaging of modal content in large-mode-area fibers. *Optics Express* **16**, 7233–7243 (2008).

Acknowledgements

Author Contributions

J.H.O., M.Ch., B.D., F.D., F.A. and F.Ge. worked on the fiber fabrication. J.H.O., M.Ch. and F.Ge. worked on fiber loss measurements. J.H.O., F.Gi. and L.V. worked on the simulations. J.H.O., M.M. and F.D. performed S² measurements. J.H.O. and M.Co. worked on the model for the modal transformations. J.H.O. performed the experiments on the modal transformations and wrote the paper. F.B. coordinated the research project. All the authors discussed the results and reviewed the manuscript.

Additional Information

Competing Interests: The authors declare no competing interests.

Publisher's note: Springer Nature remains neutral with regard to jurisdictional claims in published maps and institutional affiliations.

List of Publications and Conferences

Publications

[1] Martin Cordier, Philippe Delaye, Matthieu Chafer, Fetah Benabid, and Isabelle Zaquine. *Raman-free fibered photon-pair generation in hollow-core fiber.* In preparation.

[2] Martin Cordier, Adeline Orieux, Benoit Debord, Frédéric Gérome, Alexandre Gorse, Matthieu Chafer, Eleni Diamanti, Philippe Delaye, Fetah Benabid, and Isabelle Zaquine. *Active engineering of four-wave mixing spectral entanglement in multiband hollow-core fibers.* Opt. Express, 27(7):9803, 2019

[3] Jonas H Osorio, Matthieu Chafer, Benoit Debord, Fabio Giovanardi, Martin Cordier, Martin Maurel, Frederic Delahaye, Foued Amrani, Luca Vincetti, Frédéric Gérome, et al. *Tailoring modal properties of inhibited-coupling guiding fibers by cladding modification.* Scientific reports, 9(1):1376, 2019.

[4] M. Cordier, A. Orieux, R. Gabet, T. Harlé, N. Dubreuil, E. Diamanti, P. Delaye, and I. Zaquine. *Raman-tailored photonic crystal fiber for telecom band photon-pair generation.* Opt. Lett., 42(13):2583-2586, Jul 2017.

Communications

Oral Presentations: (*presenter)

[CLEO Europe 2019*] *Controllable Photon-Pair Spectral Correlations*

[CLEO Europe 2019] *Core modal spatial-structuring in inhibited-coupling hollow-core fibers*

[CLEO US 2018*] *Shaping photon-pairs time-frequency correlations in inhibited-coupling hollow-core fibers*

[CLEO US 2018] *Mode transformation in an inhibited-coupling guiding asymmetric tubular hollow fiber*

[CEWQO 2018*] *Experimental demonstration of inhibited-coupling hollow-core fibers for shaping photon-pair time-frequency correlations*

[QIM 2017*] *Liquid Filled Photonic Crystal Fiber : A Flexible Tool For Fibered Photon-Pair Generation*

[CLEO Europe 2017*] *Correlation engineering for a flexible Raman free fibered photon source*

[CLEO Europe 2017] *Influence of fibre homogeneity on Four Wave Mixing pair generation*

[EOSAM 2016*] *Toward a Raman-free fibered photon pair source at telecom wavelength*

Posters:

[GdR IQFA 2018] *Polymorphic Photon-Pair Spectral Correlations*

[ICIQP 2018*] *Engineering four-wave mixing spectral entanglement in hollow-core fibers*

[GdR IQFA 2018*] *Polymorphic Photon-Pair Spectral Correlations*

[QIM 2017] *Constraints on photonic crystal fibers homogeneity for photon pair generation*

[GdR IQFA 2016*] *Liquid Filled Photonic Crystal Fiber Photon-Pair Source For Quantum Information*

[JNOG 2016*] *Vers une source de paires de photons aux longueurs d'onde télécom en fibre à coeur liquide*

[YQIS 2015*] *Towards Raman-free Entangled Photon Pairs Generation in Liquid-filled Hollow-core Photonic Crystal Fibers*

Bibliography

[1] David P DiVincenzo. The physical implementation of quantum computation. *Fortschritte der Physik: Progress of Physics*, 48(9-11):771–783, 2000.

[2] Paul G Kwiat, Klaus Mattle, Harald Weinfurter, Anton Zeilinger, Alexander V Sergienko, and Yanhua Shih. New high-intensity source of polarization-entangled photon pairs. *Physical Review Letters*, 75(24):4337, 1995.

[3] Jianwei Wang, Stefano Paesani, Yunhong Ding, Raffaele Santagati, Paul Skrzypczyk, Alexia Salavrakos, Jordi Tura, Remigiusz Augusiak, Laura Mančinska, Davide Bacco, et al. Multidimensional quantum entanglement with large-scale integrated optics. *Science*, page eaar7053, 2018.

[4] Matthew A Hall, Joseph B Altepeter, and Prem Kumar. Drop-in compatible entanglement for optical-fiber networks. *Optics express*, 17(17):14558–14566, 2009.

[5] Matthew A Hall, Joseph B Altepeter, and Prem Kumar. Ultrafast switching of photonic entanglement. *Physical review letters*, 106(5):053901, 2011.

[6] Chuang Liang, Kim Fook Lee, Todd Levin, Jun Chen, and Prem Kumar. Ultra stable all-fiber telecom-band entangled photon-pair source for turnkey quantum communication applications. *Optics express*, 14(15):6936–6941, 2006.

[7] Shellee D Dyer, Burm Baek, and Sae Woo Nam. High-brightness, low-noise, all-fiber photon pair source. *Optics express*, 17(12):10290–10297, 2009.

[8] Milja Medic, Joseph B Altepeter, Matthew A Hall, Monika Patel, and Prem Kumar. Fiber-based telecommunication-band source of degenerate entangled photons. *Optics letters*, 35(6):802–804, 2010.

[9] Qiang Zhou, Wei Zhang, Tian-zhu Niu, Shuai Dong, Yi-dong Huang, et al. A polarization maintaining scheme for 1.5 μm polarization entangled photon pair generation in optical fibers. *The European Physical Journal D*, 67(9):202, 2013.

[10] Brian J Smith, P Mahou, Offir Cohen, JS Lundeen, and IA Walmsley. Photon pair generation in birefringent optical fibers. *Optics express*, 17(26):23589–23602, 2009.

[11] Bin Fang, Offir Cohen, and Virginia O Lorenz. Polarization-entangled photon-pair generation in commercial-grade polarization-maintaining fiber. *JOSA B*, 31(2):277–281, 2014.

[12] Jay E Sharping, Jun Chen, Xiaoying Li, Prem Kumar, and Robert S Windeler. Quantum-correlated twin photons from microstructure fiber. *Optics Express*, 12(14):3086–3094, 2004.

[13] JG Rarity, J Fulconis, J Duligall, WJ Wadsworth, and P St J Russell. Photonic crystal fiber source of correlated photon pairs. *Optics express*, 13(2):534–544, 2005.

[14] Jérémie Fulconis, Olivier Alibart, Jeremy L O'Brien, William J Wadsworth, and John G Rarity. Nonclassical interference and entanglement generation using a photonic crystal fiber pair photon source. *Physical Review Letters*, 99(12):120501, 2007.

[15] J Fan, MD Eisaman, and A Migdall. Bright phase-stable broadband fiber-based source of polarization-entangled photon pairs. *Physical Review A*, 76(4):043836, 2007.

[16] Elizabeth A Goldschmidt, Matthew D Eisaman, Jingyun Fan, Sergey V Polyakov, and Alan Migdall. Spectrally bright and broad fiber-based heralded single-photon source. *Physical Review A*, 78(1):013844, 2008.

[17] Matthaeus Halder, Jeremie Fulconis, Ben Cemlyn, Alex Clark, Chunle Xiong, William J Wadsworth, and John G Rarity. Nonclassical 2-photon interference with separate intrinsically narrowband fibre sources. *Optics express*, 17(6):4670–4676, 2009.

[18] Offir Cohen, Jeff S. Lundeen, Brian J. Smith, Graciana Puentes, Peter J. Mosley, and Ian A. Walmsley. Tailored photon-pair generation in optical fibers. *Physical review letters*, 102(12):123603, 2009.

[19] Govind P Agrawal. *Nonlinear fiber optics*. Academic press, 2007.

[20] JS Wang, EM Vogel, and E Snitzer. Tellurite glass: a new candidate for fiber devices. *Optical materials*, 3(3):187–203, 1994.

[21] C Xiong, LG Helt, AC Judge, GD Marshall, MJ Steel, JE Sipe, and BJ Eggleton. Quantum-correlated photon pair generation in chalcogenide as 2 s 3 waveguides. *Optics express*, 18(15):16206–16216, 2010.

[22] Fetah Benabid. Hollow-core photonic bandgap fibre: new light guidance for new science and technology. *Philosophical Transactions of the Royal Society of London A: Mathematical, Physical and Engineering Sciences*, 364(1849):3439–3462, 2006.

[23] Francesco Poletti, Marco N Petrovich, and David J Richardson. Hollow-core photonic bandgap fibers: technology and applications. *Nanophotonics*, 2(5-6):315–340, 2013.

[24] M Azhar, GKL Wong, W Chang, NY Joly, and P St J Russell. Raman-free nonlinear optical effects in high pressure gas-filled hollow core pcf. *Optics express*, 21(4):4405–4410, 2013.

[25] Margaux Barbier, Isabelle Zaquine, and Philippe Delaye. Spontaneous four-wave mixing in liquid-core fibers: towards fibered raman-free correlated photon sources. *New Journal of Physics*, 17(5):053031, 2015.

[26] Martin A Finger, Timur Sh Iskhakov, Nicolas Y Joly, Maria V Chekhova, and Philip St J Russell. Raman-free, noble-gas-filled photonic-crystal fiber source for ultrafast, very bright twin-beam squeezed vacuum. *Physical review letters*, 115(14):143602, 2015.

[27] MA Finger, NY Joly, P St J Russell, and MV Chekhova. Characterization and shaping of the time-frequency schmidt mode spectrum of bright twin beams generated in gas-filled hollow-core photonic crystal fibers. *Physical Review A*, 95(5):053814, 2017.

[28] Warren Paul Grice. *Interference and Indistinguishability in Ultrafast Spontaneous Parametric*. PhD thesis, University of Rochester, 1997.

[29] Margaux Barbier. *Génération de paires de photons corrélés par mélange à quatre ondes spontané dans des fibres microstructurées à coeur liquide*. PhD thesis, Institut d'Optique Graduate School, 2014.

[30] Robert W Boyd. Nonlinear optics. In *Handbook of Laser Technology and Applications (Three-Volume Set)*. Taylor & Francis, 2003.

[31] KJ Blow, Rodney Loudon, Simon JD Phoenix, and TJ Shepherd. Continuum fields in quantum optics. *Physical Review A*, 42(7):4102, 1990.

[32] Nicolás Quesada and JE Sipe. Effects of time ordering in quantum nonlinear optics. *Physical Review A*, 90(6):063840, 2014.

[33] Hiroki Takesue and Kaoru Shimizu. Effects of multiple pairs on visibility measurements of entangled photons generated by spontaneous parametric processes. *Optics Communications*, 283(2):276–287, 2010.

[34] K. Garay-Palmett, H. J. McGuinness, Offir Cohen, J. S. Lundeen, R. Rangel-Rojo, A. B. U'ren, M. G. Raymer, C. J. McKinstrie, S. Radic, and I. A. Walmsley. Photon pair-state preparation with tailored spectral properties by spontaneous four-wave mixing in photonic-crystal fiber. *Optics express*, 15(22):14870–14886, 2007.

[35] Bryn Bell, Alex McMillan, Will McCutcheon, and John Rarity. Effects of self- and cross-phase modulation on photon purity for four-wave-mixing photon pair sources. *Physical Review A*, 92(5), November 2015.

[36] Warren P Grice, Alfred B U'Ren, and Ian A Walmsley. Eliminating frequency and space-time correlations in multiphoton states. *Physical Review A*, 64(6):063815, 2001.

[37] CK Law, IA Walmsley, and JH Eberly. Continuous frequency entanglement: effective finite hilbert space and entropy control. *Physical Review Letters*, 84(23):5304, 2000.

[38] A Yu Bogdanov, Yu I Bogdanov, and KA Valiev. Schmidt modes and entanglement in continuous-variable quantum systems. *Russian Microelectronics*, 35(1):7–20, 2006.

[39] Peter J Mosley, Jeff S Lundeen, Brian J Smith, and Ian A Walmsley. Conditional preparation of single photons using parametric downconversion: a recipe for purity. *New Journal of Physics*, 10(9):093011, 2008.

[40] B Brecht, Dileep V Reddy, C Silberhorn, and MG Raymer. Photon temporal modes: a complete framework for quantum information science. *Physical Review X*, 5(4):041017, 2015.

[41] Julio T Barreiro, Tzu-Chieh Wei, and Paul G Kwiat. Beating the channel capacity limit for linear photonic superdense coding. *Nature physics*, 4(4):282, 2008.

[42] Jonathan Leach, Eliot Bolduc, Daniel J Gauthier, and Robert W Boyd. Secure information capacity of photons entangled in many dimensions. *Physical Review A*, 85(6):060304, 2012.

[43] Claude Cohen-Tannoudji, Franck Laloe, and Bernard Diu. *Mécanique quantique*, volume 3. EDP Sciences, 2017.

[44] Evan Meyer-Scott, Nicola Montaut, Johannes Tiedau, Linda Sansoni, Harald Herrmann, Tim J Bartley, and Christine Silberhorn. Limits on the heralding efficiencies and spectral purities of spectrally filtered single photons from photon-pair sources. *Physical Review A*, 95(6):061803, 2017.

[45] Jacob G Koefoed, Søren MM Friis, Jesper B Christensen, and Karsten Rottwitt. Spectrally pure heralded single photons by spontaneous four-wave mixing in a fiber: reducing impact of dispersion fluctuations. *Optics Express*, 25(17):20835–20849, 2017.

[46] Fumihiro Kaneda, Karina Garay-Palmett, Alfred B. U'Ren, and Paul G. Kwiat. Heralded single-photon source utilizing highly nondegenerate, spectrally factorable spontaneous parametric downconversion. *Optics Express*, 24(10):10733, May 2016.

[47] Justin B Spring, Paolo L Mennea, Benjamin J Metcalf, Peter C Humphreys, James C Gates, Helen L Rogers, Christoph Söller, Brian J Smith, W Steven Kolthammer, Peter GR Smith, et al. Chip-based array of near-identical, pure, heralded single-photon sources. *Optica*, 4(1):90–96, 2017.

[48] Vahid Ansari, Emanuele Roccia, Matteo Santandrea, Mahnaz Doostdar, Christof Eigner, Laura Padberg, Ilaria Gianani, Marco Sbroscia, John M Donohue, Luca Mancino, et al. Heralded generation of high-purity ultrashort single photons in programmable temporal shapes. *Optics express*, 26(3):2764–2774, 2018.

[49] Vahid Ansari, John M Donohue, Benjamin Brecht, and Christine Silberhorn. Tailoring nonlinear processes for quantum optics with pulsed temporal-mode encodings. *Optica*, 5(5):534–550, 2018.

[50] Nicolas J Cerf, Mohamed Bourennane, Anders Karlsson, and Nicolas Gisin. Security of quantum key distribution using d-level systems. *Physical Review Letters*, 88(12):127902, 2002.

[51] Jonathan Roslund, Renné Medeiros De Araujo, Shifeng Jiang, Claude Fabre, and Nicolas Treps. Wavelength-multiplexed quantum networks with ultrafast frequency combs. *Nature Photonics*, 8(2):109–112, 2014.

[52] Jingyun Fan, Alan Migdall, and Lijun Wang. A twin photon source based on all-optical fiber. *Optics and Photonics News*, 18(3):26–33, 2007.

[53] MG Raymer and IA Walmsley. Iii the quantum coherence properties of stimulated raman scattering. In *Progress in Optics*, volume 28, pages 181–270. Elsevier, 1990.

[54] Bernhard Schrader. *Infrared and Raman spectroscopy: methods and applications*. John Wiley & Sons, 2008.

[55] Jake Bromage. Raman amplification for fiber communications systems. *Journal of Lightwave Technology*, 22(1):79–93, 2004.

[56] J Fulconis, O Alibart, WJ Wadsworth, P St J Russell, and JG Rarity. High brightness single mode source of correlated photon pairs using a photonic crystal fiber. *Optics Express*, 13(19):7572–7582, 2005.

[57] Q Lin, F Yaman, and Govind P Agrawal. Photon-pair generation in optical fibers through four-wave mixing: Role of raman scattering and pump polarization. *Physical Review A*, 75(2):023803, 2007.

[58] JH Odhner, DA Romanov, and RJ Levis. Filament-based stimulated raman spectroscopy. In *Nonlinear Frequency Generation and Conversion: Materials, Devices, and Applications IX*, volume 7582, page 75820M. International Society for Optics and Photonics, 2010.

[59] Vladimir S Gorelik, Anatolii V Chervyakov, Ludmila I Zlobina, and Olga N Sharts. Raman and fluorescence spectra of fluoro-organic compounds. *Proceeding SPIE*, 3855(15):16–27, 1999.

[60] Govind P Agrawal. Nonlinear fiber optics. In *Nonlinear Science at the Dawn of the 21st Century*, pages 195–211. Springer, 2000.

[61] Jingyun Fan and Alan Migdall. A broadband high spectral brightness fiber-based two-photon source. *Optics express*, 15(6):2915–2920, 2007.

[62] Robert JA Francis-Jones, Rowan A Hoggarth, and Peter J Mosley. All-fiber multiplexed source of high-purity single photons. *Optica*, 3(11):1270–1273, 2016.

[63] John D Harvey, Rainer Leonhardt, Stéphane Coen, Gordon KL Wong, JonathanC Knight, William J Wadsworth, and Philip St J Russell. Scalar modulation instability in the normal dispersion regime by use of a photonic crystal fiber. *Optics letters*, 28(22):2225–2227, 2003.

[64] Liang Cui, Xiaoying Li, Cheng Guo, YH Li, ZY Xu, LJ Wang, and Wei Fang. Generation of correlated photon pairs in micro/nano-fibers. *Optics letters*, 38(23):5063–5066, 2013.

[65] Yong Meng Sua, John Malowicki, Masaaki Hirano, and Kim Fook Lee. Generation of high-purity entangled photon pair in a short highly nonlinear fiber. *Optics letters*, 38(1):73–75, 2013.

[66] Jun Chen, Kim Fook Lee, Chuang Liang, and Prem Kumar. Fiber-based telecom-band degenerate-frequency source of entangled photon pairs. *Optics letters*, 31(18):2798–2800, 2006.

[67] Hiroki Takesue and Kyo Inoue. 1.5-µm band quantum-correlated photon pair generation in dispersion-shifted fiber: suppression of noise photons by cooling fiber. *Optics express*, 13(20):7832–7839, 2005.

[68] Kim Fook Lee, Jun Chen, Chuang Liang, Xiaoying Li, Paul L Voss, and Prem Kumar. Generation of high-purity telecom-band entangled photon pairs in dispersion-shifted fiber. *Optics letters*, 31(12):1905–1907, 2006.

[69] Chaitali Joshi, Alessandro Farsi, Stéphane Clemmen, Sven Ramelow, and Alexander L Gaeta. Frequency multiplexing for quasi-deterministic heralded single-photon sources. *Nature communications*, 9(1):847, 2018.

[70] Feng Zhu, Wei Zhang, and Yidong Huang. Fiber-based frequency-degenerate polarization entangled photon pair sources for information encoding. *Optics express*, 24(22):25619–25628, 2016.

[71] Philip Russell. Photonic crystal fibers. *science*, 299(5605):358–362, 2003.

[72] Fetah Benabid, Jonathan C Knight, G Antonopoulos, and P St J Russell. Stimulated raman scattering in hydrogen-filled hollow-core photonic crystal fiber. *Science*, 298(5592):399–402, 2002.

[73] F Couny, Fetah Benabid, PJ Roberts, PS Light, and MG Raymer. Generation and photonic guidance of multi-octave optical-frequency combs. *Science*, 318(5853):1118–1121, 2007.

[74] F Benabid, PJ Roberts, Francois Couny, and Philip S Light. Light and gas confinement in hollow-core photonic crystal fibre based photonic microcells. *Journal of the European Optical Society-Rapid publications*, 4, 2009.

[75] Fetah Benabid and PJ Roberts. Linear and nonlinear optical properties of hollow core photonic crystal fiber. *Journal of Modern Optics*, 58(2):87–124, 2011.

[76] F Couny, Fetah Benabid, PJ Roberts, MT Burnett, and SA Maier. Identification of bloch-modes in hollow-core photonic crystal fiber cladding. *Optics Express*, 15(2):325–338, 2007.

[77] Philip S Light, François Couny, Ying Ying Wang, Natalie V Wheeler, P John Roberts, and Fetah Benabid. Double photonic bandgap hollow-core photonic crystal fiber. *Optics express*, 17(18):16238–16243, 2009.

[78] P St J Russell, P Hölzer, Wonkeun Chang, A Abdolvand, and JC Travers. Hollow-core photonic crystal fibres for gas-based nonlinear optics. *Nature Photonics*, 8(4):278, 2014.

[79] Limin Xiao, Wei Jin, MS Demokan, Hoi L Ho, Yeuk L Hoo, and Chunliu Zhao. Fabrication of selective injection microstructured optical fibers with a conventional fusion splicer. *Optics Express*, 13(22):9014–9022, 2005.

[80] Cristiano MB Cordeiro, Eliane M Dos Santos, CH Brito Cruz, Christiano JS de Matos, and Daniel S Ferreira. Lateral access to the holes of photonic crystal fibers–selective filling and sensing applications. *Optics Express*, 14(18):8403–8412, 2006.

[81] Yanyi Huang, Yong Xu, and Amnon Yariv. Fabrication of functional microstructured optical fibers through a selective-filling technique. *Applied Physics Letters*, 85(22):5182–5184, 2004.

[82] Sylvie Lebrun, Minh Châu Phan Huy, Philippe Delaye, and Gilles Pauliat. Efficient stimulated raman scattering in hybrid liquid-silica fibers for wavelength conversion. *Proceeding SPIE*, 10021(01):1002104–1002104, 2016.

[83] G Antonopoulos, Fetah Benabid, TA Birks, DM Bird, JC Knight, and P St J Russell. Experimental demonstration of the frequency shift of bandgaps in photonic crystal fibers due to refractive index scaling. *Optics Express*, 14(7):3000–3006, 2006.

[84] LG Weyer and S-C Lo. Spectra–structure correlations in the near-infrared. *Handbook of vibrational spectroscopy*, 2006.

[85] WLJ Hasi, ZW Lu, S Gong, SJ Liu, Q Li, and WM He. Investigation of stimulated brillouin scattering media perfluoro-compound and perfluoropolyether with a low absorption co-efficient and high power-load ability. *Applied optics*, 47(7):1010–1014, 2008.

[86] Vladimir S Gorelik, Anatolii V Chervyakov, Ludmila I Zlobina, and Olga N Sharts. Raman and fluorescence spectra of fluoro-organic compounds. In *Photonics East'99*, pages 16–27. International Society for Optics and Photonics, 1999.

[87] Arman B Fallahkhair, Kai S Li, and Thomas E Murphy. Vector finite difference modesolver for anisotropic dielectric waveguides. *Journal of Lightwave Technology*, 26(11):1423–1431, 2008.

[88] Kiarash Zamani Aghaie, Michel JF Digonnet, and Shanhui Fan. Experimental assessment of the accuracy of an advanced photonic-bandgap-fiber model. *Journal of Lightwave Technology*, 31(7):1015–1022, 2013.

[89] Renaud Gabet, Philippe Hamel, Yves Jaouën, Anne-Francoise Obaton, Vincent Lanticq, and Guy Debarge. Versatile characterization of specialty fibers using the phase-sensitive optical low-coherence reflectometry technique. *Journal of Lightwave Technology*, 27(15):3021–3033, 2009.

[90] James A West, Charlene M Smith, Nicholas F Borrelli, Douglas C Allan, and Karl W Koch. Surface modes in air-core photonic band-gap fibers. *Optics Express*, 12(8):1485–1496, 2004.

[91] Samuel Serna, Jérèmy Oden, Marc Hanna, Charles Caer, Xavier Le Roux, Christophe Sauvan, Philippe Delaye, Eric Cassan, and Nicolas Dubreuil. Enhanced nonlinear interaction in a microcavity under coherent excitation. *Optics express*, 23(23):29964–29977, 2015.

[92] Francesco Poletti, Angela Camerlingo, Periklis Petropoulos, and David J. Richardson. Dispersion management in highly nonlinear, carbon disulfide filled holey fibers. *IEEE Photonics Technology Letters*, 20(17):1449–1451, Sep 2008.

[93] Ryszard Stepien, Jaroslaw Cimek, Dariusz Pysz, Ireneusz Kujawa, Mariusz Klimczak, and Ryszard Buczynski. Soft glasses for photonic crystal fibers and microstructured optical components. *Optical Engineering*, 53(7):071815–071815, 2014.

[94] Frédéric Désévédavy, Gilles Renversez, Johann Troles, Patrick Houizot, Laurent Brilland, Ion Vasilief, Quentin Coulombier, Nicholas Traynor, Frédéric Smektala, and Jean-Luc Adam. Chalcogenide glass hollow core photonic crystal fibers. *Optical Materials*, 32(11):1532–1539, 2010.

[95] X Jiang, TG Euser, A Abdolvand, F Babic, F Tani, NY Joly, JC Travers, and P St J Russell. Single-mode hollow-core photonic crystal fiber made from soft glass. *Optics express*, 19(16):15438–15444, 2011.

[96] Peter D Drummond and Mark Hillery. *The quantum theory of nonlinear optics*. Cambridge University Press, 2014.

[97] Emanuel Knill, Raymond Laflamme, and Gerald J Milburn. A scheme for efficient quantum computation with linear optics. *nature*, 409(6816):46, 2001.

[98] Artur K Ekert, John G Rarity, Paul R Tapster, and G Massimo Palma. Practical quantum cryptography based on two-photon interferometry. *Physical Review Letters*, 69(9):1293, 1992.

[99] Nicolas Gisin and Rob Thew. Quantum communication. *Nature photonics*, 1(3):165, 2007.

[100] Dik Bouwmeester, Jian-Wei Pan, Klaus Mattle, Manfred Eibl, Harald Weinfurter, and Anton Zeilinger. Experimental quantum teleportation. *Nature*, 390(6660):575, 1997.

[101] Jian-Wei Pan, Dik Bouwmeester, Harald Weinfurter, and Anton Zeilinger. Experimental entanglement swapping: entangling photons that never interacted. *Physical Review Letters*, 80(18):3891, 1998.

[102] Chong-Ki Hong, Zhe-Yu Ou, and Leonard Mandel. Measurement of subpicosecond time intervals between two photons by interference. *Physical review letters*, 59(18):2044, 1987.

[103] Xi-Lin Wang, Luo-Kan Chen, Wei Li, H-L Huang, Chang Liu, Chao Chen, Y-H Luo, Z-E Su, Dian Wu, Z-D Li, et al. Experimental ten-photon entanglement. *Physical review letters*, 117(21):210502, 2016.

[104] Rainer Kaltenbaek, Bibiane Blauensteiner, Marek Żukowski, Markus Aspelmeyer, and Anton Zeilinger. Experimental interference of independent photons. *Physical review letters*, 96(24):240502, 2006.

[105] Benjamin Brecht, Andreas Eckstein, Andreas Christ, Hubertus Suche, and Christine Silberhorn. From quantum pulse gate to quantum pulse shaper—engineered frequency conversion in nonlinear optical waveguides. *New Journal of Physics*, 13(6):065029, 2011.

[106] Luis Edgar Vicent, Alfred B U'Ren, Radhika Rangarajan, Clara I Osorio, Juan P Torres, Lijian Zhang, and Ian A Walmsley. Design of bright, fiber-coupled and fully factorable photon pair sources. *New Journal of Physics*, 12(9):093027, 2010.

[107] Philip G Evans, RS Bennink, WP Grice, TS Humble, and J Schaake. Bright source of spectrally uncorrelated polarization-entangled photons with nearly single-mode emission. *Physical review letters*, 105(25):253601, 2010.

[108] Joshua W Silverstone, Raffaele Santagati, Damien Bonneau, Michael J Strain, Marc Sorel, Jeremy L O'Brien, and Mark G Thompson. Qubit entanglement between ring-resonator photon-pair sources on a silicon chip. *Nature communications*, 6:7948, 2015.

[109] Offir Cohen, Jeff S Lundeen, Brian J Smith, Graciana Puentes, Peter J Mosley, and Ian A Walmsley. Tailored photon-pair generation in optical fibers. *Physical review letters*, 102(12):123603, 2009.

[110] Christoph Söller, Benjamin Brecht, Peter J Mosley, Leyun Y Zang, Alexander Podlipen-sky, Nicolas Y Joly, P St J Russell, and Christine Silberhorn. Bridging visible and tele-com wavelengths with a single-mode broadband photon pair source. *Physical Review A*, 81(3):031801, 2010.

[111] Robert J. A. Francis-Jones, Rowan A. Hoggarth, and Peter J. Mosley. All-fiber multiplexed source of high-purity single photons. *Optica*, 3(11):1270, Nov 2016.

[112] K Saitoh, NA Mortensen, and M Koshiba. Air-core photonic band-gap fibers: the impact of surface modes. *Optics Express*, 12(3):394–400, 2004.

[113] Rodrigo Amezcua-Correa, NGR Broderick, MN Petrovich, F Poletti, and DJ Richardson. Optimizing the usable bandwidth and loss through core design in realistic hollow-core photonic bandgap fibers. *Optics Express*, 14(17):7974–7985, 2006.

[114] Rodrigo Amezcua-Correa, Frédéric Gérôme, Sergio G Leon-Saval, NGR Broderick, Tim A Birks, and Jonathan C Knight. Control of surface modes in low loss hollow-core photonic bandgap fibers. *Optics Express*, 16(2):1142–1149, 2008.

[115] Hyang Kyun Kim, Jonghwa Shin, Shanhui Fan, Michel JF Digonnet, and Gordon S Kino. Designing air-core photonic-bandgap fibers free of surface modes. *IEEE Journal of Quantum Electronics*, 40(5):551–556, 2004.

[116] Michel JF Digonnet, Hyang Kyun Kim, Jonghwa Shin, Shanhui Fan, and Gordon S Kino. Simple geometric criterion to predict the existence of surface modes in air-core photonic-bandgap fibers. *Optics Express*, 12(9):1864–1872, 2004.

[117] Martin Cordier, Adeline Orieux, Renaud Gabet, Thibault Harlé, Nicolas Dubreuil, Eleni Diamanti, Philippe Delaye, and Isabelle Zaquine. Correlation engineering for a flexible raman free fibered photon source. In *Lasers and Electro-Optics Europe & European Quantum Electronics Conference (CLEO/Europe-EQEC, 2017 Conference on)*, pages 1–1. IEEE, 2017.

[118] Benoît Debord, Foued Amrani, Luca Vincetti, Frédéric Gérôme, and Fetah Benabid. Hollow-core fiber technology: The rising of "gas photonics". *Fibers*, 7(2):16, 2019.

[119] John von Neumann and Eugene P Wigner. Über merkwürdige diskrete eigenwerte. In *The Collected Works of Eugene Paul Wigner*, pages 291–293. Springer, 1993.

[120] Chia Wei Hsu, Bo Zhen, A Douglas Stone, John D Joannopoulos, and Marin Soljačić. Bound states in the continuum. *Nature Reviews Materials*, 1(9):16048, 2016.

[121] B Debord, A Amsanpally, M Chafer, A Baz, M Maurel, JM Blondy, E Hugonnot, F Scol, L Vincetti, F Gérôme, et al. Ultralow transmission loss in inhibited-coupling guiding hollow fibers. *Optica*, 4(2):209–217, 2017.

[122] Fabio Giovanardi, A Cucinotta, and Luca Vincetti. Inhibited coupling guiding hollow fibers for label-free dna detection. *Optics express*, 25(21):26215–26220, 2017.

[123] Benoît Debord, Meshaal Alharbi, Tom Bradley, C Fourcade-Dutin, YY Wang, Luca Vincetti, Frédéric Gérôme, and F Benabid. Hypocycloid-shaped hollow-core photonic crystal fiber part i: Arc curvature effect on confinement loss. *Optics Express*, 21(23):28597–28608, 2013.

[124] Enrique AJ Marcatili and RA Schmeltzer. Hollow metallic and dielectric waveguides for long distance optical transmission and lasers. *Bell Labs Technical Journal*, 43(4):1783–1809, 1964.

[125] JA Stratton. Electromagnetic theory, mcgrow-hill, new-york. *Electromagnetic theory. McGraw-Hill, New York.*, page 524, 1941.

[126] MMZ Kharadly and JE Lewis. Properties of dielectric-tube waveguides. In *Proceedings of the Institution of Electrical Engineers*, volume 116, pages 214–224. IET, 1969.

[127] Luca Vincetti and Valerio Setti. Waveguiding mechanism in tube lattice fibers. *Optics express*, 18(22):23133–23146, 2010.

[128] Anton N Kolyadin, Alexey F Kosolapov, Andrey D Pryamikov, Alexander S Biriukov, Victor G Plotnichenko, and Evgeny M Dianov. Light transmission in negative curvature hollow core fiber in extremely high material loss region. *Optics express*, 21(8):9514–9519, 2013.

[129] YY Wang, Natalie V Wheeler, Francois Couny, PJ Roberts, and F Benabid. Low loss broadband transmission in hypocycloid-core kagome hollow-core photonic crystal fiber. *Optics letters*, 36(5):669–671, 2011.

[130] Fei Yu, William J Wadsworth, and Jonathan C Knight. Low loss silica hollow core fibers for 3–4 µm spectral region. *Optics express*, 20(10):11153–11158, 2012.

[131] Matthias Zeisberger and Markus A Schmidt. Analytic model for the complex effective index of the leaky modes of tube-type anti-resonant hollow core fibers. *Scientific reports*, 7(1):11761, 2017.

[132] Matthias Zeisberger, Alexander Hartung, and Markus Schmidt. Understanding dispersion of revolver-type anti-resonant hollow core fibers. *Fibers*, 6(4):68, 2018.

[133] Benoît Debord, Meshaal Alharbi, Tom Bradley, C Fourcade-Dutin, YY Wang, Luca Vincetti, Frédéric Gérôme, and F Benabid. Hypocycloid-shaped hollow-core photonic crystal fiber part i: Arc curvature effect on confinement loss. *Optics Express*, 21(23):28597–28608, 2013.

[134] Luca Vincetti. Empirical formulas for calculating loss in hollow core tube lattice fibers. *Optics express*, 24(10):10313–10325, 2016.

[135] KE Lynch-Klarup, ED Mondloch, MG Raymer, Damien Arrestier, Frédéric Gérôme, and F Benabid. Supercritical xenon-filled hollow-core photonic bandgap fiber. *Optics express*, 21(11):13726–13732, 2013.

[136] M Azhar, NY Joly, JC Travers, and P St J Russell. Nonlinear optics in xe-filled hollow-core pcf in high pressure and supercritical regimes. *Applied Physics B*, 112(4):457–460, 2013.

[137] Kevin Zielnicki, Karina Garay-Palmett, Daniel Cruz-Delgado, Hector Cruz-Ramirez, Michael F O'Boyle, Bin Fang, Virginia O Lorenz, Alfred B U'Ren, and Paul G Kwiat. Joint spectral characterization of photon-pair sources. *Journal of Modern Optics*, 65(10):1141–1160, 2018.

[138] Yoon-Ho Kim and Warren P Grice. Measurement of the spectral properties of the two-photon state generated via type ii spontaneous parametric downconversion. *Optics Letters*, 30(8):908–910, 2005.

[139] Marco Liscidini and JE Sipe. Stimulated emission tomography. *Physical review letters*, 111(19):193602, 2013.

[140] Bin Fang, Offir Cohen, Marco Liscidini, John E Sipe, and Virginia O Lorenz. Fast and highly resolved capture of the joint spectral density of photon pairs. *Optica*, 1(5):281–284, 2014.

[141] Andreas Eckstein, Guillaume Boucher, Aristide Lemaître, Pascal Filloux, Ivan Favero, Giuseppe Leo, John E Sipe, Marco Liscidini, and Sara Ducci. High-resolution spectral characterization of two photon states via classical measurements. *Laser & Photonics Reviews*, 8(5), 2014.

[142] Iman Jizan, Bryn Bell, LG Helt, Alvaro Casas Bedoya, Chunle Xiong, and Benjamin J Eggleton. Phase-sensitive tomography of the joint spectral amplitude of photon pair sources. *Optics letters*, 41(20):4803–4806, 2016.

[143] E Ortiz-Ricardo, C Bertoni-Ocampo, Z Ibarra-Borja, R Ramirez-Alarcon, D Cruz-Delgado, H Cruz-Ramirez, K Garay-Palmett, and AB U'Ren. Spectral tunability of two-photon states generated by spontaneous four-wave mixing: fibre tapering, temperature variation and longitudinal stress. *Quantum Science and Technology*, 2(3):034015, 2017.

[144] Antoine Monmayrant, Sébastien Weber, and Béatrice Chatel. A newcomer's guide to ultrashort pulse shaping and characterization. *Journal of Physics B: Atomic, Molecular and Optical Physics*, 43(10):103001, 2010.

[145] Pierre Tournois. Acousto-optic programmable dispersive filter for adaptive compensation of group delay time dispersion in laser systems. *Optics communications*, 140(4-6):245–249, 1997.

[146] Frederic Verluise, Vincent Laude, Z Cheng, Ch Spielmann, and Pierre Tournois. Amplitude and phase control of ultrashort pulses by use of an acousto-optic programmable dispersive filter: pulse compression and shaping. *Optics letters*, 25(8):575–577, 2000.

[147] Jennifer Erskine. *Characterization and Modification of Fiber-based Photon Pair Sources*. PhD thesis, Université d'Ottawa/University of Ottawa, 2018.

[148] Thibault Harlé. *Sources fibrées de paires de photons : caractérisation et influence de la non-uniformité*. PhD thesis, Laboratoire Charles Fabry; Unviservité Paris Saclay, 2018.

[149] Shellee D Dyer, Martin J Stevens, Burm Baek, and Sae Woo Nam. High-efficiency, ultra low-noise all-fiber photon-pair source. *Optics express*, 16(13):9966–9977, 2008.

[150] Hugues De Riedmatten, Valerio Scarani, Ivan Marcikic, Antonio Acín, Wolfgang Tittel, Hugo Zbinden, and Nicolas Gisin. Two independent photon pairs versus four-photon entangled states in parametric down conversion. *journal of modern optics*, 51(11):1637–1649, 2004.

[151] PR Tapster and JG Rarity. Photon statistics of pulsed parametric light. *Journal of Modern Optics*, 45(3):595–604, 1998.

[152] Justin B Spring, Patrick S Salter, Benjamin J Metcalf, Peter C Humphreys, Merritt Moore, Nicholas Thomas-Peter, Marco Barbieri, Xian-Min Jin, Nathan K Langford, W Steven Kolthammer, et al. On-chip low loss heralded source of pure single photons. *Optics express*, 21(11):13522–13532, 2013.

[153] Wolfgang Mauerer, Malte Avenhaus, Wolfram Helwig, and Christine Silberhorn. How colors influence numbers: Photon statistics of parametric down-conversion. *Physical Review A*, 80(5):053815, 2009.

[154] NI Nweke, P Toliver, RJ Runser, SR McNown, JB Khurgin, TE Chapuran, MS Goodman, RJ Hughes, CG Peterson, K McCabe, et al. Experimental characterization of the separation between wavelength-multiplexed quantum and classical communication channels. *Applied Physics Letters*, 87(17):174103, 2005.

[155] Dik Bouwmeester, Jian-Wei Pan, Matthew Daniell, Harald Weinfurter, and Anton Zeilinger. Observation of three-photon greenberger-horne-zeilinger entanglement. *Physical Review Letters*, 82(7):1345, 1999.

[156] Jian-Wei Pan, Dik Bouwmeester, Matthew Daniell, Harald Weinfurter, and Anton Zeilinger. Experimental test of quantum nonlocality in three-photon greenberger–horne–zeilinger entanglement. *Nature*, 403(6769):515, 2000.

[157] Maria Corona, Karina Garay-Palmett, and Alfred B U'Ren. Third-order spontaneous parametric down-conversion in thin optical fibers as a photon-triplet source. *Physical Review A*, 84(3):033823, 2011.

[158] Johannes Nold, P. Hölzer, N. Y. Joly, G. K. L. Wong, A. Nazarkin, A. Podlipensky, M. Scharrer, and P. St J. Russell. Pressure-controlled phase matching to third harmonic in ar-filled hollow-core photonic crystal fiber. *Optics letters*, 35(17):2922–2924, 2010.

Titre : Génération de paires de photons dans les fibres à cristaux photoniques à cœur creux

Mots clés : information quantique, paires de photons, mélange à quatre ondes, intrication, fibre

Résumé : Les sources de paires de photons sont un composant essentiel des technologies émergentes en information quantique. De nombreux travaux ont permis des avancées importantes utilisant des processus non linéaires d'ordre 2 dans les cristaux et les guides d'ondes, et d'ordre 3 dans les fibres. Les limitations viennent dans le premier cas, des pertes et en particulier des pertes de couplage avec les fibres optiques et dans le second cas, du bruit dû à l'effet Raman dont le spectre est très large dans les fibres de silice. Ce projet propose une nouvelle architecture basée sur des fibres à cristal photonique à coeur creux (FCPCC) que l'on peut remplir de liquide ou de gaz non linéaire. Cette configuration permet la génération paramétrique de paires de photons corrélés par mélange à quatre ondes sans l'inconvénient de la diffusion Raman. Cette technologie offre une large gamme de paramètres à explorer en s'appuyant sur les propriétés physiques et linéaires contrôlables des FCPCC et la possibilité de remplissage de ces fibres avec des fluides aux propriétés non-linéaires variées. En effet, par une conception judicieuse de la FCPCC et un choix approprié du liquide ou du gaz, il est possible de (i) contrôler la dispersion et la transmission pour générer des photons corrélés sur une large gamme spectrale avec lacondition d'accord de phase la plus favorable, (ii) d'ajuster la taille de coeur de la fibre et/ou sa forme pour augmenter sa nonlinéarité ou son efficacité de couplage avec d'autres fibres et (iii) de s'affranchir totalement de l'effet Raman si on utilise par exemple un gaz monoatomique, ou d'obtenir des raies Raman fines, aisément discriminables des raies paramétriques dans le cas d'un liquide.

Title : Photon-pair generation in Hollow-Core Photonic Crystal Fiber

Keywords : quantum information, photon-pair, four-wave mixing, entanglement, fiber

Abstract: Photon pair sources are an essential component of the emerging quantum information technology. Despite ingenious proposals being explored in the recent years based on either second order nonlinear processes in crystals and waveguides or on third order processes in fibers, limitations remain, due to losses and specifically coupling losses in the former case and due to Raman generation in silica, giving rise to a broad spectrum noise in the latter. These limitations have been challenging to lift because of the limited alternative nonlinear materials that fulfil the conditions for the generation of bright and high fidelity photon pairs in integrable photonic structures. In the present project, we develop a new and versatile type of photonic architecture for quantum information applications that offers access to a variety of nonlinear optical materials that are micro-structured in optical fiber forms to generate photon pairs, without the drawback of Raman scattering and with a large design parameter-space. Indeed, with a careful design of the HCPCF along with the appropriate choice of fluid, one can (i) control the dispersion and the transmission to generate photons with the most favourable phase-matching condition over a large spectral range, (ii) adjust the fibre core size and/or shape to enhance nonlinearity or the coupling efficiency with other fibres, (iii) totally suppress the Raman effect in monoatomic gases for instance or have only narrow and separated Raman lines that can thus be easily separated from the useful parametric lines in liquids.